



The Effects of Hydrogen Peroxide and Sodium Hypochlorite Oxidizing Treatments on the Color Properties of Naturally Colored Green Cotton

Ali Serkan Soydan¹, Arzu Yavaş¹, Osman Ozan Avinç¹, Gizem Karakan Günaydın²,
M. Niyazi Kivılcım³, Mehmet Demirtaş³, Sema Palamutcu*¹

¹ Pamukkale University, Textiles Engineering Department, Denizli, Turkey

² Pamukkale University, Buldan Vocational School, Buldan, Denizli, Turkey

³ Cotton Research Institute, Nazilli, Aydın, Turkey

*Corresponding Author email: spalamut@pau.edu.tr

Abstract

The cultivation of naturally colored cotton has captured the attention lately due to the increasing environmental concerns and problems. The green color in cotton fibers is owing to a lipid biopolymer (suberin) sandwiched between the lamellae of cellulose microfibrils in the secondary wall. Naturally colored green cotton fiber does not need dyeing or coloration process due to their inherent color characteristics leading to more ecological and sustainable textile production. Naturally colored cotton growers and producers have less requirement for the pesticides, insecticides since these varieties have already insect and disease-resistant qualities as well as they exhibit property for drought and salt tolerant leading to more environmental friendly cotton fiber production. The colorimetric (CIE L*, a*, b*, C*, h°, K/S etc.) properties of studied naturally green colored Turkish cotton fiber were explored before and after scouring (with NaOH), and oxidizing processes with hydrogen peroxide and sodium hypochlorite (with different sodium hypochlorite concentrations and different oxidizing treatment periods and at different pH levels, with or without scouring process as a precursor treatment etc.) in comparison with their greige (un-treated) counterpart. The application of scouring process with NaOH to naturally green colored cotton fiber increases the color yield levels leading to darker appearance. Similarly, hydrogen peroxide and sodium hypochlorite oxidizing processes resulted in an increase in the color yield levels of naturally green colored cotton fibers leading to darker appearance. Even at high sodium hypochlorite concentrations such as 200 ml/l at pH 12 and room temperature for 48 hours, the naturally green colored cotton fibers maintain their color.

Key words

naturally colored cotton, oxidizing, sodium hypochlorite, hydrogen peroxide, color

1. INTRODUCTION

It is known that naturally colored cotton originated around 5,000 years ago in the Andes region. Therefore, naturally colored cotton is not a novel concept and its cultivation history dates back 5000 years [1-4]. Naturally colored cottons, containing natural cotton fibers with natural pigments, have been planted for thousand years but have captured limited interest till the recent years owing to their short fiber length and poor fiber strength features [5, 6]. With the sophisticated genetic breeding techniques, nevertheless, naturally colored cotton fibers in various

shades of green and brown have been effectively manufactured with existing conventional textile machineries [7]. Unlike conventional cotton fibers dyed with synthetic dyes, the colors of which tend to fade, the natural color of the naturally colored cotton fiber actually deepens after repeated washings [8]. Apart from their inherent color characteristics, these fibers also display natural flame resistance properties leading to increased attention for different end-use applications [9,10]. Naturally colored cotton fiber is naturally pigmented fiber which grows in different shades of green and brown. Historical records also state the existence of browns with the shades of pink and lavender tints [11]. Naturally colored cottons have a minor niche market and naturally colored cotton fibers available today are usually shorter, weaker, and finer than regular Upland cottons. However, these fibers can be spun effectively into ring and rotor yarns for many different applications [12]. These fibers also can be blended with conventional off-white cotton fibers or mixed amongst themselves. Naturally colored cotton fibers are currently grown in China, Peru, and Israel. Also, Turkey produces naturally colored cotton fibers in different shades of brown and green. Different shades of brown and green naturally colored fibers are the main colors which are available in the market. Other different colors such as mauve, mocha, red are also available in Peru in a very limited supply and some other new shades are under investigation. The color for brown and red-brown naturally colored cotton fibers appears to be in vacuolar tannin material bodies in the lumen of the fiber. The different shades of brown and red-brown are mostly because of catechin-tannins and protein-tannin polymers [13].

On the other hand, green color in naturally colored cotton fibers is because of a lipid biopolymer (suberin) sandwiched between the lamellae of cellulose microfibrils in the secondary wall [13-14]. It is right point to state that brown naturally colored cotton fibers (and white lint) do not comprise suberin. Green naturally colored cotton fibers are categorized by high wax content (14 –17% of the dry weight) while white and brown fibers comprise about 0.4 –1.0% wax [13]. Latest research studies regarding naturally colored cottons reported that naturally colored brown cotton fiber is very similar in morphology to off-white (white) cotton fiber while naturally colored green cotton fiber is different as it comprises suberin. Suberin comprising primarily bifunctional fatty acids can theoretically generate a three dimensional network in the existence of glycerol, which is also found in green cotton fiber nevertheless not in white cotton fiber. How this 3D network affects the structure of the individual crystallites of cotton fiber cellulose was examined in that study. According to their outcomes, the researchers stated that the presence of suberin does not affect the structure of the individual crystallites nonetheless obstructs the development of the crystallites in the naturally colored green cotton fibers [15]. In the literature, it is stated that green is the second important commonly occurring lint color in cotton fibers. Therefore, green color in naturally colored cotton fibers is less common than brown shade and ensues primarily in two shades such as green and lighter green shade. Green color is more prone to fading and naturally green colored cotton fiber fades quicker than the naturally brown colored cotton fiber. Extended exposing to sunlight during boll opening resulted in quick fading of green color and the color turns to white, off-white or brownish shades. It is also reported that part of lint that is not directly subjected to sunlight preserves its original lint color [16]. It is known that the loom state cotton fiber fabric contains approximately 8-12% natural impurities of total weight of the cotton fiber [17]. Alkali treatment, scouring or hydrophilizing treatment are generally applied to cotton fibers in order to remove these impurities in the cotton fibers. Although bleaching and/or dyeing processes may generally not be applied to naturally colored cotton fibers, scouring process (alkali treatment or hydrophilizing treatment) is generally applied to naturally colored cotton fibers in order to increase the hydrophilicity levels of cotton fibers. In comparison to off-white cotton fibers, naturally brown colored cotton fibers have similar percentage of wax in their content however naturally green colored cotton fibers have much higher wax content in the fiber. This higher wax content of naturally green colored cotton fiber with pectin and lignin could decrease the moisture absorbency of treated naturally green colored cotton fibers with warm water and NaOH solution to decrease the hydrophobic content and enhance moisture regain of green cotton fibers. After alkali treatment process, naturally green colored cotton fibers displayed higher moisture absorbency and decrease on the crystalline region of the fiber. [18].


Hypochlorites as bleaching substances are still popular even though the anti-chlorine lobby and ecological pressures against the usage of hypochlorites in textile processes. Sodium hypochlorite, a sodium salt of hypochlorous acid (HOCl), solution is strongly alkali (pH ~ 11.55) and the free caustic presence in the solution acts as a stabilizer. After bleaching with hypochlorite, the fiber is generally treated with dilute hydrochloric acid to neutralize any alkaline present in the fabric. An antichlor treatment with sodium thiosulphate or bisulphite can be also advised to eliminate any residual chlorine from the fabric. Finally, the fabric is then washed with water to rinse out acid from the fabric [17]. Hydrogen peroxide is an oxidizing agent and also very common for cotton bleaching process. As mentioned earlier, even though bleaching process may generally not be applied to naturally colored cotton fibers, the behavior of naturally colored cotton fibers and their colorimetric property changes (such as color permanency performance and shade shifting possibility etc.) after the application of bleaching treatments such as hydrogen peroxide and sodium hypochlorite oxidizing treatments can arouse curiosity and interest. Therefore, in this study, colorimetric (CIE L^* , a^* , b^* , C^* , h^0 , K/S etc.) properties of studied naturally green colored cotton fiber were investigated before and after scouring (with NaOH), and oxidizing processes with hydrogen peroxide and sodium hypochlorite (with different sodium hypochlorite concentrations and different oxidizing

treatment periods, with or without scouring process as a precursor treatment etc.) in comparison with their greige (un-treated) counterpart.

2. MATERIALS AND METHODS

Naturally green colored cotton unique fiber type was selected and cultivated for this study under the control of the Turkey Nazilli Cotton Research Institute in the Aegean region of Turkey. This utilized naturally green colored unique Turkish cotton fiber is *Gossypium hirsutum* L. Visual appearance and properties of the used naturally green colored cotton fiber type are given in the Table 1.

Table 1 Detailed information of used Turkish naturally green colored cotton fiber [19]

Registered Name of the Cotton Fiber	Akdemir
Visual appearance	
Color of the fiber	Green
Scientific Species Name	<i>Gossypium hirsutum</i> L.
Registered fiber length (UHM) (mm)	25.8
Registered fiber fineness (micronaire)	3.3
Registered average fiber strength (1000 lb/inch ²)	72.9
Registered Ginning efficiency (%)	21.6
Average Days of maturity (days)	116
Plant type	In conical form

Scouring and Oxidizing Processes

Scouring process (with NaOH), conventional bleaching process [with hydrogen peroxide (H₂O₂), and sodium hypochlorite (NaOCl)] and the combination application of scouring and bleaching processes together (scouring + bleaching) were applied to studied naturally colored green Turkish cotton fiber type in order to examine their colorimetric (CIE L^* , a^* , b^* , C^* , h^0 , K/S) properties before and after different wet pre-treatments. The application procedures of implemented scouring and bleaching processes for studied naturally colored green cotton fibers are shown in Table 2. In this study, there are three different types of pre-treatment processes. First one is only scouring process with sodium hydroxide. The second one is a direct bleaching process with hydrogen peroxide or sodium hypochlorite without any scouring process involvement (directly from greige to bleached). The third process type is the combination sequential usage of scouring and bleaching processes (scouring then bleaching = scouring + bleaching with hydrogen peroxide or sodium hypochlorite). Moreover, different sodium hypochlorite oxidizing treatments (in varying concentrations: 40-100-200 ml/l sodium hypochlorite at various pHs: pH 11, pH 11.7, and pH 12) were applied to naturally green colored cotton fibers. Scouring and hydrogen peroxide bleaching processes of naturally green colored cotton fibers were carried out at 90°C for 30 minutes and 60 minutes, respectively, using Ataç Lab Dye HT model IR sample dyeing machine via the exhaustion process. Different sodium hypochlorite oxidizing treatments were applied to green cotton fibers at ambient room temperature (~20°C) for 6, 24 and 48 hours. In this study, the effects of bleaching with sodium hypochlorite at their inherent natural pH levels but without the involvement NaOH on the color properties of naturally green colored cotton fiber was also examined at ambient room temperature (The rightmost hand side column of Table 2). Afterwards, all treated naturally green colored cotton fibers were washed firstly with warm water for 10 minutes then rinsed under tap water for 10 minutes. After washing cycles, fibers were flat-air-dried at room temperature. Then, the changes in the colorimetric properties of green naturally colored cotton fibers were determined after these pre-treatment processes in detail in comparison with their greige cotton fiber counterpart.

Table 2 Application conditions of implemented scouring and oxidizing processes to the naturally green colored cotton fiber

Application Conditions	Scouring	Bleaching with hydrogen peroxide	Bleaching with sodium hypochlorite	Bleaching with sodium hypochlorite
Concentrations	1 ml/l sequestering agent 1 ml/l non-ionic wetting agent % 2 caustic soda (NaOH)	2.5 g/l caustic soda 2.5 ml/l hydrogen peroxide (50%) (H ₂ O ₂) 2 g/l non-ionic wetting agent 1 g/l stabiliser	3 g/l caustic soda 1 ml/l non-ionic wetting agent 40 ml/l sodium hypochlorite (at pH 12)	1 ml/l non-ionic wetting agent 40-100-200 ml/l sodium hypochlorite (at pH 11, 11.70, 12)
Temperature (°C)	90	90	20	20
Time	30 minutes	60 minutes	6, 24, 48 hours	6, 24, 48 hours
Liquor ratio	1/25	1/25	1/25	1/25
After treatment (Washings)	Rinsing at 50 °C for 2 minutes then cold washing for 2 minutes	Rinsing at 50 °C for 2 minutes then cold washing for 2 minutes then neutralization with 1ml/l acetic acid for 2 minutes afterwards cold washing for 1 minute	Rinsing at 20 °C for 30 minutes with 10 g/l sodium sulfite	Rinsing at 20 °C for 30 minutes with 10 g/l sodium sulfite

Colorimetric Measurements

The CIE L^* , a^* , b^* , C^* , and h^0 coordinates were measured and the K/S (Color strength) values calculated from the reflectance values at the appropriate wavelength of maximum absorbance (λ_{max}) for un-treated and treated naturally colored green cotton fiber samples using a DataColor SpectraFlash 600 (DataColor International, Lawrenceville, NJ, USA), spectrophotometer (D65 day light, 10° standard observer). Each naturally colored green cotton fiber sample was read in four different areas, twice on each side of the fibers for consistency, and the average value was calculated and reported. The definitions and color measurement equations are shown below [20];

L^* = Lightness, darkness (100 = white, 0 = black)

a^* = red(+a), green (-a)

b^* = yellow(+b), blue (-b)

$$\text{Kubelka – Munk equation } (K/S) = (1 - R)^2 / 2R \quad (1)$$

$$C^*(\text{Chroma}) = [(a^*)^2 + (b^*)^2]^{1/2} \quad (2)$$





$$h^0 = \arctan(b^*/a^*) \quad (3)$$

3. RESULTS AND DISCUSSION

Color Properties of naturally green colored cotton fibers before and after bleaching with hydrogen peroxide

When Table 3 and Figure 1 were examined, the color yield of the greige (un-treated) naturally green colored cotton was 3.7 (K/S). After scouring treatment, the color yield value increased to 6.77 (K/S) leading to darker appearance. This determination is in line with the results of the study of Kang et. al. [21]. In their study, the influence of scouring process on the colorimetric properties of naturally colored cotton fibers was investigated. Three naturally colored cotton fibers (buffalo brown, coyote brown, and green cotton) were treated with two alkali solutions (sodium carbonate and sodium hydroxide) and one enzyme solution (mixture of pectinase and cellulase). In their research, similar darkening effect was obtained for colored cotton fibers after alkali treatment. After alkali treatment, the shade of cotton fiber became deeper and darker, and the alkali treatment solutions were also deeply colorized. Their outcomes displayed that the naturally colored cotton fibers became swollen and pigment in the colored cotton fibers moved toward the outer layer of the cotton fibers following alkali treatment. The colorized solutions could be expressed by the release of pigments from the cotton fiber [21]. Direct bleaching with hydrogen peroxide without the scouring treatment application as a precursor treatment resulted in 5.75 (K/S) leading to higher color yield than greige (un-treated) green cotton fiber (Table 3 and Figure 1). It is important to state that only scoured green cotton fiber exhibited stronger color yield with darker appearance in comparison with only bleached, with hydrogen peroxide, green cotton fiber (6.77 versus 5.75 K/S). Also scoured+ bleached, with hydrogen peroxide, green cotton fiber displayed higher color yield value than greige green cotton fiber (5.44 versus 3.70; Table 3). It can be stated that overall scouring process alone, bleaching process alone with hydrogen peroxide and scouring + bleaching process with hydrogen peroxide led to stronger color yield with darker appearance in comparison with greige (un-treated) naturally green colored cotton fiber. These measured results are actually in line with the visual observation from Table 3.

Table 3 Color properties of naturally green colored cotton fiber before and after hydrogen peroxide bleaching processes

Pre-Treatment type	L^*	a^*	b^*	C^*	h^0	K/S	
Greige (un-treated)	63.4	1.5	22.3	22.3	86.1	3.70	
Scoured	50.4	-0.3	17.4	17.4	91.0	6.77	
Bleached with hydrogen peroxide	50.1	1.1	17.0	17.0	86.2	5.75	
Scoured+ Bleached with hydrogen peroxide	52.5	2.2	19.0	19.2	83.5	5.44	

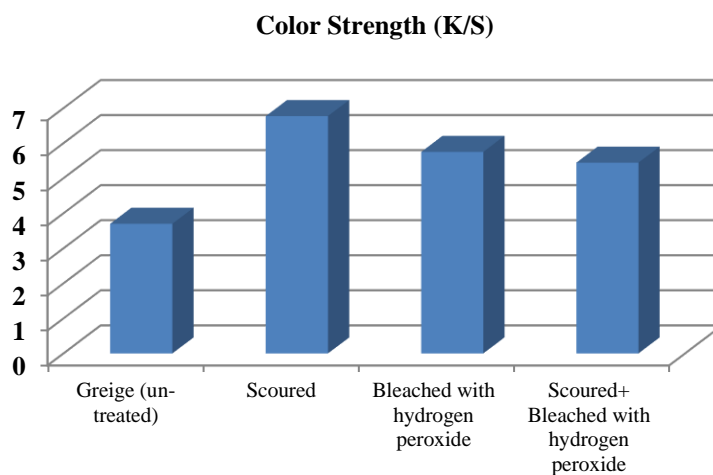


Figure 1 Measured color strength levels of green cotton fiber after scouring and hydrogen peroxide bleaching processes

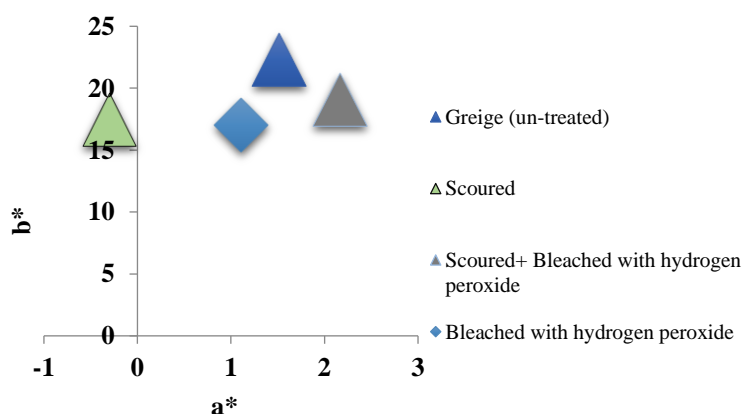


Figure 2 $a^* - b^*$ plot

Lightness (L^*) values of naturally green colored cotton fiber decreased after all three treatment types of scouring process alone, bleaching process alone with hydrogen peroxide and scouring + bleaching process with hydrogen peroxide leading to darker appearance in comparison with the greige green cotton fiber, as expected, which is in parallel with the aforementioned color yield increase after these processes (Table 3). When $a^* - b^*$ plot (Figure









2) is examined, scoured naturally green colored cotton fiber were slightly less yellow and slightly more green. When it comes to hue angle (h^0) results (Table 3), the hue angle of naturally green colored cotton fiber increased after scouring alone treatment from 86.1 to 91.0. Green cotton fiber bleached with hydrogen peroxide alone treatment displayed similar hue angle level with the greige green cotton fiber. On the other hand, scouring + bleaching with hydrogen peroxide combination process resulted in lower hue angle value than greige green cotton fiber (83.5 versus 86.1, Table 3). These measured slight hue shifts were in line with the visual observation from Table 3.

Color properties of naturally green colored cotton fiber before and after bleaching with sodium hypochlorite

When Table 4 and Figure 3 were examined, bleaching treatments with sodium hypochlorite in company with NaOH, without scouring process involvement as a precursor treatment, (direct bleaching without scouring process) displayed higher color yield values with higher K/S values (5.54, 5.49, 5.92; Table 4) than the color yield value of greige green cotton fiber (3.7).

It was found that the period (in hours) of hypochlorite bleaching application at room temperature did not exhibit an important influence on the color yield level of green colored cotton fiber. Scoured and then bleached, with sodium hypochlorite in company with NaOH, green cotton fibers also displayed high color yield values (K/S of 6.34, 6.56, and 6.29 for 6, 24 and 48 hours, respectively; Table 4 and Figure 3) which were slightly lower than the color yield of only scoured green cotton fiber (6.77, K/S).

Table 4 Color properties of naturally green colored cotton fiber before and after sodium hypochlorite bleaching processes

Pre-Treatment type	L^*	a^*	b^*	C^*	h^0	K/S	
Greige (un-treated)	63.4	1.5	22.3	22.3	86.1	3.70	
Scoured	50.4	0.3	17.4	17.4	91.0	6.77	
Bleached (with 40 ml/l hypochlorite at pH 12) for 6 hours	53.6	0.6	18.3	18.3	88.0	5.54	
Bleached (with 40 ml/l hypochlorite at pH 12) for 24 hours	54.6	1.0	19.3	19.3	87.0	5.49	
Bleached (with 40 ml/l hypochlorite at pH 12) for 48 hours	53.3	0.6	19.0	19.0	88.1	5.92	
Scoured + Bleached (with 40 ml/l hypochlorite at pH 12) for 6 hours	52.0	0.6	19.0	19.0	88.1	6.34	
Scoured + Bleached (with 40 ml/l hypochlorite at pH 12) for 24 hours	51.0	0.1	18.8	18.8	90.4	6.56	
Scoured + Bleached (with 40 ml/l hypochlorite at pH 12) for 48 hours	49.7	0.2	17.2	17.2	90.8	6.29	

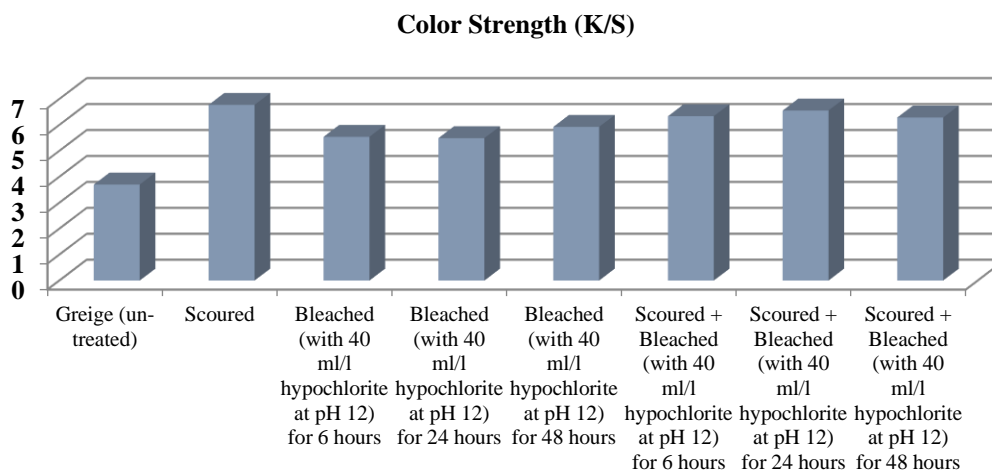


Figure 3 Measured color strength levels of green cotton fiber after scouring and sodium hypochlorite bleaching processes

Lightness (L^*) values of naturally green colored cotton fiber decreased after all three treatment types of scouring process alone, bleaching process alone with sodium hypochlorite and scouring + bleaching process with sodium hypochlorite leading to darker appearance in comparison with the greige green cotton fiber, as expected, which is in parallel with the aforementioned color yield increase after these processes (Table 4 and Figure 3). When $a^* - b^*$ plot (Figure 4) is examined, both bleached (bleached with 40 ml/l sodium hypochlorite at pH 12) green cotton fiber and the scoured and then bleached (scoured + bleached with 40 ml/l sodium hypochlorite at pH 12) green cotton fiber sample were slightly less red and slightly less yellow in comparison with greige green cotton fiber. Only scoured naturally green colored cotton fiber were slightly greener and slightly less yellow when compared with sodium hypochlorite bleached green cotton fiber samples (Figure 4). It is known that sodium hypochlorite solution is strongly alkali (pH ~ 11.55) and the free caustic presence in the solution behaves as a stabilizer.

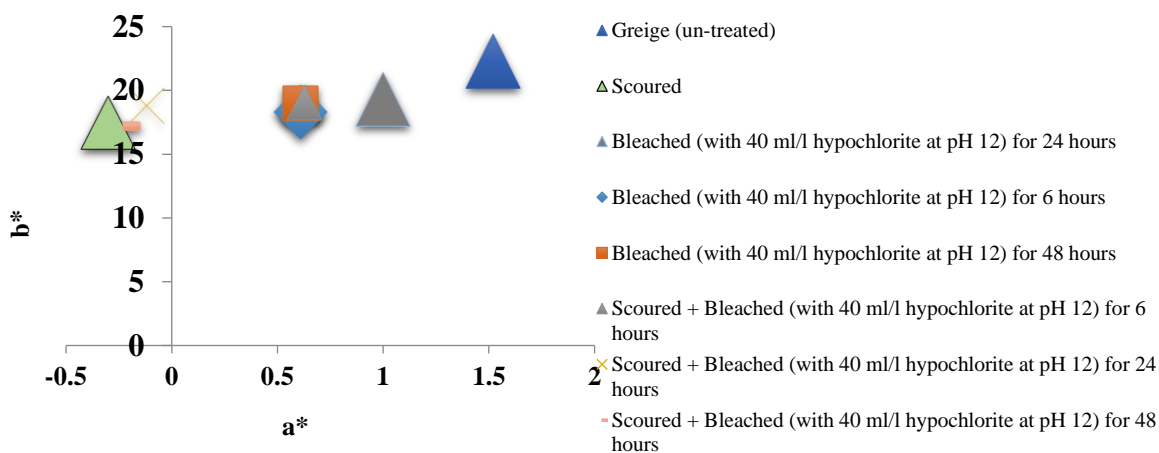


Figure 4 $a^* - b^*$ plot

The effects of bleaching with sodium hypochlorite at their inherent natural pH levels but without the involvement NaOH on the color properties of naturally green colored cotton fiber was also examined at ambient room temperature. When Table 5 and Figure 5 were investigated, the bleaching process pH value was found to vary depending on the sodium hypochlorite concentration in the bleaching process. As the sodium hypochlorite concentration increases, the pH value of the bleaching bath increases. It is obvious that the color yields of naturally green colored cotton fibers after various hypochlorite bleaching processes are lower than the color yield of scoured green cotton fiber (Table 5 and Figure 5). It seems that the period of sodium hypochlorite bleaching does not cause any significant change in color yield. However, the increase in sodium hypochlorite concentration causes significant changes in color yield. As the sodium hypochlorite concentration increases, the color yield value decreases and the lightness (L^*) value increases leading to lighter appearance with lower color yield levels.

The naturally green colored cotton fiber bleached (with 200 ml/l sodium hypochlorite, such high concentration, at pH 12) for 48 hours displayed significantly lower color yield value than the color yield of scoured green cotton fiber (3.77 versus 6.77, K/S; Table 5 and Figure 5). However, it is right place to point out that this sample (bleached with 200 ml/l sodium hypochlorite at pH 12 for 48 hours) exhibited similar color yield level with the greige (un-treated) naturally green colored cotton fiber (3.77 versus 3.70, K/S; Table 5 and Figure 5). Naturally green colored cotton fibers do not lose their color after sodium hypochlorite bleaching. Sodium hypochlorite bleached naturally green colored cotton fibers are redder and yellower than the scoured naturally green colored cotton fiber (Figure 6).

Table 5 Color properties of naturally green colored cotton fiber before and after sodium hypochlorite bleaching processes varying in sodium hypochlorite concentration and application period

Pre-Treatment type	L*	a*	b*	C*	h^o	K/S	
Greige (un-treated)	63.4	1.5	22.3	22.3	86.1	3.70	
Scoured	50.4	-0.3	17.4	17.4	90.1	6.77	
<i>Bleached (with 40 ml/l hypochlorite at pH 11) for 6 hours</i>	52.1	0.1	17.9	17.9	89.6	5.80	
<i>Bleached (with 40 ml/l hypochlorite at pH 11) for 24 hours</i>	52.2	0.1	18.9	18.9	89.6	5.74	
<i>Bleached (with 40 ml/l hypochlorite at pH 11) for 48 hours</i>	53.4	0.1	18.3	18.3	89.4	5.50	
<i>Bleached (with 100 ml/l hypochlorite at pH 11.7) for 6 hours</i>	57.7	2.3	21.4	21.5	84.0	4.82	
<i>Bleached (with 100 ml/l hypochlorite at pH 11.7) for 24 hours</i>	58.2	2.8	21.4	21.6	82.5	4.66	
<i>Bleached (with 100 ml/l hypochlorite at pH 11.7) for 48 hours</i>	58.0	1.61	19.89	19.95	85.4	4.35	
<i>Bleached (with 200 ml/l hypochlorite at pH 12) for 6 hours</i>	63.8	3.82	23.5	23.81	80.8	3.65	
<i>Bleached (with 200 ml/l hypochlorite at pH 12) for 24 hours</i>	62.5	3.34	22.29	22.54	81.5	3.65	
<i>Bleached (with 200 ml/l hypochlorite at pH 12) for 48 hours</i>	61.6	3.32	21.77	22.02	81.3	3.77	

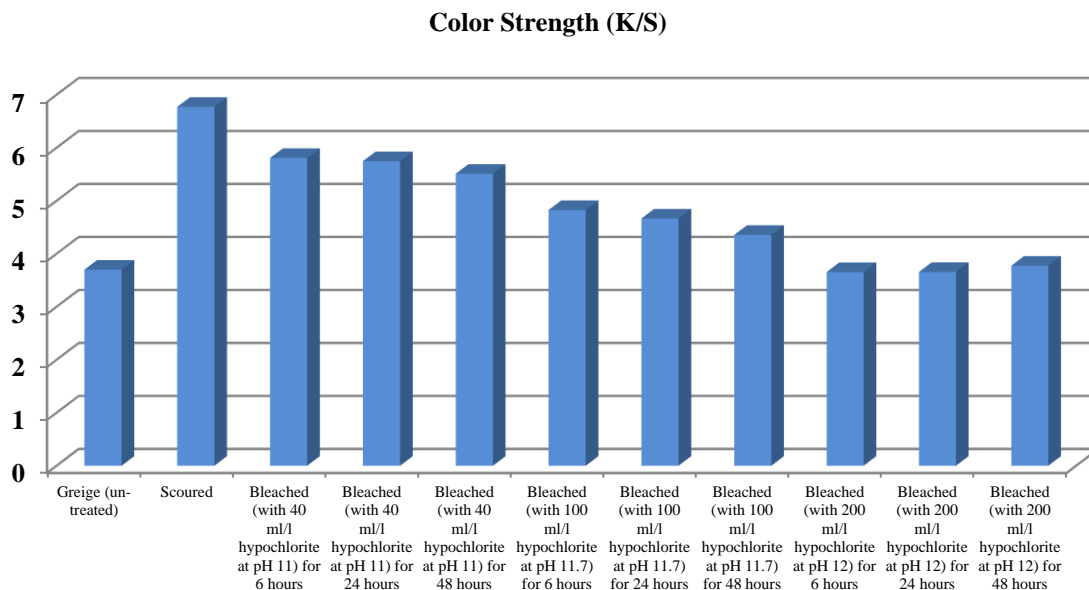


Figure 5 Measured color strength levels of green cotton fiber after scouring and sodium hypochlorite bleaching processes varying in sodium hypochlorite concentrations

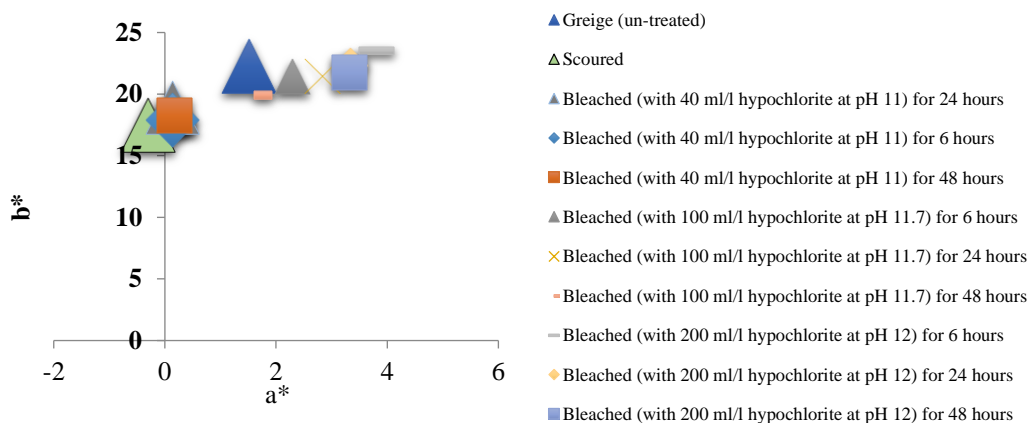


Figure 6 a* -b* plot

4. CONCLUSIONS

The cultivation of naturally colored cotton fiber has captured the attention lately due to the increasing ecological concerns and problems. In this study, colorimetric (CIE L^* , a^* , b^* , C^* , h^0 , K/S etc.) properties of studied naturally green colored Turkish cotton fiber were explored before and after scouring (with NaOH), and oxidizing processes with hydrogen peroxide and sodium hypochlorite (with different sodium hypochlorite concentrations and different oxidizing treatment periods, with or without scouring process as a precursor treatment etc.) in comparison with their greige (un-treated) counterpart. Naturally green colored cotton unique fiber type (*Gossypium hirsutum L.*) was selected and cultivated for this study under the control of the Turkey Nazilli Cotton Research Institute in the Aegean region of Turkey. According to the results of this study, the application of scouring process with NaOH to naturally green colored cotton fiber increases the color yield levels and darkens the color leading to darker appearance. It is known that natural inherent pigments inside the naturally colored cotton fibers moves toward the outer layer of the naturally colored cotton fibers after alkali scouring process leading to darkening effect and therefore darker appearance. Hydrogen peroxide and sodium hypochlorite bleaching oxidizing processes resulted in an increase in the color yield levels of naturally green colored cotton fibers leading to darker appearance. The further increase of the sodium hypochlorite concentration leads to the decrease on the color yield levels leading to lighter appearance. However, this drop in color yield is close to the color values of the un-treated greige naturally colored green cotton fiber sample. Even at high sodium hypochlorite concentrations such as 200 ml/l at pH 12, the naturally green colored cotton fibers maintain their natural color.

REFERENCES

- [1]. Vreeland, J. and James, M. (1999). The revival of colored cotton. *Scientific America*, 280 (4), 112-119
- [2]. Lee, J. (1996). A new spin on naturally colored cotton. *Agricultural Research* 44 (4), 20-21
- [3]. Mohammadioun, M., Gallaway, M. and Apodaca, J. K. (1994). An economic analysis of organic cotton as a niche crop in texas. University of Texas at Austin, Bureau of Business Research, Austin, Texas
- [4]. Burnett, P., 1995, Cotton naturally, *Textile Horizons*, Vol.15, February, pp 36–38
- [5]. Robbins, J. *Destination Discovery* 1994, 18–21, Khadi, B. M.; Kulkarni, V. N. *Indian Text J* 1996, 106(11), 72–76
- [6]. Lee, J. *Agric Res* 1996, 44, 20–21, Elesini, U. S.; Richards, A. F.; Rowe, T. *Proceedings 30th International Symposium on Novelties in Textiles*, Ljubljana, 1996, pp 122–125
- [7]. Kohel, R. *Crop Sci* 1985, 25, 793–797, Fox, S. V. *Proceedings: Sixth Annual Engineered Fiber Selection Conference*, May 3–5, 186–189
- [8]. Williams, B. L.; Horridge, P. *Text Tech Int* 1997, 31–36
- [9]. VanZandt, M. J.; Horridge, P.; Dever, J. K. *Clothing Text Res J* 1997, 15(4), 246–251
- [10]. Chen, H. L., & Yokochi, A. (2000). X-ray diffractometric study of microcrystallite size of naturally colored cottons. *Journal of Applied Polymer Science*, 76(9), 1466-1471.
- [11]. Matusiak M, Frydrych I. Investigation of Naturally Coloured Cotton of Different Origin – Analysis of Fibre Properties, *FIBRES & TEXTILES in Eastern Europe* 2014; 22, 5(107): 34-42
- [12]. Kimmel, L.B. and Day, 2001, M.P., *AATCC Rev.*, 1(10), 32, 2001
- [13]. Ryser, U., Cotton fiber initiation and histodifferentiation, in *Cotton Fibers, Developmental Biology, Quality Improvement, and Textile Processing*, Basra, A.S., Ed., Haworth Press, Binghamton, New York, 1999, chap. 1, pp. 21–29
- [14]. Ryser, U., Meier, H., & Holloway, P. J. (1983). Identification and localization of suberin in the cell walls of green cotton fibres (*Gossypium hirsutum* L., var. green lint). *Protoplasma*, 117(3), 196-205.
- [15]. Elesini, U. S., Cuden, A. P., & Richards, A. F. (2002). Study of the green cotton fibres. *Acta Chim. Slov*, 49, 815-833.
- [16]. P Singh, V V Singh, V. N Waghmare, Naturally Coloured Cotton, *CICR Technical Bulletin* NO: 4, http://www.cicr.org.in/pdf/naturally_colored_cotton.pdf
- [17]. Karmakar, S. R. (1999). *Chemical technology in the pre-treatment processes of textiles* (Vol. 12). Elsevier.
- [18]. Sho Yeung Kang, Helen H. Epps. (2009) Effect of scouring and enzyme treatment on moisture regain percentage of naturally colored cottons. *Journal of the Textile Institute* 100:7, pages 598-606.
- [19]. Osman Çağırğan, Ayhan Barut, “Nazilli Pamuk Araştırma Enstitüsündeki Genetik-Stok Pamuk Çeşitlerinin Özellikleri”, T.C. Tarım ve Köyişleri Bakanlığı Tarımsal Araştırmalar Genel Müdürlüğü Nazilli Pamuk Araştırma Enstitüsü Müdürlüğü, Yayın No:58, Nazilli, 2000, page 30.
- [20]. Avinc, O., & Yavas, A. (2017). Soybean: For Textile Applications and Its Printing. In *Soybean-The Basis of Yield, Biomass and Productivity*. InTech.
- [21]. Sho Yeung Kang; Epps, Helen H., Effect of Scouring on the Color of Naturally-colored Cotton and the Mechanism of Color Change, *AATCC Review*. Jul 2008, Vol. 8 Issue 7, p38-43. 6p



Design of a Robotic Pneumatic Pruner for Robotic Apple Harvesting

Erhan Kahya^{1*}, Selçuk Arın²

¹ Control and Automation Technology Department, Technical Sciences Vocational School, Namık Kemal University, 59030, Tekirdağ, Turkey

² Department of Agriculture Machine, Faculty of Agriculture, Namık Kemal University, 59030, Tekirdağ, Turkey.

*Corresponding Author email: ekahya@nku.edu.tr

Abstract

The robotic systems firstly developed in industrial production domain. But, in countries, in which the number of agricultural workers is limited and the costs are high, there is a tendency towards robotic technology in agricultural production. For this reason, the robotic system implementations started to seem in many agricultural activities. In the present study, the robotic system was discussed in terms of harvesting that is one of the agricultural activities. The robotic harvesting system consists of image processor, robotic arm, and gripper, which performs the final action. In this study, the position of fruit was determined in real-time by using the image processing. The X- and Y-coordinates sent to robotic arm directed the movement of it. Z-axis, which is the third axis and provides the forwards movement, was controlled using distance sensor. The designed pneumatic pruner system was mounted at the tip of robotic arm. The experiments were carried out on 100 Golden apples at different locations on the branch. Based on the coordinates of fruit, 85% positioning accuracy and 73% success rate were obtained in cutting the fruit from branch. The cutting success was statistically analyzed. At the end of study, the position of fruit stem corresponding to the tip of pruner, the position of pruner corresponding to the body of fruit, the fruit, or the beginning of stem rather than the stem itself, and the position of pruner on the shoot of stem were observed to cause failure during cutting procedure. According to the results obtained from experiments, it was concluded that the system to be used in such systems is the pneumatic pruner system.

Key words

Robotics, Harvesting, Apple, Pneumatic

1. INTRODUCTION

Mechanization technology field in the agriculture is in the important development in both our country and all around the world because of some reasons such as obtaining quality product and decreasing the labor force. Traditional production techniques have given its place to agricultural mechanization applications. For that reason, mechanization applications have become widespread in some fields such as planting, spraying, harvesting in different production areas. These kind of computer-aided systems have been used in the agriculture

with the advancement of technology and the introduction of the computer technology. In particular, all workings are automatically maintained in combine harvesters. Such systems provide us the transition to the robotics agriculture. Robotics agriculture, hydraulic and pneumatic systems are the agricultural systems that include both computer control systems and image processing technologies.

Even if produced systems are intelligent systems, all encodings must be performed by people. The system must be encoded with the help of the control parameters according to the process can be applied. It is expected that the machine must act in the way that it encoded by the people by understanding of the complexity of the workings. This act is called as robotics system action.

Robotics system action depends on the human factor entirely. Sensibility in the defining of the parameters which belong to workings affects the robotics system action. If the parameters are not suitable for the working expected result will not be proper. Environmental impacts, product features, the structure of the field, weather conditions are the factors that determine the robotics system action.

All input and output results must be well-analyzed for the expected action. The codes and expected results must be encoded exactly. Other additional equipments which will be used in robotics agriculture must be chosen correctly. Which system is needed, which controllers will control these systems and the selection of them are the factors that affect the functioning of the system. If these descriptions are inadequate and incomplete wrong harvesting, wrong seed planting, incorrect operation of automatic irrigation or incorrect amount of water can occur.

Kataoka et al. (2001) conducted a study for an automatic discovery system in detecting the location of apples for robotic apple harvesting. Decisions involving embalming. They stated that the fruit is the most important criterion to decide the harvest time. The Munsell color system is pre-primed, colored and separated in XYZ color units. According to this color, the time of harvest was found according to apple color.

Bulanon et al. (2004) conducted a research on the development of a real-time machine vision system for the apple harvesting robot. In this research, the red Fuji apple harvester has developed a real-time machine vision system for robot manipulator guidance. They took images from apple garden with CCD camera. The acquired images were transferred to the PC and the locations of the appliances were determined by image processing method. Under different light conditions, it is possible to recognize the fruits and determine their location. The red and green coefficients are used to identify the fruit. As a result of the research, they defined the fruit with an accuracy of 80% and an error margin of less than 3%.

Mao et al. (2009) conducted a study on the determination of the location of apples for robotic apple harvesting. They used two high-resolution digital cameras at the location of the fruit. They determined the selection of the fruit using color and shape analysis. The software they use for image processing is Microsoft C++ based RelCtrl. RelCtrl for C++ 'in vfw32.lib, JpegLib.lib, PRSDK.lib, and CDSDK.lib. They used their libraries. They are based on the following algorithm for the program. They determined 9.4% error rate in the process.

The important point for the above-mentioned systems is to obtain the data and information about the product to be harvested. Robotics system actions are provided at the end of the collected data and information. In the collected data; the robot is moved over this coordination by finding the coordination of the systems and lands.

Robotics agriculture systems use many technologies. It is an environmental approach that has a tight bond with the development of many technologic fields. Drug utilization, fertilization, irrigation and harvesting can be made more sensible. Robotics agriculture provides more sensitive agriculture. Energy consumption is maximum expense in the agriculture. It is required to provide the energy consumption less than before. Applications are applied only specific areas so, the lower energy consumption can be provided.

It can be achieved that more production will be done with less power and more efficient in the agriculture as a result of all this studies. Sensitive agriculture can provide that there can be less pollution in the world.

2. MATERIAL AND METHODS

2.1. MATERIAL

Figure 1 shows the locations of the values entered into the calculations for the pneumatic shear system. Table 1 shows the characteristics of the parallel holder used.

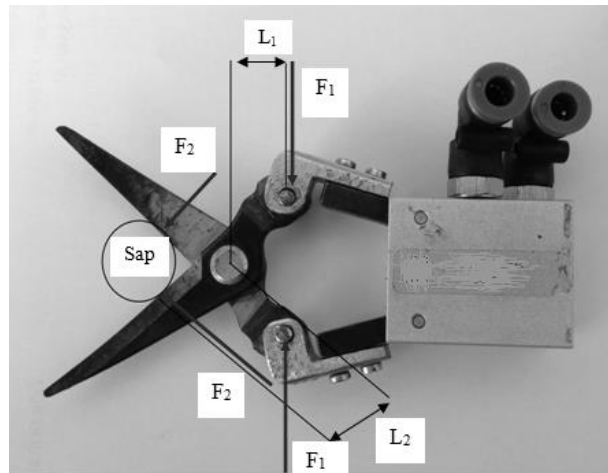


Figure 1. Values for pneumatic system

Calculation of the machine cutting force:

Cutting Strain(D. Dursun 2001) :

$$\tau = \frac{F}{A} \tag{1}$$

τ =Cutting Strain(N mm⁻¹)

A= Cross-section area (mm²) (D. Dursun 2001)

F=Force(N)

$$A = \frac{\pi \cdot d^2}{4} \tag{2}$$

d=Stem Diameter(mm)

Cutting Force(D. Dursun 2001) :

$$F_1 * L_1 = F_2 * L_2 \tag{3}$$

L₁=Steam length(mm)

L₂=Cutting Length(mm)

F₁= Force applied to the arm(N)

F₂=Cutting Force(N)

Pneumatic pressure (D. Dursun 2001):

$$P = \frac{F}{A} \tag{4}$$

P=Pressure(Pascal)

F=Force(N)

A= Cross-section area (mm²)

The system in Figure 1 is attached to the robotic system for cutting the fruit over the handle. Formulas 1, 2, 3 and 4 are used for the cutting stress applied during the cutting of the fruit. During formulas calculations, stem thicknesses were measured with calipers and values were recorded.

For L₁ and L₂ lengths,the measured values of pneumatic hose inner diameter with caliper are given below.

L₁=20 mm

L₂=25 mm

The inner diameter of the hose is 4 mm.

Hose Area (A) = 12,56 mm².

Table 1 Parallel the holder properties

Parallel the holder	
Movement Type	Double act
Pipe Type (mm)	16
Port Size	M5x0.8
Working environment	Air
Average pressure ratio (kgf cm ⁻²)	1.5~ 7 (0.15~0.7 MPa)
Operating temperature (C°)	-5 ~ +60
Max. Frequency (Devir d ⁻¹)	180
Max. Arm length (mm)	30
Free Devergence Angle	-10° ~ 30°
Technical moment(kgf cm ⁻¹)	Close 0.4 x P /Open 0.5 x P.
Clamp Force (F) (kgf)	F=M / L x 0.85
Sensor key	RCE , RCE1
Weight (gr.)	53

Table 2. Pneumatic cutting system

	Pressure Ratings (Bar)			
	5	6	7	8
F ₁ (N)	6.28	7.53	8.79	10.04
F ₂ (N)	5.02	6.03	7.03	8.04

2.2. METHODS

The most important variable is to know the space coordinate axes of the fruits in order to harvest the fruit with robotics system. Image processing technique has been applied in order to find the coordinate axes. 2D camera model has been used for image processing. Both horizontal axis (x) and vertical axis (y) have been found in the space coordinate axis of the fruits with this camera. Ultrasonic sensor has been used for the distance (z) which is the third coordinate axis. The code has been written in C# for the use of this sensor and the robot has been prevented when it reaches a certain distance. Necessary smooth and kinematic calculations have been written in C# which is necessary for image processing. These calculations and the program have been installed to the processor in the robotics system control card with USB port. The communication between the writing of the program and 2D camera has been provided. Coordinate axes to be obtained as a result of image processing and 2D camera coding have been found. Obtained results have been identified by using 2D camera interface and it

has been recorded. It has been provided that robotics arm stops and cut when it is 10cm in front of the fruit according to the value from the ultrasonic sensor via written program.

The most important point in the system is to introduce the fruit shape to the camera with the program in the camera. Shape recognition screen is shown in Figure 2.

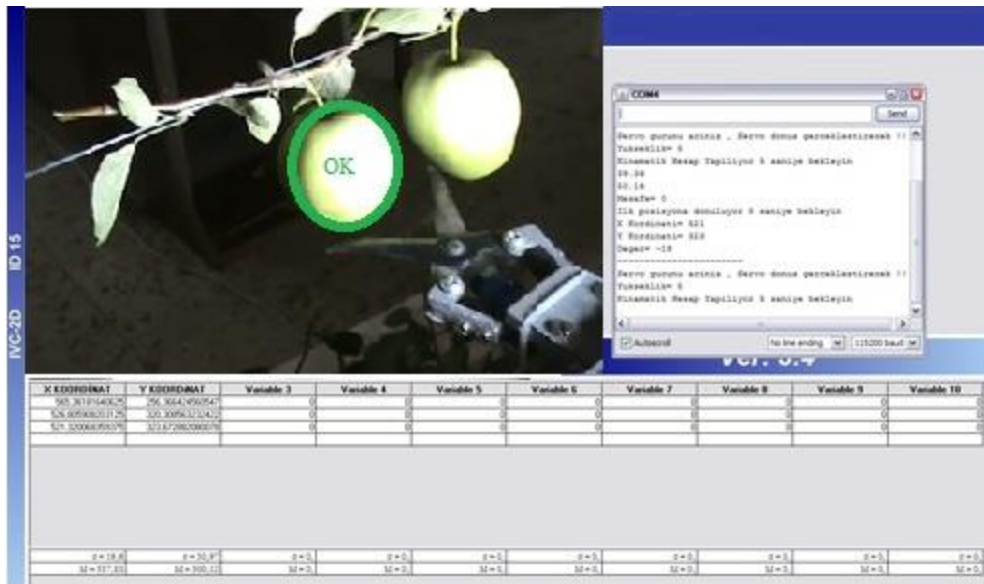


Figure 2. Shape Recognition Screen

Robot arm's movement has been provided after the calculation according to the coordinate from the camera in the Robotics Control card. Coordinate values from camera to processor are shown in Figure 3.

Index	DB Value	Value	Description
994	0	0	
995	0	0	
996	0	0	
997	0	0	
998	0	0	
999	0	0	
1000	160.402...	160.40225...	X KOORDINAT
1001	76.8049...	76.804977...	Y KOORDINAT
1002	0	0	
1003	0	0	
1004	0	0	
1005	0	0	
1006	0	0	
1007	0	0	
1008	0	0	

Figure 3. Coordinate values from camera to processor

The positioning of the robot arm has been conducted for both kiwi and apples. Fruits have been cut with the help of pneumatic cutting. Cutting action for apple is shown in Figure 4.



Figure 4. Cutting for apple

3.RESULTS AND DISCUSSION

The pressure value of the compressor which enables the operation of the pneumatic system varies between 5 - 8 bar. The force (F1) applied to the arm is calculated by the formula (4), the cut force (F2) by the formula (3). In Table 2, values F1 and F2 are shown.

The force (F1) and the cut stretching (F2) applied to the arm calculated by using formulas 3 and 4 are substituted into formula 1 and the cut stretching (τ) is calculated. For each type of fruit, 100 calculations were statistically analyzed. Statistical analysis was calculated according to the cutting conditions of the fruits. The results are summarized in Table 3.

Table 3. Exchanges cutting force for Apple

		Sum of Squares	df	Mean Squares	F	Sig.
a*	Between Groups	95.118	73	1.865	4.111E32	.000
	In-Group	.000	27	.000		
	Total	95.118	100			
b*	Between Groups	137.609	73	2.698	8.753E32	.000
	In-Group	.000	27	.000		
	Total	137.609	100			
c*	Between Groups	186.847	73	3,664	1.188E33	.000
	In-Group	.000	27	.000		
	Total	186.847	100			
d*	Between Groups	244.169	73	4.788	6.351E32	.000
	In-Group	.000	27	.000		
	Total	244.169	100			

*a=5 bar, b=6 bar, c=7 bar, d=8 bar

At the end of the experiments, the wrong value of the robot arm has been determined as 15% for apples. The reason for this is that the camera chooses the fruit randomly during finding the coordinate in the fruits that stand side by side or back to back in the experiments. It has been determined that the most suitable fruit coordinates

have been given. It is required to choose color camera which processes three-dimensional image in order to prevent this.

The cut rate for the fruit is 73%. It has been found that the cause of the difference between finding and cutting is the location of the fruit on the scissors. As a result of the constructed T-test, it has been determined that not only the x-axis but also the y-axis are important for breaking the fruit over the branch. It has been found that during positioning of the scissors, the y-axis scissors are positioned on the stalk of the fruit. When the stalk of the fruit is on the tip of the scissors, when the scissors touches the fruit, when both fruit and the stalk of the fruit come to the initial point, they can cause errors for breaking process. According to the Anova test, pressure values ranging from 5 to 8 bar applied by the compressor were found to be significant for the cutting force. It is understood that the compressor pressure operating the pneumatic system provides sufficient pressure for the cutting operation. The change in pressure between 5 and 8 bar was found to have sufficient pressure values for the shear force. It has been determined that the pressure change in the compressor will not affect the cutting force.

4. CONCLUSION

It is understood that the system to be used in the gripper for the robotic system fruit harvesting is the pneumatic system. It has been determined that the applied pressure values are sufficient for cutting. It has been shown that the fruit must be pulled inward from the point of the scissors and held constant to increase the success rate in the cutting process. It was understood that the cutting performance would be increased by the vacuum system attached to the scissors system. It is considered that the special design of the fruit of the vacuum pad at the end of the vacuum generator used for pulling the fruit into the fruit will increase the success of holding the fruit constantly. It is understood that with this research the most important factor in the robot design is the gripper which provides the latest movement. As a result of the study, it has been seen that pneumatic cutting is the factor that will affect the system success besides all the parts and software of the robotic system.

REFERENCES

- [1]. Kataoka T, Okamoto H, Hata S (2001). Automatic Detecting System Of Apple Harvest Season For Robotic Apple Harvesting. 2001 ASAE Annual International Meeting, Sacramento Convention Center Sacramento, Paper Number: 01-3132, California, USA.
- [2]. Bulanon D.M, Kataoka T, Ota Y, Hiroma T (2004). Estimation Of Apple Fruit Location Using Machine Vision System For Apple Harvesting Robot. Internatioan Commision of Agricultural and Biosyemes Engineering the CIGR Journal of Scientific Research and Development, Volume 3, 1-6.
- [3]. Mao W, Ji B, Zhan J, Zhang X, Hu X (2009). Apple Location Method For the Apple Harvesting Robot. [Image and Signal Processing, CISP '09, 2nd International Congress on](#), ISBN:978-1-4244-4229-7, Chine.
- [4]. D. Dursun, 2001. *Cisimlerin Dayanımı Temel Ders Kitabı*. Milli Eğitim Basımevi, ISBN 975-11-1913-8, Ankara



The Importance of Waste and Environment Management in Printing Industry

Pelin Hayta^{1*}, Mehmet Oktav²

¹Sinop University, Department of Graphic Design, 57600, Gerze/Sinop, Turkey.

²Marmara University, Department of Printing Technologies, 34722, Göztepe/İstanbul, Turkey.

*Corresponding Author email: peлин@hayta.com.tr

Abstract

All kinds of materials that become useless during production activities, damage the environment and must be exterminated are generally called waste. Waste is also defined as all materials thrown away by its manufacturer or a person or entity who owns it and causes a harmful change at environment.

The most important of the solid, liquid and gaseous wastes produced in the printing industry before, during and after the printing process are waste ink, ink sludge and solvents emerging after machine washing, wastewater of water-based ink, plate and film developer and fixer solutions, waste papers, waste films, faulty prints, cleaning solvents and volatile organic compound (VOC) emissions emerging from IPA use. Some of these wastes fall into the hazardous waste category due to their processing characteristics during the production process. Effective and regular extermination of these wastes is necessary to protect the environment and employee health. This can be provided only by the application of waste management. Some wastes are recycled and reused at printing industry, but in some cases that recycling is impossible, these wastes should be eliminated without harming human health and environment. Especially the materials whose disposal is compulsory should be classified at the source and sent to licensed disposal companies.

As a new sector, waste management industry should develop new and special processes for printing technologies wastes. Owners of printing companies should be informed about waste management. At waste management process, the most appropriate clean production techniques should be used, waste production should be prevented or minimized and wastes should be recycled effectively.

The aim of this study is to provide suggestions and contributions for the possible best ways of preventing the wastes from harming the nature and disposing or recycling of the wastes generated during production in the printing industry.

Key words

Waste Management, Printing Wastes, Protecting the Environment

1. INTRODUCTION

Systems created and sustained by interrelationships between living creatures within a certain area and surrounding inanimate environments are named as “ecosystems”.

An ecosystem is consisted of four fundamental components: autotrophs, heterotrophs, saprophytes and habitat. The first three components represent living creatures existing within the inanimate environment created by the latest component. External factors affecting the rings of the habitat chain causes all the system to be harmed. Especially unconscious management of wastes, which is defined as all kinds of materials occurred and thrown away or left as a result of any activity in Environmental Laws, has a great effect on imbalance of ecosystem and rapid exhaustion of natural resources.

As a sector having a close interrelation with environment, printing industry is bound to natural raw materials for paper, ink and printing auxiliary production. As the source of cellulose, trees are highly needed especially in paper manufacturing sector. Trees also have a fundamental role in human life as source of oxygen. During production process, paper manufacturing sites use chemical auxiliaries and pollute the environment by releasing wastewater, chemical gases and various solid wastes besides exhausting oxygen sources rapidly by using trees in production. Usage and waste of paper as an end product requires a reproduction process using raw materials and creating waste. Therefore, paper recycle has an important role in ecosystem balance in terms of causing a dramatic decline in waste production and tendency of using natural raw materials. When used and wasted without waste management, ink, plastics, bath waters of films and plates and chemicals also become hazardous wastes polluting air and water.

Global Footprint Network, a company studying on human-based consumption tendency on world scale, has stated that the amount of the sources consumed at first 7 months of 2017 is higher than the amount that can be renewed in 12 months. This means humans released carbon, fished, logged and consumed water in an amount beyond the tolerance limit of oceans and forests. [1].

Waste is defined as something lying unproductive, inhabited, or desolate. Generally all waste appears in three forms, namely: solid waste, wastewater (liquid waste), and air emission [2].

Wastes generated in the printing house must be disposed of. The disposal methods can cause a serious threat to the environment and human life [3].

Ink, paper and chemical wastes may be solid, liquid and gaseous in printing industry. Management of these wastes is highly important in terms of minimizing the harms given to human and nature besides raising recycle awareness. By integrating consumed materials in production process, we may help ecosystem to become a renewable source in frame of sustainable life principle and economic growth.

2. EMERGENCE AND RECYCLING OF PRINTING INDUSTRY WASTES

The printing industry uses various printing technologies for printing books, magazine, newspapers, business documents, catalogues, form, etc. These technologies include lithography, rotogravure, flexography, screen, letter-press, and digital technologies including inkjet and electro-photography. The use of these technologies depends on the required quality of the print, number of impressions to be printed, availability of required resources, cost of the equipment, consumables cost per unit, need to use variable content, and other factor [4].

Printing process requires various fundamental printing technologies. Raw materials and chemicals used in production generate or become waste, as water used in some printing systems.

When the waste generated causes financial loss to a company and poses a threat to the environment-air, water, and land, then it becomes a problem to society at large [5].

The waste emerging in production process of printing system should be studied, categorized and treated according to an appropriate waste management procedure.

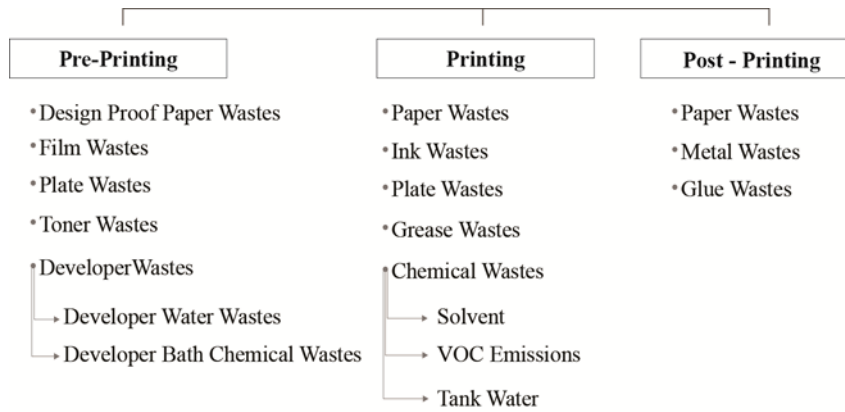


Figure 1. Printing Wastes [6], [7]

2.1. Inks

Ink is the diffusion of colouring agents in an adhesive system and transfers the image on a swage plate material. Inks generally consist of four fundamental materials; pigment, adhesive, solvent and additive agents. Liquid and badigeon inks contain pigment or colorants. Heavy metal content of this colorants pollute environment via waste inks. Titanium dioxide, chromate and molybdenum are some of the heavy metals used in printing inks.

Badigeon inks are used in offset, letterpress and sometimes screen printing systems while liquid inks are used in flexo and gravure printing systems. Solvents in liquid inks used in flexo and gravure printing systems are inflammable. Moreover, toluene in gravure ink is a toxic and inflammable material. Web offset inks also contain high levels of volatile organic compounds (VOC). When the solvents are volatilised and inks are used uncontrolled, these substances pose danger for human health [8].

According to the report of Trucost, a company providing consultancy service about environment and waste, printing plants affect environment by not only waste amount, but also greenhouse gas (disposed to be stored, burnt, reused or recycled) and volatile organic compounds (Volatile Organic Compound – VOC, except metan) they release. [9], [10].

Table 1. Sample formulations of gravure inks

General	Printing	Packaging	Water-based Printing Inks
%20 Pigment and Toner	% 8 Phthalo Blue	%33 Titanium Dioxide	% 15 Phthalo Blue
%28 Resin	% 15 Chlorinated Rubber	%22 Nitrocellulose Varnish	%47 Acrylic Resin
%47 Solvent	% 10 Phenolic Modified Resin	%37 Resin Ester Varnish	%30 Aqua
%5 Wax, Plasticiser and Additive Agents	%5 Plasticiser	%3 Plasticiser	%2 Alkali
	%1 PE Wax	%5 Wax Compounds	% 1 Foam Inhibitor
	%51 Toluene		% 2 PE Wax
	% 10 Ethyl Acetate		%3 Isopropanol

All solvents in printing inks (except water) are air contaminants. Therefore, waste printing inks should be recycled in frame of a controlled transformation procedure in order to protect human health and environment. The best method of controlled transformation is recycling or burning the solvent. While liquid inks as flexo and gravure ink solvents are generally recycled, web offset inks tend to be burnt.

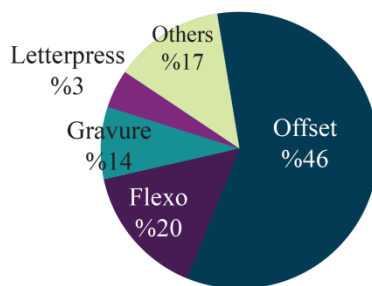


Figure 2. Ink consumption in 2012 according to worldwide printing techniques [11].

Flexo and gravure inks are recycled by a technique requiring organic solvents in printing press dryer exhaust to be imposed in a cabinet frozen by activated carbon and transferred to another cabinet to be cooled. When the exhaust is refrigerated, vapour and solvents are condensed and split into two layers and recycling process is over. Recycled solvents are re-integrated into production process by being sold or reused as a diluting solvent in printing press.

Burning: burning is the best technique to minimise final waste amount besides generating energy as an important recycling product. Moreover, burning is the most expensive recycling method [12].

Burning method aims to neutralise or shrink hygienically or, if economical, use the solid wastes for generating energy [13]. Solvents are burnt and eliminated by three methods; thermal burning, catalytic burning and cooling-condensation.

2.2. Paper / Paperboard in Press Industry

Printed papers are used in a wide range of products as books, magazines, newspapers, cardboard boxes, labels, etc. Paper is defined as printable sheets produced from pulp consisting of virgin fibres obtained from herbal cellulose via mechanic or chemical methods or fibres of used papers [14]. Pulp is the fundamental of all paper types and consists of cellulose, fibres and additive agents. Cellulose is the raw material of paper production process and obtained from trees which are at least 50% cellulose, some plants that are 98% cellulose and recycled papers.

When growth period and production volume of trees and other plants integrated in production process, it can be seen that amount of consumed trees and plants affect the ecosystem.

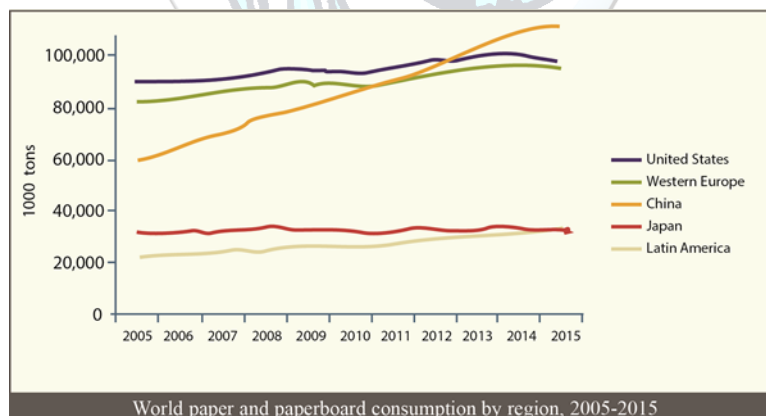


Figure 3. World paper and paperboard consumption by region, 2005 -2015 [15].

Besides a constant growth in production, it is also predicted that volume of paper and paper products will reach at 279 million tonnes in 2018 [16]. This figure shows that production process is in a huge need of raw material. When waste papers are recycled and integrated into production, less amount of raw material will be provided from environment and production costs will be reduced. Moreover, paper recycling enables to save from energy and water resources.

Recycling methods of paper wastes are defined according to paper quality and fibre structure of the papers. Each recycled kinds of paper cannot be integrated in each paper type. For example, as cardboard and corrugated cardboards cannot be used in newspaper production, paper wastes should be categorized after collected. Therefore, there are two types of processing before recycling;

- Special mechanical cleaning process not requiring cleaning the ink. They are integrated in cardboard and corrugated cardboard production processes.
- Mechanical and chemical cleaning process requiring cleaning the ink. Fibres integrated in newspaper, printing paper and carbon paper production process.

The first phase of recycling process is categorisation of papers. Categorisation process is carried out via an infrared sorting machine (this machine is developed by SORT IT European Union Research Project and used in a waste sorting plant in Linz, Austria, where papers coming from all over the Europe are sorted). Halogen lamp in the machine illuminates the wastes to be sorted. The light causes organic substances in papers to vibrate and give some kind of spectral fingerprint according to their compounds. By this means, inky and inkless products can be separated. Sorted papers are then cleaned at pulp production unit by being divided into fibres, grinded, bleached and washed. Then, fibres are transferred into machine approach unit and mixed and diluted. While this process is being carried out, the mixture is sent to pulp mixing unit after required chemicals and fillings are added. Paper machine then produces recycled paper by sieving, pressing, drying and calendaring the pulp coming in a certain thickness and width.

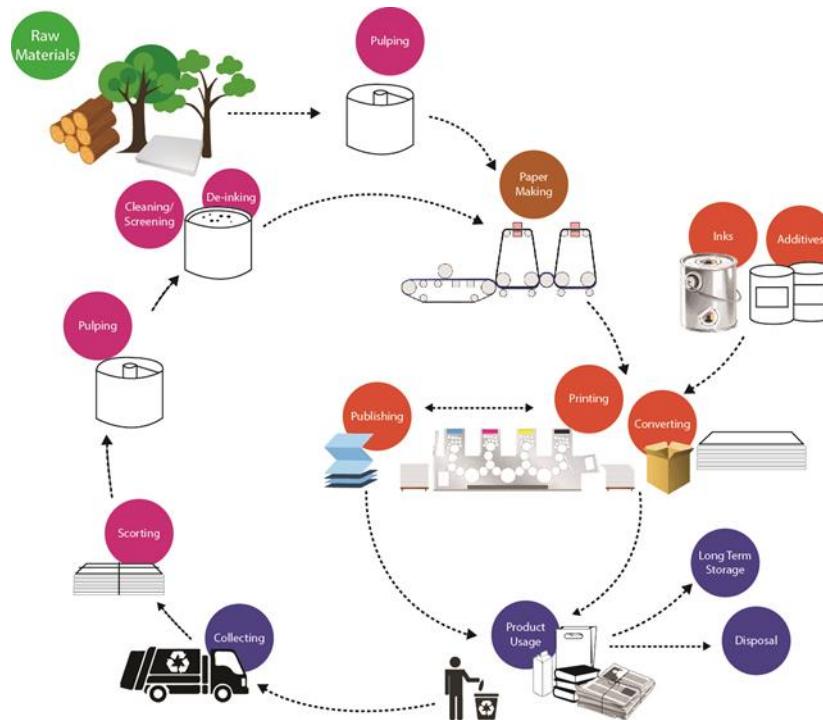


Figure 4. Recycling and Reuse of Waste Paper

Most of the digital and inkjet-printed papers were not be able to be recycled because of the surface coating enabling printing until recently. Organizations as International Association of the Deinking Industry (INGEDE) supporting researches carried out in deinking and collaborating with paper and press machine manufacturers, paper termination industry and additive agents suppliers has been seeking solutions for this problem. Digital Print De-inking Alliance (DPDA) has succeeded in most of the deinking tests on inkjet-papers recently [17]. This developments in paper recycle are shows that special papers produced for printing press can be recycled and integrated in production process in accordance with technological possibilities.

It is seen that recycling waste paper enables to save from water and energy needed for production. Figure 5 shows the advantages of paper recycling according to The State of the Paper Industry, Monitoring the Indicators of Environmental Performance-[15].

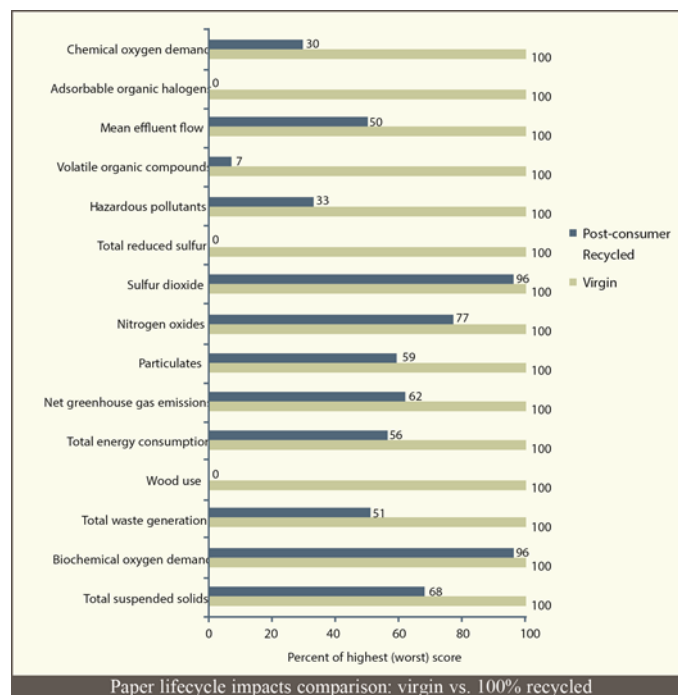


Figure 5. Paper lifecycle impacts comparison: virgin vs. 100% recycled.

2.3. Water and Chemicals

A great amount of wastewater can easily be generated during the printing process, due to the usage of chemicals that are either toxic or difficult to decompose: ink residues (containing zinc, chromium, barium, lead, manganese, benzene, dibutyl/ethyl acetates); waste fountain and cleaning solutions (spent organic solvents, including trichloroethane, methylene chloride, carbon tetrachloride, acetone, methanol); and other solvents and container residues (toluene, xylene, glycol ethers, methyl ethyl ketone, and ethanol). The greatest attention in printing industry deserves a purification and regeneration of wastewater [18].

Each phase of printing process, re-printing, printing and post-printing, generates chemical wastes. While pre-printing process generates plate bath chemicals and bath water wastes, in printing process ink, solvent, roller/plate/blanket cleaners, varnish, UV lacquer and tank water wastes and in post-printing process adhesive and varnish wastes emerge.

When the volume of printing industry is considered, the level of the damage caused by chemical wastes and water wastes can be understood better. Especially toluene, xylene, isophorone and solvents are the most hazardous chemicals. While toluene and xylene are compounds of ink, isophorone is found in some printing inks and adhesives. Solvents are chemicals used for different purposes.

Solvents are mostly used in;

- Flexo printing, gravure printing and screen printing as diluting solvent,
- Roller and blanket cleaning chemicals,
- Plate cleaning chemicals,
- Plate bath chemicals.

Chemical wastes (solvent, ink wastes or tank water wastes) should be burnt by using air filters and recycled by professional chemical waste recycling companies in accordance with related laws. Besides chemical wastes, tank water wastes and bath water wastes are released into environment in various ways and pollute the environment by going into sewage. Manufacturers should be linked to water infrastructure plants via sewage systems to exterminate wastewater. In this way, wastewater can be sorted and exterminated besides preventing contamination of underground waters, seas and potable waters.

2.4. Waste Gases

VOCs are defined as organic substances in 293,15 Kelvin (20°C) and 0,01kPa or higher vapor pressure. [19]. VOC is the abbreviation of volatile organic compound. VOCs are chemical having the potential of harming

people and human health. Some international regulations and legislation have been made and some precautions have been taken to decrease VOC emission amount and protect human health. These regulations decrease the limit the amount of solvent used in chemicals used for various purposes as pickling to 20%.

A Volatile Organic Compound (VOC) contains one or more carbon atoms and has a high vapour pressure that allows it to readily evaporate into the atmosphere. Once in the atmosphere, the compound participates in atmospheric photochemical reactions. Ground-level ozone is produced when nitrogen oxides and volatile organic compounds (VOC's) react in the presence of sunlight. This is a major component of urban smog, which, at elevated levels, presents a potential health hazard to people of all ages and possibly damages vegetation and degrades the environment [20].

A number of industrial activities make use of chemical products containing volatile organic compounds (VOCs), which are widely used mainly due to their high volatility. Among the activities that can result in the emission of such compounds in its working environments are the offset printing processes. The main indoor sources for VOCs are solvents and inks in the printing industry due to their low vapour pressure, significant amounts of toluene, xylenes, and other volatile compounds are emitted during the printing process, polluting the workplace environment. In addition, the cleaning procedures can result in exposures that are ten times higher than during other tasks because these cleaning products are petrol-based. The inks used in the offset process are made basically of a mixture of resins, vegetable or mineral oils, pigments, and solvents. The main ingredients of the conventional inks are pigments, binders, carriers and additives [21]. Volatile organic compounds (VOC emissions) consist the 98% or 99% of all toxic gas emissions generated by printing industry. VOC emissions emerge during cleaning of printing solutions, adhesives used in binding and drying phases [22].

3. WASTE MANAGEMENT

Waste management includes environment management activities as diminishing the waste at source, sorting, collecting, temporary storage, interim storage, recycling, exterminate and post-extermination control [23].

Waste management in printing industry varies according to each manufacturer activity and producing process. When pre-printing, printing and post-printing processes are considered, waste management should be applied according to raw material usage and production style. Therefore, ink wastes, paper and paper product wastes, wastewaters and chemical wastes require different waste and environment management methods.

The first aim of waste management is to prevent waste generation as much as possible or recycling the wastes. Accordingly, each manufacturer should define a system in accordance with his/her production style and raw material usage to be able to apply a waste management procedure. Figure 6 shows a general waste management sample in printing industry.



Figure 6. General waste management in printing industry

In waste management process ink wastes, wastewater and waste gases are the types requiring some precautions. This wastes contain hazardous chemicals and therefore should be eliminated after use.

The fundamental precaution is to use vegetable-based inks without heavy metals for printing and to keep the cap of the ink containers tightly closed not to contact with air. Printing process should be carried out in rooms including air tunnel to prevent emergence of waste gases. Moreover, required precautions should be taken to prevent chemicals to contact with human body.

As ink wastes, wastewater, chemical wastes and waste gases are impossible to be recycled, these should be exterminated in accordance with related laws.

Paper and paper wastes are recyclable within waste management system. Process of sorting after production, transferring to recycling plants via paper collecting companies and recycling the papers raises energy save in environment management besides diminishing raw material need to be met from nature.

4. CONCLUSION AND RECOMMENDATIONS

This study examines environment and waste management approach in printing industry. Each production step of printing process generates waste. These wastes may be categorized as solid, liquid and gaseous wastes and some are defined as hazardous wastes. Especially in preventing or recycling of hazardous wastes, printing industry should apply and appropriate waste management procedure.

Printing sector mostly generates paper and cardboard wastes. Paper and cardboards are one of the oldest and most used packaging materials and generate some of the wastes in edge trimming and sizing process, some in printing adjustment process and some in post-printing process. Most of the paper and cardboard wastes can be recycled and integrated as secondary fibres to production process after sorted, washed and deinked. This provides cellulose, the fundamental raw material of paper, to be originated from recycled papers to an extent. Recycling method of paper wastes should be defined according to paper quality and fibre structure.

The second printing material generating most waste is ink. Ink wastes emerge in post-printing phase but they are also hazardous in printing and post-printing phases, because the solvents they contain evaporates and pollutes air (except water-based inks). Therefore, inks should be recycled under control. The safest ways to recycle inks are recycling or burning the solvent they contain. While flexo and gravure inks are generally recycled, web offset inks are burnt. Besides recycling and extermination, modifying production process to prevent wastes is a method of avoiding wastes. This can be realised by use of water or vegetable-based inks in production.

VOC emissions evaporate as gaseous wastes and in hazardous waste class as toxic chemicals in printing industry. Most of the chemicals used in either pre-printing, printing or post-printing phase of each printing technique contains VOC emissions and requires some precautions. These precautions are to use water-based and organic solvents, use CTP while preparing printing press and preferring dry printing.

Waste management process should be carried out in frame of clean production techniques protecting environment and human health and aiming sustainable no waste production. Waste and environment management is also important in terms of maintaining the sustainability of ecosystem besides getting economic advantage by minimizing costs. Preventing the emergence of solid, liquid and gaseous wastes and recycling or extermination of the used products have become a necessity for protecting environment and human health.

When worldwide production volume of printing industry is considered, it can be seen that consumption may be integrated in production by collection, transfer and recycling of all types of wastes. Recycling and reuse of especially paper and cardboard wastes originated from natural raw materials diminish costs, saves energy and supports national economy. Therefore, each manufacturer should define a waste management plan considering its operation style and raw material type it uses. In frame of this plan, manufacturers should pay attention to prefer eco-friendly raw materials, minimizing waste generation in production process and recycling the generated wastes. Usage of non-recyclable and hazardous raw materials should be kept under control.

REFERENCES

- [1]. Hürriyet newspaper, 31.07.2017.
- [2]. Appiah, I. K., Printing techniques, Kumasi, Ghana: Kwame Nkrumah, University of Science & Technology Publishing, 2002.
- [3]. Causes and Sources of Waste in the Printing Industry in Ghana: A Study of Printing Houses in the Cities of Accra and Kumasi International Business Research July, Vol.1 No. 3, 2008
- [4]. Romano, F., An investigation into printing industry trends (PICRM-2004-01). Rochester, NY: Rochester Institute of Technology, Printing Industry Center, 2004.
- [5]. Appiah, I. K., Printing techniques. Kumasi, Ghana: Kwame Nkrumah, University of Science & Technology Publishing, 2002.
- [6]. Environmental, Health, and Safety Guidelines for Printing , International Finance Corporation, April 30, 2007.
- [7]. Journal of Cleaner Production, Management strategy for hazardous waste from atomised SME: Application to the printing industry L. Cristóbal Andrade, C. Gómez Míguez, M.C. Taboada Gómez, P.M. Bello Bugallo *Dept. of Chemical Engineering, School of Engineering, University of Santiago de Compostela, 15782 Santiago de Compostela, Spain.

- [8]. Matbaacının mürekkep hakkında bilmesi gerekenler, Dr. Nelson R. Eldred, s. 64, 178, 312 – 315, 2012.
- [9]. S&P Dow Jones Indices ESG Analysis (<https://www.trucost.com/>)
- [10]. Matbaa Haber, Sürdürülebilirlik başarı getiren yeşil ışık, Catherine Carter, 8 March 2012, <http://www.matbaahaber.com/tr/magazine/103/5579>
- [11]. A. Katariya, Presentation on future of water based inks, page 7, 2012.
- [12]. Atık, Çeşitleri, Atık Yönetimi, Geri Dönüşüm ve Tüketici: Çankaya Belediyesi ve Semt Tüketicileri Örneği
A. Anıl GÜNDÜZALP, Seval GÜVEN
- [13]. A.YILMAZ, Y. BOZKURT, Türkiye'de kentsel katı atık yönetimi uygulamaları ve kütahya katı atık birliği (KÜKAB) örneği, Suleyman Demirel University, The Journal of Faculty of Economics and Administrative Sciences, Vol.15, No.1 pp.11-28, Y.2010
- [14]. A. YAKUT, Geri dönüştürülebilir kullanılmış Kağıttan Yeni Kağıt Üretiminin İrdelenmesi, Tesisat Mühendisliği, Sayı 127, s. 70-73, Ocak/Şubat 2012.
- [15]. The State of the Paper Industry, Monitoring the Indicators of Environmental Performance, A collaborative report by the Steering Committee of the Environmental Paper Network, s. 15, 2007.
- [16]. B. Çevik, Kağıt ve ürünleri sektörü, İktisadi araştırmalar bölümü, Türkiye İş Bankası Raporu, s. 7-8, Mayıs 2016.
- [17]. The State of the Paper Industry, Monitoring the Indicators of Environmental Performance, A collaborative report by the Steering Committee of the Environmental Paper Network, s. 15, 2007.
- [18]. International Finance Corporation (IFC) (2007) Environmental, Health, and Safety Guidelines for Printing. pp. 1-18, (http://www.ifc.org/wps/wcm/connect/Topics_Ext_Content/IFC_External_Corporate_Site/IFC+Sustainability/Sustainability+Framework/Environmental,+Health,+and+Safety+Guidelines/. Accessed 10.10.2016.)
- [19]. European Union, 21.04.2004, Retrieved on 28.09.2010.
- [20]. CANADIAN PRINTING INK MANUFACTURERS ASSOCIATION WHAT ARE VOCs? VOC December 2010 Page 1 of 2
- [21]. H. Gecol, J.F. Scamehorn, S.D. Christian, B.P. Grady, F. Riddell, Use of surfactants to remove waterbased inks from plastic films, Colloids Surf.A: Physicochem.Eng. Aspects 189 (2001) 55–64. VOC emissions to air constitute approximately 98 to 99 percent of all toxic releases in the printing industry
- [22]. Environmental, Health, and Safety Guidelines for Printing, International Finance Corporation and World Bank Group, APRIL 30, 2007.
- [23]. Çevre Online, Atık Yönetimi, (<http://cevreonline.com/atik-yonetimi/> 10.09.2017)



MATLAB GUI Model for PV System Feasibility of a House Electricity Consumption in Turkey

Kubra Nur Akpınar^{1*}, Ayse Ceyda Bilu², Bedri Kekezoglu²

¹Ondokuz Mayıs University, Department of Electrical Electronics Engineering, Samsun, Turkey.

²Yildiz Technical University, Electrical Engineering, İstanbul, Turkey

*Corresponding Author email: kubranurbirlik@omu.edu.tr

Abstract

In this study, feasibility analysis was done with a program that created a simulation model in the MATLAB GUI environment for the PV system installation in the production of electricity requirement of a house in Turkey conditions. The energy consumption is calculated through the data of the operating hours in a day and the number of running days in a year which entered by user. Once the panel and zone selection options have been specified, the program calculates the annual energy need for the house, the energy generated, the number of panels required to produce this energy, and the area required for system. Monthly energy distribution is shown graphically. Calculations are being revised for different panel number usage. In the economic analysis part, system cost, payback period and annual earnings are determined. PV system model, consumers will invest in renewable energy that will help to make the pre-feasibility and can be used as a decision-making mechanism.

Key words

Feasibility analysis, MATLAB GUI, Payback Period, Photovoltaic System, Renewable Energy

1. INTRODUCTION

According to the definition of the International Energy Agency (IEA), renewable energy is defined as a type of energy that is constantly renewed and obtained from natural processes. According to this; solar energy, wind, biomass, biofuels, geothermal, hydraulic power, ocean resources and hydrogen energy obtained from natural sources are the energy sources that make up this concept [1]. Reducing foreign dependency since it is obtained from countries' own natural resources, being continuous as long as natural resources exist, lack of harms against the environment unlike fossil resources and the fact that it is safe are the reasons of preference of renewable energy. It helps economic development by creating new business areas in the country with the decrease of energy import [2].

In order to increase the use of our country's high renewable energy potential, green energy investments are being developed under the Renewable Energy Laws (REN). Wind and solar energy investments come to the forefront, based on the incentives and practices of these laws [2]. While wind energy is preferred for systems with great power, individuals throughout the world and especially in Germany produce their own energy by using solar energy without harming the environment by integrating PV panels into the roofs which are one of the smallest energy systems. Since this solar-generated energy has wave characteristic, it can be connected to the grid at times

when the sun is insufficient and can take electricity from the interconnected system or use storage tools such as accumulator, battery, etc.

In this study, the feasibility of integrating the PV system into the dwellings of a 4-member family, like in many other developed countries, was realized with the MATLAB GUI program.

2. MATERIALS AND METHODS

In the created model, it is waited from the user to enter the data of electrical devices powers, operating hours of them in a day and number of day in a year to calculate the total energy need in a year. If user need more devices to specify the power that undefined in the program, he/she can use the option "other" labeled.

After the entering power of devices, the next step of the program is PV panel and location choices. User selects one of the PV panels from the popup menu to install the system with, then chooses the location where it will be installed. Yingli Solar PV panels were used for the program as panel options and three districts from Izmir; Cigli, Dikili and Menderes as location examples in this study. Later on, exchange rate of dollar/Turkish liras is defined with the value of the day, to calculate the sale price of the surplus energy.

Then the run button is clicked and the program shows the results. It calculates the annual energy need and, required area, setup cost, installed power, panel number required of the suitable PV system according to the energy need, and annual energy production, annual earning, depreciation time of the system and the graph of generated energy by month. If the user has a thought to install the system with different panel number from calculated by program, he/can specify a new one. The screen of the program as shown below (Figure 1), without entering any data.

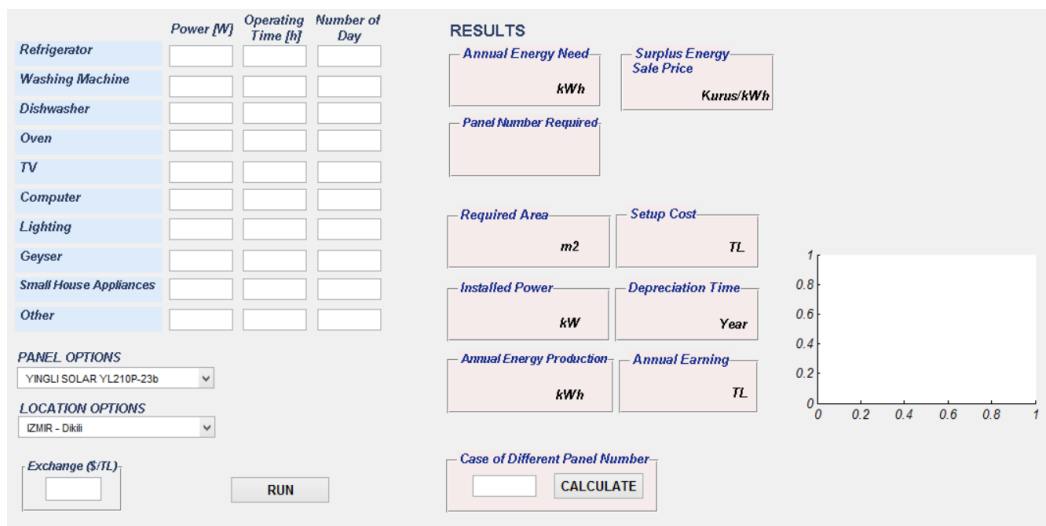


Figure 1. First screen of the program

Solar energy data are taken from SEPA (Solar Energy Potential Atlas) for selected regions. In this study, by using the global radiation values of the Dikili district of İzmir province, energy reaching a house in that area were calculated. When we look at the one-year radiation distribution in the SEPA radiation bar graph Figure 2, it appears that the selected zone is suitable for solar energy investment.

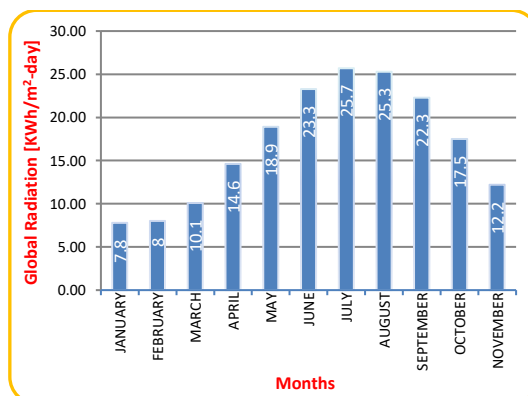


Figure 2: Izmir - Dikili Global Radiation Values [3]

Figure 3 shows air temperature data for selected regions, taken from the RETScreen program. RETScreen is a renewable energy feasibility program used by the Canadian government that supplies all atmospheric data from NASA. Detailed atmospheric solar data from the RETScreen program was also used in calculations to support global radiation data from SEPA for the selected region.

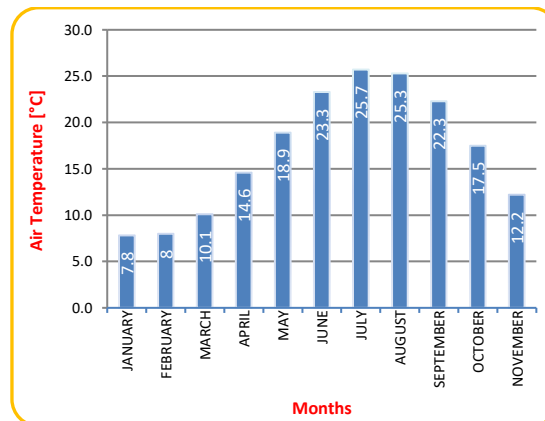


Figure 3: Air Temperature of Dikili [4]

3. MATHEMATICAL BACKGROUND

After providing the potential of solar energy and weather temperature data, the total solar energy, the required number of panels and the panel area is calculated. After the power of the annual energy requirement devices and the annual working hours are entered into the program as hours and days, with the multiplication and subsequent collection of the data of each device in itself, the number of panels required, is calculated by dividing the calculated energy requirement by the energy generated by one of the selected panels on the program in the selected region. The required space for the system setup is obtained by multiplying the selected panel by the required number of panels [5].

3.1. Calculation of Energy from the PV

NOCT (nominal cell operating temperature) is the cell temperature module with solar radiation of 0,8 kW/m², air temperature of 20°C and wind speed of 1 m/s [6]. T_{cell} [°C] is the cell temperature calculated from the air temperature, T_{air} [°C]. S is the solar radiation value [kW/m²]. The cell temperature was calculated under PTC conditions (PVUSA Test Conditions - air temperature = 20°C, radiation $S = 1$ kW/m²). P [kW] is PV panel power calculated using P_{mpp} (maximum power point) and κ [%/°C] (estimated power loss for each temperature value around 25°C) values. Annual solar energy E [MWh] is calculated by adding 10% operational loss, multiplying solar panel power with daily sun peak hour strike (solar peak hour/day).

$$T_{cell} = T_{air} + [(NOCT - 20^\circ\text{C})/0,8] \cdot S \quad (1)$$

$$P = P_{mpp} \cdot [1 - \kappa \cdot (T_{cell} - 25^\circ\text{C})] \quad (2)$$

$$E = P \cdot (\text{sun peak hour/day}) \cdot 365 \text{ day/year} \cdot 0,9 \quad (3)$$

$$\text{Panel Number} = \frac{\text{Daily Energy Demand}}{(\text{Power of a PV}) \cdot (\text{Sunshine Duration})} \quad (4)$$

3.2. Economic analysis

As a result of calculating the annual energy requirement, the next step is economic analysis. The following formulas are used to calculate the annual earnings and payback period obtained from the PV system.

$$\text{Payback Period} = \frac{\text{CAPEX}[TL]}{\text{Yearly Energy Produced}[kWh] \cdot 0,40[TL/kWh]} \quad (5)$$

The system cost (CAPEX: Capital Expenditure) is calculated by multiplying the system installation cost, which is taken as 4500 TL per kilowatt, with the installed power.

4. CASE STUDY

In this study, the pre-feasibility analysis of a complete house for a four-person household in the case of the complete supply of energy from the PV system was carried out using the MATLAB GUI program. The investor calculates the annual energy consumption by entering the data of the power of each household electrical appliances, the working hours, and the number of days the appliances work for each year into the program. To supply the consumed energy from the PV system, panel options are selected as desired. Region selection is made for the planned system to be established. Finally, the current dollar parity is entered and the results are evaluated.

As an example, required data to calculate annual energy need for a family of four, electrical devices powers was entered by us as shown below (Figure 4), YINGLI SOLAR YL200P-23b named PV model and Izmir-Dikili location was chosen and dollar parity value was typed as 3.7 for that day.

	Power [W]	Operating Time [h]	Number of Day
Refrigerator	1100	24	365
Washing Machine	2000	2	120
Dishwasher	1200	2	120
Oven	2500	1	75
TV	100	5	365
Computer	75	4	365
Lighting	90	5	365
Geysler	2000	1	365
Small House Appliances	500	1	100
Other	1000	2	120

Figure 4: Energy demand chart for each device

As output, the annual energy need and the optimum number of panels (53) required for the system are calculated. Accordingly, the area that needs investor, system installed power, annual generated energy, system cost, payback period, annual earnings and generated energy by month are calculated as shown below (Figure 5). If the person planning to install the system wants to use with different number of panels, he/she can change the panel number (i.e. 70 panels) on the program and accordingly the results on the screen are updated (Figure 6).

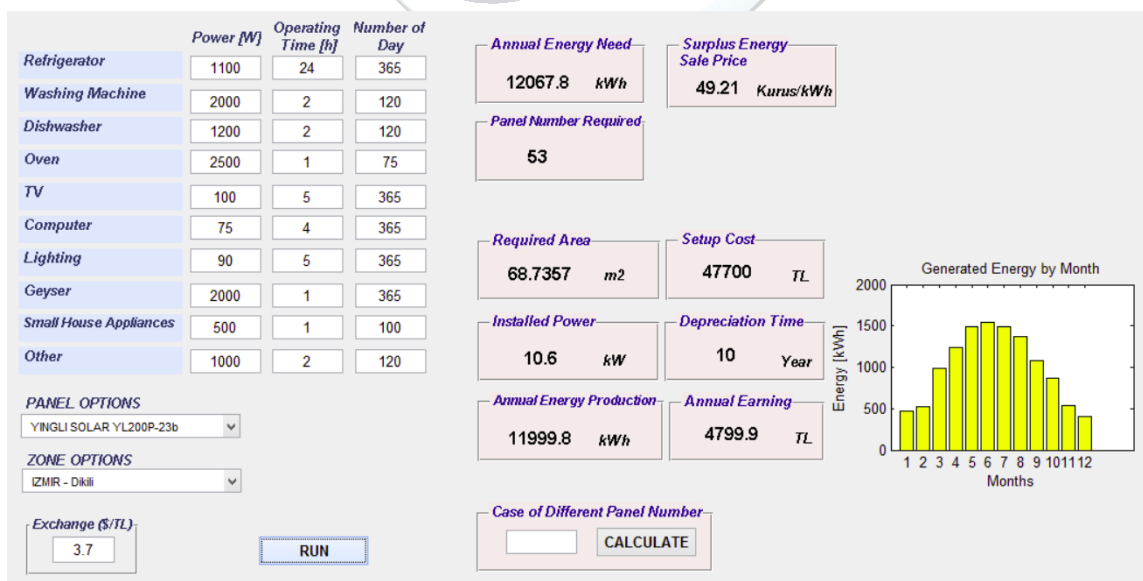


Figure 5: The results of the program according to defined example

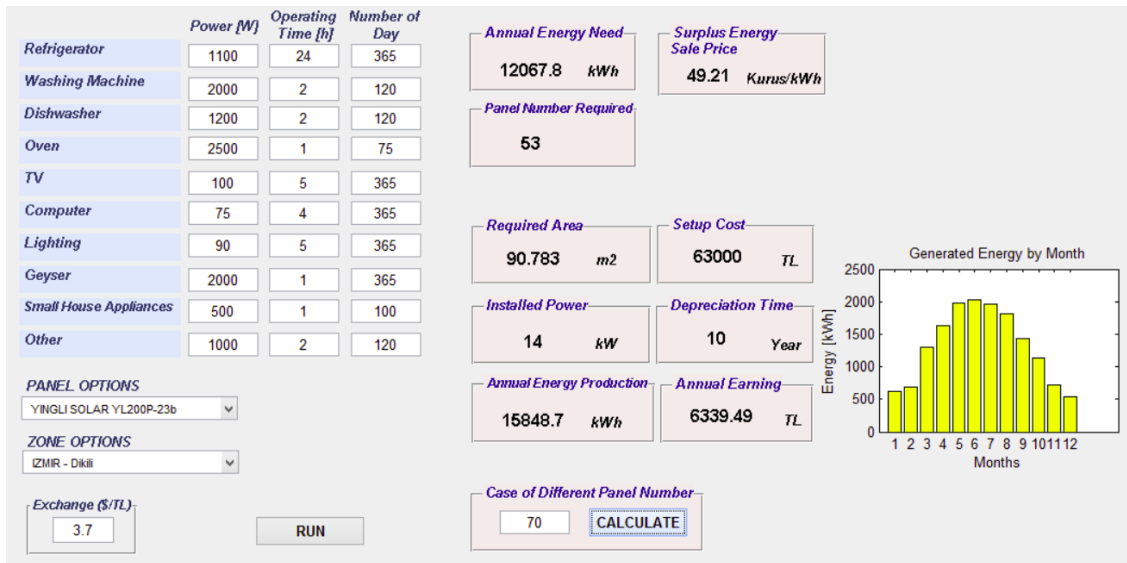


Figure 6: Screenshot of the program for the second case, with different panel number

5. CONCLUSIONS

In this paper, a MATLAB GUI program is created to calculate the annual energy production, component number, required area for producing this energy, payback period and installed power from PV panel. Calculations are based on a four-person household in the case of the complete energy supply from the PV system. Consumed energy is calculated through the data of the operating hours in a day and the number of running days in a year which entered by user. There are various PV panel and region options in the program. Monthly generated energy distribution is shown graphically. System cost, payback period and annual earnings are also calculated in the economic analysis part so that will help to make the pre-feasibility and can be used as a decision-making mechanism for investors.

REFERENCES

- [1]. Ç. Karadağ, I. Gülsaç, A. Ersöz, M. Çalışkan, "Çevre Dostu ve Temiz: Yenilenebilir Enerji Kaynakları", *Bilim ve Teknik Dergisi*, vol. 498, pp. 24-27, May 2009.
- [2]. S. Y. Özkaya. (2004) Yenilenebilir Enerji Kaynakları. Uluslararası Ekonomik Sorunlar Dergisi [Online] Available: <http://www.mfa.gov.tr/yenilenebilir-enerji-kaynaklari.tr.mfa>
- [3]. (2017) EIE website. Available: <http://www.eie.gov.tr/MyCalculator/pages/35.aspx>
- [4]. (2017) Retscreen website. Available: <http://www.retscren.net/>
- [5]. M. Kaltschmitt, W. Streicher, A. Wiese, *Renewable energy: technology, economics, and environment*, page 55, Springer, 2007.
- [6]. Gilbert M. Masters, *Renewable and Efficient Electric Power Systems, United States of America*, page 476, John Wiley & Sons 2004.



A Useful Way to Dispose of Phenolic-rich Agro-industrial Wastes: Mushroom Cultivation

Funda Atıla^{1*}

¹Kırşehir Ahi Evran University, Department of Horticulture, 40100, Kırşehir, Turkey.

*Corresponding Author email: funda.atila@ahievran.edu.tr

Abstract

The by-products resulting from the agricultural productions are arised in extrem quantities every year. Some agricultural by-products such as olive press waste, green walnut husks, tea wastes, coffee pulp etc. have been recognized as phenolic-rich wastes. The high polyphenol content in these wastes could have negative impact on soil and flora, if they are not disposed properly. Moreover, some studies have investigated the toxicity of phenolic compounds on aquatic organisms. Burning of these wastes may cause to increase amount of carbondioxide in atmosphere. Conversion of phenolic-rich wastes by different processes is therefore a desired aim. Mushroom has been used either as a therapeutic and protein-rich foods for many centuries. Mushroom cultivation on agricultural wastes could be a promising method to reduce the the environmental pollution problems as well as production of tasty and healty foods. This paper reviews the potential uses of phenolic-rich materials as substrate in cultivation of edible and medical mushrooms.

Key words

coffee husk, grape pomace, green walnut husk, mushroom cultivation, olive press wastes, tea wastes

1. INTRODUCTION

Phenol is aromatic hydrocarbon and produced through both natural and anthropogenic processes [1]. US Environmental Protection Agency classified phenols as Priority Pollutants. They exhibit several toxic effects including chromosomal aberrations [2], endocrine disrupting effect [3,4], serious kidney and liver damage [5], mutagenicity and carcinogenicity [6].

Phenolic-rich agro-industrial wastes have no value as commercially. If inattentively disposed of in the surrounding environment by burying, burning, or dumping at unplanned and uncontrolled landfills, these wastes lead to climate change and environmental pollution. For that reason, there is a tendency to find a way to convert into valuable resources through proper management, with their utilization leading to reduced environmental pollution and further economic growth. Phenolic-rich agro-industrial wastes have potential to biochemically dissolved to produce several products like production of biogas, bio-ethanol etc. These wastes could also represent a possible source for mushroom cultivation as growing substrate.

Mushrooms are distinct both from plants and animals and belong to a separate group in the Fungi Kingdom. They are classified as a group of macrofungus. Chang and Miles [7] have defined mushroom as a macrofungus

with a fruitbody, large enough to be seen by the naked eye and to be taken by hand. They have not got leaves, buds or flowers, yet, they form fruit and produce spores. Mushrooms, can synthesize and excrete different enzymes to degrade lignocellulosic materials such as and forestry residues, which can then be absorbed by the mushrooms for their nutrients [8]. Recent estimates of the number of fungi on the world changed between 2.2 and 3.4 million species [9].

Wild mushrooms are consumed by humans since ancient times. But commercial mushroom cultivation was started in France in 1650's by *Agaricus bisporus* cultivation. Mushroom production has increased steadily after World War II, and the production of edible and medical mushrooms such as *Pleurotus* spp., *Lentinula edodes*, *Flammulina velutipes*, *Ganoderma lucidum* have also shown great increase in the past few decades [10]. The total production of mushrooms in the world was only 1 million ton in 1978 [11] whereas the world production of cultivated edible mushrooms reached 34 million tones in 2013 [12]. During those 35 years, production increased by 3300%.

Technologies and innovations for human development are expanding every day. The world population have reached 7.6 billion inhabitants as of May 2018 [13]. It is estimated to reach 11.2 billion in 2100. However, humankind, particularly in some less developed countries, face three basic problems such as inadequate nutrition, increasing health problems, and increasing environmental pollution [14]. It is expected that the importance of these problems is set to rise as the world's population continues to increase.

Mushroom cultivation techniques is gaining importance in recent years to reuse or disposal of the solid organic wastes. Mushrooms can convert lignocellulosic materials into high quality food rich in protein, vitamins, dietary fibres, mineral salts and low in fat [15,16]. Taste of mushrooms frequently is descired as umami. Mushroom cultivation is not only a source for tasty and protein-rich food, it can also contribute to the production of effective medicinal products [14,17,18]. Many species of mushrooms have been used in traditional medicine for thousands of years. Mushrooms contain several biologically active substances including high-molecular-weight polysaccharides, glucans, chitinous substances, lectins, and secondary metabolites such as terpenoids, phenols, alkaloids, antibiotics.

Many of phenolic-rich agricultural wastes, such as tea waste, viticulture waste, tea waste, coffee pulp etc. can be provided at abundant and inexpensive cost in the different part of the world. Use of phenolic rich wastes as a raw material in cultivation of mushroom could be also useful ecological and environmental as well as economical. Kües [19] reported that Basidiomycota mushrooms are useful tools for the degradation of uncontrollable pollutants such as phenols, polyaromatic hydrocarbons, bisphenols, phenolic or non-phenolic textile dyes, halogenated aromatics, , naphthols etc. White-rot fungi can secrete some ligninolytic enzymes such as peroxidases and polyphenol oxidases destroying phenolic compounds [20,21].

As you can see, mushroom cultivation could be may contribute to the solution of these three key underlying problems that mentioned before. Finally, the aim of the presented review is to discuss the disposal of phenolic content rich agricultural wastes by mushroom cultivation. Moreover, the ability of mushrooms to remove phenolic compounds has also been investigated.

2. USES OF SOME PHENOLIC-RICH AGRO-INDUSTRIAL WASTES ON MUSHROOM CULTIVATION

A huge amount of phenolic-rich agro-industrial wastes and effluents are produced every year through the oil, juice, beverage, wine industries. These wastes are lignocellulosic, rich in source of nutrients, abundantly available and cheap. They contain high concentration of oil, phenol, lignin, cellulose, hemicellulose, ash, nitrogen and dissolved solids as shown in Table 1. In the following section, some of studies about the possibility of using of these phenolic rich agro-industrial wastes as growing media in the mushrooms production were presented.

Table 1. The composition of some of phenolic-rich agro-industrial wastes

	Ash (%)	Lipits (%)	Protein (%)	Hemicellulose (%)	Lignin (%)	Cellulose (%)	Sources
Olive press cake	1.4-2.4	3.9-8.7	2.9-4.8	7.9-11.0	8.5-14.2	14.5-24.1	[22]
Grape pomace	5.5	-	12.2	-	2.2-2.3	-	[23,24]
Tea waste	5.2	-	12.3	18.9	37.8	28.8	[25,26]
Coffee husk	5.4	0.5-3.0	8.0-11.0	7.0	9.0	43.0	[27]
Green walnut husk	1.86	-	8.3	3.5	13.5	17.7	Atila, F. (unpublished)

2.1. Olive Mill Wastes

Olive mill wastes are major environmental problem in Mediterranean Basin, due to its high phenol concentrations, that have a toxic impact for water, air, plants and soil microorganisms [28,29]. The two-phase extraction system generated about 0.8 ton of solid waste for per ton of processed olives [30]. According to the data, annual production of olive mill wastes reaches to million of tons in the world. So, large amounts of generated olive mills wastes should be disposed by appropriate methods to prevent environmental damage.

Kalmış and Sargın [31] suggested that 25–50% concentrations of olive mill wastewater (OMWW) can be used at for the moistening of the wheat straw substrate for *Pleurotus sajor-caju* and *Pleurotus cornucopiae* var. *citrinopileatus* cultivation. This can be a promising alternative method for the mushroom cultivation and disposal of OMWW. However, 75% OMWW or 100% OMWW was not adaptable with cultivation of these mushroom species. Zervakis et al. [32] also reported that the 75% OMWW has toxic effects on mycelial growth and yield of *Pleurotus eryngii* and *Pleurotus pulmonarius*. It was determined that when 75% OMWW was used in wetting of substrates, colonisation period was prolonged and BEs of *Pleurotus eryngii* and *Pleurotus pulmonarius* decreased 50%.

Kalmış et al. [33] investigate the feasibility of using OMWW as an alternative moisturing agent for *Pleurotus ostreatus* cultivation. Moreover they determined that effect of OMWW on some food quality characteristics of mushrooms. the use of 25%OMWW was suitable for *P. ostreatus* cultivation. Although food quality was not effected by increasing concentration of OMWW in the moisturing mixture, fruitbody shape was deformed in high concentrations of OMWW. The use of OMWW up to 25% as moisturizer could be suggested for *Pleurotus ostreatus* cultivation. In addition, it could be an an environmentally friendly and pratical solution for disposal of OMWW

Ruiz-Rodriguez et al. [34] used wheat straw supplemented with 0 up to 90% olive mill waste for cultivation seven *Pleurotus ostreatus* strains. They reported that all *P. ostreatus* strains could grow but high OMW concentrations resulted in a prolonged cultivation period, losses of yield, biological efficiency and fruiting bodies quality. OMW concentrations did not affected total phenolic content and antioxidant activity of fruitbodies and phenolic compounds from OMW were not detected in the fruiting bodies.

Atila [35] reported that sawdust substrate could be supplemented with 25-75% portions of OMW to prepare the growing media for *Pleurotus djamor*, *Pleurotus eryngii* and *Pleurotus citrinopileatus* cultivation and using OMW as a substrate in mushroom cultivation provides an eco-friendly method for disposing of OMW.

Altieri et al [36] and Parati et al. [37] suggested composted olive mill solid waste for cultivation of *Agaricus bisporus*.

Koutrotsios et al [38] reported that *Hericium erinaceus* exhibited high yield in OMWW and olive pruning residues-based media. Moreover it was observed that phenolics and toxicity were decrease on OMWW. Uses of olive press cake was also suggested for *Hericium erinaceus* [39] and *Hericium americanum* production [40] in other previous studies.

According to results from several studies, using by-products from the olive oil industry in mushroom cultivation could help to reduce the environmental impact and production costs.

2.2. Grape Pomace

Grape (*Vitis* spp.) is produced 70 million tons every year in the world [41]. Grape pomace, consisting of the seed, skin, and stem, is the main solid organic waste from winery industries. Grape pomace represent, in general, 20–30% of the original grape weight [42]. This waste has highly lignified fibre, so its use as animal feed is limited. Moreover, these residues also have highpolyphenol content. Makris et al. [43] reported that that extracts of grape seeds (either white or red) contain 10.3–11.1% of total polyphenols. Christ and Burrit [44] reported that the wine industry might have a negative impact on local water resources.

A relatively few studies have focused on the use of grape pomace as a substrate for mushrooms production. Koutrotsios et al [45] cultivated *Pleurotus ostreatus*, *Pleurotus eryngii*, and *Pleurotus nebrodensis* on growing media containing grape marc substrate. Grape marc substrates led to large increase of fruit-bodies content in total phenolics, antioxidant activity, β -glucans as well as mushroom yield.

Sanchez et al [46] evaluated the bioconversion of vineyard pruning and grape pomace by cultivation of *Pleurotus* spp. Biological efficiency and bioconversion of vineyard pruning and grape pomace ranged from 37.2 to 78.7% and from 16.7 to 38.8%, respectively. They suggested that uses of viticulture residues on *Pleurotus* spp. cultivation has great potential.

Pardo et al. [47] composted by- products from grape cultivation and wine industry such as vine shoots, grape stalks and grape pomace under controlled conditions for cultivation of two varieties of *Agaricus bisporus*. It was

reported that composted vine shoots, grape stalks and grape pomace did not exhibit higher biologically efficient than traditional compost, but these substrates could be economically viable and environmentally advantageous.

2.3. Coffee Husk

Coffee is the second largest traded product in the world after petroleum. Grape (*Vitis* spp.) is produced 70 million tons every year in the world [48]. The coffee industry creates over ten million tonnes of residues in the world every year [49]. Generally, most coffee husk is burned to remove this toxic waste.

These by-products are rich in nutrients, caffeine, tannins and polyphenols [50]. Phenolic content of coffee husk limits the uses of it [51]. Maziero [52] studied the production of *Pleurotus* with coffee husk for, but it was not obtained success. Beaux and Soccol [53] used the coffee husk for *Lentinus edodes* production. They reported poor mycelial growth in comparison to other substrates in this substrate. Tan and Chang [54] studied the effect of tannic acid and caffeine on the growth of *L. edodes*. The results showed that tannic acid and caffeine have a toxic effect on the growth of *L. edodes*. Fan et al., [55] reported that the toxic content was higher in the coffee husk than that in the coffee pulp. Previous studies shown that immersion in water [56] or boiling [57] the coffee husk can be an effective method to remove toxic compounds from the substrate and to increase mushroom yield. Martinez et al. [58] confirmed that the toxic materials can be minimised by hot water treatment, but it also was noted that the other residue (waste water) would lead to environmental pollution [59].

On the other hand some previous studies showed that *Pleurotus ostreatus* has ability in producing fruiting body in coffee husk and coffee pulp. Leifa et al. [60] investigated the possibility of using coffee husk and coffee spent-ground as substrates for the cultivation of *Flammulina velutipes*. They reported that using as substrate coffee husk and coffee spent-ground is appropriate for cultivation of *F. velutipes*. evaluated the feasibility of using coffee husks as substrate for *P. ostreatus* and *P. sajor-caju* cultivation. They reported about 97% of BE *P. ostreatus*. The results of Fan et al. [55] showed that it is possible to use coffee husk for *Pleurotus* spp. cultivation.

2.4. Tea Wastes

Tea is one of the most popular beverages in the world. A large amount of tea waste is left after extracting water-soluble components from tea leaves. Therefore, accumulated tea waste is a significant problem for many tea processing industries.

Yang et al. [61] suggested that the substrates contain 40–60% tea waste could be used as growing substrate for *Pleurotus ostreatus* cultivation substrate with high yield, biological efficiency and relatively shorter cropping time. It was investigated that the possibility of using tea production waste as a new casing material in *Agaricus bisporus* cultivation by Gülser and Pekşen [62]. They did not suggest using tea production waste alone as a casing material in *Agaricus bisporus* cultivation, but also they reported a mixture of tea production waste with peat in 1:1 (v:v) ratio increased the mushroom yield. Chukowry et al [63] obtained satisfactory results from substrate mixture containing 75 % sugarcane bagasse and 25 % tea wastes on cultivation of *Pleurotus ostreatus*. They reported using tea wastes as supplement material to prepare mushroom growing medium could reduced cost of fruiting bag preparation. Baktemur et al. [64] suggested that tea waste can be used successfully as substrate material in *Pleurotus* cultivation. Tea waste was also used in *Ganoderma lucidum* production by Peksen and Yakupoglu [26] and the successful results were obtained.

2.5. Green Walnut Husks

The consumption of walnuts is increased by the highly nutritional properties of the seed as well. The main by-product of walnut processing is the green husk. Generated amounts of green walnut husk are quite high. Yılmaz et al [65] reported that the ratio of fresh green walnut husk biomass to total fresh green walnut biomass varied between 65.37%–43.22%. There is a low utilization ratio of green husk because of its toxic content, called juglone. Juglone is an organic compound and occurs naturally in leaves, roots, husks, and bark of plants in Juglandaceae family [66]. Also, Stampar et al. [67] has shown that within walnut green husk, juglone is the major phenolic compound. Burying or spreading of green walnut hulls to the soil can cause phytotoxicity. Several studies showed that juglone has inhibitory effects [68,69] and allelopathic activity on several plants [70].

To the best of our knowledge, no study has been conducted to date on the use of green walnut husks in the preparation of mushroom growing media. The high quantities of these waste materials indicate the need for their assessment as an economical substrate for mushroom cultivation. Using green walnut husk on mushroom cultivation could provide extra income to walnut producers and help disposal of green husk.

3. DEGRADATION OF PHENOLIC COMPOUNDS FROM AGRO-INDUSTRIAL WASTES BY MUSHROOMS

It is also possible to enhance nutrition quality of agricultural wastes through mushroom cultivation. It has been emphasized in many studies that protein and mineral content of the agricultural wastes may be increased by mushroom cultivation [393,40,60]. In addition to improving the nutrient content of the agricultural wastes, several studies are focused on the elimination of phenolic compounds. Ntugias et al [71] evaluated utilization of olive mill wastewater for cultivation of 49 diverse white-rot strains. They found that using of olive mill wastewater for cultivation of white-rot fungi resulted to the increments of total phenolics (>60%) and reduction of color in mushroom fruit bodies. Moreover, culture extracts from some strains reduced olive mill wastewater phenolics within a nine days period.

Tsioulpas et al. [62] investigated the ability of several *Pleurotus* spp. strains to eliminate phenolic compounds from OMW. In addition, they also studied the toxicity of the treated substrates, in order to select strains able to detoxify OMW. They concluded that *Pleurotus* spp. strains can be grown in OMW and the strains have ability to remove a significant portion of phenolic compounds from OMW.

Zerva et al. [73] reported the use of OMWW for mushroom cultivation can lead to valorization of this toxic waste but also they highlighted the ability of *Pleurotus citrinopileatus* LGAM 28684 and *Irpex lacteus* LGAM 238 species in terms of complete degradation of the phenolics content in OMWW. Saavedra et al. [74] suggested *Pleurotus ostreatus* was effective in elimination of phenolic compounds, the initial concentration in the wet olive cake being reduced by around 90% in the wet olive cake treated with *P. ostreatus*. They reported the spent substrate could be used as soil amendments. Sanchez et al. [46] also reported some antinutritional factors of grape pomace such as phenolic components can be diminished by *Pleurotus* spp. using a solid state fermentation. Echeverria and Nuti [49] reported that caffeine (60%) and tannins (70%) content decrease in coffee husk after mushroom cultivation.

Wong and Wang [75] demonstrated that *Pleurotus sajor-caju* has ability to elimination of tannin in coffee spent ground. Brand et al. [76] reported the content of caffeine and phenolic compounds in coffee pulp as 0.75% caffeine and 3.7% phenolic compounds, while in coffee husks it was 1.2% caffeine and 9.3% phenolic compounds. It is noted that the toxic compounds (caffeine and phenolic compounds) in Brazilian coffee husk are much higher than in coffee pulp, so it is more difficult to treat coffee husk than pulp.

Fan et al. [55] evaluated use of coffee husk for *Pleurotus ostreatus* and *Pleurotus sajor-caju* cultivation. It was determined tanin content (79.2%) and caffeine content (60.7%) was decreased in substrate after cultivation. Although tannic concentration decreased in the medium, it was not determined tannic acid in the mycelia. This result concluded that *Pleurotus* spp. had the capacity of degrading tannic acid.

Sampedro et al [77] reported that olive mill waste is a promising substrate for mushroom cultivation. However, mushroom need long colonization times to reach stabilization of the organic matter and for removal of toxic content from the waste.

Leifa et al. [60] reported that caffeine (10.2%) and tannins (20.4%) contents decrease in coffee husk after *Flammulina velutipes* cultivation. The decrease of tannin content was 28% in coffee spent ground. They [60] suggested that caffeine or tannins were not adsorbed by *F. velutipes* fruitbody. They attributed the decrease in caffeine or tannin content of spent mushroom substrates to degradation of these contents by the mycelium. However Echeverria and Nuti [49] reported that caffeine was found in the fruiting body in some cases and this is a evidence that caffeine was not completely degraded.

Concluding Remarks

Accumulation of phenol-rich agro-industrial wastes in large quantities in places or disposal of them by burning causes environmental problems. The enzymes of Basidiomycota are efficient tools for the destruction of phenols from agro and industrial wastes. The use of phenolic-rich agricultural wastes for production of mushroom is a promising method of elimination these toxic contents. Phenol-rich agro-industrial wastes are rich in nutrient composition as well as bioactive compounds. The use of these wastes as mushroom growing substrates not only help to solve environmental problems, but also can prevent loss of valuable materials and reduce the mushroom production cost. Furthermore, phenolic-rich agro-industrial wastes can improve health preventive compounds in fruitbody such as antioxidants. Thus, mushroom production and distribution can serve as agents for promoting healthy society.

In conclusion, mushroom cultivation can lead to a agricultural revolution in the world, especially in less-developed countries. It has a great potential for generating great environmental and socio-economic impacts in human life. Moreover, spent mushroom substrates could be used to feed ruminants because toxic content decrease while protein increase.

ACKNOWLEDGMENT

This work was supported by the Kirsehir Ahi Evran University Research Council 2018 Grant No. ZRT.A4.18.020

REFERENCES

- [1]. A.A. Gami, M.Y. Shukor, K.A. Khalil, F.A Dahalan, A. Khalid and S.A. Ahmad, “Phenol and its toxicity”, *J Environ Microbiol Toxicol*, vol. 2, pp.11–24, 2014.
- [2]. M.C. Silva, J. Gaspar, I.D. Silva, D. Leão and J. Rueff, “Induction of chromosomal aberrations by phenolic compounds: possible role of reactive oxygen species”, *Mutat Res*, vol. 540, pp. 29–42, 2003.
- [3] X. Peng, Y.Yua, C.Tanga, J. Tana, Q. Huanga and Z. Wang, “Occurrence of steroid estrogens, endocrine–disrupting phenols, and acid pharmaceutical residues in urban riverine water of the Pearl River Delta, South China”, *Sci Total Environ*, vol. 397, pp. 158–166, 2008
- [4]. J. Li, M. Ma and Z. Wang, “In vitro profiling of endocrine disrupting effects of phenols”, *Toxicol In Vitro*, vol. 24, pp. 201–207, 2010
- [5]. O.O. Olujimi, O.S. Fatoki, J.P. Odendaal and J.O. Okonkwo, “Endocrine disrupting chemicals (phenol and phthalates) in the South African environment: a need for more monitoring”. *Water SA*. vol.36, pp. 671–682, 2012
- [6]. P.P. Zhang, Y. Wen, J. An, Y.X. Yu, M.H. Wu and X.Y. Zhang, DNA damage induced by three major metabolites of 1,3–butadiene in human hepatocyte L02 cells. *Mutat Res*, vol. 47, pp. 240–245, 2012.
- [7]. S.T Chang and P.G. Miles, “Mushroom biology: A new discipline”, *Mycologist*, vol. 6, pp. 64–65, 1992.
- [8]. S.T. Chang, P.G. Miles, *Mushroom: Cultivation, nutritional value, medicinal effect, and environmental impact*, 2nd ed., Boca Raton, FL: CRC Press., 2004.
- [9]. D.L. Hawksworth, R. Lücking. “Fungal diversity revisited: 2.2 to 3.8 million species”. *Microbiol Spectr*, 5 (2017)Article ID. FUNK–0052– 2016.
- [10]. S.T. Chang, J.A. Buswell, Development of the world mushroom industry: Applied mushroom biology and international mushroom organizations, *Int J Med Mushroom*, vol. 10, pp. 195–208, 2008.
- [11]. Q. Tan, H. Cao, New development of the mushroom industry in China institute of edible fungi, Shanghai Academy of Agricultural Sciences, Shanghai 201106, P. R. China, 2010, http://wsmbmp.org/Bulletin_2_Content.html.
- [12]. D.J. Royse, J. Baars and Q. Tan, *Current overview of mushroom production in the world*. D.C. Zied, Ed., Edible and medicinal mushrooms: Technology and applications. New York: John Wiley & Sons, 2017.
- [13]. (2018) Wikipedia website. [Online]. Available: (https://en.wikipedia.org/wiki/World_population).
- [14]. S.T. Chang and S.P. Wasser, “The role of culinary–medicinal mushrooms on human welfare with a pyramid model for human health”, *Int J Med Mushroom*, vol. 14, pp. 93–134, 2012.
- [15] F.S. Reis, L.Barros, A. Martins amd I.C.F.R. Ferreira, “Chemical composition and nutritional value of the most widely appreciated cultivated mushrooms: an inter– species comparative study”, *Food Chem Toxicol*, vol. 50, pp.191–197, 2012.
- [16] X.M. Wang, J. Zhang, , L.H., Wub, Y.L. Zhao, T. Li, J.Q. Li, , Y.Z.Wang, H.G. Liu, A mini–review of chemical composition and nutritional value of edible wild–grown mushroom from China, *Food Chem*, vol. 151, pp. 279–285, 2014.
- [17] S. P. Wasser, “Medicinal mushroom science: History, current status, future trends, and unsolved problems,” *Int J Med Mushroom*, vol. 12, pp. 1–16, 2010.
- [18] S.P. Wasser, “Medicinal mushroom science: Current perspectives, advances, evidences, and challenges,” *Biomed J*, vol. 35, pp. 516–528, 2014.

- [19] U. Kües, "Fungal enzymes for environmental management," *Curr Opin Biotechnol*, vol. 33, pp. 268–278, 2015.
- [20] L. Martirani, P. Giardina, L. Marzullo and G. Sannia, "Reduction of phenolic content and toxicity in olive oil mill waste waters with the ligninolytic fungus *Pleurotus ostreatus*," *Water Res*, vol. 30, pp. 1914–1918, 1996.
- [21] G. Olivieri, A. Marzocchella, P. Salatino, P. Giardina, G. Cennamob and G. Sannia, "Olive mill wastewater remediation by means of *Pleurotus ostreatus*," *Biochem Eng J*, vol. 31, pp. 180–187, 2006.
- [22] A.G. Vlyssides, M. Loizidou, K. Gimouhopoulos and A. Zorpas, "Olive oil processing wastes production and their characteristics in relation to olive oil extraction methods", *Fresen Environ Bull*, vol. 7, pp. 308-313, 1998.
- [23] A. Llobera and Jaime Canellas, "Dietary fibre content and antioxidant activity of Manto Negro red grape (*Vitis vinifera*): pomace and stem", *Food Chem*, vol. 101, pp. 659-666, 2007.
- [24] F. Saura-Calixto, I. Goni, E. Manas and R. Abia, "Klason lignin, condensed tannins and resisitant protein as dietary fibre constituents: Determination in Grape Pomaces", *Food Chem*, vol. 39, pp. 299-309, 1991.
- [25] A. Demirbaş, "Evaluation of biomass materials as energy sources: Upgrading of tea waste by briquetting process", *Energ Source*, vol. 21, pp. 2115-220, 1999.
- [26] A. Peksen and G. Yakupoglu, "Tea waste as a supplement for the cultivation of *Ganoderma lucidum*", *World J Microbiol Biotechnol*, vol. 25, pp. 611–618, 2009.
- [27] A.S. Franca and L.S. Oliveira, "Coffee processing solid wastes: current uses and future perspectives". In: F Clumbus (ed) *Agricultural wastes*, Nova Publishers, New York, 2009.
- [28] M Della Greca, P Monaco, G Pinto, A Pollio, L Previtera and F Temussi, "Phytotoxicity of low molecular weight phenols from olive mill waste waters", *Bull Environ Contam Toxicol*, vol. 67, pp. 352–357, 2001.
- [29] G. Rana, M. Rinaldi and M.Introna, "Volatilisation of substances after spreading olive oil waste water on the soil in a Mediterranean environment", *Agric Ecosyst Environ*, vol. 96, pp. 49–58, 2003.
- [30] F. Cerrone, M.M. Sánchez–Peinado, B. Juárez–Jimenez, J. González–López, C. Pozo, "Biological treatment of two–phase olive mill wastewater (TPOMW, alpeorujo): polyhydroxyalkanoates (phas) production by azotobacter strains", *J Microbiol Biotechnol*, vol. 20, pp. 594–601, 2010
- [31] E. Kalmıs, S. Sargin, "Cultivation of two *Pleurotus* species on wheat straw substrates containing olive mill waste water", *Int Biodeter Biodegr*, vol. 53 , pp. 43–47, 2004.
- [32] G. Zervakis, P. Yiatra, C. Balis, "Edible mushrooms from olive oil wastes", *Int Biodeter Biodegr*, vol. 38, pp. 237–243, 1996.
- [33] E. Kalmıs, N. Azbar, H. Yıldız and F. Kalyoncu, "Feasibility of using olivemill effluent (OME) as a wetting agent during the cultivation of oyster mushroom", *Bioresour Technol*, vol. 99, pp. 164–169, 2008.
- [34] A. Ruiz–Rodriguez, C. Soler–Rivas, I. Polonia and J.H. Wichers, Effect of olive mill waste (OMW) supplementation to oyster mushrooms substrates on the cultivation parameters and fruiting bodies quality, *Int Biodeter Biodegr*, vol. 64, pp. 638–645, 2010.
- [35] F. Atila, "Cultivation of *Pleurotus* spp., as an alternative solution to dispose olive waste", *J Agric Ecol Res Int*, vol. 12, pp. 1–10, 2017.
- [36] R. Altieri, A. Esposito, F. Parati, A. Lobianco and M. Pepi, Performance of olive mill solid waste as a constituent of the substrate in commercial cultivation of *Agaricus bisporus*, *Int Biodeter Biodegr*, vol.63, pp. 993–997, 2009.
- [37]. F. Parati, R. Altieri, A. Esposito, A. Lobianco, M. Pepi, L. Montesi and T. Nair, "Validation of thermal composting process using olive mill solid waste for industrial scale cultivation of *Agaricus bisporus*", *Int Biodeter Biodegr*, vol. 65, pp. 160–163, 2011.

- [38]. G. Koutrotsios, E. Larou, K.C. Mountzouris, G. Zervakis, “Detoxification of olive millwastewater and bioconversion of olive crop residues into high–value–added biomass by the choice edible mushroom *Hericium erinaceus*”, *Appl Biochem Biotechnol*, vol.180, pp. 195–209, 2016
- [39]. F. Atila, Y.Tuzel, J.A. Fernandez, A.F. Cano, “The effect of some agro– industrial wastes on yield, nutritional characteristics and antioxidant activities of *Hericium erinaceus* isolates”, *Sci Hort*, vol. 238, pp. 246–254, 2018
- [40]. F. Atila, Y. Tuzel, A.F. Cano, J.A. Fernandez, “Effect of different lignocellulosic wastes on *Hericium americanum* yield and nutritional characteristics”, *J Sci Food and Agric*, vol. 97, pp. 606–612, 2017
- [41]. FAOSTAT2016, Food and Agriculture Organization of the United Nations Statistics Division. [Online] <http://faostat3.fao.org/download/Q/QC/E> (Accessed 30 September 2018).
- [42]. K. Dwyer, F. Hosseinian, M. Rod, “The market potential of grape waste alternatives”, *J Food Res*, vol. 3, pp. 91–106, 2014
- [43]. D.P. Makris, G. Boskou, N.K., Andrikopoulos, “Polyphenolic content and in vitro antioxidant characteristics of wine industry and other agri–food solid waste extracts”, *J Food Compos Anal*, vol. 20, pp. 125–132, 2007
- [44]. K.L. Christm, R.L.Burritt, “Critical environmental concerns in wine production: an integrative review”, *J Clean Prod*, vol. 53, pp. 232–242, 2013
- [45]. G. Koutrotsios, N. Kalogeropoulos, A.C. Kaliora, G.I. Zervakis “Toward an increased functionality in oyster (*Pleurotus*) mushrooms produced on grape marc or olive mill wastes serving as sources of bioactive compounds”, *J Agric Food Chem*, vol. 66, pp. 5971–5983, 2018
- [46]. A. Sánchez, F. Ysunza, M.J. Beltrán–García and M. Esqueda, “Biodegradation of viticulture wastes by *Pleurotus*: a source of microbial and human food and its potential use in animal feeding”, *J Agric Food Chem*, vol. 50, pp. 2537–2542, 2002.
- [47]. A.Pardo, , M.A.Perona and J. Pardo, “Indoor composting of vine by–products to produce substrates for mushroom cultivation,” *Span J Agric Res*, vol. 5, pp. 417–424, 2007.
- [48]. S.I. Mussatto, E.M.S. Machado, S. Martins and J.A. Teixeira, “Production, composition, and application of coffee and its industrial residues,” *Food Bioprocess Tech*, vol. 4, pp. 661–672, 2011.
- [49]. M.C. Echeverria and M. Nuti, “Valorisation of the residues of coffee agro–industry: perspectives and limitations”, *Open Waste Manag J*, vol. 10, pp. 13–22, 2017.
- [50]. E. Bondesson, A nutritional analysis on the by–product coffee husk and its potential utilization in food production. Bachelor thesis. Faculty of Natural Resources and Agricultural Sciences, Uppsala, 2015.
- [51]. A. Pandey, C.R. Soccol, P. Nigam, D. Brand, R. Mohan and S. Roussos, “Biotechnological potential of coffee pulp and coffee husk for bioprocesses”, *Biochem Eng J*, vol. 6, pp. 153–162, 2000.
- [52]. R. Maziero, Substratos alternativos para o cultivo de *Pleurotus* sp. São Paulo, (Master Science Thesis, Faculdade de Ciências da USP, 1990).
- [53]. M.R. Beaux and C.R. Soccol, “Cultivation of edible mushroom *Lentinula edodes* in agroindustrial residues from Paraná using solidstate fermentation”, *Bol Cent Pesqui Process Aliment*, vol.14, pp. 11–24, 1996
- [54]. Y.H., Tan, and S.T., “Chang, Effect of growth regulators, enzyme inhibitors and stimulatory additives on the vegetative development and fructification of *L. Edodes*”. Proceedings of the twelfth international congress on the science and cultivation of edible fungi. September, Braunschweig, Germany, 1987.
- [55]. L. , Fan, A.T., Soccol, A., Pandey, L.P., Vandenberghe de Souza and C.R., Soccol, “Effect of caffeine and tannins on cultivation and fructification of *Pleurotus* on coffee husks”, *Braz J Microbiol*, vol. 37, pp. 420–424, 2006

- [56]. M.D. Nunes, M.C.S. da Silva, J.G.S. Schram, J.S. da Silva, Y. Tamai and M.C.M. Kasuya, "Pleurotus ostreatus, mushrooms production using quick and cheap methods and the challenges to the use of coffee husk as substrate", *Afr J Microbiol Res*, vol. 11, pp. 1252–1258, 2017.
- [57] M.C.S. da Silva, J. Naozuka, J.M.R. da Luz, L.S. de Assunção, P.V. Oliveira, M.C.D. Vanetti, D.M.S. Bazzolli and M.C.M. Kasuya, "Enrichment of Pleurotus ostreatus mushrooms with selenium in coffee husks", *Food Chem*, vol. 131, pp. 558–563, 2012.
- [58] C.D.Martinez, C. Soto and G. Guzman, "Cultivo de Pleurotus ostreatus en pulpa de café com paja como substrato", *Rev Mex Micol*, vol. 1, pp. 101–108, 1985.
- [59] L. Fan, A.T. Soccol, A. Pandey and C.R. Soccol, "Cultivation of Pleurotus mushrooms on Brazilian coffee husk and effects of caffeine and tannic acid", *Micol Aplicada Int*, vol. 15, pp. 15–21, 2003.
- [60]. F., Leifa, A., Pandey and C.R., Soccol, "Production of Flammulina velutipes on coffee husk and coffee spent-ground", *Braz Arch Biol Technol*, vol. 44, pp. 205–212, 2001
- [61]. D. Yang, J. Liang, Y. Wang, F. Sun, H. Tao, Q. Xu, L. Zhang, Z. Zhang, C.T. Ho and X. Wan, "Tea waste: An effective and economic substrate for oyster mushroom cultivation," *J Sci Food Agric*, vol. 96, pp. 680–684, 2016
- [62]. C., Gülser, and A., Pekşen, "Using tea waste as a new casing material in mushroom (*Agaricus bisporus* (L.) Sing.) cultivation", *Bioresour Technol*. vol. 88, pp. 153–156, 2003
- [63]. N.D. Chukowry, R.D. Nowbuth and B.Lalljee, "Evaluation of tea wastes as an alternative substrate for oyster mushroom cultivation", *Univ Maurit Res J*, vol. 15, pp. 458–473, 2009
- [64]. G.Baktemur, H. Taşkın, Y.E. Güzelel, O. Büyükalaca and H. Akıllı "Use of the tea wastes in Pleurotus cultivation as an alternative substrate material in Turkey under conventional controlled climate", *Int J Adv Sci Eng Technol*, vol.6, pp. 13–16, 2018
- [65]. S.Yılmaz, Y. Akça and S. Saçlık, "Green husk and inshell biomass production capabilities of six walnut cultivars", *J Int Sci Publ*, vol. 5, pp.389–397, 2017.
- [66]. S. Ercisli and C. Turkkal, "Allelopathic effects of juglone and walnut leaf extracts on growth, fruit yield and plant tissue composition in strawberry cvs. 'Camarosa' and 'Sweet Charlie,'" *J Hort Sci Biotechnol*, vol. 80, pp. 39–42, 2005
- [67]. F. Stampar, A. Solar, M. Hudina, R.Veberic and M. Colaric, "Traditional walnut liqueur – cocktail of phenolics", *Food Chem*. vol. 95, pp. 627–631, 2006.
- [68]. I., Kocacaliskan and I., Terzi "Allelopathic effects of walnut leaf extracts and juglone on seed germination and seedling growth", *J Hort Sci Biotechnol*, vol. 7, pp. 436–440, 2001
- [69]. I., Terzi, "Allelopathic effects of Juglone and decomposed walnut leaf juice on muskmelon and cucumber seed germination and seedling growth", *Afr J Biotechnol*, vol. 7, pp. 1870–1874, 2008
- [70]. H. Zhang, J.M Gao, W.T. Liu, J.C. Tang, X.C. Zhang, Z.G. Jin, Y.P. Xu and M.A. Shao "Allelopathic substances from walnut (*Juglans regia* L) leaves", *Allelopathy J*, vol. 21, pp. 354–362, 2008
- [71]. S. Ntougias, P. Baldrian, C. Ehaliotis, F. Nerud, V. Merhautová and G.I. Zervakis, "Olive mill wastewater biodegradation potential of white-rot fungi--Mode of action of fungal culture extracts and effects of ligninolytic enzymes", *Bioresour Technol*, vol. 189, pp. 121–130, 2015
- [72]. A.Tsioulpas, D. Dimou, D. Iconomou, G.Aggelis, "Phenolic removal in olive oil mill wastewater by strains of Pleurotus spp. in respect to their phenol oxidase (laccase) activity", *Bioresour Technol*, vol. 84, pp. 251–257, 2002
- [73]. A. Zerva, G.I. Zervakis, P. Christakopoulos, E. Topakas, "Degradation of olive mill wastewater by the induced extracellular ligninolytic enzymes of two wood-rot fungi", *J Environ Manage*, vol. 203, pp. 791–798, 2017

- [74]. Saavedra, M., Benitez, E., Cifuentes, C. and Nogales, R., “Enzyme activities and chemical changes in wet olive cake after treatment with *Pleurotus ostreatus* or *Eisenia fetida*”, *Biodegradation*, vol. 17, pp. 93–102, 2006
- [75]. Wong, Y.S. and Wang, X., “Degradation of tannins in spent coffee grounds by *Pleurotus sajor-caju*”, *World J Microbiol Biotechnol*, vol. 7, pp. 573-574, 1991
- [76]. Brand, D., Pandey, A. Roussos, S. and Soccol, C.R., “Biological detoxification of coffee husk by filamentous fungi using a solid state fermentation system”, *Enzyme Microbiol Technol*. vol. 27, pp. 127–133, 2000
- [77]. Sampedro, I., Marinari, S., D’Annibale, A., Grego, S., Ocampo, J.A. and GarcíaRomera I., “Organic matter evolution and partial detoxification in two-phase olive mill waste colonized by white-rot fungi”, *Int Biodeter Biodeg*, vol. 60, pp.116–125, 2007





Characteristics of Some Turkish Lignites and Potential of Using in Agricultural Sector

Nazan Yalçın Erik^{1*}, Faruk Ay²

¹Sivas Cumhuriyet University, Department of Geological Engineering, 58140, Sivas, Turkey.

²Sivas Cumhuriyet University Department of Antropology, 58140, Sivas, Turkey.

*Corresponding Author email: nyalcin@gmail.com

Abstract

Recently, a lot of progress have been obtain towards progress on the quality and quantity in agriculture. The advances and development in agriculture depend on mechanisation and the development on the soil characteristic which also help to increase the product efficiency. This study aims to determine some Turkish low rank coal samples for applications in the agricultural sector and assesses the suitability of a certain coal either as soil conditioner or as raw material for manufacturing organic fertilizers. They improve the soil structure and improve physical properties of soil by increasing the exchange capacity and buffering qualities, promoting the chelation of many elements and making these available to plants. Humic substances can ameliorate negative soil properties; improve the plant growth and nutrients uptake. Twenty-six samples of subbituminous coal obtained from several Turkish coal deposits such as Arguvan, Çayırılı, Artova and Zile, Kangal-Gemerek-Divriği were studied. When optimum parameters were used, the most promising samples for utilization are the coal samples from Arguvan, Artova and Zile, since they yielded high HA contents (≥ 30 wt). Although the Artova and Arguvan samples display high HA contents, they are also rich in S and release Fe, which might be threatening for the plants.

Key words

Coal, fulvic acid, humic substances, humic acid, organic fertilizer, Turkey

1. INTRODUCTION

People have tried different techniques and supportive products to increase the agricultural productivity and to get higher quality. In this context, the usage of chemical fertilizers is the most leading methods for decades. By means of this technics, the plant provides many nutrients necessary for them. However, especially in the production phase, because of the additional cost and polluting the groundwater, rivers and lakes, the chemical fertilizers have also become a current problem in terms of environment and ecology with their harmful sides. For this reason, new techniques have also started to be investigated to increase vegetative productivity, which is not harmful for both environment and the livings.

Organic materials are important soil additives to improve soil physical, chemical and biological properties. It has been scientifically proved that fulvic and humic acid, the most important organic component of the soil, make important effects to the growth of the plant materials in terms of physical, chemical and microbiologically [1]. These natural components have supported the plant yield and quality, by increasing the flowering and the root and stem development, providing more water and air from the soil. At the same time,

as well as economic benefits, humic and fulvic acids have been helped to protect the environment by increasing the effectiveness of the chemical fertilizers and inhibiting the excessive fertilizer usage [2, 3]. This is important to sustain the productivity of soils particularly in semi-arid regions (such as Turkey) where there is low input of organic materials. Therefore, usage of organic-based materials has gained importance within the last few years for sustainable agriculture and preventing soil degradation.

Due to Turkish agricultural lands have alkaline reaction (85%), and are poor in terms of organic matter (94%), and has a chalky structure (58%), insufficient water storage results in mudslide together with soil loss with erosion and quality impairment in vegetative production, depending on the insufficiency of the elements (phosphorus, potassium, iron, and zinc) feeding the plant [3]. In many regions in Turkey, especially in Central Anatolia, the organic matter content of soils has fallen below 2 or 1 %. For this reason, the agricultural production in such areas must be supported with fertilizer.

Humic acids and their salts, derived from coal and other natural sources, which have modes of action similar to synthetic fertilizer, have been evaluated as potential eco-friendly soil fertilizer. The advantage of humic substances is the refractory nature of their chemical structures that makes them more resistant to microbial attacks. However, at the end of a certain period of time, no matter how much fertilizer is used, the danger of desertification is also in question because it will be difficult to get the soil productivity. Since the addition of sufficient amount of organics fertilizers to whole lands of the country is not possible, it has been determined that productivity potentials might be increased by applying the lower amounts of humic and fulvic acids, which is active fraction of organic matter and humus, when compared to organic fertilizers. The structure of the organic fertilizer consists of humus containing humic and fulvic acid, which is the result of the microorganism action [4, 5, 6].

Humic substances are the most widely found organic components on the Earth crust. These are a general category of naturally occurring, biogenic, heterogeneous organic matters that can generally be characterised as being yellow to black in colour, of high molecular weight and refractory. These components form most of the organic ingredient of soil, peat and natural waters, they effect the process of genesis of fossil fuels, and play a major role in the global carbon cycle. In the same time humic substances (especially humic acids) may be regarded as a valuable item which may found various uses for different purposes and their industrial production and application is growing. Humic and fulvic acid are present in the composition of the all organic materials in the nature. However, with the ratio ranging between 40% to 90%, organic material containing the highest amounts of humic and fulvic acid is brown coal, with its other name "leonardit". At present, low-rank coals are used for the production of HA, which are in the form of alkali-soluble humate salts or as N-rich coal HA (ammonium nitrohumates) [5, 6].

In our country, there is low-quality lignite (20-40% humic and fulvic acid of composition) to be used in the production of 5 million tons of leonardite, which has more than 40% of humic and fulvic acid and 7-8 million tons of solid and liquid K-Humate. However, because the leonardit having these properties and low-quality lignites have an energy amount of 800-1000 kcal/kg, they do not provide any economical returns and are removed as mine waste material. But, when assessed these materials having an estimated reserve of 12-13 million tons as resources of leonardit, solid and liquid humic-fulvic acid in agricultural lands, soil productivity can be increased and soil loss with erosion can be decreased [5, 6]. All of these will result in an increase in the vegetative production and economic benefits. In this study, it has been aimed the determination of humic components of some Tertiary aged and low-quality coals and their usage in agricultural lands.

1.1. Experimental

For this study, 26 samples were collected from the tops to the bases of the seams in the various coal fields (Arguvan-Malatya, Çayırılı-Erzincan, Artova-Tokat, Zile-Tokat, Kangal-Sivas, Gemerek-Sivas, Divriği-Sivas). These samples were taken from along ~ 1 m lines using the channel-sampling technique. Coal-quality data (total moisture, ash, volatile matter, fixed carbon, gross calorific value) were obtained using an IKA 4000 adiabatic calorimeter; elementary contents were determined using a LECO analyzer. For the determination of humic acids (HA) and fulvic acids (FA) contents a method combining the procedures proposed by ISO 5073 (1985) and the International Humic Substances Society [7] was followed.

2. RESULTS AND DISCUSSION

2.1. Proximate and Ultimate analysis

Moisture, ash yields and pH values of bulk samples are listed in Table 1. Most of the samples reveal ash yields between 20 and 50 wt.% and are very low-grade coals. The majority of the samples show an acidic to slightly acidic character (pH 4.5–7.4); samples Arguvan and Artova are strongly acidic (pH < 4.5), whereas samples Zile, Çayırılı, Kangal, Gemerek, and Divriği display neutral pH values (6.6–7.4).

The total C contents range from 42.52–80.2 wt.% (Table 1), with the majority of the samples showing contents greater than 50 wt.%. The H and N contents range from 3.46–5.79 wt.% and up to 2.1 wt.%, respectively. Sulphur contents range from 2.0–6.3 wt.%.

2.2. Humic substances content

Humic substances (HS) are the most widespread natural organic compounds. These are complex organic compounds and have endurance to degradation. Humin (HU) and Humic acid (HA) generally represent the major fraction of HS and appear to display similar analytical characteristics and chemical structures.

Table 1. Some proximate ve ultimate analyses results of investigated coal samples.

Area	Moisture (db) wt%	Ash (db)wt%	C wt.%	H wt.%	N wt.%	S wt.%
Arguvan	23.3	32.28	43.25	3.46	1.1	6.3
Çayırılı	10.38	14.43	80.20	3.95	1.5	2.0
Artova	29.69	43.43	57.1	4.34	1.1	3.6
Zile	25.75	47.97	53.98	4.28	1.2	4.7
Kangal	43.22	22.11	42.52	5.79	2.1	5.3
Gemerek	31.09	17.45	65.66	4.03	1.8	4.0
Divriği	10.68	24.04	60.02	4.32	1.0	5.6

HA occur naturally in low-rank coals and can account for an important fraction of the organic matter. The HS contents of the studied coals are shown in Table 2. The HA contents range between 4.12 and 57.55wt.% with Çayırılı coal sample shows the lowest value, due to the higher rank (R_o ; 0.61). The highest HA content was measured in Artova coal sample. Fulvic acid (FA) contents range between 3.2 and 33.33 wt.%. In general, the Çayırılı coal samples show the lowest HS contents (Table 2). The total concentrations of HA and FA in the studied samples indicate that, coal samples of Arguvan, Artova, Zile areas contain the highest amount of HS ($HA+FA > 50$ wt.%, on a dry basis).

Table 2. Humic substance composition of the investigated coal samples.

Area	Humic Acid (wt.%)	Fulvic Acid (wt.%)	pH	Humic Substances (wt.%)
Arguvan	39.70	12.10	2.3	51.8
Çayırılı	4.12	3.20	6.0	7.32
Artova	57.55	15.12	2.4	72.67
Zile	45.28	12.84	5.4	58.12
Kangal	21.45	23.55	6.7	45.00
Gemerek	5.30	33.33	7.1	38.63
Divriği	8.60	11.33	7.4	19.93

3. RESULTS AND DISCUSSION

The usage in the agricultural areas of the low-quality coals which is economically not very valuable is very important in terms of the prevention of the environmental hazards by minimizing the usage of chemical fertilizers. At the same time, this kind of material can improve the quality of soil and contribute the plant growth and yields. Coal samples used in this study had occurred in similar precipitation conditions and geological age range. But it has been seen that humic composition is different depending on the effect of coalification degree to the precipitation conditions or the type of organic material during the precipitation together with the physicochemical conditions and the tectonic activity. The most promising samples for utilization are the coal samples Arguvan, Artova and Zile, since they yielded high HA contents (≥ 30 wt). Although the Artova and Arguvan samples display high HA contents, they are also rich in S and release Fe, which might be threatening for the plants. Additionally, samples with pH values between 6 and 7 (Çayırılı, Kangal, Gemerek, Divriği samples), could be applied in heavily degraded, acidic soils such as mine spoils; this can promote the biotic activities.

ACKNOWLEDGMENT

The authors would like to thank Dr. Ergun Kasaka, due to the help in the laboratory studies.

REFERENCES

- [1]. F.J. Stevenson, Geochemistry of soil humic substances. In: Aiken, G.R., McKnight, D.M., Wershaw, R.L., MacCarthy, P. (Eds.), Humic Substances in Soil, Sediment, and Water, vol. 2. Wiley, New York, NY, 13–52, 1985.
- [2]. International Organization for Standardization (ISO) 5073, Brown Coals and Lignites -Determination of Humic Acids. Geneva, Switzerland, 1985.
- [3]. A.U. Imbufe, A.F. Patti, D. Burrow, A. Surapaneni, W.R. Jackson, A.D. Milner, Effects of potassium humate on aggregate stability of two soils from Victoria, Australia. Geoderma 125, 321–330, 2005.
- [4]. S. Kalaitzidis, S. Papazisimou, A. Giannouli, A. Bouzinos, K. Christanis, Preliminary comparison analyses of two Greek Leonardites. Fuel 82, 859–861, 2003.
- [5]. K. Gürüz, Oxy-ammoniation of Elbistan lignite to produce a nitrogenous fertilizer. Fuel 59, 772–776, 1980.
- [6]. M. Yıldırım, G. Özbayoğlu, Production of ammonium nitrohumate from Elbistan lignite and its use as a coal binder. Fuel 76, 385–389, 1997.
- [7]. R.S. Swift, Organic matter characterization. In: Bigham, J.M. (Ed.), Methods of Soil Analysis. Part 3. Chemical Methods. Soil Sci. Soc. Am. Book Series, vol. 5. Soil Sci. Soc. Am., Madison, Wisconsin, pp. 1011-1069, 1996.



A Research on to Effective on Yield and Earliness of Different Sowing Times and Growing Techniques in Sweet Corn (*Zea mays saccharata* Sturts) in Kahramanmaraş Conditions

Cüneyt CESUR^{1*} Veyis TANSI²

¹ Karamanoğlu Mehmetbey University, Engineering Faculty, Department of Energy Systems Engineering, 66100, Karaman, Turkey

² Çukurova University, Agricultural Faculty, Department of Field Crops 1170, Adana, Turkey.

* cuneytcesur@kmu.edu.tr

Abstract

In order to investigate the effect of different sowing times and growing techniques. On yield and earliness of two sweet corn varieties, this study, was done in Kahramanmaraş conditions in 1997 – 1998 growing years. Kahramanmaraş research station conditions. Field trials arranged in split – split plot design with there replications, varieties sowing times and growing techniques were used an as main, sub and sub – sub plots, respectively. In this study, Merit and Jubilee varieties used as sweet corn varieties.

According to result obtained from the experiment interm of starch ration, number of grain per ear and number of plant per unit Merit variety was found to be superior but interm of days two maturity ear lenght Jubilee was superior. It was determined that earliness sweet corn growing was possible by using covered growing techniques on that covered growing techniques possitively influenced the all characteristic studied starch ratio and ear lenght. Effect of sowing times on days the maturity wasn't significant. If the temperature is low plant adapted itself till the temperature research optimum. But days the maturity increased vice verse decreased. The optimum sowing times for the Kahramanmaraş conditions was 30 March.

Keywords

Sweet corn (*Zea mays saccharata* Sturts), sowing dates, growing techniques

1. INTRODUCTION

We are in the century where agricultural research will become more important every day. In the last three centuries people have exploited the natural resources irresponsibly by the development of industry and technology. This exploitation is unfortunately still going on. The inexhaustible performance of the western countries, especially in the hands of technology, has brought the whole world to a catastrophic threshold. At the current point, they are talked which about issue such as global warming, decline of biological diversity, climate change than incresing productivity. Until today, it was tried to fulfill the cultivation of forest and grassland for food needs with the help of agriculture. Even if these processes are continued in some parts of the world, it is

also stated that the places that were opened as farming areas in the past, should be abandoned in favor of forest and grassland, according to some researchers, even to the end of new fields to be opened. We understand from this information that the new field areas is no longer in the world. It is then necessary to obtain high efficiency from the unit side in order for the feeding population. Research should develop in this direction. In other words, it is essential to produce more in both quantities and varieties from unit area during the breeding period. For this purpose, many methods of cultivating and renewing crops such as co-cultivation, intercropping, sliver cultivation, sub-cropping, cover cropping and mixed cultivation are carried out in many parts of the World (1).

It is directly related to the genetic structure of plant production material, soil characteristics and climate movements. Climate conditions play the most important role in the selection of crops to be cultivated in a region (2). Light, temperature, day length and precipitation are the most important factors (3). Temperature is one of the most important issues with the transport of photosynthesis, the determination of the developmental periods and especially the effect of filling the grains (4).

As the seeds of corn are used as feed for human beings and pulp as well as the sugar corn types for fresh consumption, the market value can be two or three times higher when they are introduced to the first market. Therefore, it is extremely important for economic reasons to be able to produce as early as possible. In order to increased productivity and earliness in production, unveiled agriculture technique has emerged in recent years (5, 6,7,8).

The main factor limiting early planting in corn is temperature. Early seeding is possible when the temperature environment required for corn is provided. Early planting can be done by creating low tunnels. In sugar corn which can be obtained earliness for 10 - 21 days according to common sowing method (8,9,10,11).

Polyculture farming can be done easily in the large lands of Kahramanmaraş in Mediterranean climate. Many of the plants can continue their development if the necessary environment can be prepared in terms of temperature even from February to March. Plant seedling and low tunnel applications will make it possible to make more efficient farming with earliness.



Figure 1. General view of research area

This study was carried out to investigate the effects of different sowing times and growing techniques on yield and earliness of sugar corn in Kahramanmaraş conditions.

2. MATERIAL AND METHOD

2.1. Material

2.1.1. Used material in experimental area

In the study, jubile and merit sugar corn varieties which are suitable for region conditions were used. Seeds are germinated in small nylon tubes. Mixed soils were used to germinate seeds. Pure nitrogen was used at 20 kg / da. 10 kg / da ammonium nitrate (A.N.) was used as fertilizer and 10 kg / da was used as urea as top fertilizer.

2.1.2. Soil characteristics of experimental area

Some physical and chemical analysis characteristics experimental area soil which is taken from 0-30 cm depth are given in Table 1.

Table 1. Some physical and chemical analysis characteristics of experimental area

Depth	Tekstur class	Ph	Lime (%)	Convenient P (P ² O ⁵)	Organic matter (%)	Saturation with water (%)
0-30 cm	Clay - loamy	7.50	20.24	5.9	0.95	54

*Soil analysis, K.S.Ü Agricultural Faculty Soil Department laboratory

2.1.3. Climatic properties of experimental area

The climate data for Kahramanmaraş province between March and July 1997, 1998 and long years are given in the Table - 2. According to the table, the highest and lowest temperature values for March and April were unusual for many years. Rainfall totals differed in April and May.

Table 2. Climatic datas of March – July months in Kahramanmaraş province

Months	Minimum temperature (°C)	Maximum temperature (°C)	Average temperature (°C)	Proportional humidity (%)	Total precipitation (mm)
March	3.4	13.4	6.2	53.3	46.8
1997	4.6	14.5	4.9	61.0	134.0
1998	-6.0	25.6	10.4	63.2	90.4
Long years average					
April	6.2	17.3	12.0	62.5	105.3
1997	10.8	22.4	16.6	57.8	166.7
1998	-1.8	32.6	14.9	69.8	68.7
Long years average					
May	15.0	28.7	21.7	55.1	88.2
1997	14.3	25.7	19.8	57.0	39.4
1998	15.4	36.3	19.9	55.5	35.0
Long years average					
June	18.4	31.6	24.6	51.4	14.9
1997	19.5	33.4	25.9	54.9	15.6
1998	20.3	39.6	24.3	49.5	7.0
Long years average					
July	22.3	34.5	27.6	48.6	-
1997	23.1	44.3	29.8	55.6	2.0
1998	16.4	41.6	27.8	51.7	3.0
Long years average					

* Kahramanmaraş meteorological station 1997, 1998 years with (1940 – 1990) long years average datas.

2.2. Method

2.2.1. Experimental Method

This research was carried out on Kahramanmaraş Agricultural Research Center Provincial Directorate. The trials were established in March and July 1997 and 1998. In the experiment, three different times (March 15, March 30 and April 15) were planted seedling on the tubes, seedling under cover and seeding techniques in open field. To cover the plots, a low tunnel roof was made of thin construction iron and covered with transparent plastic linoleum (*Figure 2*). The trial was established according to divided into three divided trials plan. Varieties were formed in the main parcels, planting times in the sub - parcels, and cultivating techniques in the sub – sub parcels. The planting distances of the plants were determined as 70 cm x 20 cm the rows, and the parcel area (sub-bottom) was $5 \times 24 = 12 \text{ m}^2$, with each parcel being in 5 m length and in 2.4 m width. Closed parcels were opened and ventilated opening in sunny times by following the temperature condition of the air and fully opened towards the end of April.



Figure 2. Low tunnel in used experimental area

2.2.2. Investigated properties in experimental

In this study were investigated properties as ear length, ear diameter, number of grain per ear, number of plant per unit, number of ear per unit, ratio and starch ratio. While the Polarimeter method was used for Starch analysis in the laboratories of the Faculty of Agriculture, the other characteristics were determined in the 10 samples of plants obtained from each plot. Statistical analyzes of the obtained datas were calculated on the MSTATC package program.



Figure 3. Outlook of two different applications in experiement.

3. RESULT AND DISCUSSION

3.1. Ear length (cm)

The mean values and formed groups of two years (1997 - 1998) showing the effect of cultivar, sowing time and growing techniques on the ear length were given in *Table 3*.

Table 3 Two-year mean values indicating the effect on the ear length of cultivar, sowing time and growing techniques used in the experiment.

Growing techniques	Merit			
	15 march	30 march	15 april	c x g.t
Covered plant	18.0 ^{ef}	19.3 ^{abcde}	18.8 ^{abcdef}	18.7 ^b
Covered seed	19.1 ^{abcde}	18.5 ^{bcdef}	18.1 ^{ef}	18.6 ^b
Normal sowing	19.9 ^{abc}	19.3 ^{abcde}	19.4 ^{abcde}	19.6 ^a
c x e.z	19.0	19.0	18.8	18.9
Growing techniques	Jubile			
	15 march	30 march	15 april	c x g.t
Covered plant	18.7 ^{abcdef}	17.5 ^f	18.6 ^{bcdef}	18.2 ^b
Covered seed	18.4 ^{def}	19.6 ^{abcd}	20.1 ^a	19.4 ^a
Normal sowing	18.5 ^{bcdef}	20.0 ^{ab}	20.0 ^{abc}	19.5 ^a
c x s.t	18.5 ^b	19.0 ^{ab}	19.5 ^a	19.0
LSD	g.t (%1):0.6070; c x g.t (%5):0.6435; cx s.t x g.t (%1):1.487			

c: cultivar, g.t: growing techniques, s.t: sowing time

According to the table, in the merit cultivar, the c x s.t interaction is not significant, whereas the highest ear length (19.0 cm) was obtained from 15 and 30 March sowings.

While the c x g.t interactions of the Merit cultivar was important, the highest value of the study, which was found in the merit cultivar from normal cultivation as 19.6 cm(14). In the jubilee cultivar, the c x s.t interactions were significant (15), while the highest ear length was obtained as 19.5 cm in the April 15 plantations. In the jubilee cultivar, the value of the obtained ear length was obtained as 19.5 cm from the normal sowing while it was important in the c x g.t. The interactions c x s.t x g.t between the Merit and the jubilee cultivars were not important.



Figure 4. Ear length of jubilee cultivar

Although the difference is insignificant, the highest ear length was obtained from the jubilee cultivar as 19 cm. As can be seen from the values, higher ear length was obtained from normal cultivation according to the other cultivation techniques. These results seem to be consistent with studies that indicate that the ear length is higher in normal sowing than in other techniques (12), and that the ear length is lower in the plant seedling techniques(13). When sowing time is considered, the time of sowing in merit cultivar was not important but

the ear length was decreasing, it has increased in the jubilee cultivar. It can be said that this is a cultivar feature, and that the cultivar of jubilee is generally longer than the ear length of cultivar merit (14).

3.2. Ear diameter (cm)

In Table 4 was shown the mean values and formed groups of two years (1997 - 1998) showing the effect of cultivar, sowing time and growing techniques on the ear diameter. When the Table 4 is examined, it is possible to observe that the ear diameter was smaller as the sowing time was delayed, although there was no statistical significance among the factors.

Table – 4. Two-year mean values indicating the effect on the ear diameter of cultivar, sowing time and growing techniques used in the experiment.

Growing techniques	Merit			
	15 march	30 march	15 april	c x g.t
Covered plant	5.0	4.8	4.8	4.9
Covered seed	5.0	4.9	4.5	4.8
Normal sowing	4.1	4.9	4.5	4.5
c x s.t	4.7	4.9	4.6	4.7
Growing techniques	Jubile			
	15 march	30 march	15 april	c x g.t
Covered plant	5.0	4.6	4.6	4.7
Covered seed	5.0	4.5	4.8	4.7
Normal sowing	4.3	4.5	4.5	4.5
c x s.t	4.8	4.5	4.7	4.7
LSD	Sowing time: n.s, cultivar: n.s			

c: cultivar, y.t: growing techniques, s.t: sowing time, n.s: no significant

Both the merit and the jubile cultivars were found to have a diameter of 5 cm in the March 15 plantings and a drop of 4.5cm in the April 15 plantings.

According to the cultivation techniques, it is understood that the diameter of the cocoon in normal cultivation (5cm) was thicker than that of covered cultivation (4.1cm). The interactions of cultivar x sowing time x growing techniques were to 4.7cm. It see that the ear diameter was decreasing as the sowing time was delayed, and it seems that the datas werecompatible with similar studies (12,13,17,18). According to the results obtained in our study, it was seen that the cultivation techniques do not have a significant effect on the eardiameter. However, some researchers report that direct sowing forms a thicker ear diameter than other applications (12,13). It can be said that this contrast is made according to the genetic material and ecological regions used in the studies.

3.3. Number of grain per ear

In Table 5 was shown the mean values and formed groups of two years (1997 - 1998) showing the effect of cultivar, sowing time and growing techniques on the number of grain per ear.

It is seen that cultivar, sowing time and growing techniques have a statistically significant effect on the number of grain per ear at 1% level, cultivar x sowing time, cultivar x growing techniques and x cultivation time x growing techniques interactions is significantly at 5% level.

Table – 5. Two-year mean values indicating the effect on the number of grain per ear of cultivar, sowing time and growing techniques used in the experiment.

Growing techniques	Merit			
	15 march	30 march	15 april	c x g.t
Covered plant	566.7 ^{def}	617.9 ^{abcd}	621.1 ^{abcd}	601.9 ^{ab}
Covered seed	640.7 ^{ab}	630.5 ^{abc}	570.1 ^{def}	613.8 ^a
Normal sowing	505.5 ^{gh}	642.3 ^{ab}	565.9 ^{def}	569.6 ^{bc}
c x s.t	569.3 ^b	630.2 ^a	585.7 ^b	595.1^a
Growing techniques	Jubile			
	15 march	30 march	15 april	cx g.t
Covered plant	519.7 ^{fg}	512.6 ^{fgh}	533.1 ^{efg}	521.8 ^d
Covered seed	551.2 ^{efg}	615.0 ^{abcd}	655.6 ^a	607.3 ^a
Normal sowing	455.7 ^h	572.0 ^{cdef}	585.2 ^{bcd}	537.6 ^{cd}
c x s.t	508.9 ^c	566.5 ^b	591.3 ^b	555.6^b
LSD	s.t(%1):37.03; c(%1):428.3; cxs.t(%5):38.01; g.t (%1):34.51; cxs.txg.t(%5):59.78; cxg.t(%5):34.51			

c: cultivar, g.t: growing techniques, s.t: sowing time

From the obtained data, according to interactions of c x g.t x s.t , it can be seen that the number of grain per ear obtained in merit cultivar (595.1) is higher than the number of jubilee cultivar (555.6). In the c x g.t interactions, the highest value was obtained as 613.8 per from covered seed application of merit cultivar. It was understood that the application of covered seed in the jubilee cultivar showed the highest value as 607.3 per. It was seen that the highest value was obtained from the March 30 application of the highest the number of grain per ear of merit cultivar in the c x s.t interactions, while the highest value of the jubilee cultivar was found on the 15 April cultivars as 591.3 per. According to these results, it can be said that the most suitable sowing technique is the covered seed technique and the most suitable sowing time is between March 30 and April 15(12). According to the c x e.z x y t interaction, it can be said that the merit cultivar has better values than the jubilee cultivar compared to the climate and application conditions (14, 29). This result is consistent with the findings of researchers who say that very genotypic is effective (16,20). In the area where the experiment was established, the March climate values averaged around -6 ° C for the long years and 3.4 - 4.6 ° C for the years when the tests were conducted. Therefore, it is expected that the 15 March applications will not be suitable for the cultivation of corn plants. Minimum temperature requirements for maize plant are 13 - 15 ° C(3).

3.4. Number of plant per unit (per/da)

In Table6 was given the mean values and formed groups of two years (1997 - 1998) showing the effect of cultivar, sowing time and growing techniques on the number of plant per unit. In Table – 6, it can be observed to be effective of year, sowing time, variety, variety x sowing time and growing techniques on number of plant per unit (per/da) at 1% level.

Table – 6. Two-year mean values indicating the effect on the number of plant per unit (per/da) of cultivar, sowing time and growing techniques used in the experiment.

Growing techniques	Merit			
	15 march	30 march	15 april	c x g.t
Covered plant	5094.8	4154.5	5761.5	5003.6
Covered seed	3844.6	6904.3	6083.0	5610.6
Normal sowing	1833.1	5.47.5	5499.6	4126.7
c x s.t	3590.8 ^d	5368.7 ^{ab}	5781.3 ^a	4913.6^a
Growing techniques	Jubile			
	15 march	30 march	15 april	c x g.t
Covered plant	4844.8	3880.5	5440.0	4721.7
Covered seed	4321.0	4666.3	4487.8	4491.7
Normal sowing	2178.1	4368.6	4333.6	3626.8
c x s.t	3781.3 ^d	4305.1 ^{cd}	4753.8 ^{bc}	4280.1^b
LSD	year(% 1):5646.7; s.t(% 1):559.4; c(% 1):5646.7; cxs.t(% 1):791.1; g.t(% 1):544.4			

c: cultivar, g.t: growing techniques, s.t: sowing time

While the highest number of plant per unit was obtained as 4913 from the merit cultivar according to c x y.t x e.z interaction, this data could be obtained from the jubile cultivar as 4280.1. According to the c x s.t interaction, The highest value of the Merit cultivar was obtained from the April 15 plantations as 5781 pieces, and this value was realized as 4753.8 pieces in the jubile cultivar from the April 15 plantations. According to c x g.t Interaction, the highest number of plant per unit was obtained from covered seed applications, although statistically insignificant in both types. While the number of plant per unit obtained from the Merit cultivar was 5610.6, the number of plant per obtained from the jubile cultivar was 4491.7. The fact that there is no difference between covered sowing and planting shows compatibility with literature studies (12,21). According to the results obtained by experiment, the covered seed application of April 15 plantings of merit cultivar indicates the most efficient application. It can be said that the merit cultivar had different values according to the jubilee cultivar, indicating that genotypes given different responses (23).

As can be seen from Table-6, the number of plants increases in late sowing. This is due to the increase in temperatures. As temperature increases, the germination power of seeds and the germination fidelity increase (21, 22). Sweetcorn varieties are affected by temperatures too much. The opinions of Cross and Zuber (1972), which states that the most useful classification method of temperature-dependent classification is supporting our data(24).

3.5. Number of ear per unit

In Table 7 was shown the mean values and formed groups of two years (1997 - 1998) showing the effect of cultivar, sowing time and growing techniques on the number of ear plant per unit. According to table 7, year, cultivar, cultivar x sowing time and growing techniques are effective at 1% level and at 5% level of sowing time on number of ear per unit. The highest number of ear per unit according to c x e.z x y.t interaction was 5269.9 (per/da) from the jubile cultivar. According to the cultivation techniques of the cultivars, it can be said that the most suitable cultivation is covered plant application. The highest number of ear plant per unit from covered plant of March 15 application of Merit cultivar was 6737.8 (per/da). The jubile cultivar also gave the highest yield from the covered plant application. It is also say from datas that more the number of ear plant per unit (per/da) are obtained than covered sowing and planting. It is seen from the literature that these values are compatible with previous studies(25, 11).

Table – 7. Two-year mean values indicating the effect on the number of ear plant per unit (per/da) of cultivar, sowing time and growing techniques used in the experiment.

Growing techniques	Merit			
	15 march	30 march	15 april	c x g.t
Covered plant	6737.8 ^{ab}	5083.0 ^{de}	5702.0 ^{bcd}	5840.9
Covered seed	4583.0 ^e	5856.6 ^{bcd}	5249.6 ^{cde}	5229.7
Normal sowing	2083.0 ^f	5190.3 ^{de}	5190.5 ^{de}	4154.6
c x s.t	4467.9	5376.6	5380.7	5075.1
Growing techniques	Jubile			
	15 march	30 march	15 april	c x g.t
Covered plant	6321.1 ^{abc}	5702.0 ^{bcd}	7130.8 ^a	6384.6
Covered seed	5497.0 ^{cde}	4856.6 ^{de}	4761.6 ^{de}	5038.4
Normal sowing	2999.8 ^f	5214.0 ^{cde}	4892.5 ^{de}	4368.7
c x s.t	4939.3	5257.5	5595.0	5263.9
LSD	year(%1):467.80; s.t(%5):520; cxs.txg.t(%1):1109; g.t(%1):452.7			

c: cultivar, g.t: growing techniques, s.t: sowing time

3.6. Cab ration (%)

In Table 8 was given mean values and formed groups of two years (1997 - 1998) showing the effect of cultivar, sowing time and growing techniques on the cab ratio (%).

Table – 8. Two-year mean values indicating the effect on the cab ratio (%) of cultivar, sowing time and growing techniques used in the experiment.

Growing techniques	Merit			
	15 march	30 march	15 april	c x g.t
Covered plant	19.6 ^{bc}	20.2 ^{bc}	18.4 ^c	19.4
Covered seed	19.7 ^{bc}	21.6 ^{bc}	21.7 ^{bc}	21.0
Normal sowing	22.6 ^b	20.1 ^{bc}	22.8 ^b	21.9
c x s.t	20.7	20.6	21.0	20.8
Growing techniques	Jubile			
	15 march	30 march	15 april	c x g.t
Covered plant	18.7 ^c	19.6 ^{bc}	19.9 ^{bc}	19.4
Covered seed	21.6 ^{bc}	20.4 ^{bc}	19.7 ^{bc}	20.6
Normal sowing	28.5 ^a	22.7 ^b	20.1 ^{bc}	23.8
c x s.t	22.9	20.9	19.9	21.2
LSD	g.t(%1):2.364, cxg.txs.t(%5):3.559			

cultivar,
growing

c:
g.t:

techniques, s.t: sowing time

While the effect of growing techniques techniques on the cab ratio was found to be significant at the 1% level, the interactions of c x growing techniques x sowing times techniques appeared to be effective at 5% level. While the cab ratio of the Merit cultivar was determined as 20.8%, this ratio was 21.2% in the jubilee cultivar. According to datas, covered agriculture and early sowing in sweetcorn which cab ratio is be decrease, this state effects to grain yield positively. It is a negative situation that the cab ratio in normal sowing is high. Because it can be said that grain yield decreases in ear of sweetcorn affected by cold (26, 14).

3.7. Starch ratio (%)

In Table 9 was given the mean values and formed groups of two years (1997 - 1998) showing the effect of cultivar, sowing time and growing techniques on the starch ratio (%). As can be seen from the table 9, the highest starch ratio was obtained from the merit cultivar, according to c x g.t x s.t interactions as 54.1% (26). It can be said that the cultivation techniques did not have a statistically significant effect on the starch ratio. The highest starch ratio was found to be 55.9% on 30 March cultivars compared to the cultivar x sowing time interaction. April 15 plantations were in the same group with 54.0%.

Table – 9. Two-year mean values indicating the effect on the starch ratio (%) of cultivar, sowing time and growing techniques used in the experiment.

Growing techniques	Merit			
	15 march	30 march	15 april	c x g.t
Covered plant	52.7	57.3	52.0	54.0
Covered seed	53.0	55.0	54.8	54.2
Normal sowing	51.4	55.4	55.2	54.0
c x s.t	52.4 ^{bc}	55.9 ^a	54.0 ^{ab}	54.1a
Growing techniques	Jubile			
	15 march	30 march	15 april	c x g.t
Covered plant	53.7	52.0	53.5	53.1
Covered seed	50.2	51.8	54.7	52.0
Normal sowing	51.0	52.5	51.8	51.8
c x s.t	51.6 ^c	51.9 ^c	53.3 ^{bc}	52.3b
LSD	cultivar(%1):15.21, s.t(%5):1.468, cx.s.t(%5):2.076			

c: cultivar, g.t: growing techniques, s.t: sowing time

4. CONCLUSION

This study was carried out to investigate the effect of different growing techniques and sowing times on yield and earliness of two sweet corn cultivars. According to result covered seedlings growing techniques provided earliness and in the years covered seeding and plantings could be performed. It was founded when climatic factors was optimum covered seeding and plantings could be performed between 15 – 30 March. Also founded merit cultivar more adapted than jubile cultivar depth. Also, open seeding is only possible after 30 March. When deciding the proper growing techniques economic analysis including addition cost caused by plaastic, seedling procedurs compared to addition income from the earliness should be considered.

ACKNOWLEDGMENT

This article was written from (proje number of FBE 97 D-48) thesis with code no 51 of post graduate which is title “A research on to effective on yield and earliness of different sowing times and growing techniques in sweet corn (*Zea mays saccharata* Sturts) in Kahramanmaraş conditions” at the science institute of Çukurova University in 1999.

REFERENCES

- [1]. V. Tansı. “Çukurova bölgesinde mısır ve soyanın ikinci ürün olarak değişik ekim sistemlerinde birlikte yetiştirilmesinin tane ve hasıl yem verimine etkisi üzerinde araştırmalar”. Ç.Ü Fen Bilimleri Enstitüsü Tarla Bitkileri Anabilim Dalı Doktora Tezi. 1987.
- [2]. Bilgen. “Antalya ovası koşullarında iklim faktörlerinin mısırdaki (*Zea mays*) gelişme ve verim fizyolojisi üzerine etkileri”. Ç.Ü. Fen Bilimleri Enstitüsü Tarla Bitkileri Anabilim Dalı Doktora Tezi, Adana, 1996.
- [3]. D. Esen, “Tarımsal ekoloji”, A.Ü Ziraat Fak. Yay. No:287
- [4]. W.G.Duncan, and J.D.Hesketh, “Net photosynthetic rates, relative leaf growth rates and leaf number of 22 races of maize grown at eight temperatures”, *Crop Science*, 8:670 – 674, 1968.
- [5]. S.J.Mc Cormik, “The effects of sowing date of maize developments and yields of silageand grain”, *Proc.Inst.Ann.Cong.Agron.Soc.* 1971.
- [6]. M.A.Dillion, and R.E.Gwin, “How planting date and full season or early hybrids affect corn yields, *Field Crop Abst Vol.31 No.3*, 1978.
- [7]. J.M.White, “Effect of plant spacing and planting date on sweetcorn grown on muck soil in the spring, *Field Crop Abst . Vol.39 No.6*, 1984.
- [8]. S.U.Park, K.Y.Park, Y.G.Kang, H.G.Moon and S.K.Jong, “Effect of plant densityon growth and yield of sweetcorn hybrid” *Korean Journal of Crop Science*, 32(1)92-96, 1987.
- [9]. J.E.Wyatt and J.A.Mullins, “Production of sweetcorn from transplant”, *Hortscience*, 24(6):1039, 1989.
- [10]. H.Walicora, “Development and yield of sweetcorn grown in soil covered with plastic film. *Katedra Uprawny Roli Roslin ar Poznan, Poland*, 1995.
- [11]. S.Özer, S.Gökmen and M.İdi, “Şeker mısırı (*Zea mays saccharata* Sturt) agronomik özelliklerine ekim zamanı ve yetiştirme takniklerinin etkisi”, *J.of Agriculture and Forestry*, (21):65-71 (Tübitak), 1997.
- [12]. J.E.Wyatt and J.A.Mullins, *Transplanted sweetcorn, Hortscience*, 23(5):824, 1988.

- [13]. J.E.Wyatt and M.C.Akridge, Yield and quality of direct seeded and transplanted supersweet sweetcorn hybrids, Department of Plant and Soil Science, University of Tennessee Experiment Station, Jackson TN 38301.
- [14]. R.Özel and V.Tansi, Çukurova koşullarında iki şeker mısır çeşidinde şaşırtmanın ve farklı ekim zamanlarının verim ve diğer bazı özelliklere etkisi, Tarla Bitkileri Kongresi, c.I, s.300 – 312, 1994.
- [15]. M.Okant, Y.Şilbir, T.Sağlamtimur and V.Tansi, Ceylanpınarı tarım işletmesi akrepli istasyonunda ekim zamanları, beş mısır çeşidinde verim ve bazı tarımsal karakterlere etkisini saptamak amacıyla yapılan araştırma. Türkiye II. Çayır – Mer'a ve Yem bitkileri Kongresi, 1991.
- [16]. H.Gökçora, Türkiye’de yetiştirilen mısır çeşitlerinin başlıca vasıfları üzerine araştırmalar, A.Ü. Ziraat Fak. Yay. 86 s.143, 1956.
- [17]. M.A.Sharkawy, F.A.Sorour, K.Sgater and M.E.Yousef, Effect of dowing date on growing and yield of locale and imported mazie varieties (Zea mays L.) Field Crop.Abst. Vol.31, No.1, 1987.
- [18]. C.Köylü and S.Yanıkoglu, Samsun ekolojik şartlarında mısır (Zea mays L.) çeşit ekim zamanı üzerinde bir araştırma. Türkiye’de Mısır Üretimini Geliştirilmesi, Problemler ve Çözüm yolları Sempozyumu, 1987.
- [19]. L.Cesurer, Kahramanmaraş koşullarında ekim zamanı ve ekim sıklığının şeker mısırında taze koçan verimine ve diğer bazı tarımsal ve bitkisel özelliklere etkisi. Çukurova Üniversitesi Fen Bilimleri Enstitüsü Tarla Bitkileri Ana Bilim Dalı Doktora tezi Adana, 1995.
- [20]. M.Derieux, R.Bonhamme, J.B.Dubureq and F.Ruget, Variation in the number of grains in different maize genotypes. Maize Abst.2(1) p.3, 1985.
- [21]. L.J.R. Waters, R.L.Burrows, M.A.Bennett and J.Schoenecker, Seed moisture and transplant management techniques influence sweetcorn stand establishment, growth, development and yield, J.Arner.Soc.Hort Sci 115(6):888-892, 1990.
- [22]. T.Nakui, K.Nonaka, S.Hara and M.Shinoda, The effect of plastic mulch on the growth of corn plants and their TDN yield of silage in the tokachi district(Hokkaido, Japan). Research bulletin of the hokkaido national agricultural experiment station no:161, p.73-80, 1995.
- [23]. M.Furter, H.A Venter, and A.Vande, A comparasion of parameters for the assesment of relative cold tolerance of germinating kernels of maize (Zea mays L.), South African Journal of Plant and Soil 7(4)207 – 21, 1990.
- [24]. H.Z.Cross and M.S.Zuber, Prediction of flowering dates in maize based on different methods of estimating thermal units, Agron.J. 64:351 – 355, 1972.
- [25]. S.U.Park, K.Y.Park, Y.K.Kang, H.G.Moon and S.K.Jong, Effect of plant density on growth and yield of sweetcorn hybrid, Korean journal of Crop Science 32(1)92-96,1987.
- [26]. R.Özel, Çukurova koşullarında farklı ekim yöntemleri ve zamanının bazı şeker mısır çeşitlerinde verim ve bitkisel özelliklere etkisi, Çukurova Üniversitesi Fen Bilimleri Enstitüsü Yüksek Lisans Tezi kod no:889, 1994.



Influence of Opening Ratio and Position in Infill Wall on Constitutive Law of Equivalent Compression Strut

Onur Ozturkoglu^{1*}, Taner Ucar²

¹Dokuz Eylul University, Department of Civil Engineering, 35160, Buca/Izmir, Turkey.

²Dokuz Eylul University, Department of Architecture, 35160, Buca/Izmir, Turkey.

*Corresponding Author email: onur.ozturkoglu@deu.edu.tr

Abstract

Infill walls are widely used in any building to create a separation between spaces intended for different purposes. In general, partial openings exist in infill wall with different opening ratio and position due to architectural considerations, functional needs and aesthetic concerns. In current practice, buildings are considered as bare frames ignoring infills and openings. However, infill walls and partial openings may significantly affect the seismic behavior of structures. Equivalent compression strut model is frequently used in modelling of infill walls for structural analysis. Accordingly, the force-displacement (F–D) relationship of equivalent compression strut is quite important in nonlinear analysis of infilled frames. In particular, opening sizes and position are essential parameters in order to properly constitute F–D relationship of infill wall with openings simulated by means of an equivalent compression strut. In this study, F–D relationship of equivalent compression strut is determined for different opening ratios and positions in infill wall considering three different F–D relationship models available in the literature. The maximum strength of equivalent compression strut and the corresponding displacement, the compression cracking force and the corresponding displacement, the residual strength and the axial compressive stiffness of the strut are compared and discussed for different constitutive F–D laws. It is found that force values of F–D relationships decrease as opening ratio increases. However, displacement values are not generally effected by opening ratio or position. Furthermore, openings upon the diagonal are more influential on F–D relationships of equivalent compression strut in comparison to other opening positions.

Key words

Infill walls with openings, Opening ratio and positions, force-displacement relationship, equivalent compression strut

1. INTRODUCTION

In current design practice the presence of infill walls is generally neglected due to the complex composite behavior of the bounding frame and the infill wall, and the lack of a rational design procedure for masonry infilled buildings. However, the field observations after destructive earthquakes clearly illustrate that infill walls may have significant influence on seismic performance of structures by drastically altering the strength and stiffness characteristics, as well as the expected failure mechanism. Therefore, neglecting the infill walls in

practical structural analysis and design may lead to a substantial inaccuracy in estimating the seismic response of infilled structures in terms of both capacity and earthquake demand.

Numerical simulation of infill walls is essential to understand and evaluate the possible effects of infill walls on global seismic response of infilled structures during major seismic events. Accordingly, during the last decades, extensive experimental investigations and analytical studies have been performed to properly model the contribution of infill [1]–[13]. On the basis of available research works, the fundamental idea to incorporate the infill wall in numerical models is generally oriented at micro- and macro-modelling techniques. Although infill walls can be simulated more adequately using micro-models, this type of modelling technique generally requires more computational effort and found to be impractical for the analysis of three dimensional structures [9], [14]. Meanwhile, macro-models exhibit significant advantages by providing reasonable accuracy and efficiency in simulating the contribution of infill. Among these, the concept of single or multiple compressive equivalent diagonal struts has by far been the most favored one [7],[8], [10]–[18].

Estimation of nonlinear strength and stiffness characteristics of the infill during the inelastic response is the preliminary issue to be considered in nonlinear analysis. In this sense, it is essential to constitute realistic force–displacement relationships capable of representing the nonlinear behavior of the equivalent strut, which is not an easy task. Therefore, many different proposals have been made for determining the stiffness and strength characteristics of infill wall and several nonlinear constitutive F–D laws composed of three or four segments and mainly developed for solid infill walls are available in the literature [19]–[24]. The presence of prevalent openings, such as windows and doors, may possibly effect the adopted constitutive parameters causing a discontinuous load path within the infill wall. Furthermore, the variability of percentage and position of the opening reveals an important uncertainty in determination of the characteristic parameters assumed in the constitutive model.

Three different constitutive models all of which enable simulating infill walls by means of a single equivalent strut are considered. The influence of the opening in terms of both percentage and position is taken into consideration by using the derived stiffness reduction factors. The variation of stiffness reduction factor as a function of opening percentage for different positions of opening is obtained from finite element analysis considering infill wall-frame interaction. The modified F–D relationship models are constituted for specific opening percentages considering three different positions of opening as upon the diagonal, above the diagonal and under the diagonal. The stiffness and strength parameters calculated in the horizontal direction are precisely transformed to the direction of the equivalent diagonal. In order to investigate the influence of the infill wall opening percentage and the opening position on the constitutive law, the characteristic parameters assumed in constitutive models of the compressive equivalent diagonal strut in terms of strength, stiffness and displacement are compared for the reference F–D relationships.

2. STIFFNESS REDUCTION FACTORS FOR INFILL WALLS WITH OPENINGS

In order to account for the possible effects of openings on stiffness and strength of infill wall, stiffness reduction factors (k) varying between 0 (bare frame) and 1 (fully infilled frame) are introduced. Stiffness reduction factors are originally developed considering the position and the percentage of the opening within the infill wall. Infill walls are widely simulated by two-dimensional finite elements since their thickness is smaller in comparison to the length and the height. Accordingly, a modelling technique of plane finite elements is implemented to simulate infill wall. Dimension of finite elements (i.e. small pieces of shell elements) are accurately selected and openings within the wall are easily provided by erasing the related finite elements. The mutual interaction of the bounding frame and the masonry panel is modeled by means of gap elements that can only transform axial compression. The stiffness of gap element is determined as:

$$K_g = \frac{t_w \cdot a_w \cdot E_{me}}{r_w} \quad (1)$$

where t_w and E_{me} are the thickness and the elastic modulus of the infill wall, and a_w and r_w are the width and the length of the compressive equivalent diagonal strut, respectively. The implemented modelling technique is shown in Figure 1.

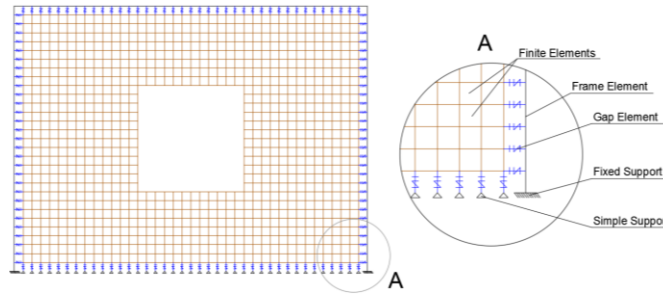


Figure 1. Modelling of the bounding frame, the infill wall and the interaction

Having completed the analytical model, a finite element analysis is conducted in elastic region for monotonic loading in order to determine stiffness reduction factors of infill walls with openings. Firstly, the lateral stiffness of one-story one-bay bare frame (k_{bare}) subjected to a horizontal load at the top level is obtained by dividing the applied load (P) to the lateral top displacement of the bare frame (Δ_{bare}). Then, applying the same procedure for a fully infilled frame yields the lateral stiffness of the fully infilled one (k_{full}). Finally, openings are provided within the infill wall and the lateral stiffness of partially infilled frame (k_{part}) is calculated. Figure 2 describes the procedure used to determine the lateral stiffness one-story one-bay infilled frame with openings.

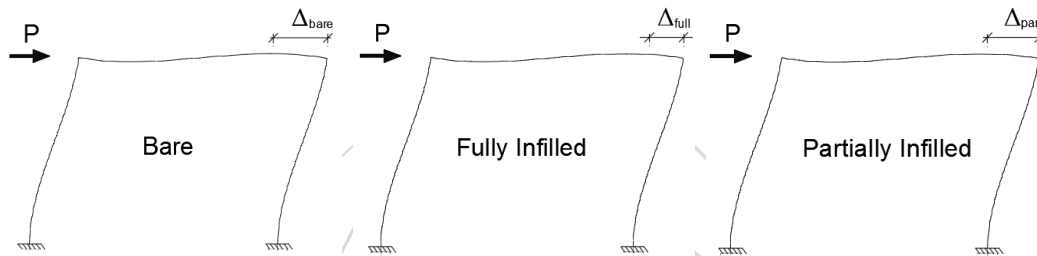


Figure 2. Determination of lateral stiffness of frames

The following equations yield the lateral stiffness of solid masonry infill panel ($k_{full,i}$) and the lateral stiffness of infill panel with openings ($k_{part,i}$), respectively:

$$k_{full,i} = k_{full} - k_{bare} \tag{2}$$

$$k_{part,i} = k_{part} - k_{bare} \tag{3}$$

Consequently, the stiffness reduction factor (k) accounting for the effect of the opening on the stiffness is obtained as the ratio of the lateral stiffness of infill wall with opening to the lateral stiffness of solid infill wall:

$$k = \frac{k_{part,i}}{k_{full,i}} \tag{4}$$

3. CONSTITUTIVE MODELLING OF INFILL WALLS

Infill walls with or without openings can significantly alter the seismic performance of structures by contributing to lateral resistance, interacting with the bounding frame and leading to different failure mechanisms expected for bare structures. In the field of nonlinear seismic analysis, the method of the compressive equivalent diagonal strut is widely used to simulate the behavior of infill panels since nonlinear micro-modelling technique requires high computational effort. The main problem containing large uncertainties is how to determine the F–D envelopes and hysteretic behavior of the diagonals. The following multi-linear constitutive models (i.e. F–D envelopes) which provide the simulation of infill wall by means of a single equivalent diagonal strut are adopted as a reference in the present study.

3.1. The Constitutive Law Proposed by Panagiotakos and Fardis

The constitutive model proposed by Panagiotakos and Fardis is composed of four segments [20]. The slope of the first branch, i.e. the initial shear stiffness of the uncracked panel (K_1), is specified as:

$$K_1 = \frac{G_w \cdot L_{in} \cdot t_w}{H_{in}} \tag{5}$$

where G_w is the shear modulus of the wall, L_{in} and H_{in} are the length and the height of the infill, respectively, and t_w is the thickness of the wall.

The yielding force (F_y) corresponding to the first cracking of infill wall (i.e. the cracking force) is associated with the tensile strength of the infill (f_{tp}) obtained from the diagonal compression test and is determined using the following equation:

$$F_y = f_{tp} \cdot L_{in} \cdot t_w \quad (6)$$

The second branch corresponds to the formation of a diagonal compressive path within the infill wall. Accordingly, the axial stiffness of the compressive equivalent diagonal strut (K_2) is:

$$K_2 = \frac{E_m \cdot t_w \cdot a_w}{r_w} \quad (7)$$

The ratio between the maximum force (F_m) and the cracking force is assumed to be 1.3. The displacement corresponding to the maximum force can easily be determined as:

$$\delta_m = \delta_y + \frac{F_m - F_y}{K_2} \quad (8)$$

where δ_y is the displacement at the cracking point.

The stiffness of the third branch representing the softening of the infill panel is assumed to range within $0.005 \cdot K_1 \leq K_3 \leq 0.1 \cdot K_1$. The residual force (F_r) is assumed $0.05 \cdot F_y \leq F_r \leq 0.1 \cdot F_y$ whereas the corresponding displacement (δ_r) is calculated as:

$$\delta_r = \delta_m + \frac{F_m - F_r}{K_3} \quad (9)$$

The fourth branch characterized by a constant residual strength describes the ultimate state of the infill wall. The F–D relationship of Panagiotakos and Fardis is shown in Figure 3 (a).

3.2. The Constitutive Law Proposed by Dolsek and Fajfar

A three-linear F–D envelope for the diagonal strut representing the masonry infill based on the results of some experimental tests is proposed by Dolsek and Fajfar [22]. The initial stiffness of the infill (K_1) is calculated according to Eq. (5). The strength of the infill (F_m) is determined as follows:

$$F_m = 0.818 \cdot \frac{L_{in} \cdot t_w \cdot f_{tp}}{C_I} \cdot \left(1 + \sqrt{C_I^2 + 1}\right) \quad (10)$$

where C_I is estimated by:

$$C_I = 1.925 \cdot \frac{L_{in}}{H_{in}} \quad (11)$$

The cracking force (F_y) is assumed to be $0.6 \cdot F_m$. The story drift corresponding to the maximum force (D_m) is 0.2% in case of solid infill panel, 0.15% in case of window opening and 0.10% in case of door opening. The ratio between the story drift at collapse of the infill panel and that at the maximum force is arbitrarily assumed as 5 (Figure 3 (b)).

For the F–D envelope of the diagonal strut, both the initial stiffness and the strength in horizontal direction have to be transformed to the direction of the diagonal, as well as in the constitutive relationship proposed by Panagiotakos and Fardis.

3.3. The Constitutive Law Proposed by Tsai and Huang

A multi-linear constitutive F–D law is used to simulate the nonlinear behavior of the compressive equivalent diagonal strut. The compressive strength of the infill (R_m) is evaluated through the following equation:

$$R_m = a_w \cdot t_w \cdot f'_{m90} \quad (12)$$

where f'_{m90} is the horizontal expected strength of the infill panel and is assumed to be 65% of the compressive strength of the infill (f'_m) which is estimated in terms of the compressive strength of bricks (f_b) and the mortar strength (f_j) as follows [2]:

$$f'_m = 0.63 \cdot f_b^{0.49} \cdot f_j^{0.32} \quad (13)$$

The displacement corresponding to the compressive strength of the infill is:

$$\Delta_m = \varepsilon'_m \cdot r_w \quad (14)$$

where ε'_m is the strain corresponding to the maximum compressive strength and is estimated by:

$$\epsilon'_m = \frac{0.27}{f_j^{0.25}} \cdot \frac{f'_m}{E_{me}^{0.7}} \tag{15}$$

The cracking force (R_y) is given by:

$$R_y = \frac{R_m - \alpha K_1 \Delta_m}{1 - \alpha} \tag{16}$$

The post-stiffness ratio (α) is assumed as 0.2. The displacement at the cracking (Δ_y) can be calculated as:

$$\Delta_y = \frac{R_y}{K_1} \tag{17}$$

Finally, the residual strength of the diagonal strut (R_r) is assumed to 30% of the cracking force. The model of Tsai and Huang, and the main involved parameters are shown in Figure 3 (c).

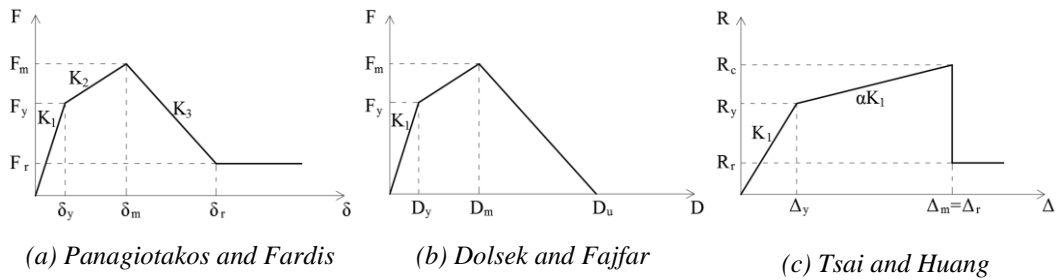


Figure 3. The adopted constitutive models

4. CASE STUDY

In order to investigate the possible influence of opening percentage and position within the infill wall on the relevant parameters of the constitutive model of the compressive equivalent diagonal strut, one-story one-bay reinforced concrete (RC) frame is considered. The bay length is 5 m and the story height is 3 m. Rectangular beams and square columns are considered in the design. Rectangular beam dimensions are 25x50 cm and square columns dimensions are 40x40 cm. The compressive strength of concrete is assumed to be 20 MPa. The masonry infill consists of hollow bricks with a thickness of $t_w = 200$ mm. The elastic modulus of infill wall is calculated as $E_{me} = 1661$ MPa considering the stress-strain relations of brick infill and mortar [2]. Three different positions of window opening as opening upon the diagonal, opening above the diagonal and opening under the diagonal, and three opening percentages (the area of the opening to the total area of infill) as 22%, 32% and 45% are considered. The typical layout of the openings is shown in Figure 4.

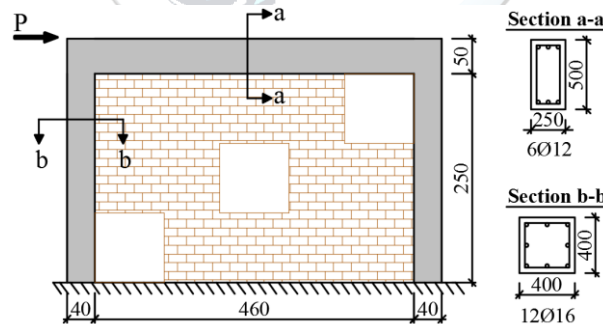


Figure 4. Layout of the openings within the wall and the bounding RC frame

4.1. Stiffness Reduction Factors

The influence of the opening in terms of both percentage and position is taken into consideration by means of stiffness reduction factors. The variation of stiffness reduction factor as a function of opening percentage for different positions of opening is obtained from finite element analysis considering infill wall-frame interaction. The finite element analysis is conducted in the elastic region for the monotonic loading using the structural analysis tool SAP2000 [25]. Figure 5 shows the derived stiffness reduction factor of infilled frame with openings in relation to opening percentage for three different positions of opening. One can easily obtain the stiffness reduction factors entering in this graph. The stiffness reduction factors determined for the opening positions and percentages considered in this study are presented in Table 1.

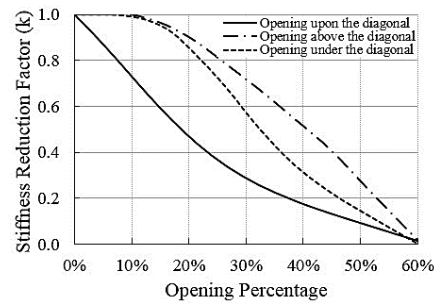


Figure 5. Variation of stiffness reduction factor in relation to opening percentage

Table 1. Stiffness reduction factors

Opening percentage (%)	Position of the opening		
	Upon the diagonal	Above the diagonal	Under the diagonal
22	0.43	0.88	0.82
32	0.26	0.68	0.52
45	0.13	0.41	0.22

With reference to Figure 5, it can be concluded that stiffness reduction factors of all opening positions decrease as opening percentage increases. However, the position of opening substantially effects the variation of the stiffness reduction factor with respect to opening percentage. Opening upon the diagonal is more influential on reducing the stiffness of the infill wall, since it gives smaller stiffness reduction factors. This position of opening significantly reduces the stiffness even in case of small opening percentages. On the other hand, opening above the diagonal is the least influential position. For opening percentages smaller than 18 both opening positions above the diagonal and under the diagonal have the same influence on stiffness of infill and for opening percentages small than 10, the presence of the opening may be neglected for those positions of the opening. On the contrary, the contribution of the infill wall with opening can be ignored regardless of the position in case infill wall opening ratio exceeds 60%.

4.2. The Modified Constitutive Relationships

Since the influence of the opening in terms of both percentage and position is taken into consideration by using the stiffness reduction factors of the study, strength and stiffness parameters of the constitutive F–D law are conveniently reduced. Accordingly, modified F–D relationships reflecting the influence of the opening are constituted for infill walls with openings. The additional necessary parameters to constitute the reference F–D relationships are taken as $G_w = 664.4$ MPa, $f_{tp} = 0.36$ MPa and $f'_{m90} = 3.02$ MPa. The width of the compressive equivalent diagonal strut is calculated as $a_w = 637$ mm for the infill wall without opening [26]. In order to properly investigate the influence of opening percentage and position on the constitutive law of the compressive equivalent diagonal strut, stiffness and strength parameters applied to the horizontal direction in the models of Panagiotakos and Fardis, and Dolsek and Fajfar are transformed to the direction of the diagonal. Accordingly, summarized in Table 2 are the constitutive parameters of the diagonal strut.

The values of constitutive parameters in terms of both strength and stiffness decrease with increasing infill wall opening ratio in all the constitutive models. The highest strength and stiffness values are obtained when the opening is considered above the diagonal and the smallest ones are calculated for the central opening. The cracking and the maximum force values of the Panagiotakos and Fardis constitutive law are relatively higher than those values of the other two models. Although its higher strength, the cracking force of the constitutive law proposed by Fardis and Fajfar is smaller than the cracking force of the Tsai and Huang constitutive law. The initial stiffness of the constitutive F–D laws of Panagiotakos and Fardis and Dolsek and Fajfar is equal while the initial stiffness of Tsai and Huang constitutive relationship is quite low. Accordingly, larger displacements are obtained in the case of the model of Tsai and Huang. K_2 stiffness of the Dolsek and Fajfar constitutive law is 60% higher than K_2 stiffness of the Panagiotakos and Fardis model, while the stiffness of the softening branch of the two model is almost the same. Displacement corresponding to the cracking point is not influenced by the infill wall opening ratio and the opening position. The displacement corresponding to the maximum force and the ultimate displacement of the infill panel with opening are found to be smaller than those values of the solid panel in the case of Dolsek and Fajfar constitutive law. However, the infill wall opening ratio does not affect these displacements. On the other hand, the constitutive displacements of the other two models do not change according to the infill wall opening ratio and the opening position.

Table 2. Constitutive parameters of the diagonal strut

Opening position	Opening percentage	R_y (kN)	A_y (mm)	R_m (kN)	A_m (mm)	R_r (kN)	A_n (mm)
Panagiotakos and Fardis							
Fully infilled	0%	377	1.19	490	3.99	38	18.27
Upon the diagonal strut	22%	164	1.19	213	3.99	16	18.27
	32%	97	1.19	126	3.99	10	18.27
	45%	49	1.19	64	3.99	5	18.27
Above the diagonal strut	22%	330	1.19	429	3.99	33	18.27
	32%	254	1.19	331	3.99	25	18.27
	45%	153	1.19	198	3.99	15	18.27
Under the diagonal strut	22%	308	1.19	400	3.99	31	18.27
	32%	196	1.19	255	3.99	20	18.27
	45%	83	1.19	108	3.99	8	18.27
Dolsek and Fajfar							
Fully infilled	0%	245	0.77	408	4.39	-	21.96
Upon the diagonal strut	22%	106	0.77	177	3.29	-	16.47
	32%	63	0.77	105	3.29	-	16.47
	45%	32	0.77	53	3.29	-	16.47
Above the diagonal strut	22%	214	0.77	357	3.29	-	16.47
	32%	165	0.77	275	3.29	-	16.47
	45%	99	0.77	165	3.29	-	16.47
Under the diagonal strut	22%	200	0.77	333	3.29	-	16.47
	32%	127	0.77	212	3.29	-	16.47
	45%	54	0.77	90	3.29	-	16.47
Tsai and Huang							
Fully infilled	0%	294	7.28	385	18.54	88	-
Upon the diagonal strut	22%	128	7.28	168	18.54	38	-
	32%	76	7.28	99	18.54	23	-
	45%	38	7.28	50	18.54	12	-
Above the diagonal strut	22%	258	7.28	337	18.54	77	-
	32%	199	7.28	260	18.54	60	-
	45%	119	7.28	156	18.54	36	-
Under the diagonal strut	22%	240	7.28	314	18.54	72	-
	32%	153	7.28	201	18.54	46	-
	45%	65	7.28	85	18.54	19	-

In Figure 6, the F–D relationships obtained for the opening position upon the diagonal, which is found to be the most influential opening position, using the constitutive parameters of Table 2 is plotted.

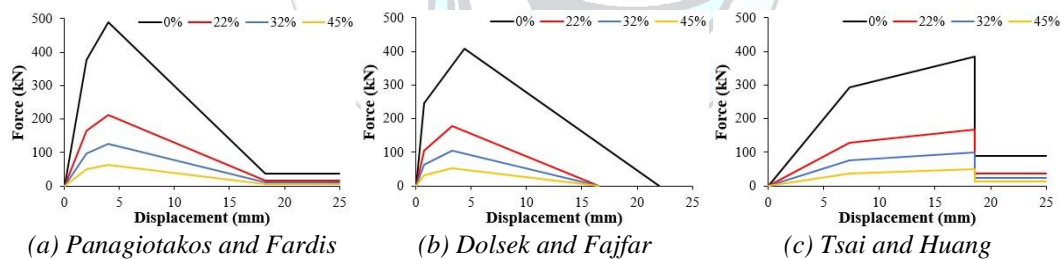


Figure 6. F–D relationships for the opening position upon the diagonal strut

5. CONCLUSIONS

The results of the study demonstrate that the stiffness and strength values of the constitutive relationships decrease as the opening ratio increases and the position of the opening has a substantial influence on those values. However, the displacements are not affected by the infill wall opening ratio and the opening position expect the displacement corresponding to the strength of the infill in the case of the constitutive law proposed by Dolsek and Fajfar. A relatively large displacement at the cracking point of the infill wall is obtained in the case of the Tsai and Huang constitutive law, while the cracking displacements of the other two models show quite close agreement. Although the constitutive law of Dolsek and Fajfar yields relatively smaller ultimate displacement, the ultimate displacements of the considered models agree quite well. Openings upon the diagonal are found to be more influential on the constitutive parameters of the considered F–D relationships of the compressive equivalent diagonal strut.

Considering the complexity of adopting a simple yet realistic constitutive law for masonry infill walls, it can be concluded that the agreement between the characteristic parameters of the different constitutive models is quite reasonable.

REFERENCES

- [1]. K. M. Mosalam, R. N. White, and P. Gergely, "Static response of infilled frames using quasi-static experimentation," *Journal of Structural Engineering*, vol. 123(11), pp. 1462–1469, 1997.
- [2]. H. B. Kaushik, D. C. Rai, and S. K. Jain, "Stress-strain characteristics of clay brick masonry under uniaxial compression," *Journal of Materials in Civil Engineering*, vol. 19(9), pp. 728–739, 2007.
- [3]. D. J. Kakaletsis, and C. G. Karayannis, "Experimental investigation of infilled reinforced concrete frames with opening," *ACI Structural Journal*, vol. 106(2), pp. 132–141, 2009.
- [4]. P. G. Asteris, D. J. Kakaletsis, C. Z. Chrysostomou, and E. E. Smyrou, "Failure modes of in-filled frames," *Electronic Journal of Structural Engineering*, vol. 11(1), pp. 11–20, 2011.
- [5]. S. M. M. Emami, and M. Mohammadi, "Influence of vertical load on in-plane behavior of masonry infilled steel frames," *Earthquakes and Structures*, vol. 11(4), pp. 609–627, 2016.
- [6]. M. Bolhassani, A. A. Hamid, C. Johnson, and A. E. Schultz, "Shear strength expression for partially grouted masonry walls," *Engineering Structures*, vol. 127, pp. 475–494, 2016.
- [7]. M. Dolsek, and P. Fajfar, "Mathematical modelling of an infilled RC frame structure based on the results of pseudo-dynamic tests," *Earthquake Engineering and Structural Dynamics*, vol. 31(6), pp. 1215–1230, 2002.
- [8]. G. Mondal, and S. K. Jain, "Lateral stiffness of masonry infilled reinforced concrete (RC) frames with central opening," *Earthquake Spectra*, vol. 24(3), pp. 701–723, 2008.
- [9]. E. Smyrou, C. Blandon, S. Antoniou, R. Pinho, and F. Crisafulli, "Implementation and verification of a masonry panel model for nonlinear dynamic analysis of infilled RC frames," *Bulletin of Earthquake Engineering*, vol. 9(5), pp. 1519–1534, 2011.
- [10]. A. Fiore, F. Porco, D. Raffaele, and G. Uva, "About the influence of the infill panels over the collapse mechanisms activated under pushover analyses: Two case studies," *Soil Dynamics and Earthquake Engineering*, vol. 39, pp. 11–22, 2012.
- [11]. E. Martinelli, C. Lima, and G. D. Stefano, "A simplified procedure for nonlinear static analysis of masonry infilled RC frames," *Engineering Structures*, vol. 101, pp. 591–608, 2015.
- [12]. P. G. Asteris, C. C. Repapis, A. K. Tsaris, F. D. Trapani, and L. Cavaleri, "Parameters affecting the fundamental period of infilled RC frame structures," *Earthquakes and Structures*, vol. 9(5), pp. 999–1028, 2015.
- [13]. O. Ozturkoglu, T. Ucar, and Y. Yesilce, "Effect of masonry infill walls with openings on nonlinear response of reinforced concrete frames," *Earthquakes and Structures*, vol. 12(3), pp. 333–347, 2017.
- [14]. G. Uva, D. Raffaele, F. Porco, and A. Fiore, "On the role of equivalent strut models in the seismic assessment of infilled RC buildings," *Engineering Structures*, vol. 42, pp. 83–94, 2012.
- [15]. A. Madan, A. M. Reinborn, J. B. Mander, and R. E. Valles, "Modeling of masonry infill panels for structural analysis," *Journal of Structural Engineering*, vol. 123(10), pp. 1295–1307, 1997.
- [16]. P. Ricci, G. M. Verderame, and G. Manfredi, "Analytical investigation of elastic period of infilled RC MRF buildings," *Engineering Structures*, vol. 33(2), pp. 308–319, 2011.
- [17]. G. Uva, F. Porco, and A. Fiore, "Appraisal of masonry infill walls effect in the seismic response of RC framed buildings: A case study," *Engineering Structures*, vol. 34, pp. 514–526, 2012.
- [18]. M. Ercolino, P. Ricci, G. Magliulo, and G.M Verderame, "Influence of infill panels on an irregular RC building designed according to seismic code," *Earthquakes and Structures*, vol. 10(2), pp. 261–291, 2016.
- [19]. S. H. Bertoldi, L. D. Decanini, and C. Gavarini, "Telai tamponati soggetti ad azioni sismiche, un modello semplificato: confronto sperimentale e numeric," in *Proc. Atti del 6° Convegno Nazionale L'ingegneria Sismica in Italia*, Perugia, Italy, 1993.
- [20]. T. B. Panagiotakos, and M. N. Fardis, "Proposed nonlinear strut models for infill panels," University of Patras, Greece, 1st Year Progress Report of HCM-PREC8 Project, 1994.
- [21]. K. B. Hanoglu, "Fiber reinforced plastic overlay retrofit of hollow clay tile masonry infilled reinforced concrete frames," PhD Thesis, Bogazici University, Istanbul, Turkey, 2002.
- [22]. M. Dolsek, and P. Fajfar, "The effect of masonry infills on the seismic response of a four-storey reinforced concrete frame—a deterministic assessment," *Engineering Structures*, vol. 30(7), pp. 1991–2001, 2008.
- [23]. H. Rodrigues, H. Varum, and A. Costa, "Simplified macro-model for infill masonry panels," *Journal of Earthquake Engineering*, vol. 14(3), pp. 390–416, 2010.
- [24]. M. H. Tsai, and T. C. Huang, "Numerical investigation on the progressive collapse resistance of an RC building with brick infills under column loss," *World Academy of Science, Engineering and Technology*, vol. 58, pp. 946–953, 2011.
- [25]. *SAP2000 Integrated Structural Analysis and Design Software, Ver.16.0.0*, Computer and Structures Inc., USA, 2016.
- [26]. *Prestandard and Commentary for the Seismic Rehabilitation of Buildings (FEMA 356)*, Federal Emergency Management Agency, Washington, D.C., 2000.



Numerical Investigation of the Effect of Twisted Tape in a Tube Using Water-TiO₂ Nanofluid on Heat Transfer Enhancement

Toygun Dagdevir¹, Orhan Keklikcioglu¹, Veysel Ozceyhan^{1*}

¹Erciyes University, Department of Mechanical Engineering, 38039, Melikgazi/Kayseri, Turkey.

*Corresponding Author email: ozceyhan@erciyes.edu.tr

Abstract

In this study, effects of inserting twisted tape into a horizontal tube and adding TiO₂ nanoparticle to water on heat transfer enhancement performance and pressure drop penalty are investigated with using CFD program. Analyses are carried out with Reynolds number of in range from 7860 to 15860, and constant heat flux of 50kW/m²K is applied to wall of the tube. To simulate turbulent nanofluid flow k- ω standard turbulent model is applied for all cases. TiO₂ particles with diameter of 10 nm dispersed in water with volume fraction of 0.2% - 2.0% are used as the working fluid. To create swirl flow and enhance heat transfer, the twisted tape (constant twist ratio is $y/W=3.0$) is used in this study. The results show that adding nanoparticle to water causes to get more convective heat transfer coefficient as from 6% (for 0.2% vol. fract.) to 11% (for 2.0% vol. fract.) in a smooth tube. Furthermore, both adding nanoparticle to water and inserting the twisted tape to the smooth tube causes to 1.44 times greater convective heat transfer coefficient than case of smooth tube and water. In addition to heat transfer performance, pressure drop penalty is investigated in this study. Increasing nanoparticles in the water increase pressure drop penalty slightly, but using twisted tape in the smooth tube increases pressure drop penalty as about 6.5 times more.

Key words

CFD, nanofluid, twisted tape, heat transfer, pressure drop

1. INTRODUCTION

At last decade, energy costs dramatically rise up day by day, since human population increase, and energy sources are consumed. Using the energy efficiently is significantly important for countries that import energy, especially. Heating or cooling systems need so much energy input such as pumping power and electrical resistant for heating, and compressor power for cooling. Within this scope, heat transfer enhanced methods are used and investigated methods. In recent years, nanofluid is used as working fluid for heat transfer devices. Choi [1] is probably the first researcher about the use of particles in nano dimension. Many researchers experimentally studied on this field and reported that nano-particles in the fluids augment heat transfer performance depends on concentration amount, particle size and Reynolds number at last three decades [2-10]. Main reason of using nanofluid is that thermal conductivity property is greater than conventional fluid. Thus, heat transfer performance enhances in comparison with using conventional fluid. The heat transfer enhanced investigations are carried out experimentally and numerically, or both.

Moghadassi et al. [11] investigated numerically the effect of water based Al₂O₃ and Al₂O₃-CuO hybrid nanofluid on forced convective heat transfer. The nanofluid with 0.1 % volume fraction and average particle size of 15nm was considered. Their results showed that higher convective heat transfer coefficient was obtained for Al₂O₃-CuO nanofluid. And they reported that average Nusselt number increase was 4.73% and 13.46% in comparison with Al₂O₃-water and distilled water, respectively. Celen et al. [12] numerically carried out an investigation for TiO₂-water nanofluids in order to observe average temperature, pressure and velocity distribution inside pipe. They used an experimental study data to validate accuracy of numerical methodology. Their results were tolerably as similar as experimental results. Demir et al.[13] searched numerically forced convection flows of nanofluids consisting of water with Al₂O₃ and TiO₂ nanoparticles in a horizontal tube with constant wall temperature used of a single-phase model. Dawood et al.[14] numerically investigated the effect of nanoparticles on heat transfer enhancement in an elliptic annulus, unlike circular pipe. Al₂O₃, CuO, SiO₂ and ZnO were employed as nanoparticles

and volume fraction and Reynolds number respectively was ranging from 0.5% to 4% and 4,000 to 10,000. Their numerical results showed that the best heat transfer was obtained for glycerin-SiO₂ mixture that was volume fraction of 4% and Reynolds number of 10,000.

2. NUMERICAL INVESTIGATION

2.1. Solution Domain

In this study, thermal performance of twisted tape inserted in a horizontal straight tube under constant heat flux is numerically investigated via a CFD program. Working fluid is selected as water and, in addition to twisted tape insert, TiO₂ nanoparticle is added to water. The solution domain 3D geometry is described as in Fig. 1. Smooth tube (ST) and twisted tape inserted tube (TTIT) are illustrated in Fig 2. The twisted tape has y/w ratio of 3.0. y and w represent the pitch length of twisted tape and width of the tape, respectively.

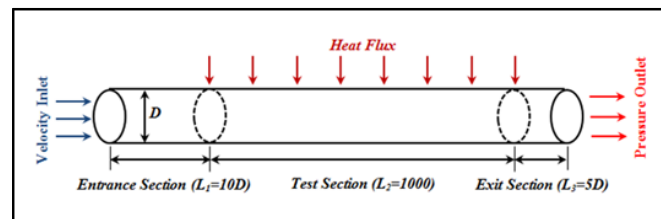


Figure 1. Solution domain and boundary condition types

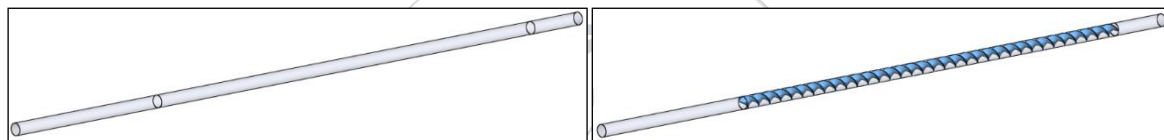


Figure 2. (a) Smooth tube (ST)

(b) twisted tape inserted tube (TTIT)

The test tube material is aluminum and selected as 19 mm diameter and an entrance section (L_1) is taken as a 10D to supply fully developed flow at the inlet of the test region, test section L_2 is considered as 1m and exit section (L_3) is chosen as 5D to defect the reverse flow. The boundary condition and definition are given in Table 1. Polyhedral mesh structure and boundary layer mesh are created both smooth tube and twisted tape as illustrated in Fig 3.

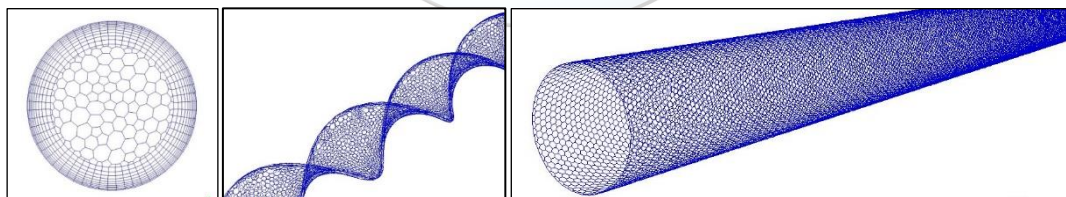


Figure 3. Mesh structure of cross sectional view of (a) the tube at inlet and outlet, (b) outer surface of twisted tape (c) outer surface of tube

Table 1. Boundary condition definitions and values

	Definition	Value
D [mm]	Diameter	19
L_1 [mm]	Entrance Section	10D
L_2 [mm]	Test Section	1000
L_3 [mm]	Exit Section	5D
q'' [kW/m ² K]	Constant Heat Flux	50
Inlet Velocity magnitude [m/s]	Velocity Inlet	Calculated depends on Re
Gauge Pressure [Pa]	Pressure Outlet	0

2.2. Data Reduction and Thermo-Physical Properties of Nanofluid

The CFD program uses differential equation to simulate and calculate flow characteristic and thermal occurrences. Used conversation equations in CFD program are as follows:

Conservation of mass equation [15]:

$$\frac{\partial \rho}{\partial t} + \nabla \cdot (\rho \mathbf{u}) = 0 \quad (1)$$

Conservation of momentum equation [15]:

$$\frac{\partial}{\partial t} (\rho \vec{v}) + \nabla (\rho \vec{v} \vec{v}) = -\nabla P + \nabla (\bar{\tau}) + \rho \vec{g} + \vec{F} \quad (2)$$

Energy equation [15]:

$$\frac{\partial}{\partial t} (\rho E) + \nabla (\vec{v} (\rho E + p)) = \nabla (k_{eff} \nabla T - \sum_j h_j \vec{J}_j + (\bar{\tau}_{eff} \cdot \vec{v})) + S_h \quad (3)$$

The results were compared with S. Eimsa-ard [16] et al. and commonly used equations that are Gnielinski Eq. (6) and Blasius Eq. (7) in terms of Nusselt number (4) and friction factor (5), respectively.

$$Nu = \frac{hD}{k} \quad (4)$$

$$f = \frac{\Delta P}{\frac{1}{2} \rho v^2 \frac{L}{D}} \quad (5)$$

Gnielinski Equation [17]:

$$Nu = \frac{\left(\frac{L}{8}\right)(Re-1000)Pr}{1 + \left[12.7\left(\frac{L}{8}\right)^{0.5} (Pr^{2/3}-1)\right]} \quad (6)$$

Blaisus Eq. [18]:

$$f = 0.316 Re^{-0.25} \quad (7)$$

2.3. Validation of the numerical methodology

To ensure validation of the numerical methodology, especially including fluid mechanics problems turbulence model should be determined, and experimental results or empirical correlations can be used for comparing numerical results. In this context, different turbulence models are tested, and k-w standard model is most matching model with reference results. Validation of the numerical study for smooth tube and water is given in Fig 4 and 5 in terms of Nusselt number and friction factor, respectively. As can be seen in these figures, a good agreement is ensured for proving accuracy of numerical methodology.

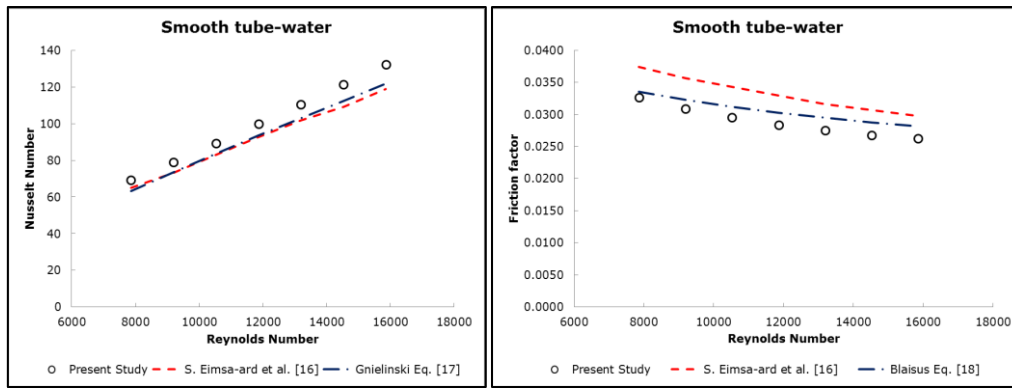


Figure 4. Numerical results for smooth tube and water in terms of (a) Nusselt number (b) friction factor

Mixture approach is employed to model nanofluids, and properties of fluid are applied as independent in temperature. Validation of nanofluid with different fraction ($\varphi=0.002, 0.006, 0.01$ and 0.02) and different nanoparticles is illustrated in Fig. 5. Good agreement is observed between the result of present study and the other studies. Thermo-physical properties of nanofluid is calculated with following equations:

Density of nanofluid:

$$\rho_{nf} = (1 - \varphi)\rho_{bf} + \varphi\rho_{np} \quad (8)$$

Specific heat of nanofluid:

$$Cp_{nf} = \frac{(1-\varphi)(\rho_{bf})(Cp_{bf})+(\varphi\rho_{np})(Cp_{np})}{\rho_{nf}} \quad (9)$$

Thermal conductivity:

$$k_{nf} = k_{bf} \frac{[k_{np}+(n-1)k_{bf}-(n-1)\varphi(k_{bf}-k_{np})]}{[k_{np}+(n-1)k_{bf}+\varphi(k_{bf}-k_{np})]} \quad (10)$$

$$n = 3/\psi \quad (11)$$

where n is the empirical shape factor and ψ is the sphericity, defined as the ratio of the surface area of a sphere to the surface area of the particle (Eq. 11), as stated by Duangthongsuk and Wongwises [19]. The sphericity value assumed as 1. Expressions of k_{nf} , k_{np} and k_{bf} are the thermal conductivity of nanofluid, nanoparticle and base fluid, respectively. Dynamic viscosity of hybrid nanofluid does not need to calculate again due not to including expect of volume fraction (φ) in the formula.

Dynamic viscosity:

$$\mu_{nf} = \mu_{bf}(123\varphi^2 + 7.3\varphi + 1) \quad (12)$$

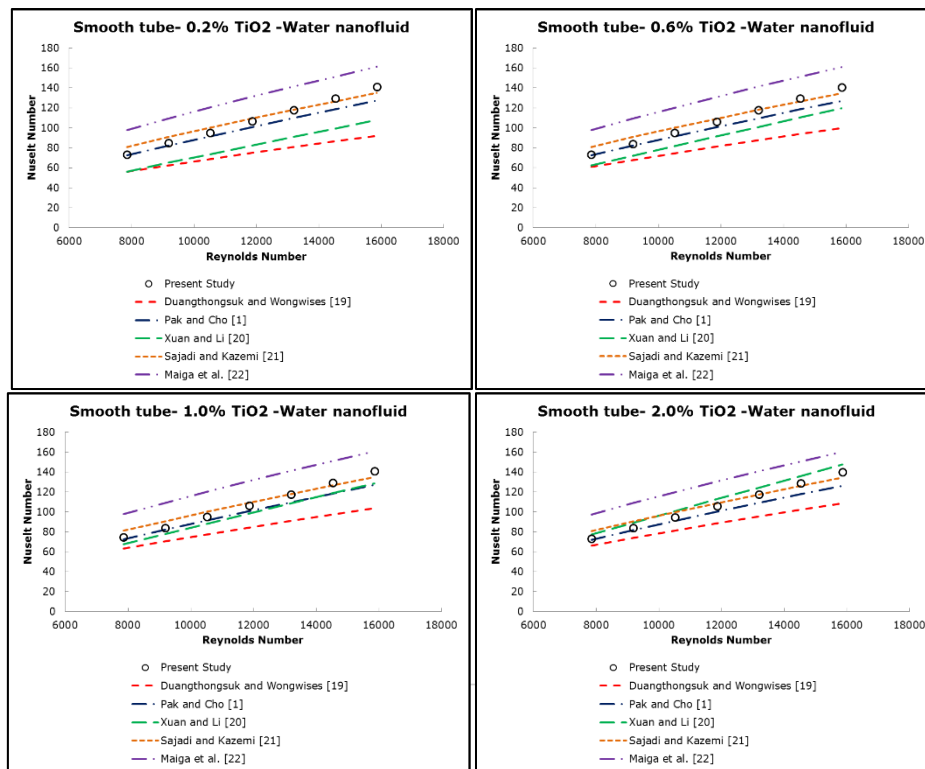


Figure 5. Validation of numerical results for smooth tube and TiO₂-water nanofluid in terms of Nusselt number versus Reynolds Number

In addition to nanofluid investigation, twisted tape effect is investigated in this study. Twisted tape inserted tube through water flow validation is ensured with Manglik and Bergles Eqs. [23] in terms of Nusselt number (13) and friction factor (14), as illustrated in Figure 6.

$$Nu = \left(1 + \frac{0.769}{\frac{y}{w}}\right) \left[0.023Re^{0.8}Pr^{0.4} \left(\frac{\pi}{\pi-4\delta/D}\right)^{0.8} \left(\frac{\pi+2-2\delta/D}{\pi-4\delta/D}\right)^{0.2}\right] \tag{13}$$

$$f = \left(1 + 2.06 \left(1 + \left(\frac{2(y/w)}{\mu}\right)^2\right)^{-0.75}\right) \left[0.079Re^{-0.25} \left(\frac{\pi}{\pi-4\delta/D}\right)^{1.75} \left(\frac{\pi+2-2\delta/D}{\pi-4\delta/D}\right)^{0.125}\right] \tag{14}$$

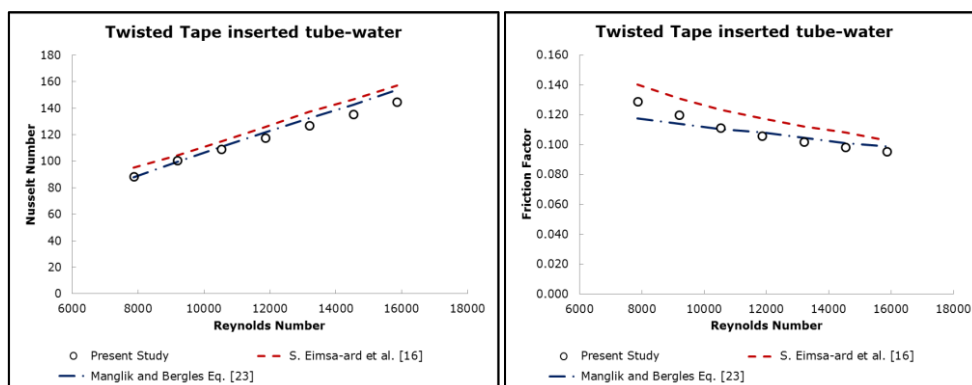


Figure 6. (a) Nusselt number results for TTIT

(b) Friction factor results for TTIT

3. RESULTS AND DISCUSSIONS

In this study, numerical investigation of effects of both TiO_2 -water nanofluid and twisted tape on thermal and hydraulic performance is carried out by using a CFD program. The nanofluid volume fraction is considered in range from 0.002 to 0.02. With developing nano technology, nanofluids have been used in heat transfer mechanisms. Because thermal conductivity of working fluid increases, heat transfer enhances for these systems. Numerical results of TiO_2 -water nanofluid through the smooth tube are given in terms of heat transfer coefficient and pressure drop in Fig 7 and 8, respectively. With increment of nanoparticle into water, heat transfer coefficient increases for increment of Reynolds number. Pressure drop increases with increment of nanoparticle into water, due to viscosity and density of the fluid increase.

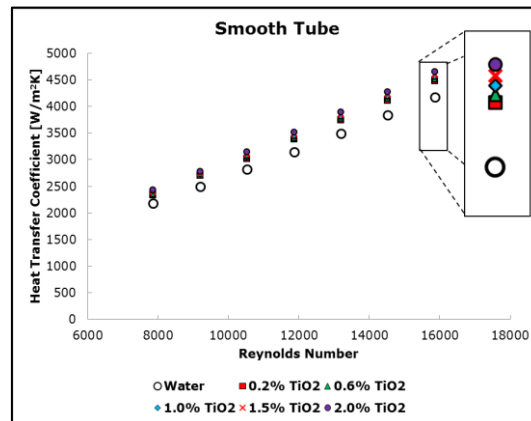


Figure 7. Results of TiO_2 -water nanofluid through the smooth tube in terms of heat transfer coefficient versus Reynolds number

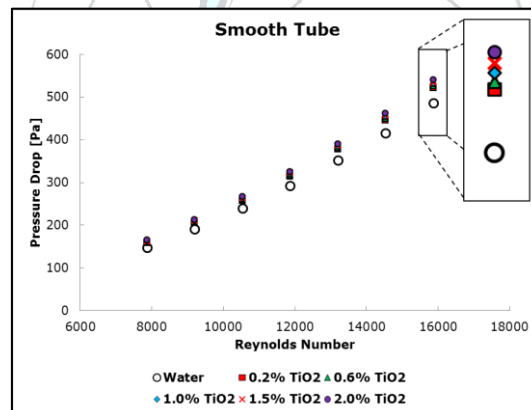


Figure 8. Results of TiO_2 -water nanofluid through the smooth tube in terms of pressure drop versus Reynolds number

In order to enhance heat transfer performance, turbulators like twisted tape insert are widely used. The twisted tape physically enhanced heat transfer by destructing thermal and hydraulic boundary layer near the inner surface of the tube. The effect of twisted tape in terms of heat transfer coefficient and pressure drop is given in Fig 9 and 10. The twisted tape inserts in tube create swirl flow, and because of that secondary flow occurs. With occurrence of the secondary flow, the fluid more contacts with heated wall and spends more time until leave the tube. The swirl flow and secondary flow is depicted in Figure 11 and 12, respectively. In other hand, inserting twisted tape cause to increase pressure drop penalty. It is expected result, because the flow counters with an obstacle surface in the flow direction.

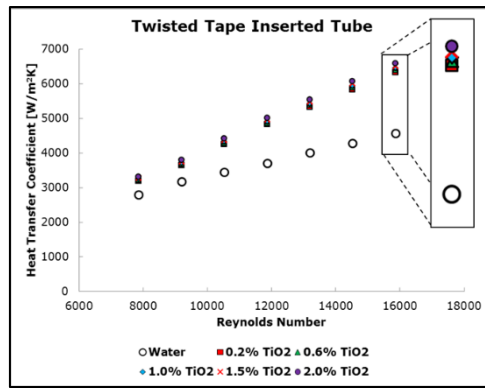


Figure 9. Results of TiO_2 -water nanofluid through the twisted tape inserted tube in terms of heat transfer coefficient versus Reynolds number

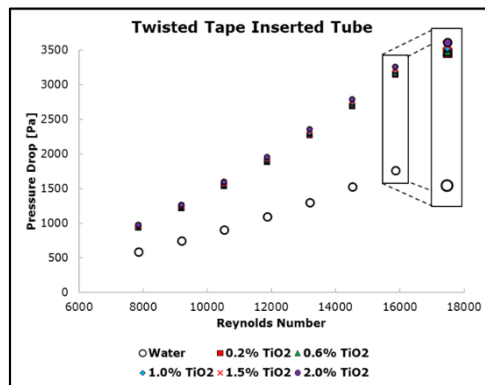


Figure 10. Results of TiO_2 -water nanofluid through the twisted tape inserted tube in terms of pressure drop versus Reynolds number

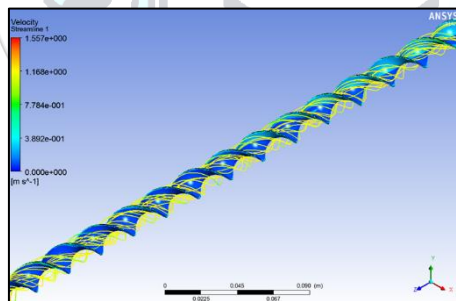


Figure 11. Swirl flow due to twisted tape through the tube

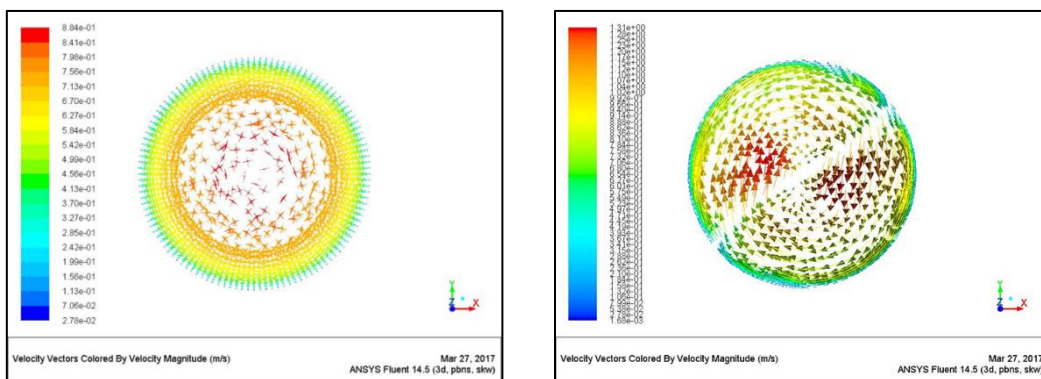


Figure 12. (a) Velocity vector contour of the smooth tube; (b) Velocity vector contour twisted tape inserted tube

4. CONCLUSION

In this study, effect of TiO₂-water nanofluid and twisted tape insert on heat transfer and pressure drop is numerically investigated by using mixture phase model. Results showed that convective heat transfer enhances for all considered volume fraction of TiO₂ nanofluid with increasing Reynolds number. Major reason of the heat transfer enhancement is that thermal conductivity of the nanofluid is so greater than distilled water. Furthermore, with inserting twisted tape into smooth tube, it is purposed generating secondary flow. Maximum heat transfer coefficient is obtained as 6593 W/m²K for the case of twisted tape inserted tube volume fraction 2.0, Reynolds number of 15,860. This value is 1.44 times greater than smooth tube for same Reynolds number.

The main findings can be summarized as physical (inserting twisted tape) and chemical (adding nanoparticle) reasons at below:

- ✓ Inserting a twisted tape in a tube increases heat transfer and pressure drop.
- ✓ The main reason of increasing heat transfer is destructing the boundary layer and occurring secondary flow.
- ✓ Maximum heat transfer coefficient is obtained as 6593 W/m²K for Reynolds number of 15860. This value is 1.44 times greater than smooth tube for same Reynolds number.
- ✓ The main reason of increasing pressure drop is that flow encounter with an obstacle surface, and increasing static pressure through the tube.

In terms of chemical reasons

- ✓ Adding nanoparticle up to volume fraction of 2.0% into water, increases the heat transfer, as well. The main reason of this result is that thermal conductivity of the nanofluid increases, and because of that, heat transfer occurs more effectively between the molecules.
- ✓ Adding nanoparticle into water slightly increase the pressure drop in comparison with heat transfer. The reason of increasing pressure drop is related with increasing viscosity and density of the nanofluid.

NOMENCLATURE

<i>Abbreviation</i>	<i>definition</i>	<i>unit</i>
Cp	specific heat,	[J/kg K]
D	tube diameter,	[m]
f	friction factor	[-]
h	heat transfer coefficient,	[W/m ² K]
k	thermal conductivity,	[W/mK]
L	length of the test tube,	[m]
N	empirical shape factor	[-]
Nu	Nusselt number	[-]
ΔP	Pressure drop,	[Pa]
Pr	Prandtl number	[-]
q	heat flux,	[W/m ²]
Re	Reynolds number	[-]
T	temperature,	[°C]
V	velocity	[m/s]
y	period length of twisted tape	[mm]
w	width pf twisted tape	[mm]

Subscripts

b	bulk fluid temp.
f	fluid
in	inlet
out	outlet
nf	nanofluid
np	nanoparticle
s	smooth tube
w	water

Greek symbols

ϕ	volume fraction	(%)
ρ	density,	[kg/m ³]
μ	viscosity,	[kg/ms]
δ	thickness of twisted tape	[mm]

REFERENCES

- [1]. B.C. Pak and Y.I. Choi, "Hydrodynamic and Heat Transfer Study of Dispersed Fluids with Submicron Metallic Oxide Particles" *Exp. Heat Transfer*, vol. 11, pp. 151–170, August 2016.
- [2]. S. Eimsa-ard, P. Promvong, Numerical study on heat transfer of turbulent channel flow over periodic grooves, *International Communications in Heat and Mass Transfer* 35 (2008) 844-852.
- [3]. A. Azari, M. Lalbasi, M. Derakhshandeh and M. Rahimi, An experimental study on Nanofluids convective heat transfer through a straight tube under constant heat flux, *Fluid Dynamics and Transport Phenomena* 21 (2013) 1082-1088.
- [4]. S. Z. Heris, S. Gh. Etemad and M. N. Esfahany, Experimental investigation of oxide nanofluids laminar flow convective heat transfer, *International Communications in Heat and Mass Transfer* 33 (2006) 529-535.
- [5]. S. Suresh, K. P. Venkitaraj, P. Selvakumar and M. Chandrasekar, Effect of Al₂O₃-Cu/water hybrid nanofluid in heat transfer, *Experimental Thermal and Fluid Science*. 38 (2012) 54-60.
- [6]. M. M. Heyhat, F. Kowsary, A. M. Rashidi, S. A. V. Esfehiani, A. Amrollahi, Experimental investigation of turbulent flow and convective heat transfer characteristics of alumina water nanofluids in fully developed flow regime, *International Communications in Heat and Mass Transfer* 39 (2012) 1272-1278.
- [7]. D. Wen and Y. Ding, Experimental investigation into convective heat transfer of nanofluids at the entrance region under laminar flow conditions, *International Communications in Heat and Mass Transfer* 47 (2004) 5181-5188.
- [8]. B. Sahin, G. G. Gültekin, E. Manay, S. Karagoz, Experimental investigation of heat transfer and pressure drop characteristics of Al₂O₃-water nanofluid, *Experimental Thermal and Fluid Science* 50 (2013) 21-28.
- [9]. M. H. Esfe, S. Saedodin, M. Mahmoodi, Experimental studies on the convective heat transfer performance and thermo physical properties of MgO/water nanofluid under turbulent flow, *Experimental Thermal and Fluid Science* 52 (2014) 68-78.
- [10]. V. Trisaksri, S. Wongwises, Critical review of heat transfer characteristics of nanofluids, *Renewable and Sustainable Energy Reviews* 11 (2007) 512-523.
- [11]. A. Moghadassi, E. Ghomi, F. Parvizian, "A Numerical Study of water based Al₂O₃ and Al₂O₃-Cu Hybrid Nanofluid Effect on Forced Convective Heat Transfer" *Int. Journal of Thermal Sciences*, 2015; 92: 50-57.
- [12]. A. Celen, N. Kayaci, A. Cebi, H. Demir, A. S. Dalkilic, S. Wongwises "Numerical Study on Application of CuO-water Nanofluid in Automotive Diesel Engine Radiator" *Modern Mechanical Engineering*, 2012; 2: 130-136
- [13]. H. Demir, A. S. Dalkilic, N. A. Kürekci, W. Duangthongsuk, S. Wongwises, Numerical investigation on the single phase forced convection heat transfer characteristics of TiO₂ nanofluids in a double-tube counter flow heat exchanger, *International Communications in Heat and Mass Transfer* 38 (2011) 218-228
- [14]. H. K. Dawood, H. A. Mohammed, N. A. C. Sidik, K. M. Munisamy, Numerical investigation on heat transfer and friction factor characteristics of laminar and turbulent flow in an elliptic annulus utilizing nanofluid, *International Communications in Heat and Mass Transfer* 66 (2015) 148-157.
- [15]. *Fluent v.6.3 User Guide*, Fluent Corporation, Lebanon, New Hampshire, 2006.
- [16]. S. Eimsa-ard, P. Seemawute, K. Wongcharee, Influences of peripherally-cut twisted tape insert on heat transfer and thermal performance characteristics in laminar and turbulent tube flows, *Experimental Thermal and Fluid Science*, 2010, vol. 34, pp. 711-719.
- [17]. F.P. Incropera, P.D. Witt, T.L. Bergman, A.S. Lavine, *Fundamental of Heat and Mass Transfer*, John-Wiley & Sons, 2006.
- [18]. Petukhov BS: Heat transfer and friction in turbulent pipe flow with variable physical properties. *In Advances in Heat Transfer*. Edited by: Hartnett JP, Irvine TS. New York: Academic Press; 1970.
- [19]. W. Duangthongsuk and S. Wongwises, An experimental study on the heat transfer performance and pressure drop of TiO₂-water nanofluids flowing under a turbulent flow regime, *International Journal of Heat and Mass Transfer*, 2010, vol. 53, pp. 334-344.
- [20]. Y. Xuan, Q. Li, Investigation on convective heat transfer and flow features of nanofluids, *ASME J. Heat Transfer*, 2003, vol. 125, pp. 151-155.
- [21]. A. R. Sajadi and M.H. Kazemi, Investigation of turbulent convective heat transfer and pressure drop of TiO₂/water nanofluid in circular tube, *International Communications in Heat and Mass Transfer*, 2011, vol. 38, pp. 1474-1478.
- [22]. M. S.E.B. Maiga, C.T. Nguyen, N. Galanis, G. Roy, T. Mare, M. Coqueux, Heat transfer enhancement in turbulent tube flow using Al₂O₃ nanoparticle suspension, *International Journal of Numerical Methods for Heat and Fluid Flow*, 2006, vol. 16, pp. 275-292.
- [23]. R. M. Manglik and A. E. Bergles, Heat Transfer and Pressure Drop Correlations for Twisted-Tape Inserts in Isothermal Tubes: Part II—Transition and Turbulent Flows, *Journal of Heat Transfer*, 1993, vol. 115, pp. 890-896.



Free Vibration Analysis of Multi-span Timoshenko Beams on Elastic Foundation Using Dynamic Stiffness Method

Baran Bozyigit^{1*}, Yusuf Yesilce¹

¹Dokuz Eylul University, Department of Civil Engineering, 35160, Buca/Izmir, Turkey.

*Corresponding Author email: baran.bozyigit@deu.edu.tr

Abstract

In this study, the exact first five natural frequencies of three-span Timoshenko beams on Winkler foundation are calculated using dynamic stiffness formulation. Different elastic foundation spring constants and different beam cross-sections are used to reflect their effects on natural frequencies. Moreover, the natural frequencies are also calculated via structural analysis software SAP2000 and tabulated with exact results. It is seen that the influence of elastic foundation spring stiffness in inner span is high in comparison with outer spans. The cross-section of the beam plays an important role on natural frequencies of multi-span Timoshenko beams on Winkler foundation.

Key words

Dynamic stiffness, free vibration, multi-span Timoshenko beam, Winkler foundation

1. INTRODUCTION

The calculation of exact natural frequencies of beams is of great interest to researchers for a long time. In the recent years, free vibration analyses of different types of beams with various loading conditions are performed using different methods [1-5]. The vibration problem of beams on elastic foundations can be encountered especially in civil engineering and mechanical engineering applications. The elastic foundations are modeled using elastic springs. The effects of elastic foundation can be important for beams or beam assembly structures. Thus, there are numerous studies about different foundation models carrying various types of beams and structures [6-10]. The dynamic stiffness method (DSM) is an effective method for calculating exact natural frequencies of beams or beam like structures as the method uses the exact shape functions. Vibration analyses of many types of beams and plates are performed by using DSM in recent years [11-17].

In this study, free vibration analysis of three-span simply supported beams on Winkler foundation is performed using DSM. Timoshenko Beam Theory (TBT) which considers shear deformation and rotational inertia is used. In the numerical analysis, different spring stiffness values for spans are selected to reveal the effect of elastic foundation on natural frequencies. To reflect the importance of beam geometry, several analyses are completed for different beam geometries. SAP2000 is a well known and widely used structural analysis software worldwide.

Thus, SAP2000 is used to obtain natural frequencies of beams on Winkler foundation and the results are compared with exact values.

2. MODEL AND FORMULATION

The mathematical model of three-span Timoshenko beam on Winkler foundation can be seen in Figure 1. Here, x and y represents the axes, k_{s1} , k_{s2} and k_{s3} are Winkler foundation spring stiffnesses, L is the span length, b is width of the beam and h is the height of the beam.

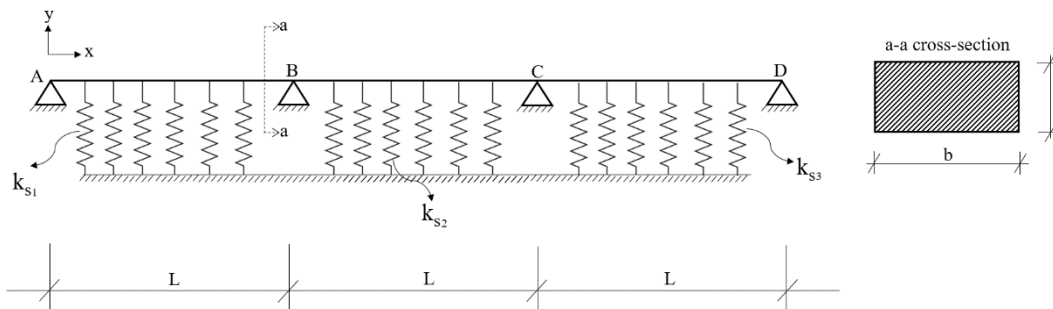


Figure 1. Three-span Timoshenko beam on Winkler foundation

Let the denomination of span AB as 1, span BC as 2 and span CD as 3.

The assumptions listed below are considered to clarify and simplicate the analysis procedure:

- 1) The beam is constructed by using an isotropic and homogenous material.
- 2) The cross-section of the beam is uniform.
- 3) The beam behaves linear and elastic.
- 4) The damping is neglected.
- 5) The foundation springs are linear and distributed along the beam length.

The governing equations of motion of vibrating Timoshenko beam resting on Winkler foundation are given as follows:

$$\frac{AG}{k} \left(\frac{\partial^2 y_n(x,t)}{\partial x^2} - \frac{\partial \theta_n(x,t)}{\partial x} \right) - \bar{m} \frac{\partial^2 y_n(x,t)}{\partial t^2} - k_{sn} y_n(x,t) = 0 \tag{1}$$

$$EI \frac{\partial^2 \theta_n(x,t)}{\partial x^2} - \bar{m} \frac{I}{A} \frac{\partial^2 \theta_n(x,t)}{\partial t^2} + \frac{AG}{k} \left(\frac{\partial y_n(x,t)}{\partial x} - \theta_n(x,t) \right) = 0$$

In Eq. (1), A is cross-sectional area, I is area moment of inertia, G is shear modulus, E is Young’s modulus, \bar{k} is shear coefficient, \bar{m} is mass per unit length. $y_n(x,t)$ and $\theta_n(x,t)$ are n th beam span’s deflection function and rotation function, respectively (n=1, 2, 3).

If the motion of the beam is harmonic and separation of variables method is applied, the following equation is obtained:

$$\frac{AG}{kL^2} \frac{d^2 y_n(z)}{dz^2} - \frac{AG}{kL} \frac{d \theta_n(z)}{dz} + \bar{m} \omega^2 y_n(z) - k_{sn} y_n(z) = 0 \tag{2}$$

$$\frac{EI}{L^2} \frac{d^2 \theta_n(z)}{dz^2} + \frac{AG}{kL} \frac{dy_n(z)}{dz} + \left(\frac{\bar{m} I \omega^2}{A} - \frac{AG}{k} \right) \theta_n(z) = 0$$

where $z=x/L$ and ω is natural frequency.

The solution is assumed as:

$$y_n(z) = \{ \bar{C} \}_n e^{isz} \tag{3}$$

$$\theta_n(z) = \{ \bar{D} \}_n e^{isz}$$

Substituting Eq.(3) into Eq.(2), $y_n(z)$ and $\theta_n(z)$ functions are given in Eq.(4) and Eq. (5), respectively.

$$y_n(z) = (\bar{C}_{n1} e^{is_{n1}z} + \bar{C}_{n2} e^{is_{n2}z} + \bar{C}_{n3} e^{is_{n3}z} + \bar{C}_{n4} e^{is_{n4}z}) \tag{4}$$

$$\theta_n(z) = (K_{n1}\bar{C}_{n1}e^{is_{n1}z} + K_{n2}\bar{C}_{n2}e^{is_{n2}z} + K_{n3}\bar{C}_{n3}e^{is_{n3}z} + K_{n4}\bar{C}_{n4}e^{is_{n4}z}) \quad (5)$$

$$\text{where } K_{nm} = \frac{-\left(\frac{AG}{kL^2}\right) + (m\omega^2) - k_{sn}}{\left(\frac{AG}{kL^2}\right)is_j}; m=1,2,3,4; j=1,2,3,4$$

The bending moment function and shear force function are defined in Eq.(6) and Eq.(7), respectively.

$$M_n(z) = \frac{EI}{L} \frac{d\theta_n(z)}{dz} \quad (6)$$

$$Q_n(z) = \frac{AG}{kL} \frac{dy_n(z)}{dz} - \frac{AG}{k} \theta_n(z) \quad (7)$$

3. DYNAMIC STIFFNESS METHOD (DSM) FOR CALCULATING NATURAL FREQUENCIES

DSM is a technique that can be used for calculating exact natural frequencies using exact mode shapes. First of all, the dynamic stiffness matrix should be obtained. The dynamic stiffness matrix can be constructed by using end displacements and end forces of beam. The vector of end displacements of beam and the vector of coefficients are given in Eqs. (8) and (9), respectively.

$$\delta_n = [y_{n0} \quad \theta_{n0} \quad y_{n1} \quad \theta_{n1}]^T \quad (8)$$

$$\bar{C}_n = [\bar{C}_{n1} \quad \bar{C}_{n2} \quad \bar{C}_{n3} \quad \bar{C}_{n4}]^T \quad (9)$$

where

$$y_{n0} = y_n(z=0), \theta_{n0} = \theta_n(z=0), y_{n1} = y_n(z=1), \theta_{n1} = \theta_n(z=1)$$

Eqs. (8) and (9) can be rewritten in the form below:

$$\begin{bmatrix} y_{n0} \\ \theta_{n0} \\ y_{n1} \\ \theta_{n1} \end{bmatrix} = \begin{bmatrix} 1 & 1 & 1 & 1 \\ K_{n1} & K_{n2} & K_{n3} & K_{n4} \\ e^{is_{n1}} & e^{is_{n2}} & e^{is_{n3}} & e^{is_{n4}} \\ K_{n1}e^{is_{n1}} & K_{n2}e^{is_{n2}} & K_{n3}e^{is_{n3}} & K_{n4}e^{is_{n4}} \end{bmatrix} \begin{bmatrix} \bar{C}_{n1} \\ \bar{C}_{n2} \\ \bar{C}_{n3} \\ \bar{C}_{n4} \end{bmatrix} \quad (10)$$

The closed form of Eq. (10) is given in Eq. (11):

$$\delta_n = A_n \bar{C}_n \quad (11)$$

where

$$A_n = \begin{bmatrix} 1 & 1 & 1 & 1 \\ K_{n1} & K_{n2} & K_{n3} & K_{n4} \\ e^{is_{n1}} & e^{is_{n2}} & e^{is_{n3}} & e^{is_{n4}} \\ K_{n1}e^{is_{n1}} & K_{n2}e^{is_{n2}} & K_{n3}e^{is_{n3}} & K_{n4}e^{is_{n4}} \end{bmatrix}$$

The end forces of the beam is given in vector form in Eq. (12):

$$F = [Q_{n0} \quad M_{n0} \quad Q_{n1} \quad M_{n1}]^T \quad (12)$$

where

$$Q_{n0} = Q_n(z=0), M_{n0} = M_n(z=0), Q_{n1} = Q_n(z=1), M_{n1} = M_n(z=1)$$

Eqs. (12) and (9) can be written in the following form:

$$\begin{bmatrix} Q_{n0} \\ M_{n0} \\ Q_{n1} \\ M_{n1} \end{bmatrix} = \begin{bmatrix} \lambda_1 & \lambda_2 & \lambda_3 & \lambda_4 \\ A_1 & A_2 & A_3 & A_4 \\ -\lambda_1 e^{i s_{n1}} & -\lambda_2 e^{i s_{n2}} & -\lambda_3 e^{i s_{n3}} & -\lambda_4 e^{i s_{n4}} \\ -A_1 e^{i s_{n1}} & -A_2 e^{i s_{n2}} & -A_3 e^{i s_{n3}} & -A_4 e^{i s_{n4}} \end{bmatrix} \begin{bmatrix} \bar{C}_{n1} \\ \bar{C}_{n2} \\ \bar{C}_{n3} \\ \bar{C}_{n4} \end{bmatrix} \tag{13}$$

where $\lambda_j = \frac{AG}{kL} i s_{nj} - \frac{AG}{k} K_{nj}$; $A_j = \frac{EI}{L} i s_{nj} K_{nj}$; $j = 1, 2, 3, 4$

The closed form of Eq. (13) can be written as:

$$F_n = \kappa_n \bar{C}_n \tag{14}$$

where

$$\kappa_n = \begin{bmatrix} \lambda_1 & \lambda_2 & \lambda_3 & \lambda_4 \\ A_1 & A_2 & A_3 & A_4 \\ -\lambda_1 e^{i s_{n1}} & -\lambda_2 e^{i s_{n2}} & -\lambda_3 e^{i s_{n3}} & -\lambda_4 e^{i s_{n4}} \\ -A_1 e^{i s_{n1}} & -A_2 e^{i s_{n2}} & -A_3 e^{i s_{n3}} & -A_4 e^{i s_{n4}} \end{bmatrix}$$

Eqs.(11) and (14) are used to construct the dynamic stiffness matrix of the n th span of the Timoshenko beam on elastic foundation.

$$F_n = \kappa_n A_n^{-1} \bar{C}_n \tag{15}$$

In Eq.(15), $\kappa_n A_n^{-1}$ represents the dynamic stiffness matrix of the n th span. The natural frequencies of the beam are calculated by equating the determinant of assembly of $\kappa_1 A_1^{-1}$, $\kappa_2 A_2^{-1}$ and $\kappa_3 A_3^{-1}$ to zero. It should be noted that the related rows and columns of dynamic stiffness matrix of the beam are erased according to boundary conditions.

4. NUMERICAL ANALYSIS AND DISCUSSION

A three-span Timoshenko beam on Winkler foundation is used for numerical analysis with the following properties: $E=2 \times 10^7$ kN/m², $G=7692308$ kN/m², $\bar{k}=1.2$, $\rho=25$ kN/m³, $L=6$ m, $b=1$ m.

The boundary conditions are same for each span and given below.

$$y_n(z=0)=0, M_n(z=0)=0, y_n(z=1)=0, M_n(z=1)=0$$

The analyses are performed for constant k_{s2} and k_{s3} with varying k_{s1} , constant k_{s1} and k_{s3} with varying k_{s2} , constant spring stiffnesses with various beam height values. The first five natural frequencies of the beam are presented in Tables (1-3). It should be noted that SAP2000 results are obtained by dividing spans into 1 cm segments for accuracy.

Table.1. First five natural frequencies ($h=0.75$ m, $k_{s2}=10000$ kN/m, $k_{s3}=10000$ kN/m)

Natural Frequency (Hz)	k_{s1} (kN/m)									
	5000		10000		15000		20000		25000	
	DSM	SAP2000	DSM	SAP2000	DSM	SAP2000	DSM	SAP2000	DSM	SAP2000
1st Mode	28.0633	27.9550	28.4933	28.3837	28.8479	28.737	29.1383	29.026	29.3761	29.263
2nd Mode	34.2849	34.1590	34.7388	34.6111	35.2293	35.100	35.7462	35.615	36.2791	36.146
3rd Mode	47.7167	47.5440	47.8373	47.6645	47.9680	47.795	48.1097	47.936	48.2637	48.089
4th Mode	97.9198	98.8130	98.0322	98.9265	98.1410	99.036	98.2463	99.142	98.3481	99.245
5th Mode	108.2491	109.1420	108.3922	109.2864	108.5373	109.433	108.6843	109.582	108.8329	109.732

Table.2. First five natural frequencies ($h=0.75$ m, $k_{s1}=10000$ kN/m, $k_{s3}=10000$ kN/m)

Natural Frequency (Hz)	k_{s2} (kN/m)									
	5000		10000		15000		20000		25000	
	DSM	SAP2000	DSM	SAP2000	DSM	SAP2000	DSM	SAP2000	DSM	SAP2000
1st Mode	28.0891	27.9805	28.4933	28.3837	28.8707	28.7591	29.2232	29.1088	29.5528	29.4346
2nd Mode	34.7134	34.5983	34.7388	34.6111	34.7642	34.624	34.7894	34.6364	34.8145	34.6488
3rd Mode	47.3841	47.2243	47.8373	47.6645	48.2986	48.1141	48.7671	48.5716	49.2421	49.0365
4th Mode	97.9209	98.8141	98.0322	98.9265	98.1421	99.0373	98.2505	99.1466	98.3576	99.2545
5th Mode	108.3738	109.2747	108.3922	109.2864	108.4108	109.2981	108.4295	109.3099	108.448	109.3218

Table.3. First five natural frequencies ($k_{s1}=k_{s2}=k_{s3}=10000$ kN/m)

Natural Frequency (Hz)	h (m)									
	0.55		0.65		0.75		0.85		0.95	
	DSM	SAP2000	DSM	SAP2000	DSM	SAP2000	DSM	SAP2000	DSM	SAP2000
1st Mode	23.5876	23.4357	25.8912	25.7561	28.4933	28.3837	31.2525	31.1793	34.0842	34.0593
2nd Mode	27.9915	27.8159	31.2701	31.1127	34.7388	34.6111	38.2623	38.1773	41.7629	41.7336
3rd Mode	37.6891	37.4618	42.8127	42.5751	47.8373	47.6645	52.7395	52.6141	57.4279	57.3597
4th Mode	75.5356	75.6747	87.0604	87.5351	98.0322	98.9265	108.3847	109.7625	118.095	119.9983
5th Mode	84.3307	84.4696	96.7702	97.2515	108.3922	109.2864	119.1587	120.5124	129.078	130.9151

It is seen from Table 1 that, the natural frequencies are increased with increasing spring stiffness of an outer span of three-span beam. Table 2 shows that there is also an augmentation in natural frequencies when the spring stiffness of middle span is increased. There is no significant difference between the particular increment of spring stiffness of middle span and an outer span on natural frequencies. Table 3 reveals that the natural frequencies are increased due to increasing beam height and higher modes are more sensitive to this effect.

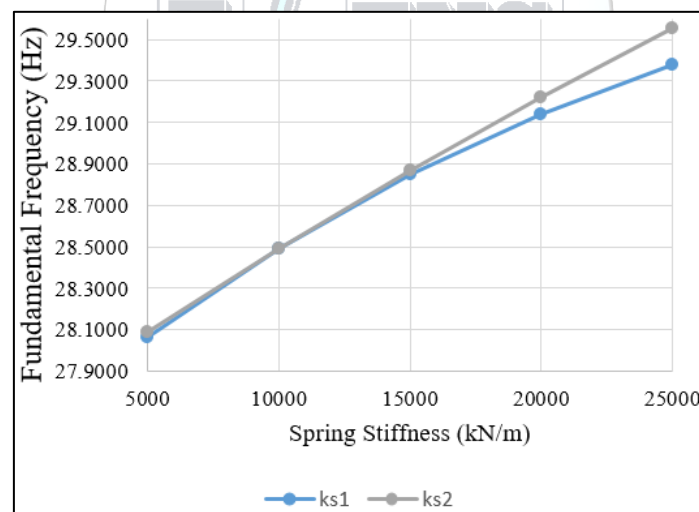
Figure.2. Fundamental frequencies for different k_{s1} and k_{s2} values

Figure 2 implies that fundamental frequency of three-span Timoshenko beam on Winkler foundation is more sensitive to spring stiffness of middle span in comparison with outer span especially for high stiffness values. Figure 3 represents the variation of first three natural frequencies with different beam height values.

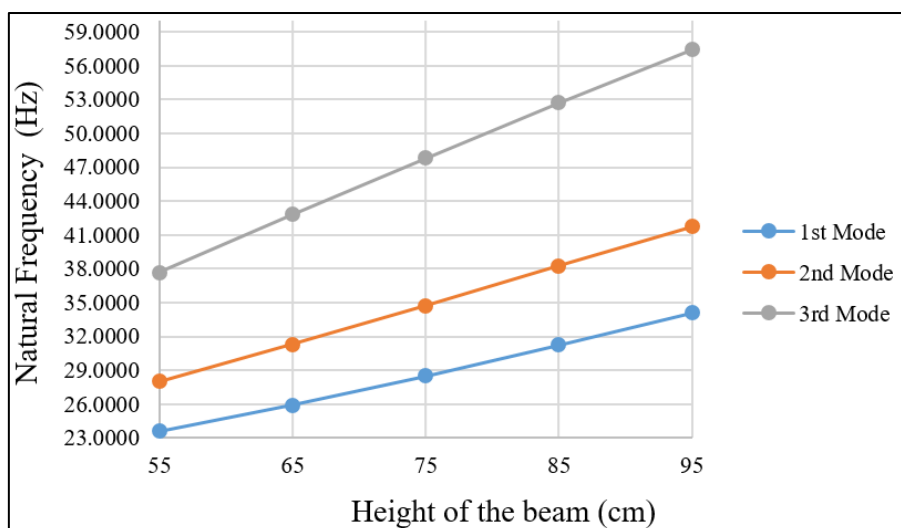


Figure.3. First three natural frequencies for different h values ($k_{s1}=k_{s2}=k_{s3}=10000$ kN/m)

6. CONCLUSIONS

The first five exact natural frequencies of three-span Timoshenko beams on Winkler foundation are obtained using dynamic stiffness approach. The spring stiffnesses of middle span is more effective than outer span. Different beam height values are used in the numerical analysis and effects on natural frequencies are observed. SAP2000 provides fairly well results when segment number increased sufficiently. The DSM can be used for calculating exact natural frequencies of multi-span Timoshenko beams on elastic foundation with different support conditions and foundation models.

REFERENCES

- [1]. Y. Yesilce, "Determination of Natural Frequencies and Mode Shapes of Axially Moving Timoshenko Beams with Different Boundary Conditions using Differential Transform Method", *Advances in Vibration Engineering*, vol. 12, pp. 89-108, 2013.
- [2]. W. R. Chen, "Parametric studies on bending vibration of axially-loaded twisted Timoshenko beams with locally distributed Kelvin-Voigt damping", *International Journal of Mechanical Sciences*, vol. 88, pp. 61-70, 2016.
- [3]. S. G. Kelly, C. Nicely, "Free vibrations of a Series of Beams Connected by Viscoelastic Layers", *Advances in Acoustics and Vibration*, Article ID 976841, 8 pages, 2015.
- [4]. G. Tan, W. Wang, Y. Jiao, "Flexural Free Vibrations of Multistep Nonuniform Beams", *Advances in Acoustics and Vibration*, Article ID 7314280, 12 pages, 2016.
- [5]. B. R. Goncalves, A. Karttunen, J. Romanoff, J. N. Reddy, "Buckling and free vibration of shear-flexible sandwich beams using a couple-stress-based finite element", *Composite Structures*, vol. 165, pp. 233-241, 2017.
- [6]. T. M. Wang, J. E. Stephens, "Natural frequencies of Timoshenko beams on Pasternak foundations", *Journal of Sound and Vibration*, Vol. 51(2), pp. 149-155, 1977.
- [7]. S. Y. Lee, Y. H. Kou, F. Y. Lin, "Stability of a Timoshenko beam resting on a Winkler elastic foundation", *Journal of Sound and Vibration*, vol. 153(2), pp. 193-202, 1992.
- [8]. M. A. De Rosa, "Free vibrations of Timoshenko beams on two-parameter elastic foundation". *Computers & Structures*, vol. 57(1), pp. 151-156, 1995.
- [9]. A. S. Kanani, H. Niknam, A. R. Ohadi, M. M. Aghdam, "Effect of nonlinear elastic foundation on large amplitude free and forced vibration of functionally graded beam", *Composite Structures*, vol. 115, pp. 60-68, 2014.
- [10]. M. Aslami, P. A. Akimov, "Analytical solution for beams with multipoint boundary conditions on two-parameter elastic foundations", *Archives of Civil and Mechanical Engineering*, vol. 16(4), pp. 668-677, 2016.
- [11]. J. R. Banerjee, "Dynamic Stiffness Formulation for Structural Elements: A General Approach", *Computers & Structures*, vol. 63, pp. 101-103, 1997.
- [12]. L. Jun, H. Hongxing, H. Rongying, "Dynamic stiffness analysis for free vibrations of axially loaded laminated composite beams", *Computers and Structures*, vol. 84, pp. 87-98, 2008.
- [13]. L. Bao-hui, G. Hang-shan, Z. Hong-bo, L. Yong-shou, Y. Zhou-feng, "Free vibration analysis of multi-span pipe conveying fluid with dynamic stiffness method", *Nuclear Engineering and Design*, vol. 241, pp. 666-671, 2011.

- [14]. J. R. Banerjee, "Free vibration of beams carrying spring-mass systems - A dynamic stiffness approach", *Computers and Structures*, vol. 104-105, pp. 21-26, 2012.
- [15]. J. R. Banerjee, D. R. Jackson, "Free vibration of a rotating tapered Rayleigh beam: A dynamic stiffness method of solution", *Computers and Structures*, vol. 124, pp. 11-20, 2013.
- [16]. H. Su, J. R. Banerjee, "Development of dynamic stiffness method for free vibration of functionally graded Timoshenko beams", *Computers and Structures*, vol. 147, pp. 107-116, 2015.
- [17]. B. Bozyigit, Y. Yesilce, "Dynamic stiffness approach and differential transformation for free vibration analysis of a moving Reddy-Bickford beam", *Structural Engineering and Mechanics*, vol. 58(5), pp. 847-868, 2016





The effect of the consideration of slab dimensions on optimum design of reinforced concrete beams

Sinan Melih Nigdeli^{1*}, Gebrail Bekdaş¹

¹Istanbul University, Department of Civil Engineering, 34320, Avclar/Istanbul, Turkey.

*Corresponding Author email: melihmig@istanbul.edu.tr

Abstract

In the design of reinforced concrete (RC) beams, the slab can be also considered as a part of the beam and a t-shaped cross section is considered. In the presented study, the optimum design of RC beams are investigated for different slab thickness values. Thus, the effect of the consideration of slab dimensions for the optimum design is investigated. In the optimization methodology, an iterative cost optimization process is proposed. The process contains the optimization of design variables such as the cross-section dimensions and amount of rebar of RC beams subjected to flexural moments. In order to find a precise optimum solution without trapping local optimums, a metaheuristic based method called harmony search is employed. The optimum values are chosen according to user selected range and the design constraints. The design constraints are generated according to ACI318- Building code requirements for structural concrete. By the increase of compressive force in the compressive section of the beam, the amount of the rebar shows a decreasing manner and this situation is effective on the optimum design and cost.

Key words

Metaheuristic algorithm, Frames, Optimization, Teaching learning based optimization

1. INTRODUCTION

In the design of reinforced concrete (RC) beams, the slab can be included in the compressive section of the beam in order to increase the force carried by the concrete. Thus, a T-shaped cross section is used and the flange width is calculated according to effective width by considering zero moment measures while the thickness of the flange is equal to the thickness of the slab. The consideration of a T-shaped section is effective on the economy in order to reduce the amount of rebar, especially in the compressive section.

In this paper, the optimum design of RC beams under flexural moments are presented for different thickness values of slab and the results are also compared with a rectangular section. The optimum design employs harmony search algorithm (HS) [1] and considers the rules of ACI318: Building code requirements for structural concrete [2] in the analyses.

Harmony search (HS) is a music inspired metaheuristic algorithm. Like genetic algorithm inspired from the evaluation theory [3] or ant colony optimization [4] inspired from the food search process of ants, HS inspired from musical performance in which a musician tries to find the best harmony in order to gain attention of the listeners. In this process, a well-known popular note can be played or it can be modified a little in order to adjust the level of admiration. Metaheuristic based methodologies are effective on the engineering problems and

several good examples can be also found for optimization of RC members like beams [5-8], columns [9-10], frames [11-12] and retaining walls [13-14].

2. METHODOLOGY

The methodology of the optimization process can be explained in five steps. These steps are summarized in the flowchart given as Fig. 1.

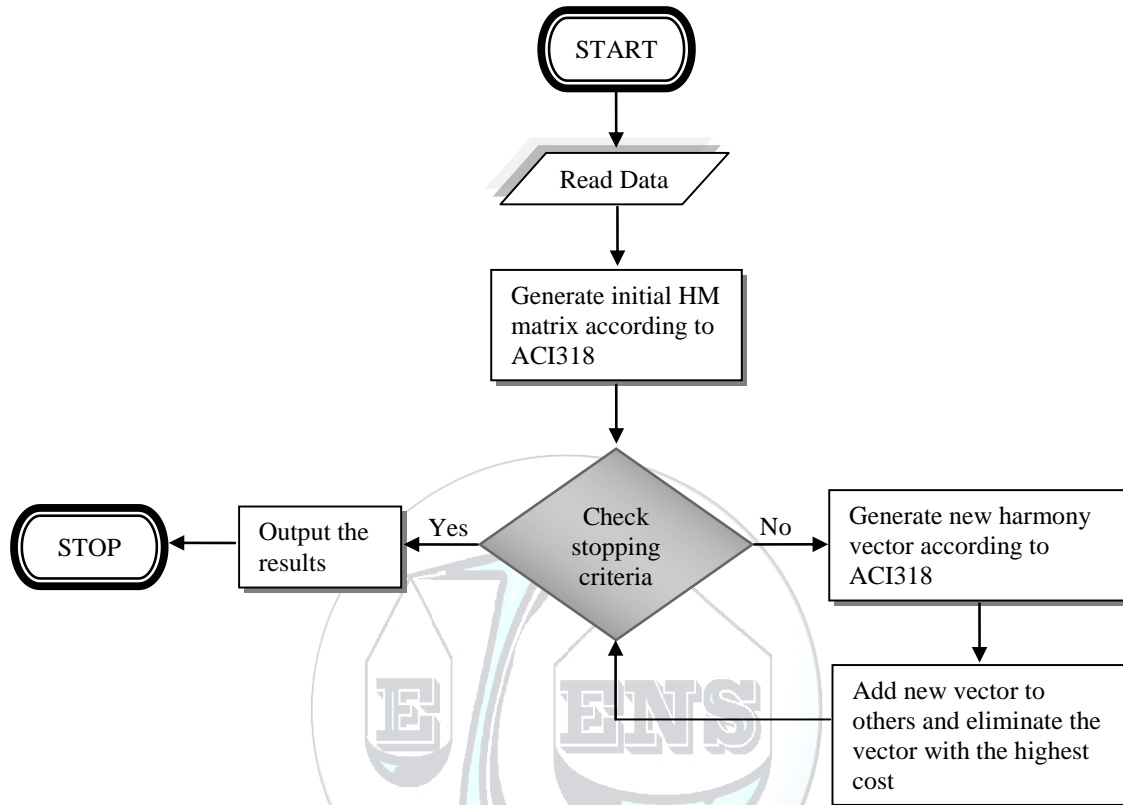


Figure 1. Flowchart of the methodology [7]

Step 1: Read Data

In this step, the design constants (given in Table 2 with the values used in numerical example), the ranges of design variables (values also given in Table 2) such as height (h) and width (b) of the beam, number (n_1 , n_2 , n_3 and n_4) and size (ϕ_1 , ϕ_2 , ϕ_3 and ϕ_4) of rebar, the algorithm parameters (HMS: harmony memory size, HMCR: harmony memory considering rate, PAR: pitch adjusting rate, values on Table 2) are defined. A T-shaped cross section which is optimized, is shown in Fig. 2.

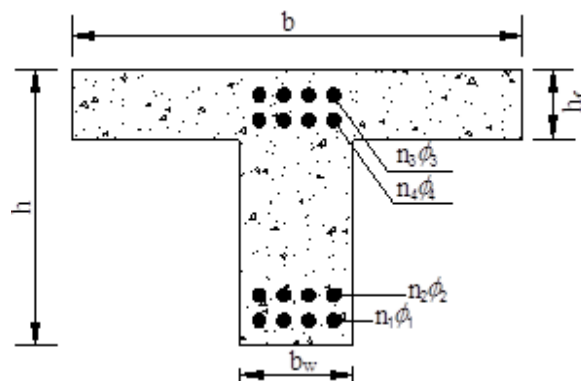


Figure 2. The T-shaped cross section

Step 2: Generate initial harmony memory (HM) matrix

In this step, initial solution vectors for design variables are randomly generated. This generation of vectors is done for HMS and the initial HM matrix is generated. In the generated values must provide the ACI-318 rules in the analyses.

Step 3: Generate a new harmony memory

After the generation of initial HM matrix, a new vector is generated in two ways. These two ways are chosen with possibility called HMCR. With HMCR possibility, a new solution is generated around existing solution by using a narrow range which is PAR times of the length of the initial solution range. The other way is to use the initial solution range in the generation of design variables. All dimension variables are rounded to values which are divisible to 50 mm and the diameters of rebar are even numbers for practical production in a construction yard.

Step 4: Elimination and update

If the newly generated solution is better than the worst existing solution, the solution is keep and the old one is eliminated. This comparison is done according to objective function which is the total material cost of unit meter.

Step 5: Check the stopping criteria

The methodology has various criteria for stopping of the iterative process given as step 3 and 4. The difference of the web width and height for different sets of solution must be smaller than 50 mm. Also, the difference in flexural moment strength and the required flexural moment capacity must be less than 0.5% of required. The required flexural moments are increased by dividing the values by 0.9 according to ACI-318. When these criteria are satisfied, the optimum results are output.

3. NUMERICAL EXAMPLE

The investigation is done for 4 cases of the slab thickness (h_f). In the first case, the section is rectangular ($h_f=0$). All numerical values used in the optimization are presented in Table 2. The required flexural moments are investigated for different values and the optimum results are given in Table 3.

Table 1. The design constants, ranges and parameters

Definition	Symbol	Unit	Value
Range of width section	b_{wmin}, b_{wmax}	mm	250-350
Range of height section	h_{min}, h_{max}	mm	300-500
Clear cover	cc	mm	35
Range of diameter of rebar	ϕ_{min}, ϕ_{max}	mm	10-30
Size of stirrups	ϕ_v	mm	10
Width of flange	b	mm	1000
			0 (case 1)
Slab thickness	h_f	mm	100 (case 2)
			120 (case 3)
			140 (case 4)
Max. aggregate diameter	D_{max}	mm	16
Yield strength of steel	f_y	MPa	420
Comp. strength of concrete	f'_c	MPa	25
Elasticity modulus of steel	E_s	MPa	200000
Specific gravity of steel	γ_s	t/m ³	7.86
Specific gravity of concrete	γ_c	t/m ³	2.5
Cost of the concrete per m ³	C_c	\$/ m ³	40
Cost of the steel per ton	C_s	\$/ m ³	400
Harmony memory size	HMS	-	5
Harmony memory considering rate	HMCR	-	0.5
Pitch adjusting rate	PAR	-	0.5

Table 2. The optimum results

Objective	50	100	150	200	250	300	350	400	450	500	
Flexural Moment (kNm)	50	100	150	200	250	300	350	400	450	500	
CASE 1	h (mm)	300	400	500	500	500	500	500	500	500	
	b _w (mm)	250	250	250	250	250	250	300	350	350	
	φ ₁ (mm)	10	12	16	16	22	30	30	30	26	30
	φ ₃ (mm)	30	16	12	14	10	10	10	10	20	22
	n ₁	5	4	3	4	3	3	3	4	5	4
	n ₃	0	0	0	0	0	3	0	4	2	3
	φ ₂ (mm)	10	12	12	14	18	10	18	10	10	16
	φ ₄ (mm)	24	14	16	30	16	18	30	18	10	20
	n ₂	3	4	4	4	3	2	4	3	8	5
	n ₄	0	0	0	0	0	0	0	0	3	0
	M _u (kNm)	55.96	112.00	172.26	222.77	280.42	343.99	393.37	451.50	501.01	572.40
	Cost (\$/m)	4.95	6.81	8.28	9.41	10.91	12.80	14.74	16.48	19.87	22.44
CASE 2	h (mm)	350	350	350	400	450	500	500	500	500	
	b _w (mm)	250	250	250	250	250	250	250	250	250	
	φ ₁ (mm)	10	12	16	16	18	24	24	28	20	24
	φ ₃ (mm)	14	18	28	12	20	22	14	26	28	16
	n ₁	2	3	3	4	3	2	2	2	4	3
	n ₃	0	0	0	0	0	0	0	0	0	0
	φ ₂ (mm)	10	10	10	10	14	12	12	14	14	22
	φ ₄ (mm)	22	30	22	22	18	26	14	20	16	20
	n ₂	2	3	4	2	2	2	4	2	3	2
	n ₄	0	0	0	0	0	0	0	0	0	0
	M _u (kNm)	36.87	67.26	105.92	133.76	168.11	201.03	236.70	268.95	300.78	360.03
	Cost (\$/m)	7.48	8.28	9.35	9.98	10.83	11.51	12.21	12.78	13.33	14.57
CASE 3	h (mm)	350	350	400	400	450	500	500	500	500	
	b _w (mm)	250	250	250	250	250	250	250	250	250	
	φ ₁ (mm)	10	12	10	16	14	24	22	28	20	24
	φ ₃ (mm)	30	10	16	30	28	14	14	24	12	16
	n ₁	3	3	5	3	4	2	3	2	4	3
	n ₃	0	0	0	0	0	0	0	0	0	0
	φ ₂ (mm)	10	10	12	10	14	10	12	12	18	16
	φ ₄ (mm)	28	14	14	14	10	26	28	22	30	22
	n ₂	2	3	3	5	3	3	2	3	2	3
	n ₄	0	0	0	0	0	0	0	0	0	0
	M _u (kNm)	46.53	67.26	100.25	134.76	167.74	202.63	243.10	273.86	307.64	337.39
	Cost (\$/m)	8.32	8.88	9.87	10.69	11.44	12.14	12.84	13.48	14.08	14.68
CASE 4	h (mm)	350	350	350	400	450	500	500	500	500	
	b _w (mm)	250	250	250	250	250	250	250	250	250	
	φ ₁ (mm)	12	12	12	14	18	16	18	24	24	26
	φ ₃ (mm)	30	26	30	24	28	28	12	30	24	28
	n ₁	2	3	4	4	3	4	4	3	3	3
	n ₃	0	0	0	0	0	0	0	0	0	0
	φ ₂ (mm)	10	10	12	16	12	12	14	10	16	16
	φ ₄ (mm)	24	28	20	12	20	24	26	22	22	28
	n ₂	2	3	4	2	3	3	2	2	2	2
	n ₄	0	0	0	0	0	0	0	0	0	0
	M _u (kNm)	45.15	67.26	103.19	137.72	172.65	203.70	235.74	269.45	306.89	345.88
	Cost (\$/m)	8.89	9.48	10.51	11.36	12.12	12.75	13.32	13.90	14.66	15.39

4. CONCLUSIONS

Generally, the rectangular design is economical for low flexural moment values as seen in the optimum results, but it must be noted that the optimum cost is only calculated by using $h_f=0$. In that case, the slab concrete cost is not taken in the consideration. Although the slab is not considered in case 1, the cost is more than other cases, if the required flexural moment is more than 250 kNm. The significant effect on the increase of the cost is because of the need for rebar in compressive section. According to the results, the thickness of the slab has no significant effect on the optimum cost, but the consideration of a T shaped design is important in optimization.

REFERENCES

- [1]. Geem, Z. W., Kim, J. H., & Loganathan, G. V. (2001). A new heuristic optimization algorithm: harmony search. *Simulation*, 76(2), 60-68.
- [2]. ACI 318M-05, Building code requirements for structural concrete and commentary, American Concrete Institute, 2005.
- [3]. Goldberg, D.E. (1989), *Genetic algorithms in search, Optimization and machine learning*, Boston MA: Addison Wesley.
- [4]. Dorigo, M., Maniezzo, V. and Colomi A (1996), "The ant system: Optimization by a colony of cooperating agents", *IEEE Transactions on Systems Man and Cybernet B*, **26**, 29-41.
- [5]. Koumousis, V. K., Arsenis, S. J. (1998), "Genetic Algorithms in Optimal Detailed Design of Reinforced Concrete Members", *Comput-Aided Civ. Inf.*, 13, 43-52.
- [6]. Govindaraj, V., Ramasamy, J. V. (2005), "Optimum detailed design of reinforced concrete continuous beams using Genetic Algorithms", *Comput. Struct.*, 84, 34-48.
- [7]. Bekdaş, G. and Nigdeli, S.M. (2012), "Cost optimization of T-shaped reinforced concrete beams under flexural effect according to ACI 318", In: 3rd European Conference of Civil Engineering, Paris, France.
- [8]. Nigdeli, S. M., & Bekdaş, G. (2016). Optimum design of RC continuous beams considering unfavourable live-load distributions. *KSCE Journal of Civil Engineering*, DOI: 10.1007/s12205-016-2045-5.
- [9]. Rafiq, M. Y., Southcombe, C. (1998), "Genetic algorithms in optimal design and detailing of reinforced concrete biaxial columns supported by a declarative approach for capacity checking", *Comput. Struct.* 69, 443-457.
- [10]. Nigdeli, S. M., Bekdas, G., Kim, S., & Geem, Z. W. (2015). A novel harmony search based optimization of reinforced concrete biaxially loaded columns. *Structural Engineering and Mechanics*, 54(6), 1097-1109.
- [11]. Camp, C. V., Pezeshk, S., Hansson, H. (2003), "Flexural Design of Reinforced Concrete Frames Using a Genetic Algorithm", *J Struct. Eng.-ASCE.*, 129, 105-111.
- [12]. Govindaraj, V., Ramasamy, J. V. (2007), "Optimum detailed design of reinforced concrete frames using genetic algorithms", *Eng. Optimiz.*, 39(4), 471-494.
- [13]. Camp, C.V. and Akin, A. (2012), "Design of retaining walls using big bang-big crunch optimization", *Journal of Structural Engineering*, Vol.138, No.3, pp.438-448, DOI:10.1061/(ASCE)ST.1943-541X.0000461.
- [14]. Temur, R, Bekdaş, G. (2016), "Teaching learning-based optimization for design of cantilever retaining walls", *Structural Engineering and Mechanics*, Vol.57, No.4, pp.763-783, DOI: 10.12989/sem.2016.57.4.763.



Metaheuristic based optimization of tuned mass dampers on single degree of freedom structures subjected to near fault vibrations

Sinan Melih Nigdeli^{1*}, Gebrail Bekdaş¹, Aikerim Aydın¹

¹Istanbul University, Department of Civil Engineering, 34320, Avclar/Istanbul, Turkey.

*Corresponding Author email: melihmig@istanbul.edu.tr

Abstract

Near fault ground motions excitations have specific characteristics comparing to regular earthquake excitations. Near fault ground motions contain directivity pulses and flint steps in different directions and these excitations are the reason of more damages than regular excitations for structures. A successful method to reduce structural vibrations is the usage of tuned mass dampers. By using optimally tuned mass dampers, it will be possible to reduce vibrations resulting from earthquake excitations. In the present study, the optimization of tuned mass dampers are done for near fault excitations. During optimization, 6 different pulse like excitations are used. Three of these excitations are directivity pulses while the other ones are flint steps. The periods of excitations are 1.5s, 2.0s and 2.5s since near fault pulses have long period and big peak ground velocity around 200 m/s. The optimization objectives are related to maximum displacement of structure in time domain, the maximum stroke limitation of tuned mass damper and transfer function of the structure in frequency domain analyses. The iterative optimization process uses both time and frequency domain analyses of the structure. Three different metaheuristic algorithms are used in the methodology. These methods are harmony search algorithm, teaching learning based optimization and flower pollination algorithm which are inspired from musical performances, education process and reproduction of flowering plants, respectively. As the numerical investigation, three different single degree of freedom structures with periods 1.5s, 2.0s and 2.5s are investigated for optimum mass, period and damping ratio of a tuned mass damper positioned on the structure.

Key words

Metaheuristic algorithm, Near fault vibrations, Optimization, Tuned mass dampers

1. INTRODUCTION

The undesired responses of structures subjected to earthquake and strong winds can be reduced by using control systems. These control systems may be passive, active, semi-active or hybrid. As a passive control system, a tuned mass damper (TMD) can be used on top of the structures. There are several existing examples of using TMDs on structures. Examples include Taipei 101, Berlin TV Tower (Fig. 1), LAX theme Building and other high rise buildings, towers or bridges.

Especially, near fault ground motions are more dangerous than far fault motions because of significant impulsive motions; namely directivity pulse and flint step. These pulses have long period and big peak ground velocity (PGV). For that reason, these motions are dangerous for structures with long period. In several studies, these

motions are formulized. The formulations of Makris [1] are the best equations which represent the behavior of motions. In order to use TMDs on structures in near fault regions, an optimum tuning is needed. In the documented methods, several formulations have been proposed [2-4], but these formulations may not be an exact solution for structures with inherent damping and effected by impulsive motions. For that reason, numerical algorithms are more suitable for the optimization problem. Especially, metaheuristic algorithms are effective on optimization [5-8].



Figure 1. Berlin TV Tower

In this study, the optimization of TMDs positioned on the top of single degree of freedom (sdof) structures was investigated for near fault motions. During the optimization, three directivity pulses and three flint steps (with periods 1.5s, 2.0s and 2.5s and 200m/s PGV) are considered by using the equations of Makris [1]. Three different algorithms such as harmony search (HS), flower pollination algorithm (FPA) and teaching learning based optimization (TLBO) have been used.

2. MATERIALS AND METHODS

The aim of the optimization is to find design variables such as mass (m_d), period (T_d) and damping ratio (ξ_d) of TMD by considering the optimization objectives such as related with maximum displacement ($f_1(v)$), stroke capacity of TMD ($f_2(v)$) and maximum value of acceleration transfer function ($f_3(v)$). In the methodology, the design constants, excitations and solution ranges are defined. Then, initial solution matrix (V) is constructed with p sets of solutions (v_i for the i^{th} solution) including randomly generated design variables from the defined solution range. The formulations of v_i , V , $f_1(v)$, $f_2(v)$ and $f_3(v)$ are given in Eqs.(1-5).

$$v_i = \begin{Bmatrix} m_{di} \\ T_{di} \\ \xi_{di} \end{Bmatrix} \quad i = 1, \dots, p \tag{1}$$

$$V = [v_1 \quad v_2 \quad \dots \quad v_i \quad \dots \quad v_p] \tag{2}$$

$$f_1(v) = \max(|x_1 \quad x_2 \quad \dots \quad x_i \quad \dots \quad x_N|) \leq x_{max} \tag{3}$$

$$f_2(v) = \frac{\max(|x_d - x_N|)_{withTMD}}{|x_N|_{withoutTMD}} \leq st_max \tag{4}$$

$$f_3(v) = \max(|TF_N(w)|)_{withTMD} \leq \max(|TF_N(w)|)_{withoutTMD} \tag{5}$$

In these equations, x_i are the displacement of i^{th} story; x_{max} is a user defined value which is iteratively increased (0 is the initial value in current study); x_d is the total displacement of TMD; st_max is a user defined value for stroke limitation (2 in the current study); $TF_N(w)$ is the acceleration transfer function which uses the Laplace transforms. After the generation of initial solution matrix, new solutions are produced according to the rules of the algorithms. The main comparisons factor is $f_1(v)$, but the function; $f_2(v)$ must be provided.

HS is music based algorithm developed by Geem et al. [9]. It imitates the musical performances in a musician tries to gain admiration of audience. FPA is a nature inspired algorithm and uses four rules proposed by Yang [10] including cross pollination, self-pollination, flower constancy and switch probability. TLBO developed by Rao et al. [11] imitates two phases of education such as teacher phase and learner phase in which self-education of students is considered. The details and formulation of the algorithms can be found in Reference [8].

3. RESULTS AND DISCUSSION

Three single degree of freedom structures with 5% inherent damping and periods 1.5s, 2.0s and 2.5s are investigated for an optimum TMD. The mass of structures are taken as a symbolic value (1kg). Three different cases of maximum damping was investigated. The maximum damping ratio is 0.2, 0.3 and 0.4 for cases 1, 2 and 3, respectively while the minimum bound is 0.01. The mass ratio of TMD was searched between 1% and 10% while T_d was optimized between 0.5 and 1.5 times of the period of main structure. For the structure with 2 s period, the maximum mass ratio is taken as 20% in order to obtain an effective control. The optimum results are shown in Table 1. The objective function and maximum acceleration values are presented in Tables 2-4 for HS, FPA and TLBO algorithms. The best solutions were obtained for TLBO algorithm. For the structure with 2.0s and 2.5s period, the optimum results are the same since the optimum damping ratio of TMD is within the ranges of case 1. For the structure with 1.5s period, the results are the same for cases 2 and 3. The time history plots of top story displacements of structures are given in Figs. 2-5 for TLBO algorithm.

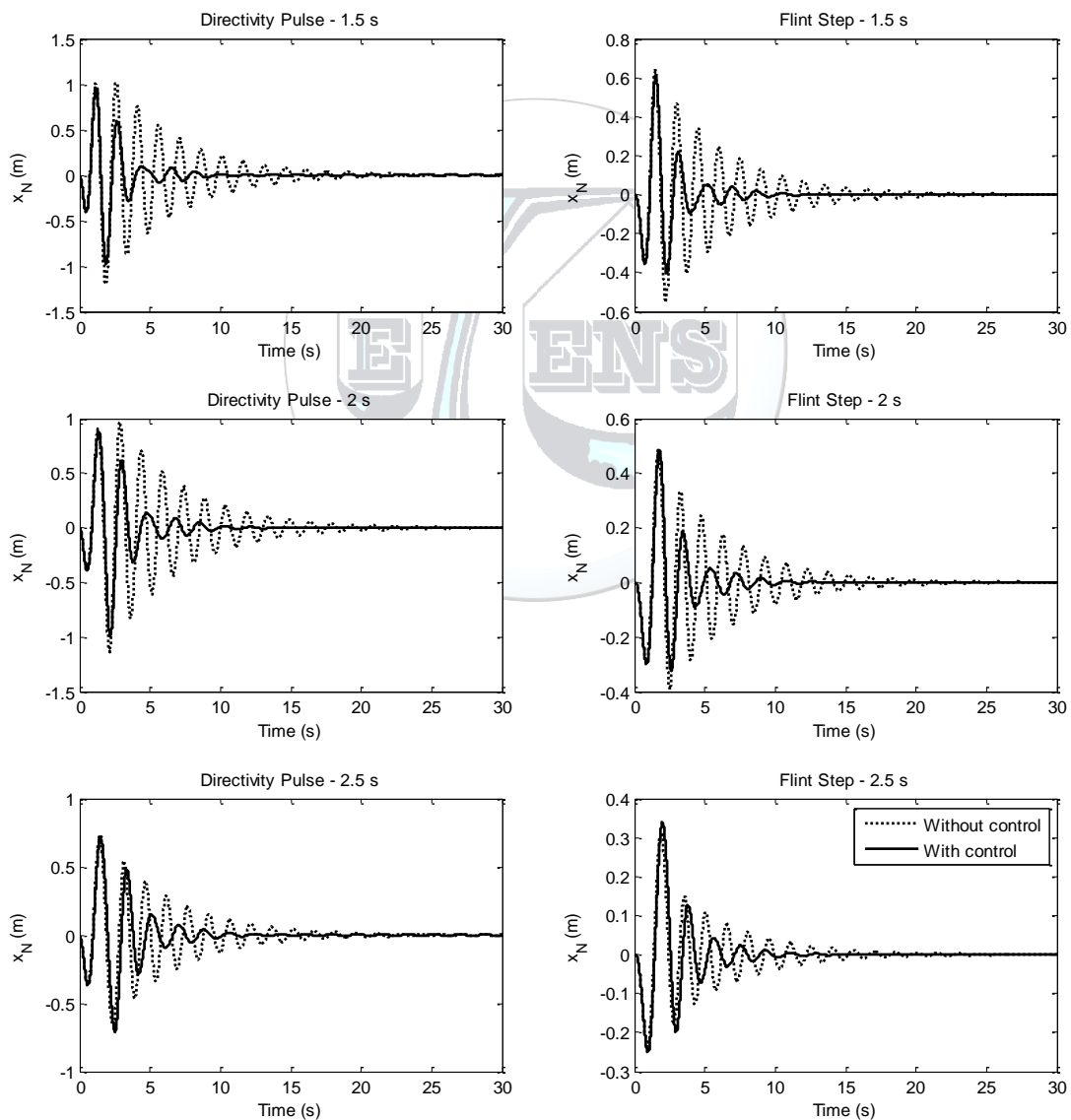


Figure 2. Time history plot for structure with 1.5s period (case 1)

Table 1. The optimum design variables

Case	Structure periods (s)	HS			FPA			TLBO		
		m_d (kg)	T_d (s)	ξ_d	m_d (kg)	T_d (s)	ξ_d	m_d (kg)	T_d (s)	ξ_d
1	1	0.100	1.597	0.190	0.100	1.653	0.200	0.100	1.653	0.200
	2	0.198	1.955	0.068	0.200	1.929	0.047	0.200	1.929	0.047
	3	0.099	2.170	0.055	0.100	2.150	0.047	0.100	2.071	0.018
2	1	0.098	1.738	0.229	0.100	1.753	0.231	0.100	1.753	0.231
	2	0.195	1.967	0.064	0.200	1.929	0.047	0.200	1.929	0.047
	3	0.099	2.070	0.024	0.100	2.071	0.018	0.100	2.071	0.018
3	1	0.099	1.729	0.227	0.100	1.753	0.231	0.100	1.753	0.231
	2	0.200	1.956	0.067	0.200	1.929	0.047	0.200	1.929	0.047
	3	0.098	2.178	0.059	0.100	2.071	0.018	0.100	2.071	0.018

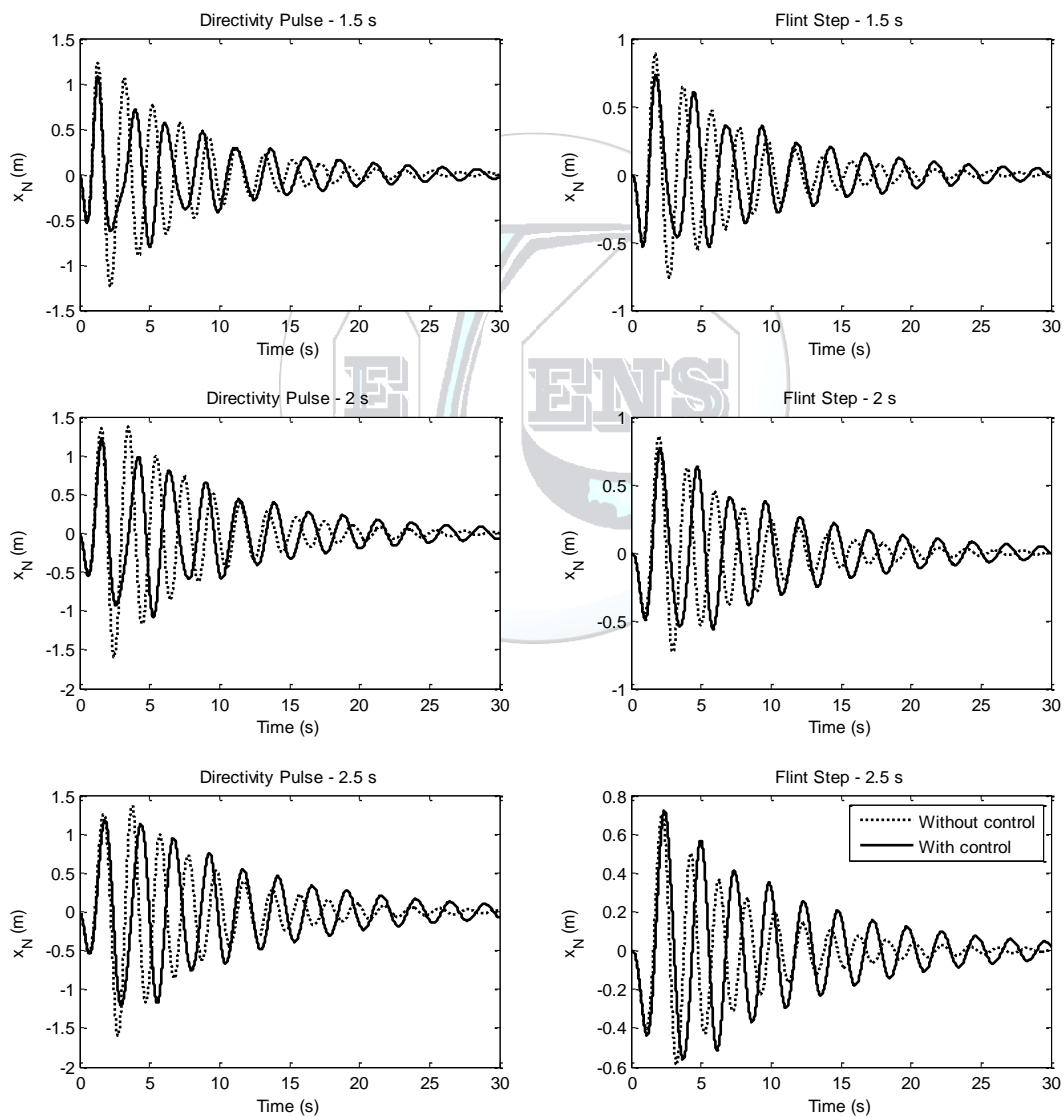


Figure 3. Time history plot for structure with 2.0s period

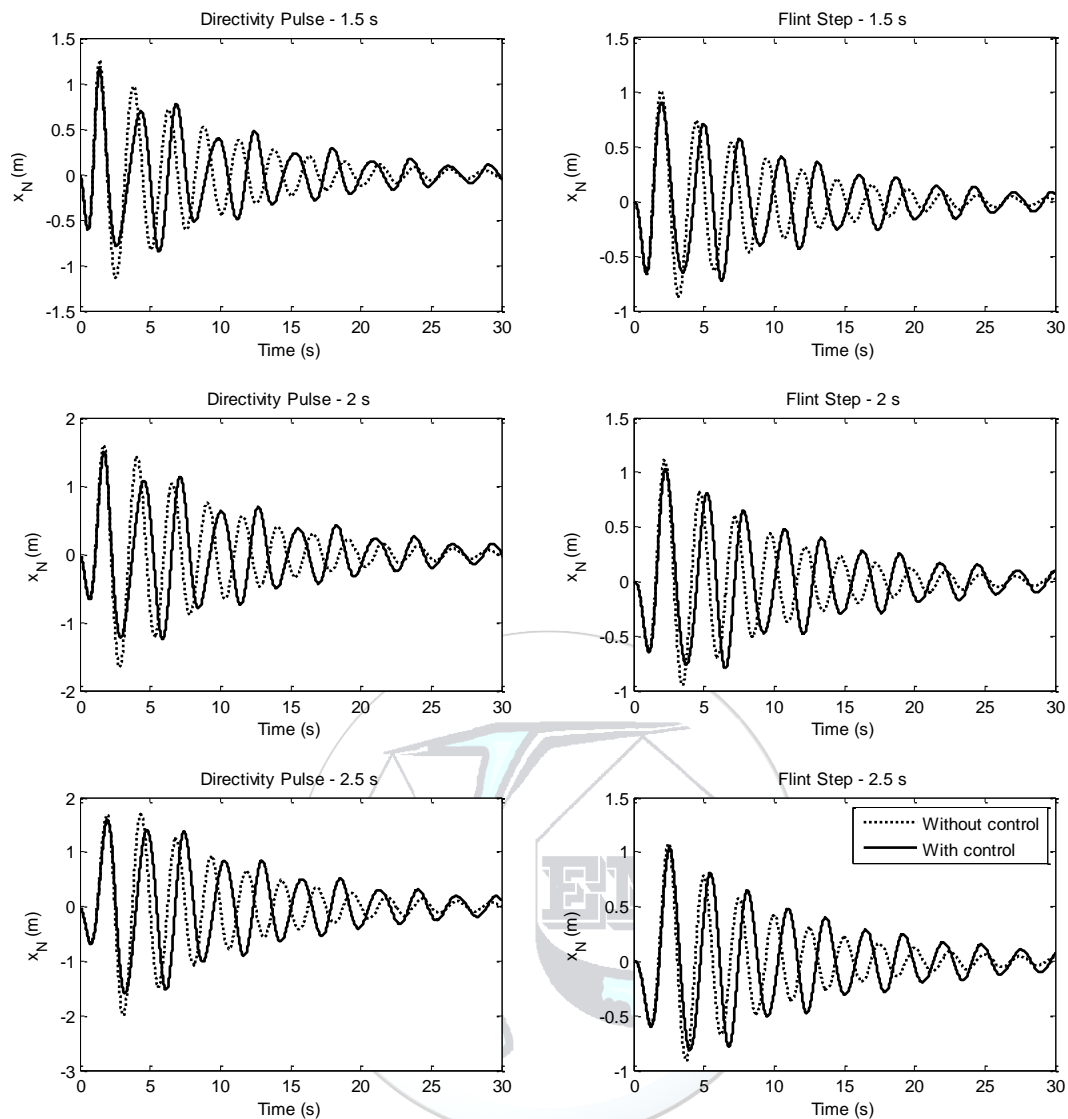


Figure 4. Time history plot for structure with 2.5s period

Table 2. The objective function values (HS)

Case	Structure periods (s)	$f_1(v)$		Maximum acceleration		$f_3(v)$		$f_2(v)$	Iteration
		With TMD	Without TMD	With TMD	Without TMD	With TMD	With TMD	Without TMD	
1	1	1.204	1.006	21.224	16.418	10.012	3.425	1.948	2184
	2	1.602	1.217	15.889	10.482	9.558	6.617	1.940	3304
	3	2.000	1.605	12.697	9.234	9.892	7.815	1.999	6373
2	1	1.204	0.998	21.224	17.033	10.012	3.882	1.994	4097
	2	1.602	1.217	15.889	10.544	9.558	6.667	1.995	1335
	3	2.000	1.604	12.697	9.109	9.892	9.760	1.967	1035
3	1	1.204	0.997	21.224	16.950	10.012	3.816	1.988	2618
	2	1.602	1.216	15.889	10.459	9.558	6.701	1.937	4062
	3	2.000	1.606	12.697	9.256	9.892	7.687	1.997	2675

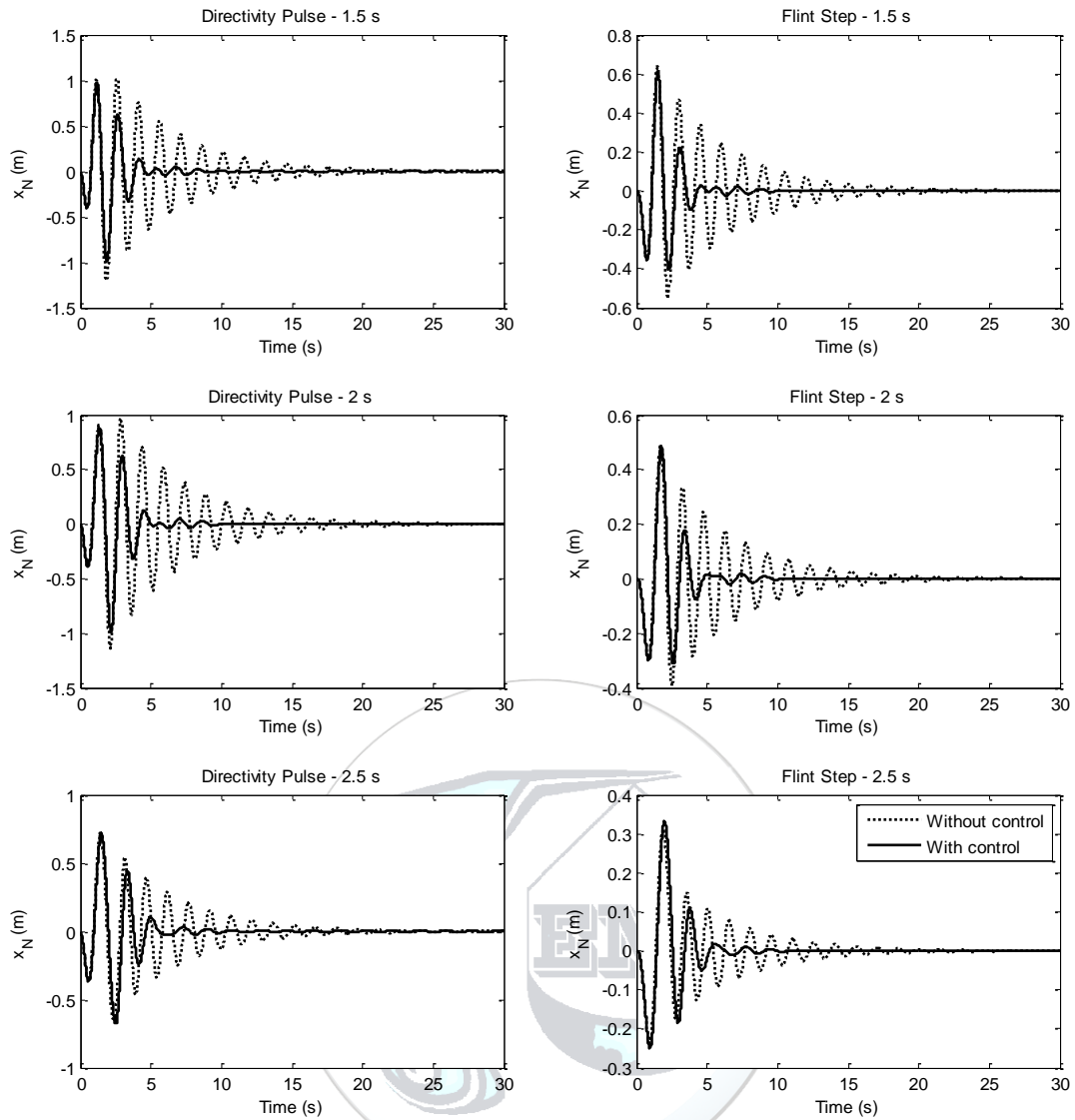


Figure 5. Time history plot for structure with 1.5s period (case 2-3)

Table 3. The objective function values (FPA)

Case	Structure periods (s)	$f_1(v)$		Maximum acceleration		$f_3(v)$		$f_2(v)$	Iteration
		With TMD	Without TMD	With TMD	Without TMD	With TMD	Without TMD	Without TMD	
1	1	1.204	0.997	21.224	16.631	10.012	3.489	2.000	3465
	2	1.602	1.209	15.889	10.381	9.558	7.488	2.000	5045
	3	2.000	1.603	12.697	9.196	9.892	8.194	2.000	2620
2	1	1.204	0.994	21.224	17.014	10.012	3.909	2.000	4055
	2	1.602	1.209	15.889	10.381	9.558	7.488	2.000	4915
	3	2.000	1.601	12.697	9.085	9.892	9.892	2.000	7370
3	1	1.204	0.994	21.224	17.014	10.012	3.909	2.000	4020
	2	1.602	1.209	15.889	10.381	9.558	7.488	2.000	5090
	3	2.000	1.601	12.697	9.085	9.892	9.892	2.000	7290

Table 4. The objective function values (TLBO)

Case	Structure periods (s)	$f_1(v)$		Maximum acceleration		$f_3(v)$		$f_2(v)$	Iteration
		With TMD	Without TMD	With TMD	Without TMD	With TMD	Without TMD		
1	1	1.204	0.997	21.224	16.631	10.012	3.489	2.000	4180
	2	1.602	1.209	15.889	10.381	9.558	7.488	2.000	4480
	3	2.000	1.601	12.697	9.085	9.892	9.892	2.000	4750
2	1	1.204	0.994	21.224	17.014	10.012	3.909	2.000	4130
	2	1.602	1.209	15.889	10.381	9.558	7.488	2.000	5160
	3	2.000	1.601	12.697	9.085	9.892	9.892	2.000	6850
3	1	1.204	0.994	21.224	17.014	10.012	3.909	2.000	4010
	2	1.602	1.209	15.889	10.381	9.558	7.488	2.000	4990
	3	2.000	1.601	12.697	9.085	9.892	9.892	2.000	6850

4. CONCLUSIONS

The optimized TMDs are effective in reduction of structural displacements and accelerations. All algorithms are effective, but FPA and TLBO can find precise optimum solutions. The iteration number for the optimum values are nearly 2000 iterations. The reduction of maximum displacements are 17%, 25% and 20% for the structure with period 1.5s, 2.0s and 2.5s, respectively. For near fault motions, these values are good, but active control system may be more effective for impulsive motions. The cost, maintain, stability problem and energy consumption are big problems of the active systems comparing to passive control methods.

REFERENCES

- [1]. Makris, N., (1997). Rigidity-Plasticity-Viscosity: Can Electrorheological Dampers Protect Base-Isolated Structures From Near-Source Ground Motions? *Earthquake Engineering and Structural Dynamics*, 26, 571-591..
- [2]. Den Hartog, J. P., (1947). Mechanical Vibrations. *McGraw-Hill*, New York..
- [3]. Warburton, G.B., (1982). Optimum absorber parameters for various combinations of response and excitation parameters. *Earthquake Engineering and Structural Dynamics*, 10, 381-401..
- [4]. Sadek, F., Mohraz, B., Taylor, A.W., Chung, R.M., (1997). A Method of Estimating The Parameters of Tuned Mass Dampers for Seismic Applications. *Earthquake Engineering and Structural Dynamics*, 26, 617-635.
- [5]. Bekdaş, G., Nigdeli, S.M., (2011). Estimating Optimum Parameters of Tuned Mass Dampers using Harmony Search. *Engineering Structures*, 33, 2716-2723.
- [6]. Hadi, M.N.S., Arfiadi, Y., (1998). Optimum Design of Absorber for MDOF Structures. *Journal of Structural Engineering-ASCE*, 124, 1272-1280.
- [7]. Bekdaş, G., & Nigdeli, S. M., (2017). Metaheuristic Based Optimization of Tuned Mass Dampers Under Earthquake Excitation by Considering Soil-structure Interaction. *Soil Dynamics and Earthquake Engineering*, 92, 443-461.
- [8]. Bekdaş G, Nigdeli SM, Yang X-S, *Metaheuristic Based Optimization for Tuned Mass Dampers Using Frequency Domain Responses*. In: Harmony Search Algorithm. Advances in Intelligent Systems and Computing, vol 514, Del Ser J. (eds) Springer, pp. 271-279, 2017.
- [9]. Geem, Z. W., Kim, J. H., & Loganathan, G. V. (2001). A new heuristic optimization algorithm: harmony search. *Simulation*, 76(2), 60-68.
- [10]. Yang, X. S., (2012). Flower Pollination Algorithm for Global Optimization. *International Conference on Unconventional Computing and Natural Computation* (pp. 240-249), Springer Berlin Heidelberg.
- [11]. Rao, R. V., Savsani, V. J., & Vakharia, D. P., (2011). Teaching-learning-Based Optimization: A Novel Method for Constrained Mechanical Design Optimization Problems. *Computer-Aided Design*, 43(3), 303-315.



An Investigation of Intelligent and Conventional Maximum Power Point Tracking Techniques for Uniform Atmospheric Conditions

Ekrem Kandemir^{1,2,*}, Numan Sabit Cetin², Selim Borekci³

¹TUBITAK National Observatory, Research & Development Department, 07058, Antalya, Turkey.

²Ege University, Solar Energy Institute, 35100, Izmir, Turkey.

³Akdeniz University, Electrical – Electronics Engineering Department, 07058, Antalya, Turkey.

*Corresponding Author email: ekrem.kandemir@tubitak.gov.tr

Abstract

In recent years, power generation from photovoltaic (PV) system has received great attention compared to other renewable sources. Due to nonlinear characteristics of PV cells, the maximum allowable power level from PV panel changes with atmospheric parameters which are solar irradiance and temperature. In this context, maximum power point tracking (MPPT) algorithms are essential to maximize the output power of PV panel for any solar irradiance and temperature values. In the literature, various MPPT techniques have been studied to deliver maximum power from PV systems. Hence, this study discusses intelligent control techniques, which are called fuzzy logic controller (FLC) and neural network controller (NNC), and compares efficiency performance and convergence speed to conventional perturb & observe (P&O) and incremental conductance (Inc. Cond.) tracking techniques for MPPT of PV system.

In this paper, 150W PV panel model is investigated for different atmospheric conditions in MATLAB. Results of simulation show that NNC based and FLC based MPPTs have 4.66% better tracking accuracy than conventional P&O and Inc. Cond. under standard test condition (STC). NNC based MPPT has best iteration response rate among the other MPPTs under uniform atmospheric conditions. Therefore, the NNC based MPPT presents best superior quality in terms of efficiency and convergence speed for PV systems among the other MPPTs.

Key words

PV Model, Maximum Power Point Tracking, Perturb & Observe, Incremental Conductance, Fuzzy Logic Control, Neural Network Control

1. INTRODUCTION

For a long term and sustainable supply of energy, it is essential to exploit and utilize the renewable sources at a much larger scale [1]. Compared to other renewable sources, photovoltaic energy (PV) has proven to be more pollution – free, noise – free and has limitless source of energy [2]. In addition, PV power has commonly used for industrial, commercial, residential and military purposes [3]. However, PV power is environment dependent such as solar irradiance and ambient temperature because of nonlinear electrical characteristics of PV cells. The development for improving the efficiency of the PV system is still a challenging field of research and the maximization of extracted PV power from PV systems is a matter concern as its conversion efficiency is low [4], [5].

In general, PV panels have only one maximum power point (MPP) on its power – voltage curve where PV panel produces its maximum power under uniform solar irradiance condition and this point changes with solar irradiance and temperature [6]. The position of MPP on the corresponding power – voltage curve varies depending on solar irradiance, temperature and also electrical load. Therefore, to make the PV power generation efficient, a capable maximum power point tracking (MPPT) techniques are used to estimate and to track the actual MPP against any environmental parameters changes such as solar irradiance and temperature [7].

Numerous MPPT techniques have been investigated in the literature such as Perturb & Observe (P&O), incremental conductance (Inc. Cond.), fuzzy logic controller (FLC) and neural network (NN) [1], [3], [8], [9]. The quality of an MPPT technique is evaluated in terms of its complexity, cost, tracking speed, accuracy and number of sensors required for its implementation [10]. Because of being simplicity and easy to implement, P&O and Inc Cond. MPPT techniques, which are known as a few of conventional MPPTs, are ones of the most preferred algorithms in the literature. Although, these methods present some drawbacks in its design such as convergence and oscillation problems around MPP region. To remove these drawbacks and enhance the performance of PV panels, intelligent or soft – computing MPPTs such as fuzzy logic and/or neural network based techniques are widely preferred in the literature [11].

In this paper, conventional MPPTs such as P&O and Inc. Cond. and intelligent MPPTs such as FLC and NN based MPPTs are investigated and compared in terms of tracking accuracy and convergence speed. Related analysis and simulation results are discussed separately for each MPPT technique and comparison tables for conventional and intelligent MPPTs are provided in detail.

2. PV CELL AND EQUIVALENT CIRCUIT MODEL

PV cells are the main components of the PV systems and they consist of p – n junction semi – conductor materials that sunlight exposure causes to release electrons around a closed circuit. Typically, they are modelled either as single diode or double diode equivalent circuits but single diode model is more preferred because of simplicity and easy to implement [11], [12].

PV panel consists of several series and/or parallel connected PV cells in order to generate higher level electrical power. Figure 1 depicts single diode equivalent circuit model of a PV cell, which transforms directly sunlight into electrical current.

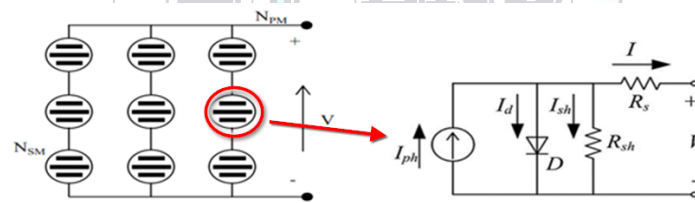


Figure 1. PV panel and single diode circuit model of a PV cell [11]

The output current of the PV cell can be expressed in Eq. (1) as,

$$I = I_{ph} - I_o \left(e^{\frac{q(V+R_s I)}{AKT}} - 1 \right) - \frac{V+R_s I}{R_{sh}} \quad (1)$$

where I and V represent PV cell output current and voltage. R_s and R_{sh} are the PV cell series and shunt resistances respectively. I_{ph} is the PV cell photo current, I_o is the diode saturation current, A is the diode quality factor ($\cong 1.2$), k is Boltzmann's constant ($1.38 \times 10^{-23} \text{ J/K}$) and T is the PV cell temperature in kelvins [6].

By solving Eq. (1) or using equivalent circuit model as shown in Figure 1, electrical characteristic curve of the related PV panel can be obtained for any environment condition in the simulations, MATLAB i.e. During uniform environment conditions where the solar irradiance is equally distributed among the PV panels, only single maximum power point is available in the PV panel's power – voltage curve as shown in Figure 2. And this MPP point changes with solar irradiance and temperature [6]. As shown in Figure 2, PV panel power is almost proportionally with the variation of solar irradiance. Hence, when solar irradiance increases, the maximum PV panel power also increases. In addition, the variation of temperature affects PV panel power inversely that PV power increases if temperature decreases.

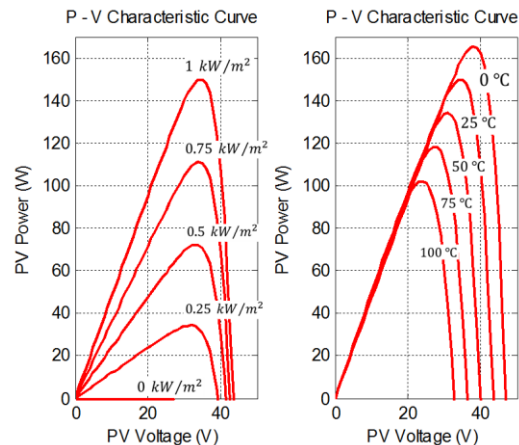


Figure 2. Voltage and power curves of PV panel for different solar irradiance and temperature conditions [6]

3. CONVENTIONAL AND INTELLIGENT MPPT TECHNIQUES

PV cells and panels operate on different power levels depending on different environmental conditions and electrical loads. Because of that, generation of maximum power is not guaranteed at all electrical loads [13]. Hence, MPPTs provide to ensure that at any environmental condition, i.e. any solar irradiance or temperature, maximum achievable power is extracted from the PV system [12].

The MPPTs can be classified in many different groups depending on several parameters, i.e. MPPT strategy, tracking speed, complexity, PV panel dependency, etc. In general, MPPT techniques are classified into two types [6]:

- Conventional techniques,
- Intelligent techniques.

The most popular conventional techniques are perturb & observe (P&O) and incremental conductance (Inc. Cond.) in the literature. These algorithms are widely used in commercial products due to their simplicity and robustness. On the other hand, intelligent MPPTs such as fuzzy logic control (FLC) and neural network (NN) tend to be more versatile, efficient and better steady state performance [1].

3.1. Perturb & Observe (P&O) Technique

This technique is commonly preferred by researchers to implement MPPT operation for the PV systems because of its simplicity and exhibiting enough convergence accuracy. In this technique, a perturbation is applied to the PV panel voltage and the PV panel output power is observed. The aim of this technique is to adjust the PV panel voltage to the voltage of the MPP of the PV panel (V_{mpp}) to extract maximum power from the PV panel for the actual environmental condition. This is done by applying small and constant perturbations to the PV voltage step by step. After each perturbation, the output PV power variation (dP) is observed according to the variation of the PV voltage (dV) [5]. If the sign of (dP/dV) is positive, the actual point is on the left side of the MPP and the PV voltage should be increased to reach the MPP; else if the sign of (dP/dV) is negative, the actual point is on the right side of the MPP and the PV voltage should be decreased to reach the MPP [6]. This process is performed until (dP/dV) equals to zero. This mechanism is also defined as below.

$$\frac{dP}{dV} = 0 \Rightarrow \text{at MPP} \quad (2)$$

$$\frac{dP}{dV} > 0 \Rightarrow \text{Left Side of MPP} \quad (3)$$

$$\frac{dP}{dV} < 0 \Rightarrow \text{Right Side of MPP} \quad (4)$$

The disadvantage of this method is that at the vicinity of the MPP, it oscillates around the MPP and this causes steady state error. Low values of perturbation size reduce steady state error at the cost of reduction in tracking speed [12]. In addition, this technique sometimes fails to track the MPP under rapidly changing environmental conditions.

3.2. Incremental Conductance (Inc. Cond.) Technique

This technique basically uses similar way but different relationship of PV characteristic curve from P&O technique to determine MPP. In this method, derivative of PV current and PV voltage are used to determine the movement of the actual operating point [6]. After each perturbation of PV voltage, the output PV current is observed to determine MPP. If the $(\Delta I/\Delta V)$ is greater than negative sign of the actual PV conductance value, the actual point is in the left side of MPP and the PV voltage should be increased to reach MPP; else the $(\Delta I/\Delta V)$ is lower than the negative sign of actual PV conductance value, the PV voltage should be increased. And this process is performed until the $(\Delta I/\Delta V)$ equals to negative sign of the actual PV conductance value. This mechanism is also defined as below.

$$\frac{\Delta I}{\Delta V} = -\frac{I}{V} \Rightarrow \text{at MPP} \tag{5}$$

$$\frac{\Delta I}{\Delta V} > -\frac{I}{V} \Rightarrow \text{Left Side of MPP} \tag{6}$$

$$\frac{\Delta I}{\Delta V} < -\frac{I}{V} \Rightarrow \text{Right Side of MPP} \tag{7}$$

As the tracking of MPP is done rapidly it helps to overcome the disadvantage of the P&O technique which fails to track the MPP control under fast varying conditions and it can be easily implemented in a simple microcontroller [6], [7]. The main disadvantage of this technique is its perturbation size, which causes oscillations and steady state error around MPP, and complexity.

3.3. Fuzzy Logic Control (FLC) Based Technique

Fuzzy logic control (FLC) based MPPT is one of the most used intelligent method to perform MPPT task for any PV system in any environment condition [4], [14]. FLC is operated by using membership functions instead of mathematical model. It consists of three stages: fuzzification, fuzzy inference engine, rule tables and defuzzification as shown in Figure 3.

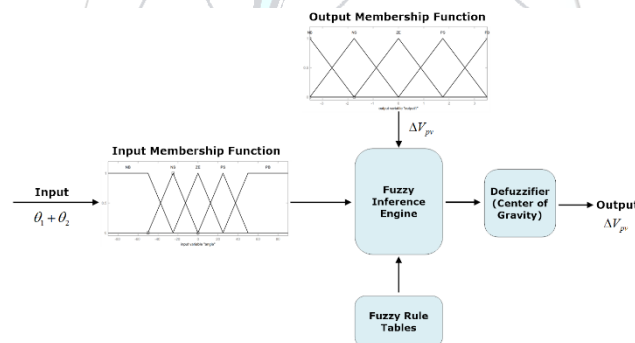


Figure 3. Block diagram of the FLC based MPPT

In the proposed FLC system, the input of FLC is sum of angle conductance and angle of increment conductance. The input variables are expressed in Eq. (8) and the MPPT determination condition is illustrated in Figure 4.

$$\theta_1 + \theta_2 = \tan^{-1}\left(\frac{dI_{pv}}{dV_{pv}}\right) + \tan^{-1}\left(\frac{I_{pv}}{V_{pv}}\right) = 0^\circ \tag{8}$$

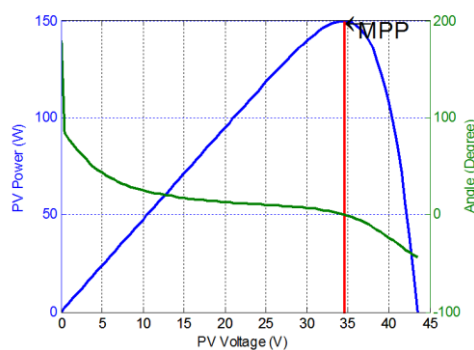


Figure 4. PV power – voltage and the angle $(\theta_1 + \theta_2)$ MPPT relation for the proposed FLC based MPPT

During fuzzification process, input variables are converted into some defined linguistic variables according to chosen membership functions. For that purpose, the linguistic variables of the input are defined as NB (Negative Big), NS (Negative Small), ZE (Zero), PS (Positive Small) and PB (Positive Big). In fuzzy inference stage, the linguistic variables get manipulated based on the fuzzy rule base which defines the behavior of the controller as shown in Figure 5. In the defuzzification process, the FLC output is converted to a numerical value from the linguistic variable using membership function for the output [7].

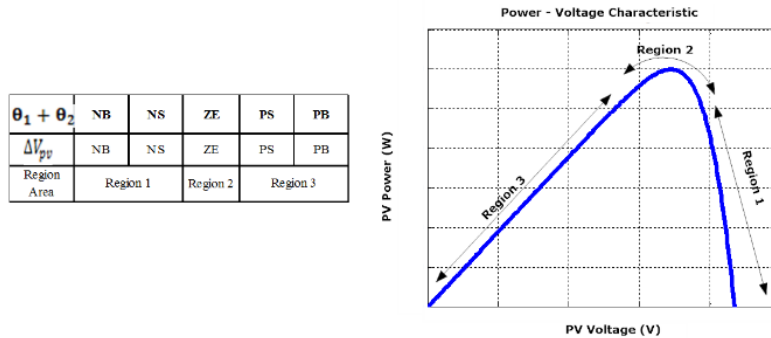


Figure 5. Fuzzy rule table and MPPT process in inference stage of the proposed FLC

The main advantages of FLCs are: no requirement of exact mathematical model of system to implement, capable of working with indefinite inputs, ability of handling non – linearity, fast and accurate convergence and tracking efficiency etc. The main disadvantages are: necessary to be tuned periodically, more complex structure, dependency to system and requiring prior knowledge of the behavior of PV system [5], [7], [12].

3.4. Neural Network (NN) Based Technique

The neural networks (NN) are becoming popular for system identification and non – linear system modelling applications. This technique is used to solve the difficult problems using parameter approximation. In recent days, NN control techniques are rising incrementally for the optimization and MPPT application of renewable power systems instead of conventional techniques [7], [9].

For MPPT operation, multi – layer feed forward neural network structure is commonly preferred and this NN structure consists of three layers: input, hidden and output layers as shown in Figure 6.

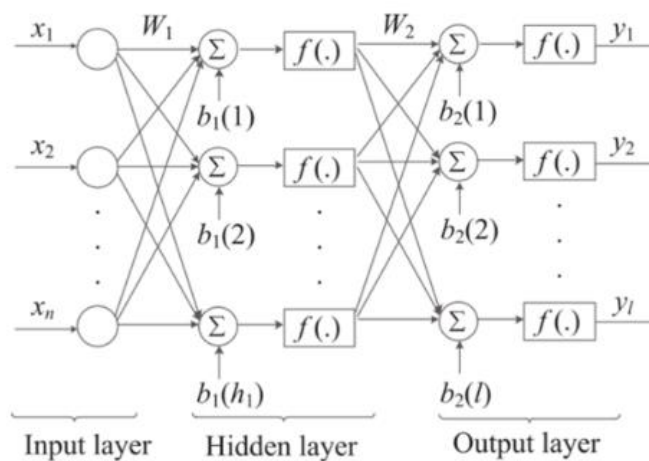


Figure 6. Architecture of multi-layer feed forward neural network [15]

The input layer receives input environmental data such as solar irradiance and temperature; second layer called as hidden layer contains 10 hidden neurons to estimate MPP value and sends to third layer. The third layer called as output layer contains single neuron to provide output to system. For MPPT purpose, 104 training data including MPP values for different solar irradiance and temperature values are applied 1000 times to train the designed NN structure. In addition, 10 different validation data, which also contains MPP values for different solar irradiance and temperature values, are used to verify and analyze performance of the trained neural network. After training the neural network 1000 times with the training data, the error of the neural network is

approx. 1.5×10^{-4} according to the verification data. The performance analysis of the neural network is shown in Figure 7.

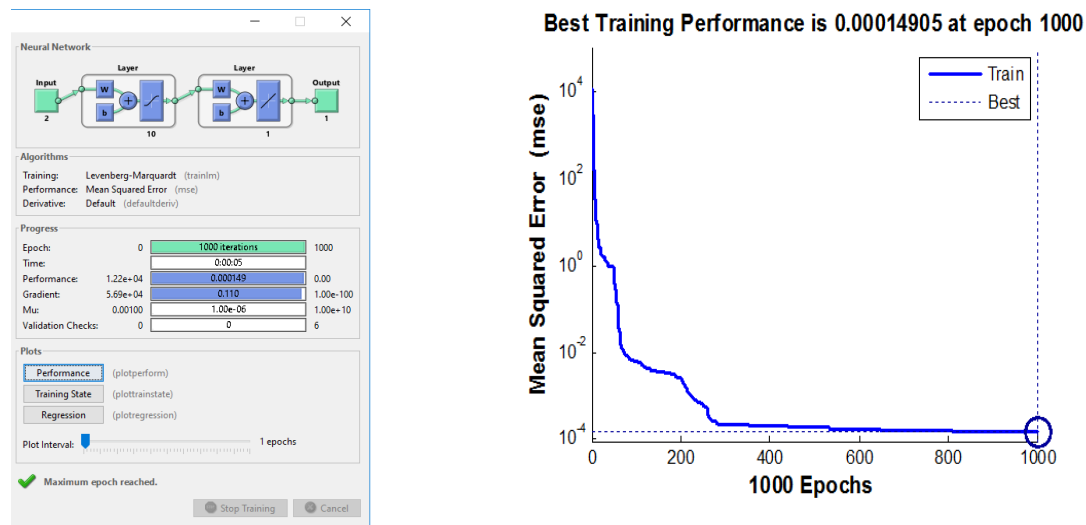


Figure 7. (a) Training result of the designed neural network

(b) Performance result and error of the neural network

The main advantage of NN based MPPT technique is that it can provide satisfactory tracking accuracy of MPP and higher convergence speed without the exact information of the model parameters. However, its disadvantage is that it has to be specifically trained for the PV system on which it has to be implemented. In addition, the neural network requires to train in regular intervals of time to ensure accurate and efficient tracking of MPP when considering that the electrical characteristic of PV panel is time varying [5].

4. COMPARISON RESULTS OF CONVENTIONAL AND INTELLIGENT MPPTS

This study investigates a comparison between conventional P&O and Inc. Cond. MPPTs and intelligent FLC and NN based MPPTs in MATLAB. The performance of P&O, Inc. Cond. MPPT techniques with 3.5 V derivation parameter, fuzzy logic and neural network based MPPT techniques performance results are given in Figure 8 for standard test condition (1 kW/m^2 , 25°C).

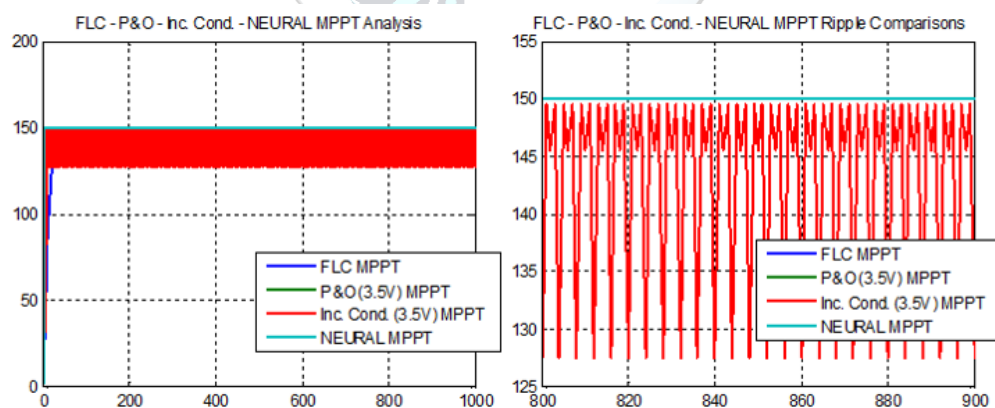


Figure 8. Conventional and intelligent MPPTs simulation results for standard test condition (1 kW/m^2 , 25°C)

As shown in Figure 8, intelligent FLC and NN based MPPTs are 4.66% more efficient than conventional P&O and Inc. Cond. MPPTs. Especially, neural network based MPPT has best iteration rate and also tracking accuracy among the other MPPTs. The conventional MPPTs have 4.45 times faster convergence speed but 4.66% less tracking accuracy than FLC based MPPT due to oscillations around MPP. The overall simulation results in terms of iteration rate and tracking accuracy performance are given in Table 1.

Table 1. Comparison results for conventional and intelligent MPPTs at standard test condition (1 kW/m^2 , 25°C)

MPPT Type	MPPT Technique	Iteration Rate	MPP Power (W)	Tracking Accuracy (%)
Conventional	P&O (3.5 V)	11	142.988	95.33 %
	Inc. Cond. (3.5 V)	11	142.988	95.33 %
Intelligent	Fuzzy Logic Control	49	149.987	99.99 %
	Neural Network	2	149.987	99.99 %

To observe tracking accuracy and convergence speed for different environment condition, the following simulation results are discussed for different solar irradiance values ($1, 0.8, 0.6, 0.4 \text{ kW/m}^2$) at a constant temperature (30°C) in Figure 9. The intelligent MPPTs have better tracking accuracy than conventional ones for different solar irradiance values due to no oscillations around MPP for fuzzy logic and neural network based MPPTs. According to the simulation results, neural network based MPPT technique is better than conventional MPPTs in terms of tracking efficiency and convergence speed and also faster than fuzzy logic based MPPT for standard and different environment conditions.

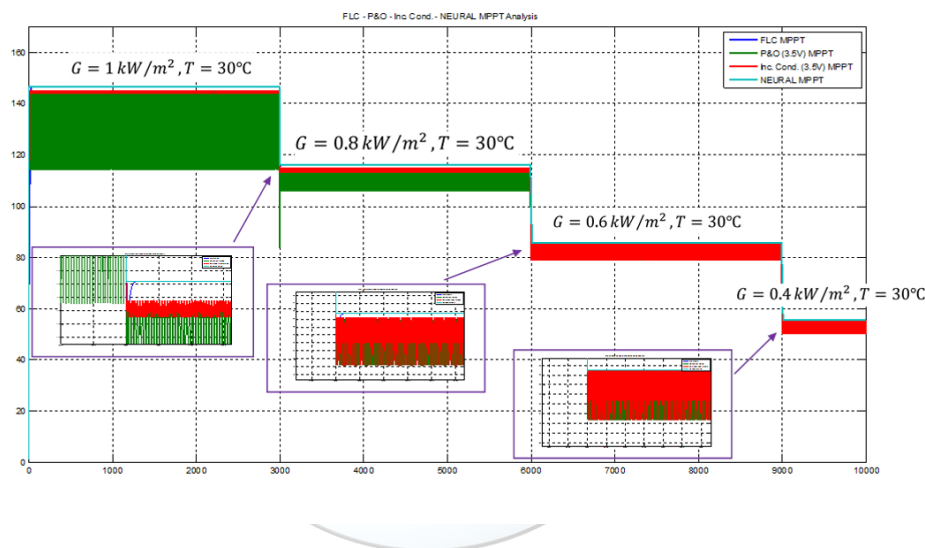


Figure 9. PV output power for conventional and intelligent MPPTs for different environment condition

Additionally, a characteristic comparison table in terms of panel dependency, tuning, tracking rate, complexity and required inputs for conventional and intelligent MPPT types, which are discussed in this paper, is presented in Table 2.

Table 2. Characteristic comparison for the MPPT techniques

MPPT Technique	PV Panel Dependency	Periodic Tuning	Tracking Rate	Complexity	Required Inputs
P&O	No	No	Variable	Low	Current, Voltage
Inc. Cond.	No	No	Variable	Moderate	Current, Voltage
Fuzzy Logic Control	Yes	Yes	High	High	Variable
Neural Network	Yes	Yes	High	Very High	Variable

Although, intelligent MPPTs are more difficult to implement and require additional PV panel information and periodic tuning; they have more efficient, robust and higher tracking rate features than conventional MPPTs.

5. CONCLUSIONS

In the last decade, PV energy generation has become one of the most used renewable energy choice instead of the fossil fuels. Compared to the other renewable sources, PV energy is more environmentally friendly, noise-free, low-cost and readily available universally. Hence, power generation from PV systems becomes important issue for the researchers. Due to non-linear characteristics of PV cells, the maximum allowable power level of PV systems is dependent on atmospheric parameters such as solar irradiance and temperature. Therefore, maximum power point tracking has turned out to be compulsory task to make energy conversion efficiently for the PV systems.

In this study, conventional P&O, Inc. Cond., intelligent FLC and NN based MPPT techniques performances are investigated and compared in terms of tracking efficiency and convergence speed for 150W PV panel under uniform environment conditions in MATLAB. According to the simulation results, intelligent MPPTs increased tracking efficiency 4.66% compared to the conventional MPPTs for the examined PV panel. Especially, NN based MPPT have best tracking and convergence performances among the other MPPTs. In addition, a characteristic comparison table for the investigated conventional and intelligent MPPT techniques is provided in this paper.

REFERENCES

- [1]. J. Ahmed and Z. Salam, "A Modified P&O Maximum Power Point Tracking Method With Reduced Steady-State Oscillation and Improved Tracking Efficiency," *IEEE Trans. Sustain. Energy*, vol. 7, no. 4, pp. 1506–1515, Oct. 2016.
- [2]. A. B. . Bahgat, N. . Helwa, G. . Ahamd, and E. . El Shenawy, "Estimation of the maximum power and normal operating power of a photovoltaic module by neural networks," 2004.
- [3]. J.-K. Shiau, Y.-C. Wei, and B.-C. Chen, "A Study on the Fuzzy-Logic-Based Solar Power MPPT Algorithms Using Different Fuzzy Input Variables," *Algorithms*, vol. 8, no. 2, pp. 100–127, Apr. 2015.
- [4]. P. Takun, S. Kaitwanidvilai, and C. Jettanasen, "Maximum Power Point Tracking using Fuzzy Logic Control for Photovoltaic Systems," in *Proceedings of the International MultiConference of Engineers and Computer Scientists*, 2011.
- [5]. A. Gupta, Y. K. Chauhan, and R. K. Pachauri, "A comparative investigation of maximum power point tracking methods for solar PV system," *Sol. Energy*, vol. 136, pp. 236–253, 2016.
- [6]. E. Kandemir, N. S. Cetin, and S. Borekci, "A comprehensive overview of maximum power extraction methods for PV systems," *Renew. Sustain. Energy Rev.*, vol. 78, pp. 93–112, 2017.
- [7]. S. Saravanan and N. Ramesh Babu, "Maximum power point tracking algorithms for photovoltaic system – A review," *Renew. Sustain. Energy Rev.*, vol. 57, pp. 192–204, 2016.
- [8]. M. A. G. de Brito, L. Galotto, L. P. Sampaio, G. de A. e Melo, and C. A. Canesin, "Evaluation of the Main MPPT Techniques for Photovoltaic Applications," *IEEE Trans. Ind. Electron.*, vol. 60, no. 3, pp. 1156–1167, Mar. 2013.
- [9]. K. Karabacak and N. Cetin, "Artificial neural networks for controlling wind–PV power systems: A review," *Renew. Sustain. Energy Rev.*, vol. 29, pp. 804–827, Jan. 2014.
- [10]. D. Gonzalez Montoya, C. A. Ramos Paja, and R. Giral, "Maximum power point tracking of photovoltaic systems based on the sliding mode control of the module admittance," *Electr. Power Syst. Res.*, vol. 136, pp. 125–134, 2016.
- [11]. E. Kandemir, N. S. Cetin, and S. Borekci, "A Comparison of Perturb & Observe and Fuzzy-Logic Based MPPT Methods for Uniform Environment Conditions," *Period. Eng. Nat. Sci.*, vol. 5, no. 1, pp. 16–23, 2017.
- [12]. A. R. Jordehi, "Maximum power point tracking in photovoltaic (PV) systems: A review of different approaches," *Renew. Sustain. Energy Rev.*, vol. 65, pp. 1127–1138, 2016.
- [13]. S. Borekci, E. Kandemir, and A. Kircay, "A Simpler Single-Phase Single-Stage Grid-Connected PV System with Maximum Power Point Tracking Controller," *Elektron. ir Elektrotehnika*, vol. 21, no. 4, pp. 44–49, Aug. 2015.
- [14]. C. S. Chiu, "T-S Fuzzy Maximum Power Point Tracking Control of Solar Power Generation Systems," *IEEE Transactions on Energy Conversion*, vol. 25, no. 4, pp. 1123–1132, 2010.
- [15]. L. L. Jiang, D. R. Nayanisiri, D. L. Maskell, and D. M. Vilathgamuwa, "A hybrid maximum power point tracking for partially shaded photovoltaic systems in the tropics," *Renew. Energy*, vol. 76, pp. 53–65, 2015.



Effects of SiO₂/Water Nanofluid Flow in a Square Cross-Sectioned Curved Duct

Recep Ekiciler^{1*}, Kamil Arslan²

¹Karabük University, Department of Mechanical Engineering, 78050, Karabük, Turkey.

²Karabük University, Department of Mechanical Engineering, 78050, Karabük, Turkey.

*Corresponding Author email: recepekiciler@karabuk.edu.tr

Abstract

Forced convection SiO₂/water nanofluid flow and heat transfer was numerically performed in 180-degree three-dimensional curved duct with square cross section under steady and laminar flow conditions in this investigation. Dean number was changed from 102 to 898. All surface of curved duct was exposed to uniform and constant heat flux of $q'' = 15000 \text{ W/m}^2$. Nanoparticle volume fractions was ranged 1.0%-4.0%. The average Nusselt number and average Darcy friction factor were determined for each nanoparticle volume fractions. Velocity and temperature profiles and secondary flows were analyzed in detail. In addition, numerical study results are expressed with engineering correlations as changing average Nusselt number and average Darcy friction factor with Dean number and nanoparticle volume fraction.

Key words

Laminar flow, Dean number, SiO₂/water nanofluid, square cross-sectioned curved duct, forced convection,

1. INTRODUCTION

Conventional heat transfer fluids such as water, oil and ethylene glycol have a low thermal conductivity. So, using conventional fluids limit the performance and compactness for example at heat exchangers and electronic equipments. The new heat transfer fluids (nanofluids) having high thermal conductivity are capable to eliminate this effect.

Nanofluids are a new kind of heat transfer fluids containing a small quantity of nano-sized particles (generally less than 100 nm) that are uniformly and stably suspended in a liquid. The dispersion of a small number of solid nanoparticles in conventional fluids remarkably changes their thermal conductivity. Compared to the existing techniques for enhancing heat transfer, the nanofluids show a superior potential for increasing heat transfer rates in a variety of cases. In fact, Maxwell (1873) firstly suggested adding solid particles for increasing of thermal properties [1]. But S. Choi firstly studied about nanofluids at 1995 [2].

Lee et al. [3] have proved that oxide ceramic nanofluids consisting of CuO or Al₂O₃ nanoparticles in water or ethylene glycol exhibit enhanced thermal conductivity. A maximum increase in thermal conductivity of approximately 20% was observed in that study, having 4.0% vol. CuO nanoparticles with mean diameter 35 nm dispersed in ethylene glycol. But larger particles with an average diameter of 40 nm led to an increase of less than 10%.

As nanofluids are rather new, relatively few theoretical and experimental studies have been reported on convective heat transfer coefficients in confined flows. Park and Cho [4] and Xuan and Li [5] obtained experimental results on convective heat transfer for laminar and turbulent flow of a nanofluid inside a tube. They produced the first

empirical correlations for the Nusselt number using Cu/water, TiO₂/water and Al₂O₃/water nanofluids. The results indicate a remarkable increase in heat transfer performance over the base fluid for the same Reynolds number.

To increase of heat transfer can apply lots of geometries. When compared the curved ducts with straight ducts, curved ducts have more pressure losses. However, curved ducts were widely used in industrial concerning heat and mass transfer devices. The applications areas of curved ducts are heat exchanger, turbomachines, air condition systems, centrifugal pumps, rocket engines and gas turbines [6].

Flow and heat transfer in curved duct has more complicated system than straight duct. Therefore, analytical study is nearly impossible [7]. Accordingly, experimental and numerically studies on curved duct are the other alternative investigations. In literature reviews, there have been various experimental and numerical study about laminar flow in curved duct at uniform surface temperature and uniform heat flux boundary condition. Facao and Oliveira [7] have used rectangular cross-sectioned curved duct and obtained Nusselt number changed with Dean number. It is found that Nusselt number is higher than at straight duct. Sturgis and Mudauer [8] investigated heat transfer enhancement using of rectangular cross-sectioned curved duct. In this study, duct curvature radiuses were changed. Working fluid was air. It is found that increasing of duct curvature radius, convection heat transfer coefficient also increased. Fang Liu [9] studied effects of geometries on heat transfer enhancement of thermal fluids in curved duct.

There are a few studies about heat transfer enhancement using of nanofluids at curved ducts. Akbarinia et al. [10] carried out numerical study of laminar mixed convection of a nanofluid in horizontal curved tubes. It is found that increasing the buoyancy forces causes to reduce the skin friction and free convection has a negative effect on the heat transfer enhancement in the presence of centrifugal force. Heat transfer coefficients are determined with SiO₂ nanoparticle in base liquid water at various concentrations. Ghaffari et al. [11] investigated numerically turbulent mixed convection heat transfer flow of Al₂O₃/water nanofluid in a horizontal curved tube. They performed the study using two phase mixture model. They analysed the effects of nanoparticle volume fractions on heat transfer. It was obtained from the numerical results that the nanoparticle volume fraction improves the Nusselt number.

The objective of this paper is to study effect of SiO₂/water nanofluid on flow and heat transfer characteristics for different Dean numbers and different nanoparticle volume fractions in 180-degree square cross-sectioned curved duct. The average Nusselt number and Darcy friction factor are presented and discussed. Also, velocity and temperature distributions are presented for varying nanoparticle volume fraction and the Reynolds number.

2. PROBLEM DESCRIPTION AND GOVERNING EQUATIONS

Nanofluid flow in 180-degree square cross-sectioned 3D curved duct was modelled in this study. SiO₂/water nanofluid was used for working fluid. Particle size was 20 nm. ANSYS 15.0 was used to obtain numerical results. Geometry of curved duct is shown in Figure 1. Curvature radius was R=60 mm and length of the one edge of square duct was 10 mm. All the duct's walls were heated by 15000 W/m². Inlet temperature of fluid flow was 300 K. The following assumptions were adopted for this numerical study: (i) Both heat transfer and fluid flow in duct are in three-dimensional and steady-state; (ii) fluid flow is incompressible and laminar flow; (iii) the physical properties of nanofluid, such as density, specific heat, thermal conductivity and viscosity are taken as temperature independent; (iv) negligible buoyancy effect, viscous dissipation and radiation heat transfer; and (v) the base fluid and the nanoparticles are in thermal equilibrium.

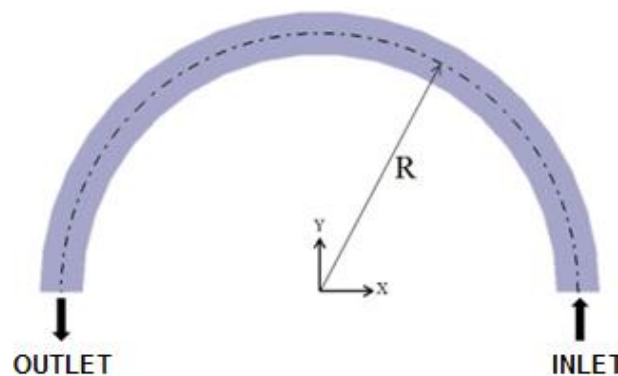


Figure 1. Schematic diagram of horizontal curved duct

Continuity, momentum and energy equations are given below for steady-state, incompressible, laminar flow condition in Eq (1) – (3), respectively.

$$\vec{\nabla} \cdot \vec{V} = 0 \quad (1)$$

$$\rho \frac{D\vec{V}}{Dt} = -\Delta p + \mu \nabla^2 \vec{V} \quad (2)$$

$$\rho C_p \frac{DT}{Dt} = k \nabla^2 T \quad (3)$$

The properties of density (ρ), specific heat (C), viscosity (μ) and thermal conductivity (k) of nanofluids have been calculated as given below, respectively [12]. Also, ϕ represents the volume fraction of nanoparticle.

$$\rho_{nf} = (1-\phi)\rho_w + \phi\rho_p \quad (4)$$

$$C_{nf} = \frac{(1-\phi)(\rho C)_w + \phi(\rho C)_p}{(1-\phi)\rho_w + \phi\rho_p} \quad (5)$$

$$\mu_{nf} = \mu_w \left(1 + \frac{\phi}{100}\right)^{11.3} \left(1 + \frac{T_{nf}}{70}\right)^{-0.038} \left(1 + \frac{d_p}{170}\right)^{-0.061} \quad (6)$$

$$k_{nf} = k_w 0.8938 \left(1 + \frac{\phi}{100}\right)^{1.37} \left(1 + \frac{T_{nf}}{70}\right)^{0.2777} \left(1 + \frac{d_p}{150}\right)^{-0.0336} \left(\frac{\alpha_p}{\alpha_w}\right)^{0.01737} \quad (7)$$

where the subscript of w, p and nf represents water, nanoparticle, and nanofluid, respectively.

The calculations of average Nusselt number (Nu), average Darcy friction factor (f) and Dean number (De) are given below:

$$Nu = \frac{hD_h}{k} \quad (8)$$

$$f = \frac{(-dp/dx)D_h}{\rho U_m^2 / 2} \quad (9)$$

$$De = Re \sqrt{\frac{D_h}{R}} \quad (10)$$

The average heat transfer coefficient was calculated with Eq. (11).

$$h = \rho U_m A_c c_p (T_{mo} - T_{mi}) / A_s (T_w - T_m) \quad (11)$$

3. NUMERICAL PROCEDURES

In the computations, the finite-volume method based commercial CFD software Ansys Fluent 15.0 was used to perform the numerical calculations by solving the governing equations along with the boundary conditions. The convection terms in mass, momentum and energy equations were discretized using a second order upwind scheme. The standard scheme was employed for discretization of pressure and the SIMPLE algorithm. The Green-Gauss cell based method was applied for discretization of the momentum and energy equations. To obtain convergence, each equation for mass, momentum, and energy were iterated until the residual falls below 1×10^{-6} . No convergence problems were observed during the calculations. The hexahedral mesh distribution was used for the curved duct having square cross-section. The numbers of mesh points or control volumes were increased close to wall of the duct to enhance the resolution and accuracy as given in Figure 2.

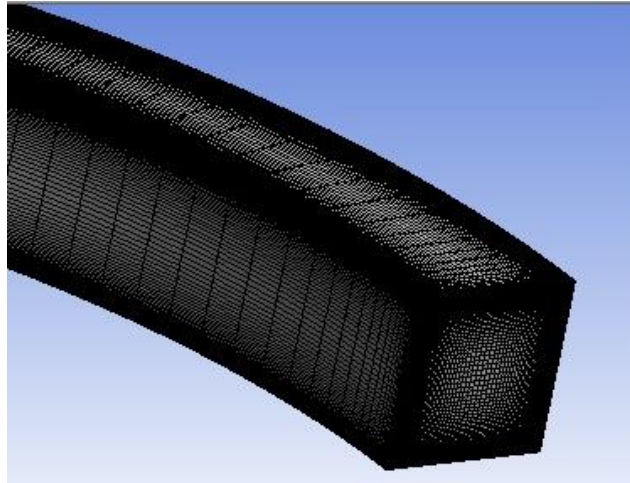


Figure 2. Mesh distribution of the curved duct

The mesh independence study was performed for the curved duct by refining the mesh number until the variation in both average Nusselt number and average Darcy friction factor are less than 0.1%. To obtain the optimum mesh number, a grid independence study was conducted using thirteen different mesh numbers changing from 5×10^2 to 1.25×10^6 for $De=898$. Changing of average Nusselt number and average Darcy friction factor values with mesh number for pure water flow is given in Figure 3 as an illustration. It was observed that a further refinement of mesh number from 4×10^5 to 1.25×10^6 , the changing of average Nusselt number and average Darcy friction factor is negligible. If Fig. 3 is observed, optimum mesh number with minimum computational time and maximum accuracy approximately can be seen at 4×10^5 .

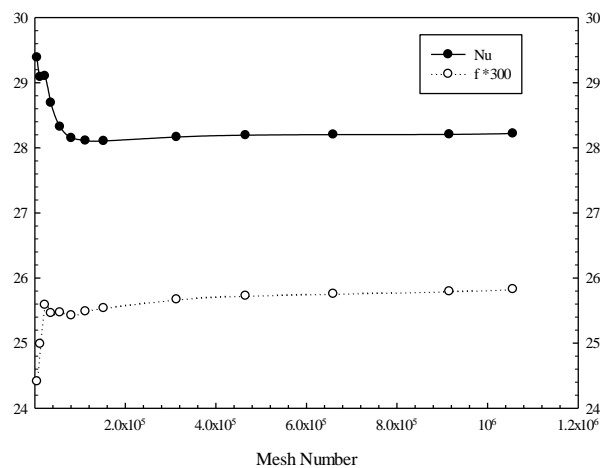


Figure 3. Changing of average Nusselt number and average Darcy friction factor with mesh number for pure water at $De=898$

To understand the accuracy of the numerical simulation for pure water, values of average Nusselt number were compared with experimental data studied by Dravid et al.[13] and Kalb and Sieder [14] in Figure 4. The results obtained by present study are good agreement with the the correlation proposed studies.

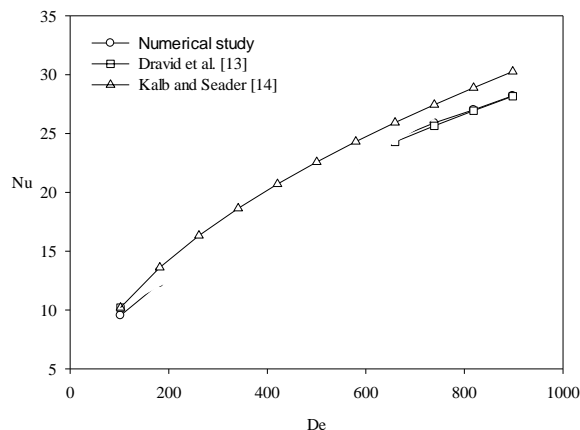


Figure 4. Comparison of average Nusselt number for pure water of the present study with experimental data given in the literature

4. RESULTS AND DISCUSSION

Laminar forced convection flow in a curved duct having square cross-sectioned is numerically investigated. Figure 5 is presented to understand the effect of nanoparticles volume fractions on average Nusselt number. As seen Figure 5, average Nusselt number increases with increasing nanoparticle volume fractions. Average Nusselt number also increases with increasing Dean number. The highest average Nusselt number was obtained at 4.0% nanoparticle volume fraction and the highest Dean number. This result is attributed that adding nanoparticles increases viscosity of nanofluid which enhances the random and irregular movement. Pure water has the lowest average Nusselt number.

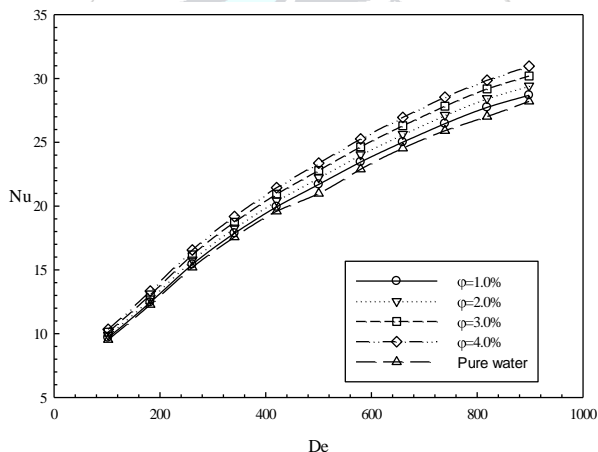


Figure 5. Changing of average Nusselt number with Dean number for different nanoparticle volume fractions of SiO₂/water nanofluid

Figure 6 shows changing of average Darcy friction factor with nanoparticle volume fractions and Dean numbers. It can be noticed that average Darcy friction factor is not affected of changing of nanoparticle volume fractions. This is advantage of SiO₂/water nanofluid flow for reducing pumping power. But, average Darcy friction factor decreases with the increasing Dean number.

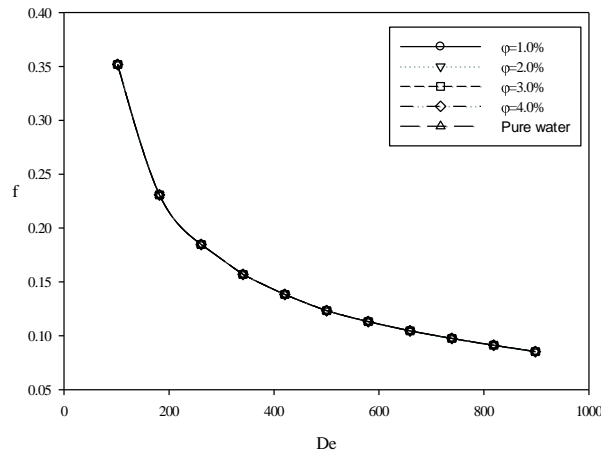


Figure 6. Changing of average Darcy friction factor with Dean number for different nanoparticle volume fractions of $\text{SiO}_2/\text{water}$ nanofluid

Figure 7 shows that temperature distributions of duct outlet at $De=500$ for different nanoparticle volume fractions. It can be revealed that temperature distributions are symmetric. The outer wall of curved duct has lower temperature compared to the inner wall because of highest flow velocity at the outer wall. Flow velocity of the outer wall is high according to flow velocity of the inner wall. Also, increasing of nanoparticle volume fractions slightly effects the temperature distributions of the inner wall.

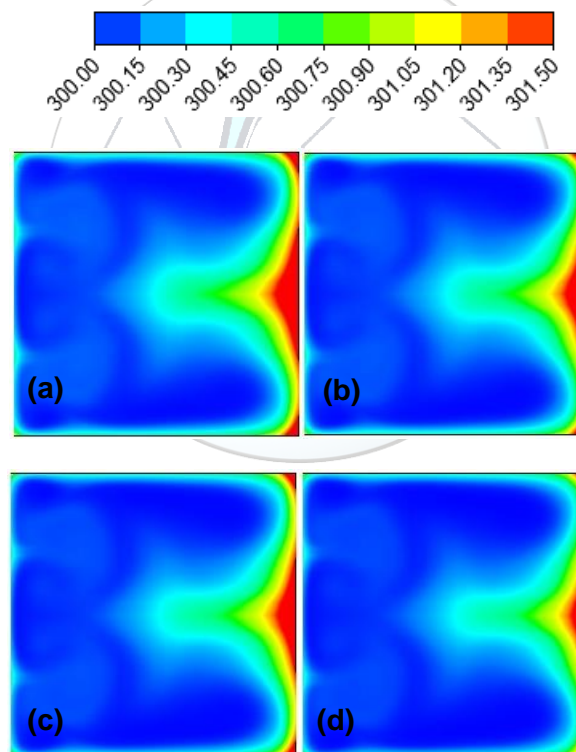


Figure 7. Temperature distribution of duct outlet for different nanoparticle volume fractions of $\text{SiO}_2/\text{water}$ nanofluid at $De=500$ (a) 1.0%, (b) 2.0%, (c) 3.0%, (d) 4.0%

Figure 8 shows that the velocity streamlines of duct outlet for different nanoparticle volume fractions of $\text{SiO}_2/\text{water}$ nanofluid at $De=500$. It was obtained that velocity distributions are symmetric and secondary flows occurs. As nanoparticle volume fraction increases, the velocity at the outer wall increases.

Figure 9 shows that temperature distribution of duct outlet for different Dean numbers for 4.0% nanoparticle volume fraction of $\text{SiO}_2/\text{water}$ nanofluid. It was revealed that Dean number significantly effects the temperature distribution in the duct. Temperature distribution decreases with increasing Dean number.

Figure 10 shows that velocity streamlines of duct outlet for different Dean number at 4.0% nanoparticle volume

fraction of SiO₂/water nanofluid. It was obtained that Dean number significantly effects velocity distributions, too. At De=102, there is a secondary flow which has one center. However, at De=500, there are a lot of secondary flow. On the other hand, at De=898, there is no secondary flow. Also, velocity distribution increases with increasing Dean number.

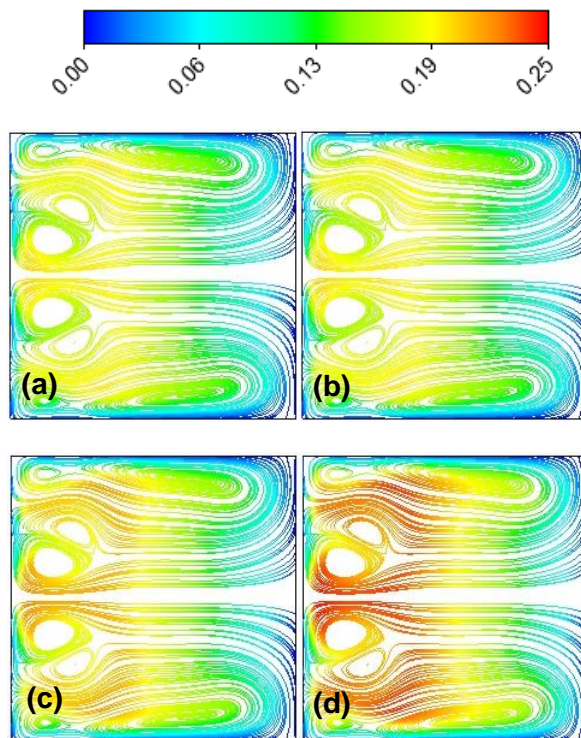


Figure 8. Velocity streamlines of duct outlet for different nanoparticle volume fractions of SiO₂/water nanofluid at De=500 (a) 1.0%, (b) 2.0%, (c) 3.0%, (d) 4.0%

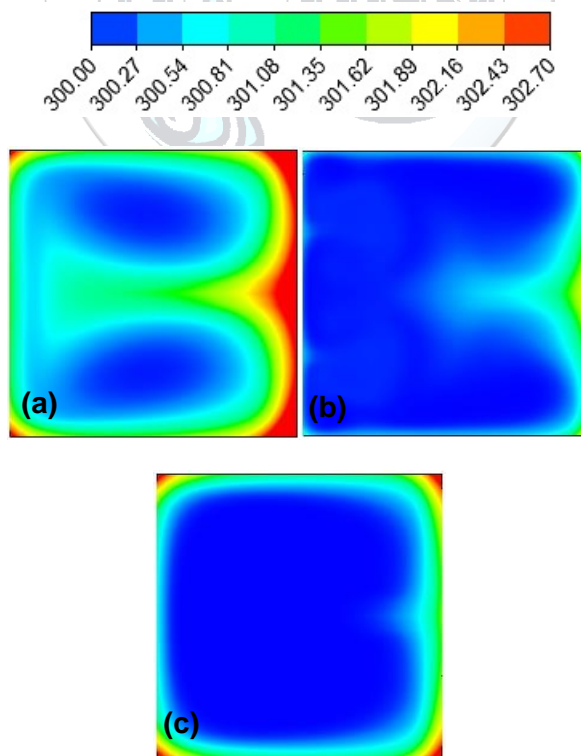


Figure 9. Temperature distribution of duct outlet for different Dean numbers at 4.0% nanoparticle volume fraction of SiO₂/water nanofluid (a) De=102, (b) De=500, (c) De=898

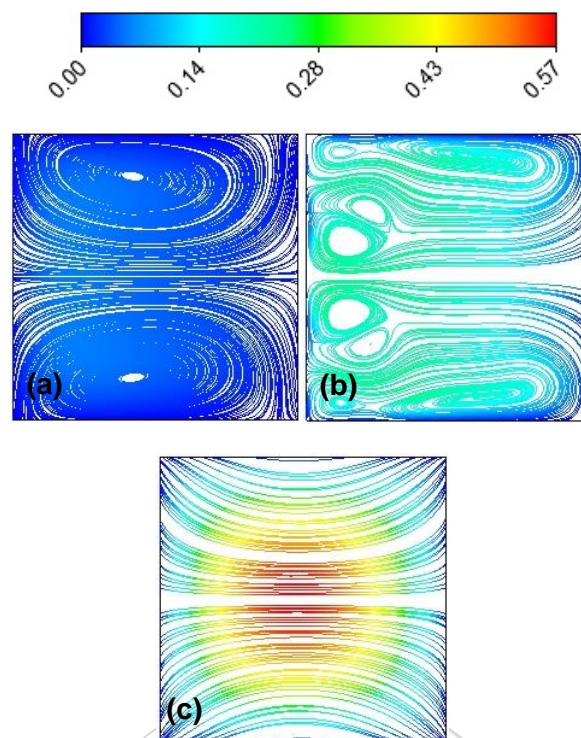


Figure 10. Velocity streamlines of duct outlet for different Dean numbers at 4.0% nanoparticle volume fraction of $\text{SiO}_2/\text{water}$ nanofluid (a) $De=102$, (b) $De=500$, (c) $De=898$

5. CONCLUSIONS

Numerical simulation of steady state laminar forced convection flow and heat transfer in a 3D square cross-sectioned curved duct using $\text{SiO}_2/\text{water}$ nanofluid is presented. Effect of different Dean numbers and the nanoparticle volume fractions were investigated. It was noticed from the numerical simulation results that $\text{SiO}_2/\text{water}$ nanofluid enhances heat transfer. The average Nusselt number increases with increasing the Dean number and nanoparticle volume fractions. Also, Darcy friction factor decreases with increasing Reynolds number. There is no effect of changing of nanoparticle volume fractions on average Darcy friction factor.

REFERENCES

- [1]. H. A. Mohammed, G. Bhaskaran, N. H. Shuaib, and R. Saidur, "Heat transfer and fluid flow characteristics in microchannels heat exchanger using nanofluids: A review," *Renewable and Sustainable Energy Rev.*, vol. 15, pp. 1502-1512, 2011.
- [2]. S. U. S. Choi, "Enhancing thermal conductivity of fluids with nanoparticles", in: D.A. Singer, H.P. Wang (Eds.), *Development and Applications of Non-Newtonian Flows*, ASME, New York, vol. 231 pp. 99-105, 1995.
- [3]. S. Lee, S. U. S. Choi, S. Li, and J. A. Eastman, "Measuring thermal conductivity of fluids containing oxide nanoparticles," *Journal of Heat Transfer*, vol. 121, pp. 280-288, 1999.
- [4]. B. C. Pak and Y. I. Cho, "Hydrodynamic and heat transfer study of dispersed fluids with submicron metallic oxide particles," *Exp. Heat Transfer*, vol. 11, pp. 151-170, 1998.
- [5]. Y. Xuan and Q. Li, "Heat transfer enhancement of nanofluids," *Int. J. Heat Fluid Flow*, vol. 21, pp. 58-64, 2000.
- [6]. M. S. Islam and N. R. Mondal, "Effects of curvature on unsteady solutions through a curved square duct flow," *5th BSME International Conference on Thermal Engineering*, vol. 56, pp. 217-224, 2013.
- [7]. J. Facao and A. C. Oliveira, "Modelling laminar heat transfer in a curved rectangular duct with computational fluid dynamics code," *J. Heat Transfer*, vol. 48, pp. 165-177, 2005.
- [8]. J. C. Sturgis and I. Mudawar, "Single-phase heat transfer enhancement in a curved, rectangular channel subjected to concave heating," *Int. J. Heat and Mass Transfer*, vol. 42, pp. 1255-1272, 1999.
- [9]. L. Fang, "Effects of geometries on heat transfer enhancement of thermal fluids in curved ducts," *Appl. Therm. Eng.*, vol. 90, pp. 590-595, 2015.
- [10]. Akbarinia and A. Behzadmehr, "Numerical study of laminar mixed convection of a nanofluid in horizontal curved tubes", *Appl. Therm. Eng.*, vol. 207, pp. 1327-1337, 2007.

- [11]. O. Ghaffari, A. Behzadmehr, and H. Ajam, "Turbulent mixed convection of a nanofluid in a horizontal curved tube using a two-phase approach," *Int. Commun. Heat and Mass Transfer*, vol. 37, pp. 1551–1558, 2010.
- [12]. W. H. Azmi, K. V. Sharma, P. K. Sarma, R. Mamat, and G. Najafi, "Heat transfer and friction factor of water based TiO_2 and SiO_2 nanofluids under turbulent flow in a tube," *Int. Commun. Heat and Mass Transfer*, vol. 59, pp. 30-38, 2014.
- [13]. A. N. Dravid, K. A. Smith and E. W. Merrill, "Effect of secondary fluid on laminar flow heat transfer in helical coiled tubes," *AICHE J.*, vol. 17, pp. 1114-1122, 1971.
- [14]. C. E. Kalb and J. D. Seader, "Fully developed viscous-flow heat transfer in curved circular tubes with uniform wall temperature," *AICHE J.*, vol. 20, pp. 340-346, 1974.





Solar Radiation Modeling with Adaptive Approach

Emre Akarslan^{1*}, Fatih Onur Hocaoglu²

¹Afyon Kocatepe University, Department of Electrical Engineering, 03200 , Afyonkarahisar, Turkey.

²Afyon Kocatepe University, Solar and Wind Application and Research Center, 03200 , Afyonkarahisar, Turkey.

*Corresponding Author email: e.akarslan@gmail.com

Abstract

The unsustainable formation of fossil fuels, increase the interest on different resources and this leads to greater emphasis on clean resources. Solar energy is one of the popular sources among the renewables. Electricity generation from PV panels directly related to the solar radiation value measured on surface of the panel. Modeling of solar radiation is important due to manage the integration of different sources to the grid. In this study, previously developed Adaptive Approach method is used for modeling the solar radiation values. This method combines linear prediction filter method with an empiric approach. Linear prediction filter used in this study utilize the current value of the solar radiation to predict next hour's solar radiation value while the empiric model utilize from the current value of the solar radiation and the deviation on extraterrestrial radiation. One year solar radiation data belong to Van region is used in this study. The accuracies of the forecasting results are compared and discussed.

Key words

Solar radiation forecasting, Adaptive approach, Empiric model, Linear prediction filter

1. INTRODUCTION

The best solutions for alternative energy sources, such as some of the solar energy and photovoltaic (PV) systems are rapidly gaining acceptance [1]. In order to integrate the electricity generated by solar energy into the grid, solar irradiation must be reasonably well forecasted, where deviations of the forecasted value from the actual measured value involve significant costs [2]. Several methods are used before for solar radiation forecasting. [3] used the combination of unsupervised k-means clustering algorithm and artificial neural networks (ANN) for hourly global horizontal solar radiation forecasting. They show that the combination of these models provide better results. In [2] a univariate Dynamic Harmonic Regression model set up in a State Space framework for short-term solar irradiation forecasting is proposed. This method is based on the frequency domain and provides a fast automatic identification and estimation procedure. Their results show that the Dynamic Harmonic Regression achieves the lowest relative Root Mean Squared Error for a forecast horizon of 24 h ahead. In [1] neural networks to predict solar radiation is used. They categorized the review under three major performance schemes such as delay, number of neurons and activation function for establishment of neural network architecture.

[4] applied Support Vector Regression (SVR), Gradient Boosted Regression (GBR), Random Forest Regression (RFR) as well as a hybrid method to combine them to downscale and improve 3-h accumulated radiation forecasts provided by Numerical Weather Prediction (NWP) systems for seven locations in Spain. They showed

that Machine Learning methods are quite effective. In [5] a novel solar radiation forecasting method based on a novel game theoretic self-organizing map (GTSOM) is proposed. They compared the proposed method with that of the K-means and the original SOM. They show that comparison demonstrates the superior performance of the proposed approach. [6] used satellite data to improve solar radiation forecasting with Bayesian Artificial Neural Networks. They show that forecasting skills are improved by including exogenous inputs to the model by using global horizontal solar irradiance satellite data from surrounding area.

In [7] linear prediction filter approach for hourly solar radiation forecasting is proposed. In this approach solar radiation time series is converted to 2-D image and this new form of the data provide better understanding about the seasonal and daily behavior of the solar data. The optimum filter coefficients are determined by scanning image with a filter template. [8] improved the linear prediction approach by developing multi-dimensional filter templates. In their method, the images obtained from different time series such as temperature, extraterrestrial and solar radiation data etc. are linked each other with filter templates. This method provides utilize from different parameters for solar radiation forecasting and up to 40% improvement is achieved as per to linear prediction filter approach. In [9] a novel adaptive approach (NAA) for solar radiation forecasting is proposed. This approach integrates an empiric model to linear prediction filter approach to improve the prediction accuracy. The solar radiation data are predicted using different methods for different weather condition cases. Two different strategies are used to decide the prediction method. Seasons and clearness index values are employed to select the forecasting method. The results show that the accuracy of the forecast is considerably improved using proposed adaptive prediction approach.

In this paper, the adaptive approach method which is developed previously [9], is employed to determine next hour solar radiation values. The clearness index values are used to determine the forecasting method. If the clearness index value is greater than a specified value, linear prediction filters otherwise an empirical model is used. The solar radiation data belong to Van region is used to test the performance of the adaptive approach method. The organization of the paper is as follows. The data used for this study are described in Section 2. The adaptive approach method is explained in Section 3. The experimental results are illustrated in Section 4. Finally, conclusions are explained in Section 5.

2. DATA USED

In this study, solar radiation data belong to Van region of Turkey is used. Van region has a good insolation characteristic as seen in Fig. 1. The solar radiation data belong to Van region is taken from the Turkish State Meteorological Service (DMI). The variation in the solar irradiance value over a 1-year period from 2014 is shown in Figure 2. The extraterrestrial irradiance is the intensity of the sun at the top of the Earth's atmosphere [8,10]. Therefore, the actual measured data on the earth's surface must be less than the extraterrestrial irradiance.

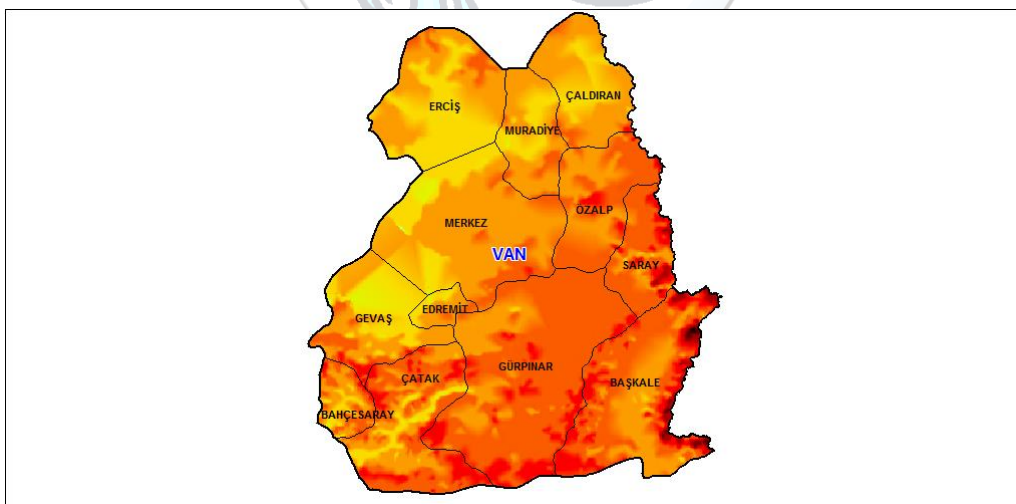


Figure 1. The insolation map of the Van region

The extraterrestrial irradiance can be calculated as follow:

$$I_s = C \sin(\varphi) / 24R^2 \quad (1)$$

where I_s is the total radiation falling on the atmosphere; C is the solar constant assumed to be $1367 \text{ (W/m}^2\text{)}$; and R is the solar radius vector (assumed to be 1). Then the solar elevation angle is calculated by using following equation:

$$\sin(\varphi) = \sin(L)\sin(D) + \cos(L)\cos(D)\cos(h) \tag{2}$$

Here, L is the latitude of the location, D is the declination angle of the sun, and h is the solar hour angle. Forecasting model is selected by using clearness index values. These values are calculated by dividing solar radiation value to extraterrestrial radiation value for each hour [11] as seen in Eq. 3:

$$K_t = I / I_0 \tag{3}$$

Here, K_t , I and I_0 represent the clearness index, solar radiation and extraterrestrial radiation, respectively.

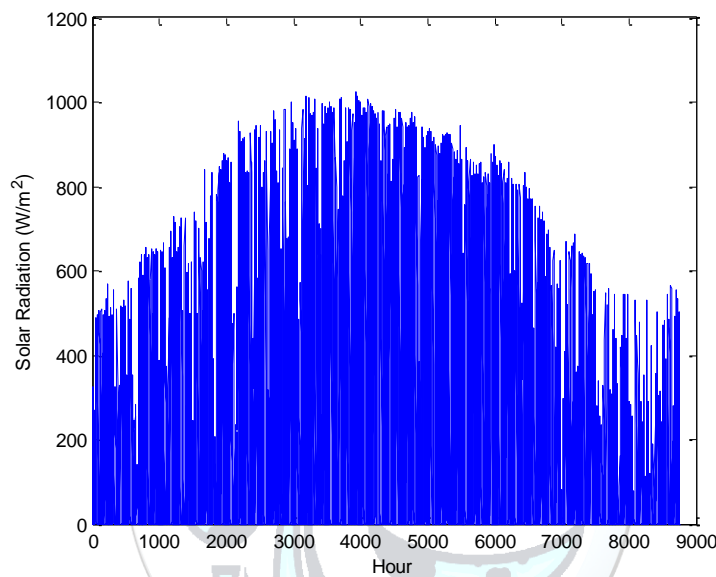


Figure 2. Variation of the solar radiation data over a 1-year period

3. ADAPTIVE APPROACH METHOD

The adaptive approach method includes combination of linear prediction filters and an empiric model. For a better understanding, linear prediction filter and empiric model used are explained in this section. Linear prediction filters for solar radiation forecasting are firstly introduced by [7]. In this approach solar radiation time series is converted to 2-D image. This image provides better understanding of seasonal and daily behavior of solar radiation. Furthermore, image processing techniques can be applied to this data after conversion. Linear prediction filter scan overall image and optimum filter coefficients which will be used for prediction are determined. In this study, filter template which use the actual data to predict one hour later data is used. Consider the 2-D linear prediction filter as follow:

$$\begin{bmatrix} Z_{i,j} & Z_{i,j+1}=? \end{bmatrix} \tag{4}$$

The prediction pixel was determined by using past pixels with the following formula:

$$\check{Z}_{i,j+1} = Z_{i,j} \cdot a_1 \tag{5}$$

i,j and $Z_{i,j}$ are identify the row and column number of the pixel and the pixel value, respectively. In 2-D linear filter approach, the estimation $\check{Z}_{i+1,j+1}$ is considered as a linear combination of past samples. After calculated prediction error for each (i,j) coordinates, the energy of total prediction error is calculated with Eq. 6:

$$\varepsilon = \sum_{i=2}^m \sum_{j=2}^n \varepsilon_{i,j}^2 \tag{6}$$

where m and n identify the size of image. By equating to zero the derivative of this function, the filter coefficients which minimize the Eq. 6 are obtained and the solution yields the following equation:

$$\begin{bmatrix} R_{11} & R_{12} & R_{13} \\ R_{21} & R_{22} & R_{23} \\ R_{31} & R_{32} & R_{33} \end{bmatrix} \begin{bmatrix} a_1 \\ a_2 \\ a_3 \end{bmatrix} = \begin{bmatrix} r_1 \\ r_2 \\ r_3 \end{bmatrix} \tag{7}$$

where R_{ij} is the correlation value between the past values, a_i is the linear filter coefficients and r_k is the correlation between the past and predicted pixel.

2-D linear prediction filters have a good forecasting performance but this approach good at linear data. The solar radiation data generally nonlinear due to weather conditions such as rain, wind, cloud etc. To overcome this weakness, an empiric model can be integrated to the linear prediction filters [9]. The empiric model used in the adaptive approach method is as follow:

$$S(t+1) = S(t) + (E(t+1) - E(t)) \tag{8}$$

In this empiric approach, the next hour solar radiation value is calculated by summing the solar radiation with the difference of actual and next hour extraterrestrial radiation. In the integration strategy, clearness index value is employed to decide which method will be used in prediction. Clearness index value is the ratio of solar radiation to the extraterrestrial radiation in a certain time and formulated with Eq. 3. In the used strategy, if the clearness index value is smaller than 0.5, the next hour solar radiation value is predicted by empiric model otherwise; the linear prediction filters are employed.

4. EXPERIMENTAL RESULTS

In this study adaptive approach method is used for hourly solar radiation forecasting. In this paper clearness index value is employed to decide combining strategy of adaptive approach method. The solar radiation data belong to Van region of Turkey is used to test this method. Van region has a good insolation characteristic. The Root Mean Square Error (RMSE) and Mean Bias Error (MBE) assessment criteria are used to evaluate the performance of adaptive approach method. The RMSE is a commonly used measure of the differences between the values extracted by a forecasting model and the observed values. The value of RMSE provides information on the short term performance [12]. The MBE provides information in the long term performance of the correlations by allowing a comparison of the actual deviation between predicted and measured values term by term. The MBE is used to describe whether a model over-(positive value) or under-(negative value) predicts the observation and has the same units as the measured variable-parameter. The ideal value of MBE is 'zero' [12,13]. To illustrate the performance of the adaptive approach method, experimental results with Linear Prediction filter and adaptive approach method are compared in Table 1.

Table 1. Experimental Results on solar radiation data of Van region, Turkey

	RMSE (W/m ²)	MBE (W/m ²)
Linear Prediction Filter	104.23	8.97
Adaptive Approach Method	76.08	11.76

As seen in Table 1, adaptive approach method outperforms the Linear Prediction Filter according to RMSE criteria. Nearly 25% improvement on prediction performance is achieved by using adaptive approach method. MBE result with adaptive approach bigger than the linear prediction filter. This means adaptive approach

method over predicts the observation and these predictions are generally greater than linear prediction filter's. However, overall estimations with adaptive approach method are better than the linear prediction filter. The correlations between the observed and predicted values are shown in Figure 3.

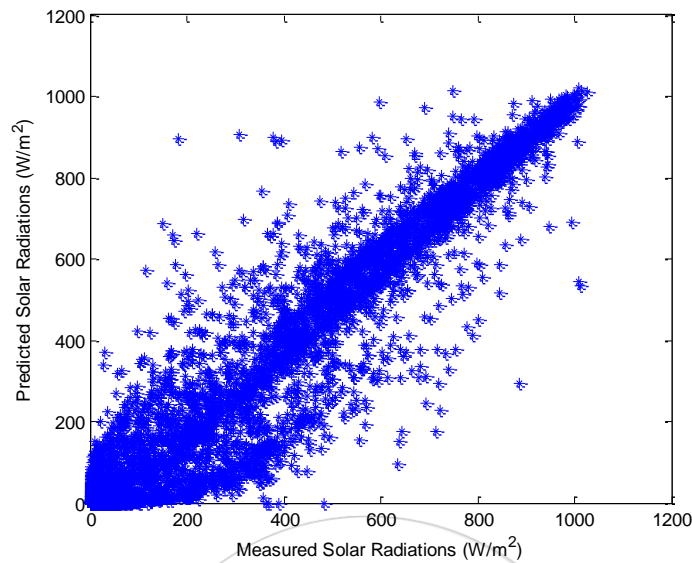


Figure 3. Correlations between the observed and predicted data

As seen in Figure 3, the predicted values are correlated with the observed values of solar radiation. The prediction results are closely matching observed data along the diagonal axis. The slope of the fit nearly 45° and scatter is so narrow. These indicate a good prediction performance. Figure 4 illustrates the mesh plot of the prediction error. The error pixels are almost uncorrelated with each other. The uncorrelated samples indicate that the prediction almost totally exploits the predictable part of the data. Therefore, the model works with very good accuracy.

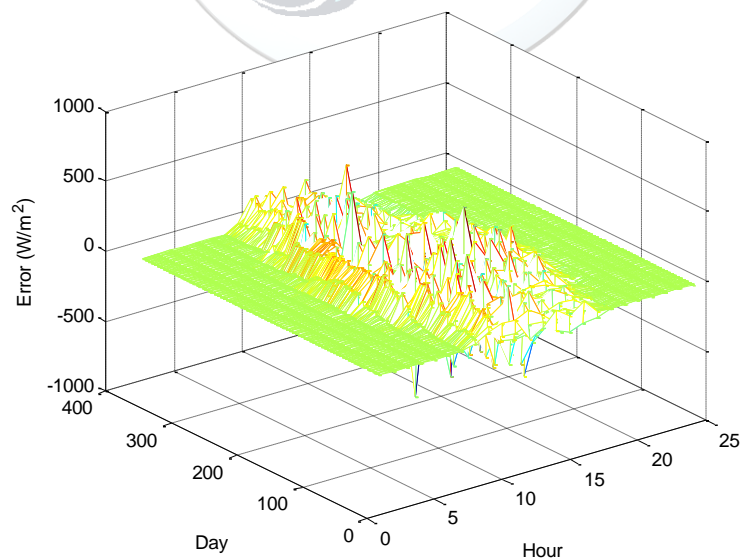


Figure 4. Mesh plot of the prediction error with adaptive approach method

5. CONCLUSION

The adaptive approach method is used in this study for hourly solar radiation modeling. adaptive approach method, combines linear prediction filter and an empiric model to improve the prediction performance. The selection of the model is managed by using actual clearness index value. The solar radiation data used in this study belongs to Van region of Turkey and measure in 1 year period from 1st Jan to 31th Dec 2014. To test the performance of the adaptive approach method, results are compared to results obtained with linear prediction filters. The experimental results show that the adaptive approach method outperforms the linear filter approach. The performance of different combining strategies with different filter templates and empiric models can be investigated as a future work.

REFERENCES

- [1]. K. Benmouiza and A. Cheknane, "Forecasting hourly global solar radiation using hybrid k-means and nonlinear autoregressive neural network models," *Energy Convers. Manag.*, vol. 75, pp. 561–569, Nov. 2013.
- [2]. J. R. Trapero, N. Kourentzes, and A. Martin, "Short-term solar irradiation forecasting based on Dynamic Harmonic Regression," *Energy*, vol. 84, pp. 289–295, May 2015.
- [3]. Y. Kashyap, A. Bansal, and A. K. Sao, "Solar radiation forecasting with multiple parameters neural networks," *Renew. Sustain. Energy Rev.*, vol. 49, pp. 825–835, Sep. 2015.
- [4]. Y. Gala, Á. Fernández, J. Díaz, and J. R. Dorronsoro, "Hybrid machine learning forecasting of solar radiation values," *Neurocomputing*, vol. 176, pp. 48–59, May 2015.
- [5]. M. Ghayekhloo, M. Ghofrani, M. B. Menhaj, and R. Azimi, "A novel clustering approach for short-term solar radiation forecasting," *Sol. Energy*, vol. 122, pp. 1371–1383, Dec. 2015.
- [6]. L. Mazorra Aguiar, B. Pereira, M. David, F. Díaz, and P. Lauret, "Use of satellite data to improve solar radiation forecasting with Bayesian Artificial Neural Networks," *Sol. Energy*, vol. 122, pp. 1309–1324, Dec. 2015.
- [7]. F. O. Hocaoglu, Ö. N. Gerek, and M. Kurban, "Hourly solar radiation forecasting using optimal coefficient 2-D linear filters and feed-forward neural networks," *Sol. Energy*, vol. 82, no. 8, pp. 714–726, Aug. 2008.
- [8]. E. Akarslan, F. O. Hocaoglu, and R. Edizkan, "A novel M-D (multi-dimensional) linear prediction filter approach for hourly solar radiation forecasting," *Energy*, vol. 73, pp. 978–986, Aug. 2014.
- [9]. E. Akarslan and F. O. Hocaoglu, "A novel adaptive approach for hourly solar radiation forecasting," *Renew. Energy*, vol. 87, pp. 628–633, Mar. 2016.
- [10]. R. G. Allen, "Environmental, and E. Water Resources Institute," Task Comm. Stand. Ref. ASCE Stand. Ref. evapotranspiration equation. Reston, Va. Am. Soc. Civ. Eng., 2005.
- [11]. N. Z. Al-Rawahi, Y. H. Zurigat, and N. A. Al-Azri, "Prediction of hourly solar radiation on horizontal and inclined surfaces for Muscat/Oman," *J. Eng. Res.*, vol. 8, no. 2, pp. 19–31, 2011.
- [12]. P. T. Nastos, A. G. Paliatsos, K. V. Koukouletsos, I. K. Larissi, and K. P. Moustris, "Artificial neural networks modeling for forecasting the maximum daily total precipitation at Athens, Greece," *Atmos. Res.*, vol. 144, pp. 141–150, Jul. 2014.
- [13]. K. P. Moustris, I. C. Ziomas, and A. G. Paliatsos, "3-Day-Ahead Forecasting of Regional Pollution Index for the Pollutants NO₂, CO, SO₂, and O₃ Using Artificial Neural Networks in Athens, Greece," *Water, Air, Soil Pollut.*, vol. 209, no. 1–4, pp. 29–43, Aug. 2009.



Macro and Micro Modeling of the Unreinforced Masonry Shear Walls

Sedat Kömürçü^{1*}, Abdullah Gedikli¹

¹Istanbul Technical University, Department of Civil Engineering, 34469, Maslak/Istanbul, Turkey.

*Corresponding Author email: komurcus@itu.edu.tr

Abstract

Masonry structures are constructed by joining masonry units (brick, stone, marble etc.) with mortar. Various methods are used for modeling of masonry walls of the structures. Micro modeling and Macro modeling are two diverse modeling techniques. In this study, these two modeling strategies are analyzed on a solid unreinforced masonry shear wall numerically. The models are implemented in ANSYS software to simulate the structural behavior of a tested wall in literature. The homogenization technique is applied to obtain the material parameters used in the macro model. Brick and mortar are modelled separately in the micro model. Stresses occurring in the walls under the effect of in-plane loads are investigated. The propagations of the cracks on the walls are analyzed numerically. The results obtained in the micro modeling and macro modeling are in consistent with the experimental study in the literature. However, macro modeling and micro modeling represent strictly disparate behavior in the material identification, and crack propagations.

Key words

Crack, Macro, Masonry, Micro

1. INTRODUCTION

Masonry structures are the first structures of the history and have a significant place among all the structures. There are many masonry monumental structures in the world such as buildings, palaces, bridges and towers. Modeling of the masonry structures has become a significant requirement to evaluate the strengths of existing masonry structures and to build modern masonry structures. Modeling of the masonry walls is a challenging issue because of their composite structures. There are several modeling techniques for modeling of walls constituting the masonry structures. Macro modeling and micro modeling are two different technique for modeling of masonry structures. In this study, the macro modeling and micro modeling techniques are investigated on the masonry walls. Masonry walls are modelled and analyzed to determine the fracture mechanisms of the walls. In-plane behaviors of unreinforced masonry walls are analyzed numerically.

Engineers and architects have worked to determine the in-plane effects on the masonry walls throughout the history. The effects of tension, pressure and shear on the masonry walls have been investigated by many scientists. The researchers used macro and micro modeling techniques to model the masonry walls. Masonry units and mortar are modelled as a single material in the macro modeling technique. The macro modeling technique was studied in [1] and [2]. Masonry units, mortar and interfaces are modelled separately in the micro modeling technique. The micro modeling technique was used in studies [3] and [4]. Lourenço made extensive work on modeling masonry structures using micro and macro modeling techniques [5], [6]. Oller were studied on the numerical modeling of masonry walls [7]. Many scientists have continued to model masonry walls.

2. MACRO AND MICRO MODELING

The main goal in modeling is to produce a model that behaves close to the real structure. The modeling of the masonry walls requires more care than other constructions because of the different characteristic of the masonry units and mortar. Various methods are used in the modeling of masonry structures. Masonry structures can be generally modelled as heterogeneous and homogeneous models. Detailed micro and simplified micro models are heterogeneous models. Macro modeling technique is known as homogeneous modeling technique. The modeling techniques diagram is shown in Figure 1.

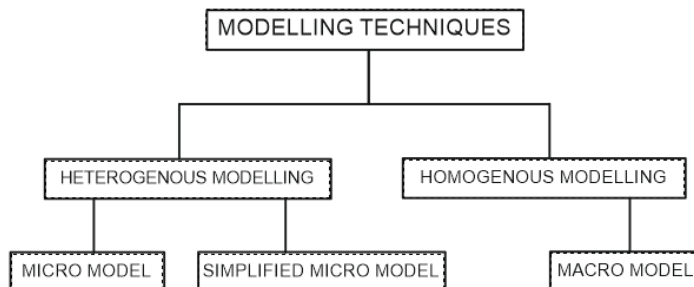


Figure 1. Modeling techniques for masonry walls

2.1. Macro Modeling

In macro modeling technique, masonry units (bricks, stone units), and the mortar between them are modelled as a single material. Application of the macro modeling technique is shown in Figure 2. Masonry walls are composite structures that can be homogenized using advanced techniques according to the macro modeling technique. It is beneficial to use elementary masonry wall parts which periodically repeat themselves on the wall in order to model the masonry walls by homogenization.

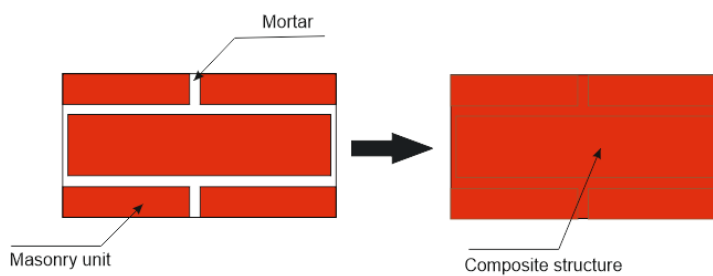


Figure 2. Macro modeling procedure

2.2. Micro Modeling

In micro technique, masonry units (brick, stone, etc.) and the mortar are modelled separately. Interfaces in the joining areas of these elements can be also included in the model. The micro modeling is shown in Figure 3. Although modeling of structures with micro modeling technique is a detailed process, local behavior of the structures can be investigated with this technique.

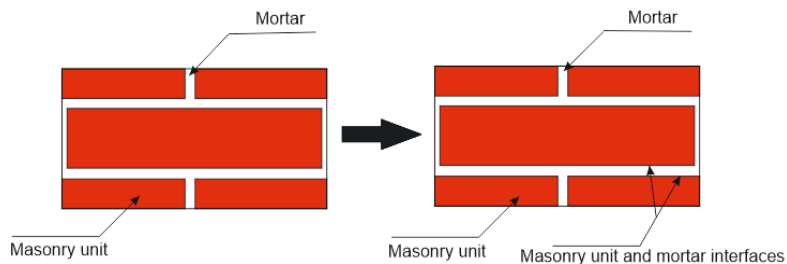


Figure 3. Micro modeling procedure

3. FINITE ELEMENT MODELS OF MASONRY WALLS

In this study, finite element analysis was performed by using micro and macro modeling techniques on unreinforced masonry walls. Experimental study was used in the literature for numerical analysis [8]. The geometry of the masonry wall and the masonry unit used at the wall are shown in Figure 4. The wall is loaded in two steps. In the first load step, the wall was loaded with a vertical pressure of 0.3 MPa to top nodes of the wall. In the second load step, horizontal displacement is given to the top nodes of the walls. The first load step is implemented by dividing by 10 equal sub-steps. The second load step is divided into 40 sub-steps.

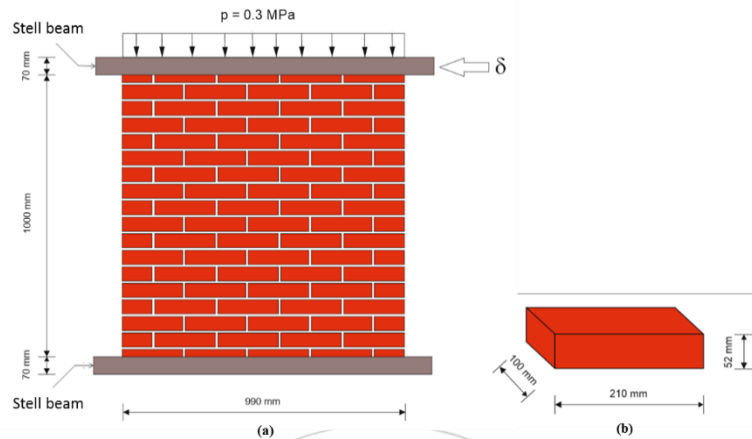


Figure 4. (a) Masonry wall geometry (b) masonry unit used in the wall

SOLID 65 finite elements in the ANSYS software was used for the finite element analysis. This element has 8 node points and each node point has 3 displacement degree of freedom in x, y and z directions. It can show collapse mechanisms both tensile and compression. Brittle materials can be modelled such as rock, stone, brick, concrete etc. This element is suitable for modeling of nonlinear behavior of structures and cracks can be determined in the structure. The structure of the SOLID 65 element is shown in Figure 5.

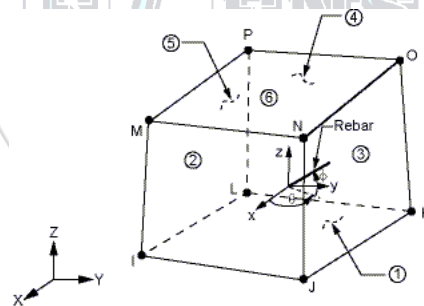


Figure 5. SOLID 65 element

Concrete material is used for the nonlinear analysis on the masonry walls. Typical Stress-strain curve of the concrete material is shown in Figure 6. Crack distribution on the wall under in-plane loading can be determined with this material model.

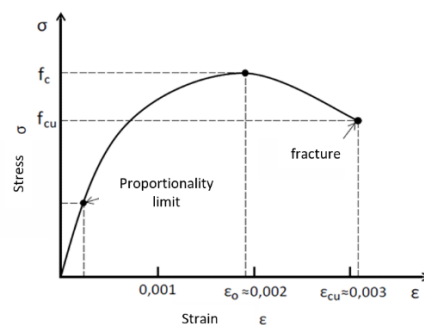


Figure 6. Typical stress-strain diagram of the Concrete material

Material parameters used in the models are shown in Table 1. Brick and mortar material parameters were implemented to micro finite element model. But, wall material parameters were obtained with homogenization of the masonry wall and were implemented to the macro finite element model.

Table 1. Material properties

Material	Modulus of Elasticity [MPa]	Poisson's Ratio	Tensile Strength [MPa]	Compressive Strength [MPa]
Brick (Micro)	16700	0,15	2	10,5
Mortar (Micro)	780	0,15	0,25	3
Wall (Macro)	3655	0,15	0,25	9

In the numerical analysis, the Willam-Warnke fracture hypothesis is used for nonlinear behavior of the masonry wall. Three-dimensional fracture surface and two-dimensional fracture surface for Willam-Warnke hypothesis is shown in Figure 7. Willam-Warnke hypothesis is a suitable hypothesis for materials having different compressive strength and tensile strength such as masonry materials. Masonry materials usually have high compressive strength and low tensile strength.

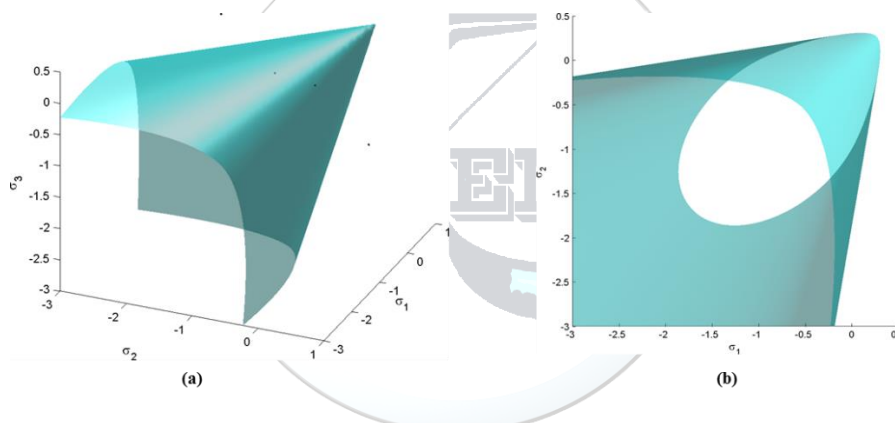


Figure 7. Willam-Warnke fracture surfaces: (a) Three dimensional space (b) Two dimensional plane

3.1. Macro Finite Element Model

In ANSYS software the geometry of the masonry wall was created by using the macro modeling technique. Masonry units and mortar were produced as a single material. Figure 8 shows the geometry and the finite element mesh of the masonry macro model. Refined mesh distribution was used in the models to investigate the crack distributions well.

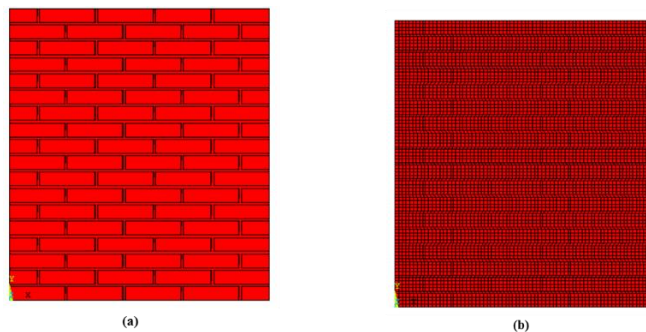


Figure 8. (a) Geometry of the wall (b) finite element mesh of the masonry macro model

Total displacement at the end of the 1. load step, minimum principal stresses at the end of the 1. load step, minimum principal stresses at $\delta=1$, total displacement at $\delta=1$ mm and shear stresses at $\delta=1$ mm are shown in Figure 9. Continuous stress distribution is determined between the bricks and mortar.

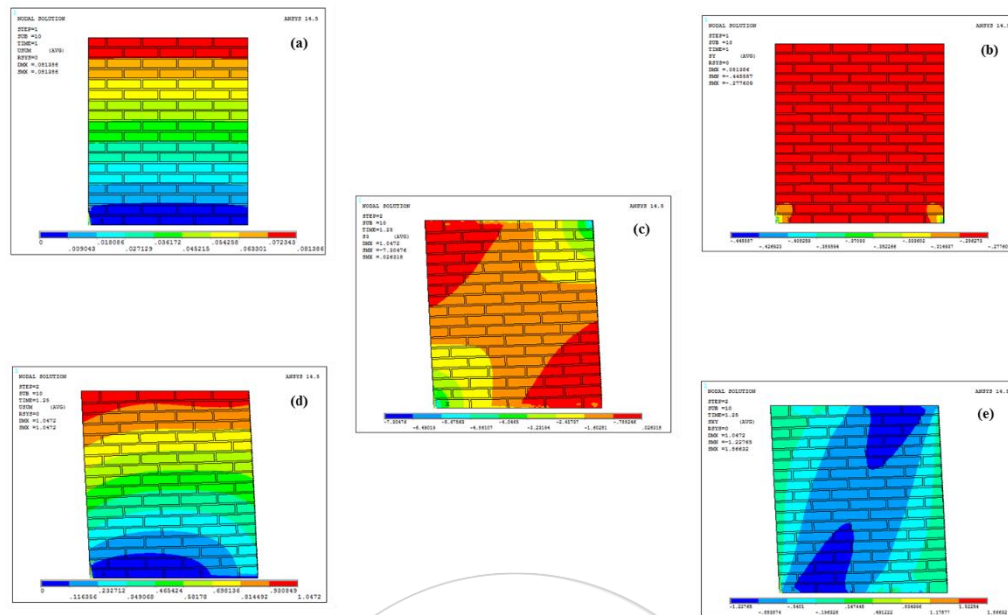


Figure 9. Macro model: (a) total displacement at the end of the 1. Load step, (b) minimum principal stresses at the end of the 1. Load step, (c) minimum principal stresses at $\delta=1$, (d) total displacement at $\delta=1$ mm, (e) shear stresses at $\delta=1$ mm

The crack distribution of the unreinforced masonry wall from $\delta=0.1$ mm to $\delta=1$ mm is given in Figure 10. Continuous cracks are obtained with the macro modeling technique according to finite element analysis.

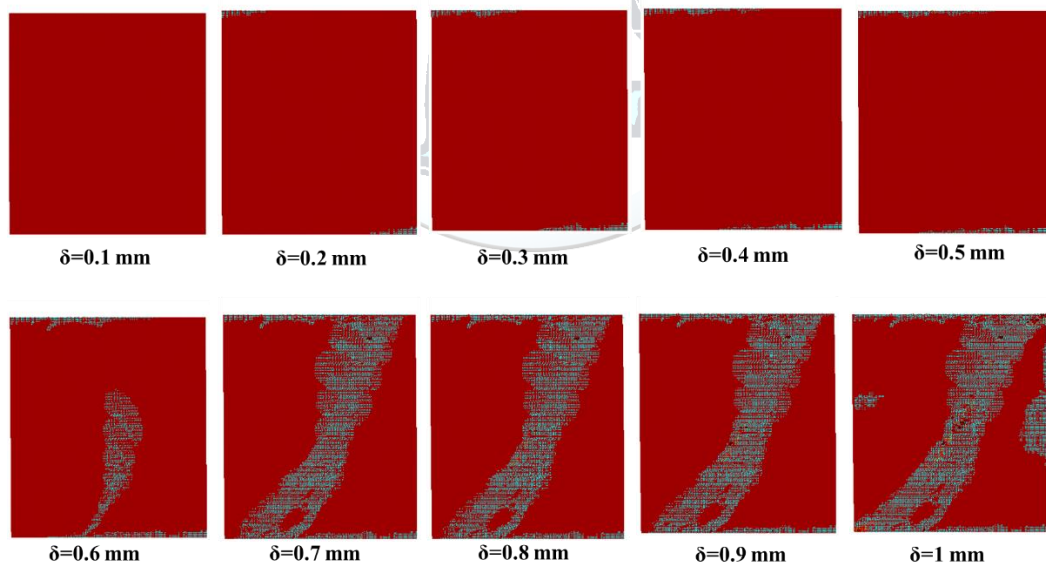


Figure 10. Crack distribution at the end of the macro modeling

It is seen that the cracks first started from the upper left and lower right corners of the wall. Next, diagonal cracks occur on the wall.

3.2. Micro Finite Element Model

Geometry of the model and finite element mesh were produced with the micro modeling technique. In this technique bricks and mortar are modelled separately. The same mesh distribution was used with the macro model. Figure 11 indicates the geometry and the finite element mesh of the micro model.

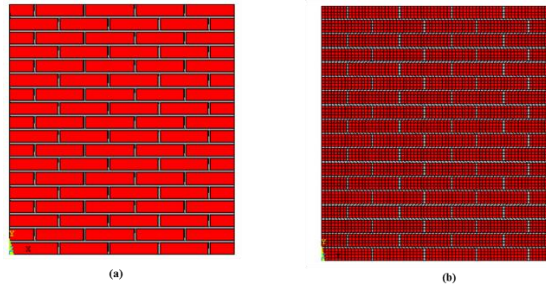


Figure 11. (a) Geometry of the wall (b) finite element mesh of the masonry micro model

Total displacement at the end of the 1. load step, minimum principal stresses at the end of the 1. load step, minimum principal stresses at $\delta=1$, total displacement at $\delta=1$ mm and shear stresses at $\delta=1$ mm according to finite element analysis are shown in Figure 12.

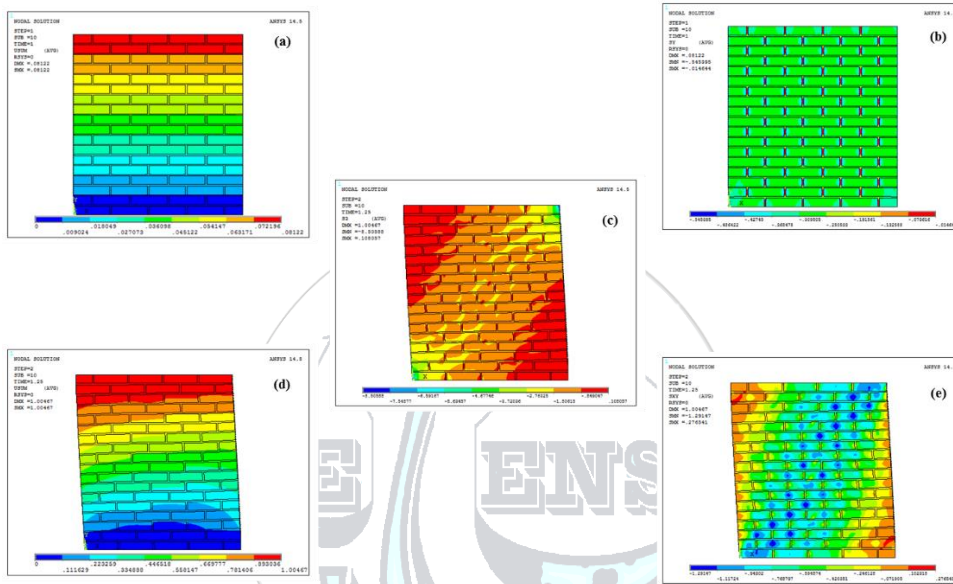


Figure 12. Micro model: (a) total displacement at the end of the 1. Load step, (b) minimum principal stresses at the end of the 1. Load step, (c) minimum principal stresses at $\delta=1$, (d) total displacement at $\delta=1$ mm, (e) shear stresses at $\delta=1$ mm

The crack distributions of the unreinforced masonry wall are given from $\delta=0.1$ mm to $\delta=1$ mm in Figure 13.

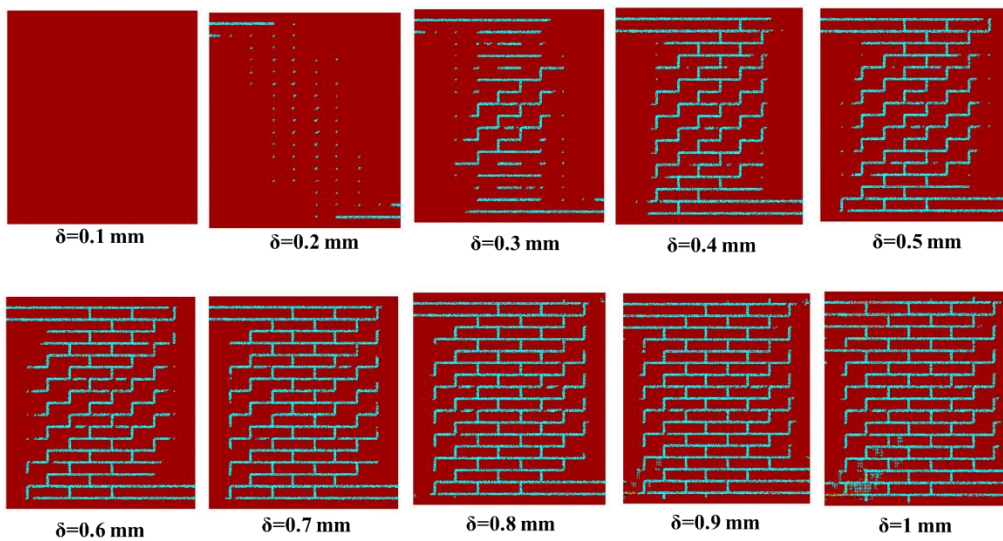


Figure 13. Crack distribution at the end of the micro modeling

It is seen that the cracks first started from the upper left and lower right corners of the wall. Next, cracks in the mortar areas spread all over the wall because of low tensile strength of the mortar areas.

4. RESULTS AND DISCUSSION

In this study, an unreinforced masonry wall was modelled and analyzed using finite element method. Stresses and strains on the wall were determined after the analysis. In addition, the cracks were investigated step by step. The reason of the cracks can be explained in terms of internal effects. Figure 14 shows the reasons of the cracks on the unreinforced masonry wall. Firstly, horizontal cracks that occur in the upper left and lower right parts of the wall shown with number (1) are tensile or shear cracks. Secondly, the cracks that occur in the upper right and lower left parts of the wall shown with number (2) are compressive cracks. Next, the diagonal cracks that occur in the middle region of the wall are represented by number (3) are caused by multiple influences.

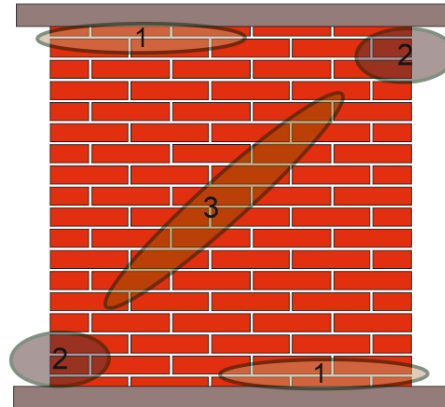


Figure 14. The reasons of the cracks on the masonry

Horizontal displacement of the top of the wall and horizontal reaction force of the wall diagram is shown in Figure 15. There are four different diagrams in the figure. Two of them shows numerical analysis and the other two diagrams shows the experimental results in the literature. It is seen that, the models have similar behavior until reaching the wall collapse state but the concrete material suddenly lost its strength in numerical analysis.



Figure 15. Load – displacement curves of the wall after the analysis

5. CONCLUSION

In micro modeling technique, masonry unit and mortar material properties are added to each model separately. However, single material parameters are used as an average property for masonry unit and mortar in macro modeling technique. In addition, the walls modelled by macro and micro methods represent consistent results with the experimental work, but does not fully reflect the post-peak behavior due to the concrete material property. While the micro modeling technique is suitable for small scale structures, the macro modeling technique is suitable for large-scale structures. Because the micro modeling technique requires more time, effort and computer capacity. Discrete cracks occur with using micro modeling technique. However, continuous cracks can be investigated with using macro modeling technique. Studies have been continued to model and analyze masonry walls.

ACKNOWLEDGMENT

This research has been supported financially by the ITU scientific research projects unit.

REFERENCES

- [1]. R.D. Quinteros, S. Oller, L.G. Nallim, “Nonlinear homogenization techniques to solve masonry structures problems,” *Composite Structures.*, vol. 94, pp. 724–730, 2012.
- [2]. H.O. Köksal, B. Doran, A.O. Kuruscu, A. Kocak, “Elastoplastic finite element analysis of masonry shear walls,” *KSCE Journal of Civil Engineering.*, vol. 20, pp. 784-791, 2016.
- [3]. J. Idris, M. Al Heib, T. Verdel, “Masonry Joints Mechanical Behavior Evolution in Built Tunnels,” *Tunneling and Underground Space Technology.*, vol. 24, pp. 617-626. 2009.
- [4]. M. Bolhassani, A.A. Hamid, A.C.W. Lau, F. Moon, “Simplified micro modeling of partially grouted masonry assemblages,” *Construction and Building Materials*, vol. 83, pp. 159-173 September 2015.
- [5]. Lourenço, “Computational Strategies For Masonry Structures” Doctoral dissertation, Delft University of Technology, The Netherlands, 1996.
- [6]. P.B. Lourenço, J.G. Rots, J. Blaauwendraad, “Two Approaches for the Analysis of Masonry Structures: Micro and Macro-Modeling,” *Heron*, vol. 40, 1995.
- [7]. S. Oller, *Numerical Simulation of Mechanical Behavior of Composite Materials*, Barcelona, Spain, Springer, 2014.
- [8]. A.Th. Vermeltoort, T.M.J. Raijmakers, “Deformation controlled meso shear tests on masonry piers,” The Netherlands: Building and Construction Research, Eindhoven, Report B-92-1156, TNO-BOUWRU, 1992.





Influence of Pouring Temperature on The Formation of Spheroidal and Lamellar Graphite In Cast Iron

Mehmet Ekici^{1*}, Uğur Öz Saraç²

¹ *Yalova University, Vocational School of Yalova, Yalova, Turkey*

² *Sakarya University, Technology Faculty, Department of Metallurgical and Materials Engineering, Sakarya, Turkey*

**Corresponding Author email: mekici@yalova.edu.tr*

Abstract

The objective of this research is to investigate the effect of pouring temperature on the microstructure of the cast iron. The pattern was designed with 300 mm of width and the thickness variations are 25 mm and poured at five different temperatures; 1300, 1325, 1350, 1375 and 1400°C. Several cast irons, prepared with different chemical compositions and microstructures (three lamellar and three spheroidal structures) have been examined by extensive mechanical testing and optical microscopy. The fluidity of spheroidal and lamellar graphite in cast iron increases with the pouring temperature. The numbers of nodules were decreased by increasing pouring temperature for spheroidal structures. Whereas, the numbers of flakes of lamellar structures changed by both pouring temperature and chemical composition. In general, with increasing pouring temperature, the amount of pearlite in the internal structure of both lamellar and spheroidal graphite cast iron materials were increased.

Key words

Spheroidal and lamellar graphite cast iron, pouring temperature, tensile test, impact test

1. INTRODUCTION

Cast iron has been widely used in dies for automobile panel, high strength steel pipes, etc., due to its excellent mechanical properties, wear resistance, heat resistance and simple production, low production cost[1-2]. With the development of sheet metal technology, the forming pressure and speed increased significantly. Wear is one of the important failure patterns for the moving mechanics parts[3]. The quality of the lost foam casting is influenced by many parameters. These parameters such as the pouring temperature, the size of the quartz sand, the density of polystyrene foam, the vibration duration, the casting size and the material composition. The higher of superheat will decrease the surface tension of liquid metal [4]. The pouring temperature has the dominant factor in determining the value of tensile strength and elongation of the casting [5]. The gas formed increases 230 % at the temperature of 750- 1300 °C [6]. The flow rate of metal alloys at high temperature will decrease with temperature because of increasing the gas volume [7]. The metal flow rate increases with temperature up to 1150 °C [8]. The thickness increasing of the pattern will be able to increase the length of metal flow [9].

2. EXPERIMENTAL STUDIES

In this study, a medium frequency induction furnace was used to produce spheroidal and lamellar graphite cast iron. The spheroidal cast iron experimental alloys were made with a constant mix of 45% cast iron scrap and

55% steel scrap of chemical compositions. The lamellar graphite cast iron experimental alloys were made with a constant mix of 40% H₂ pig iron and 60% steel scrap of chemical compositions. The charge materials, including the chemical compositions and percentages used for the production, are listed in Table 1. After spheroidisation and inoculation the molten iron was poured into Y type permanent mold given in Table 2. The pattern was designed with 300 mm of width and the thickness variations are 25 mm and poured at five different temperatures; 1300, 1325, 1350, 1375 and 1400°C.

Table 1. Details of the charge materials

Item	%C	%Si	%Mn	%S	%P	% Percentage
H ₂ Pig iron	3.95	1.55	0.65	0.06	0.02	40
Ductile cast iron	4.15	0.85	0.06	0.01	0.04	45
Steel scrap	0.10	0.19	0.66	0.02	0.02	55-60

Table 2. The chemical composition of inoculation and spheroidizing

Item	%Si	%Al	%Mg	%Ba	%Ca	Particle Size, mm
Inoculant (FeSi75)	65–75	0.5–1.5	-	2–3	1–2	0.6-3
Spheroidizer	42–48	1	6–7	-	0.8–1.2	1–10

Three cast lamellar graphite cast irons with different pouring temperature were selected as the specimens. In this study, GLJ-A, GLJ-B and GLJ-C were selected as the specimens. Three cast spheroidal graphite cast irons with different pouring temperature were selected as the specimens. In this study, GJS-A, GJS-B and GJS-C were selected as the specimens. Spheroidal and lamellar graphite cast iron with chemical compositions listed in Table 3 was prepared. The carbon equivalent (CE) value was defined by:

$$CE = \text{mass \% C} + 1/4 \text{ mass \% Si} + \text{mass } 1/2 \% \text{ P}$$

Table 3. Chemical compositions of the samples (mass %)

Sample	C	Si	Mn	P	S	Cr	Ni	Cu	Ceş
GJL - A	3.20	2.15	0.69	0.04	0.09	0.08	0.05	0.10	3.76
GJL - B	3.30	2.05	0.69	0.03	0.10	0.29	0.51	0.24	3.83
GJL - C	3.06	2.12	0.70	0.05	0.10	0.19	0.06	0.55	3.62
GJS - A	3.68	2.26	0.14	0.02	0.01	0.02	0.02	0.04	4.26
GJS - B	3.56	2.38	0.32	0.02	0.01	0.05	0.03	0.10	4.17
GJS - C	3.46	2.15	0.38	0.02	0.01	0.17	0.09	0.44	4.01

3. RESULTS AND DISCUSSION

In this study were investigated characteristic and mechanical properties of lamellar and spheroidal graphite cast iron materials which produced in different compositions and at different casting temperatures. The variation in the number of flaks and phase amounts of the materials in the flaky cast iron with flake graphite is shown in

Figure 1-2 and in graphite nodule number and size and phase in the spheroidal graphite cast iron materials is shown in Figure 3-4.

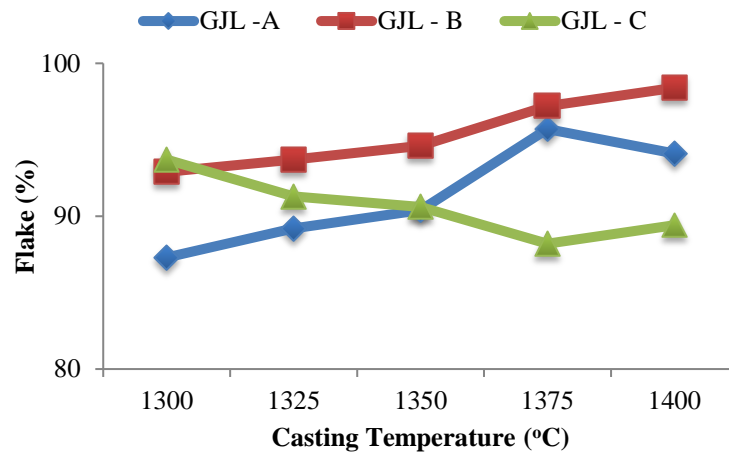


Figure 1. Change in flux amount of flake graphite cast iron materials depending on casting temperature

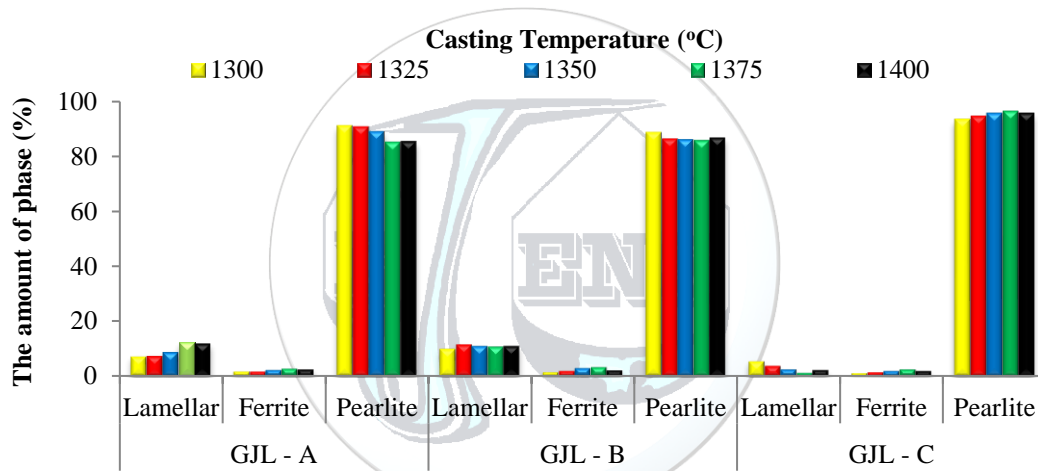


Figure 2. Change in phase amounts of casting temperature in cast iron depending on with lamel graphite

As shown in Figures 1 and 2 above, the number of flakes of casting temperature residue materials in GJL-A and GJL-B specimens in lamellar graphite cast iron has increased. However, the number of flaks appears to decrease in the GJL-C sample. In addition, the amount of lamellar phase of the samples showed an increase in the GJL-A and GLJ-B samples with increasing casting temperature, but the amount of perlite phase decreased. On the GJL-C sample, the amount of lamellar phase decreased with increasing casting temperature, but the amount of perlite phase increased.

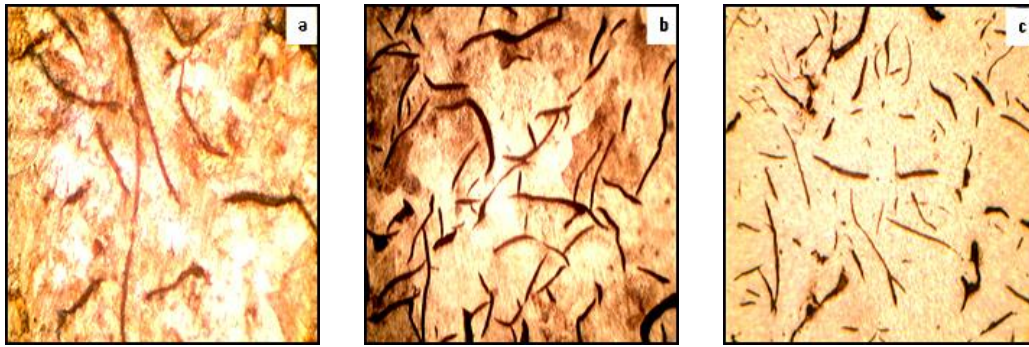


Figure 3. Microstructure drawings of specimens of lamellar graphite cast iron produced at a casting temperature of 1350°C (x200) a) GJL-A b) GJL-B c) GJL-C

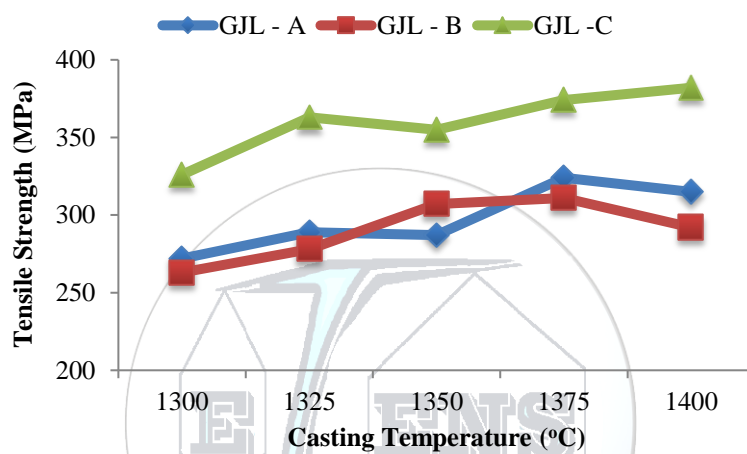


Figure 4. Tensile strength results of lamellar graphite cast iron materials produced at different casting temperatures

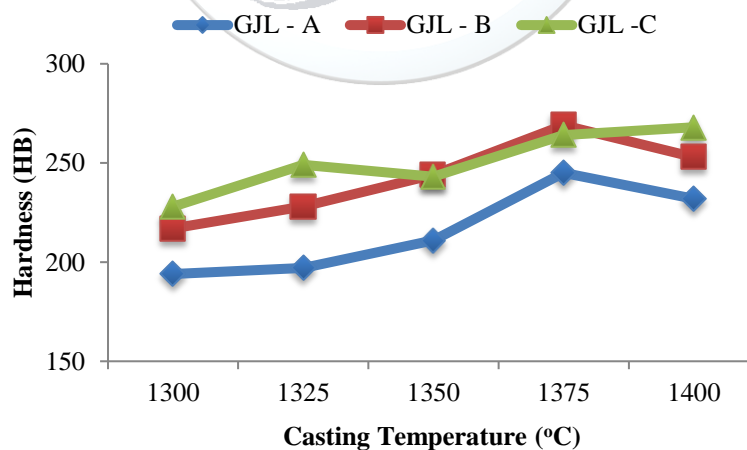


Figure 5. Hardness results of lamellar graphite cast iron materials produced at different casting temperatures

When the tensile strength and hardness results of lamellar graphite cast iron materials are examined, it has been observed that with increasing casting temperature, the tensile strength and hardness values of the samples generally increase. However, the strength properties of samples with a casting temperature of 1400 °C showed a slight decrease.

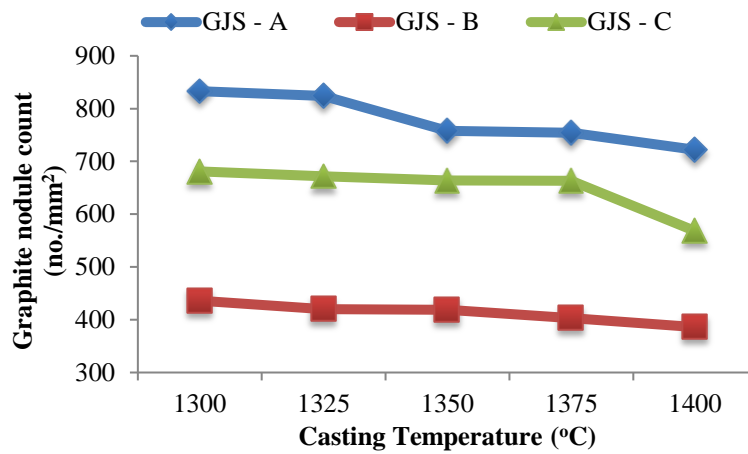


Figure 6. Change in nodule quantity of spheroidal graphite cast iron samples depending on casting temperature

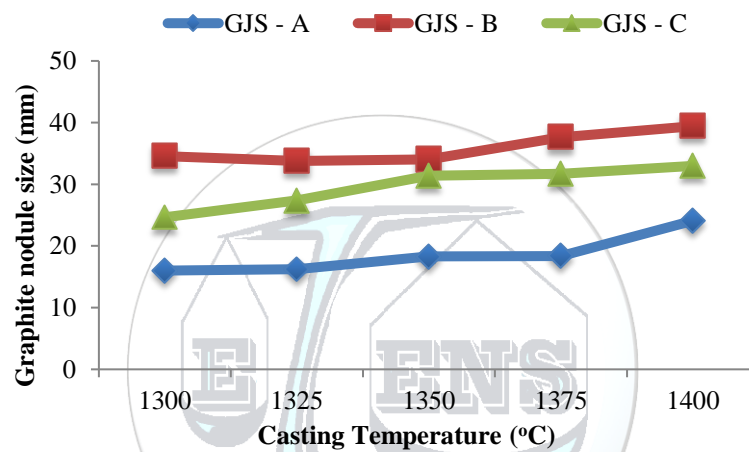


Figure 7. Change in nodule size of spheroidal graphite cast iron samples depending on casting temperature

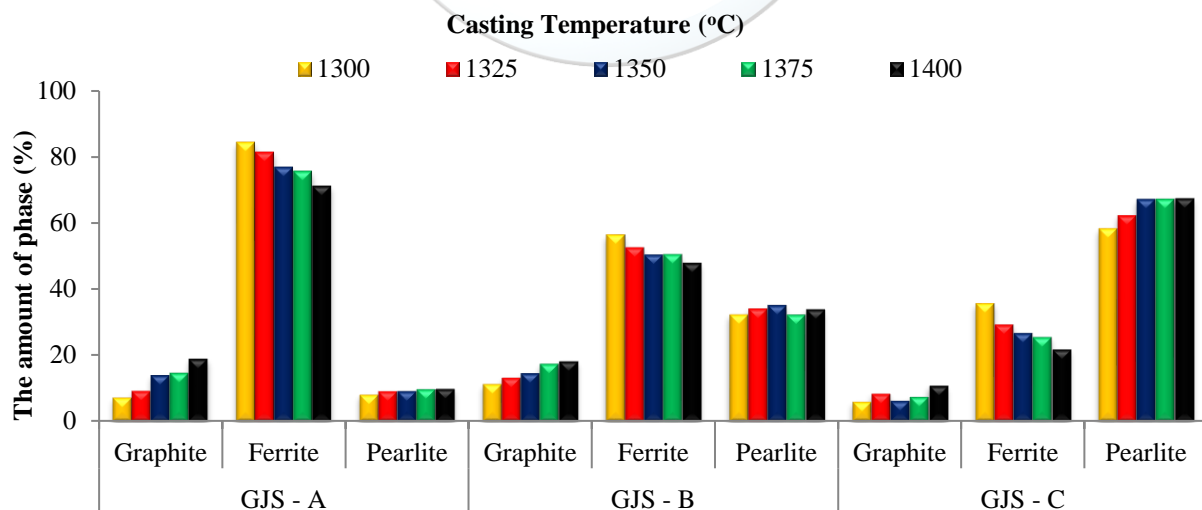


Figure 8. Change in phase amounts of casting temperature in cast iron depending on with spheroidal graphite

In spheroidal graphite cast irons, as shown in Figures 5 and 6, the amount of graphite nodule decreases with increasing casting temperature. However, graphite nodule size has been observed to increase with increasing casting temperature. With the increase in the casting temperature in the spheroidal graphite cast irons, an

increase in the amount of graphite phase was observed, but the amount of ferrite phase decreased. The amounts of perlite phases in the samples generally did not change.

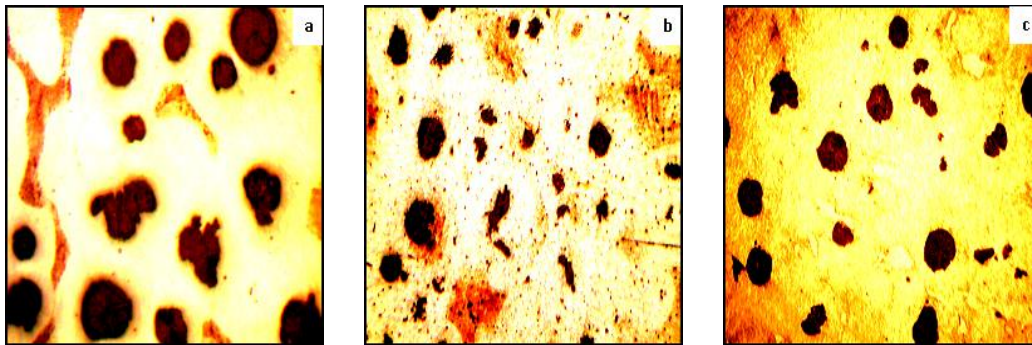


Figure 9. Microstructure drawings of spheroidal graphite cast iron specimens produced at casting temperature 1325°C a) GJS-A (x200), b) GJS-B (x100), c) GJS-C(x200)

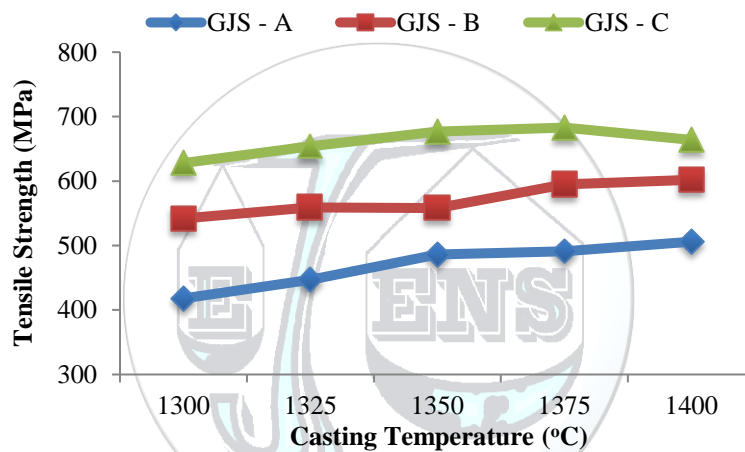


Figure 10. Tensile strength results of spherical graphite cast iron materials produced at different casting temperatures

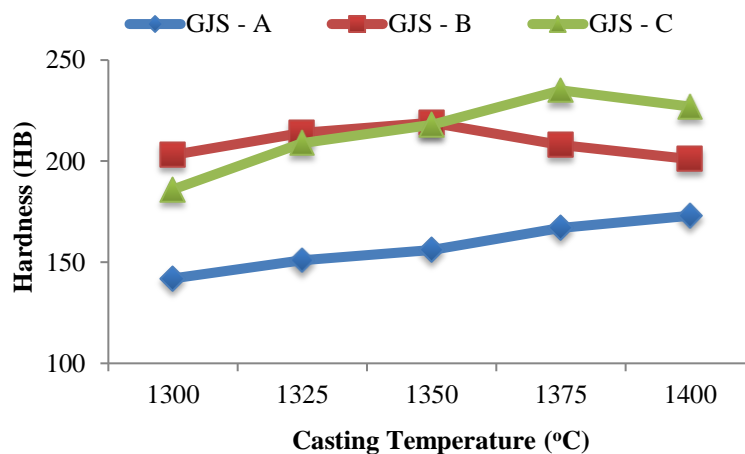


Figure 11. Hardness results of spherical graphite cast iron materials produced at different casting temperatures

When the tensile strength and hardness results of spherical graphite cast iron materials are examined, it has been observed that increase in tensile strength and hardness values of the samples are generally observed when the

increase in the casting temperature. However, the casting temperature of the GJS-B coded sample showed a decrease in hardness value after 1350°C.

4. CONCLUSION

The results obtained from the materials produced by adjusting the casting temperature between 1300 °C and 1400 °C in lamellas and spheroidal graphite cast irons with different chemical compositions are summarized below.

1. When the microstructure and mechanical properties of the materials produced at different casting temperatures are examined, it has been understood that setting the casting temperature of the lamellar graphite cast iron materials at 1325 °C to 1350 °C is suitable for the materials to be produced in the specified composition. However, it has been found that for the graphite cast iron material with the chemical composition code GJS-A, the casting temperature is higher than 1400 °C and for GJS-B and GJS-C coded samples it is set to 1350 °C to 1375 °C.
2. For lamellar graphite cast iron, the general microstructure was found to be of type A 1 according to ASTM A247, but with increasing casting temperature and an increase in the size of GJS-B coded observed.
3. In the case of the increase of the casting temperature spheroidal graphite cast irons, the decrease of the number of nodules have occurred. As a result, the amount of ferrite phase in the microstructure decreased and the amount of perlite and graphite phase increase observed.

REFERENCES

- [1]. S Z. L. Lu, Y. X. Zhou, Q. C. Rao, Z. H. Jin, *J. Mater. Process. Technol.* 116, 176-181, 2001
- [2]. L. Ribeiro, A. Barbosa, F. Viana, A. Monteiro, Baptista, C. Dias, C. A. Ribeiro, *Wear* 270, 535-540, 2011
- [3]. Z. R. Yang, D. S. Li, S. Q. Wang, M. X. Wei, *J. Iron Steel Res. Int.* 20 No.10, 81-86, 2013
- [4]. S. Kumar, P. Kumar, H. S. Shan, Effect of Evaporative Pattern Casting Process Parameters on the Surface Roughness of Al-7% Si Alloy Casting. *Journal of Materials Processing Technology.* 182, 615-623, 2007
- [5]. S. Kumar, P. Kumar, H. S. Shan, Optimization of Tensile Properties of Evaporative Casting Process Through Taguchi's Method. *Journal of Materials Processing Technology.* 204, 59-69, 2008
- [6]. X. Yao, S. Shivkumar, Molding filling characteristics in lost foam casting process. *Materials science and Technology.* 31, 841-846, 1997
- [7]. M. Khodai, N. Parvin, Pressure Measurement and Some Lost Foam Casting in Observation. *Journal of Materials Processing and Technology.* 206,1-8, 2008
- [8]. S. Shivkumar, X. Yao, M. Makhlof, Polymer Melt Interactions During Formation in the Lost Foam Process. *Metallurgica et Materialia scripta.* 33, 39-46, 1995
- [9]. S. R. Shin, Z. H. Lee, Hydrogen Gas Pic-Up of Alloy During Lost Foam Casting Melt. *Journal of Materials Science.* 39, 1536-1569, 2004.



Determination of Appropriate Distribution Functions for the Wind Speed Data Using the R Language

Ismail Kirbas*

¹Mehmet Akif Ersoy University, Department of Computer Engineering, 15100, Merkez/Burdur, Turkey.

*Corresponding Author email: ismailkirbas@mehmetakif.edu.tr

Abstract

Accurate determination of the proper distribution and parameters of this distribution according to the wind characteristics of the zone is vital for wind energy investment. In determining a wind energy potential belonging to a region, meteorological wind speed measurements have a great proposition to take place within a certain statistical distribution. In our study, the wind speed data obtained from the metrology station within 1 year was evaluated and it was determined using the R language, which is an open source statistical programming language, which is better suited to distributions such as Weibull, gamma, lognormal and logistic. The Akaike Information Criterion and Schwarz-Bayesian Information Criterion (SBIC) scores were calculated as the performance parameters of the distributions and the distribution performances were compared graphically. While gamma and lognormal distributions have better results at low wind speeds, Weibull distribution achieves higher performance for higher wind speeds.

Key words

gamma, logistic, lognormal, R language, statistical distribution, Weibull, wind speed

1. INTRODUCTION

The use of renewable energy sources is increasing day by day in the production of electricity all over the world. Along with that, electricity generation from wind energy is getting more and more popular every day. The greatest difficulty of generating electricity from wind energy is the complexity of the dynamics that make up the wind and it is very difficult to predict in long term period [1]–[3].

Before the wind energy investments are made, it is necessary to make wind speed measurements related to the installation area. The long-term results obtained are analysed by using statistical methods. Weibull distribution is the most frequently used method in the analysis process. However, for places with low wind speeds, the success of the Weibull distribution remains relatively low [4]–[6].

In our study, wind speed measurements made by Antalya International Airport meteorological station between 2016 and 2017 were examined. The meteorological station records 30-min average wind speed data. However, the data obtained was converted into a 6-hour average in order to make the evaluation of the data easier. All operations on the wind data were performed using the R language and Rstudio software.

R programming language was originally written by Robert Gentleman and Ross Ihaka alumni members of the statistical department of the Auckland University in New Zealand. These two statisticians were influenced syllabically by S language which is written by Chambers, Becker and Wilson and the scheme language developed by Susman. Statisticians who have developed R language, have aimed to use open source software due to the high cost of licensing of other statistical package programs and software, and high cost of learning and teaching. Later R software developers from different parts of the world gave themselves the name "r core team". R software was published by "r core team" on 29 February 2000. Software that includes the open source code feature is used free of charge. R language is a generous medium for statistical calculations and graphs. It has the feature of data processing and storing and special operators that can be used in the calculations of data and especially matrices. It contains compatible and co-usable graphical tools that can be used for data analysis [7], [8].

The source code for R, which is part of the GNU project, is available under the GNU General Public License and is available for various operating systems. There are also various graphical user interfaces, although the R command uses a line interface. It provides a language and environment for data processing, classification, clustering, time-series analysis, classical statistical tests, linear and nonlinear modelling calculations and graphic display. Because it is open source, it is very prone to development [9].

In this study, gamma, log-normal and logistic distributions are used together with Weibull distribution which is widely used in the literature in determination of wind energy efficiency and they are graphically compared with Weibull distribution. In Figure 1, 6-hour average annual wind speed data is shown graphically. The data and the R codes used in this study can be accessed freely via the GitHub platform [10].

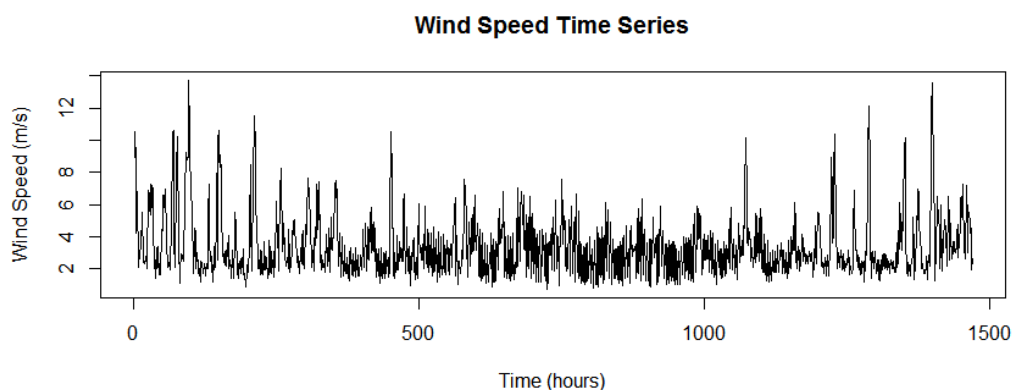


Figure 1. 6-hour average annual wind speed data from International Antalya Airport meteorological station.

Table 1 also gives some fundamental statistical information about collected data.

Table 1. Statistical results for wind speed data.

Statistical Calculation	Value
Average	3.3697
Standard Error Mean	0.0492
Standard Deviation	1.8858
Median	2.9200
Variance	3.5561
Skewness	1.7100
Kurtosis	3.8600
Range	12.980
Mode	2.4100
N for Mode	22
Maximum	13.720
Minimum	0.7400
Sum	4953.51
Quantity	1470

It is essential to use the correct statistical distribution model in assessing wind energy efficiency. In our study, firstly candidate models which are used in the literature have been determined in order to choose the best model. The comparative distributions were determined as Weibull, gamma, lognormal and logistic distributions. Since the Weibull distribution is the most commonly used model in wind energy analysis, the other models are compared one by one with the Weibull distribution. In the rest of our work, information about these distributions was given and mathematical and graphical comparisons were made using R language.

2. DISTRIBUTION MODELS

In this section, mathematical equations of Weibull, gamma, lognormal and logistic distributions are given and comparative performance ratios are graphically shown. In order to perform distribution analysis, fitdistrplus package is used in R language. In addition, ggplot and readr libraries are included for graphical drawings and reading data in csv format.

2.1. Weibull Distribution

The Weibull distribution, which is found by Professor Waloddi Weibull, has an important place in probability distributions. It is one of the most broadly used distributions in reliability analysis since it has the ability to characterize all the regions of the force curve. Weibull distribution is applied with two or three parameters according to the usage areas [11], [12]. Equation 1 gives Weibull probability distribution function with 3 parameters where γ is used for shape parameter, β for scale parameter and ω for location parameter.

$$f(x) = \frac{\gamma}{\beta} \left(\frac{x-\omega}{\beta} \right)^{\gamma-1} \cdot \exp \left(- \left(\frac{x-\omega}{\beta} \right)^{\gamma} \right), f(x) \geq 0, x \geq 0, \gamma > 0, \beta > 0, \omega \geq 0, \omega \leq x \leq \infty \quad (1)$$

Two-parameter Weibull probability distribution is obtained by taking $\omega = 0$ as shown in Equation 2.

$$f(x) = \frac{\gamma}{\beta} \left(\frac{x}{\beta}\right)^{\gamma-1} \cdot \exp\left(-\left(\frac{x}{\beta}\right)^\gamma\right), f(x) \geq 0, x \geq 0, \gamma > 0, \beta > 0 \tag{2}$$

This version of the Weibull distribution is used intensely, especially when information on wind distribution and variation in wind velocity are needed. The probability of this distribution is not symmetric but the skew is skewed and the distribution is indicated by shape and scale variables. The total likelihood of the area under this distribution equals to 1.

2.2. Gamma Distribution

In probability theory and statistical science, gamma distribution is a two-parameter continuous probability distribution. One of these parameters is the scale parameter θ ; and the other is called the shape parameter k . If k is an integer, the gamma distribution represents the sum of random variables with k exponential distributions.

$$f(x; k, \theta) = x^{\alpha-1} \frac{e^{-x/\theta}}{\theta^k \Gamma(k)}, x > 0, k > 0, \theta > 0 \tag{3}$$

Gamma probability distribution function is given in Equation 3 and cumulative gamma distribution function is shown in Equation 4.

$$F(x; k, \theta) = \int_0^x f(u; k, \theta) du = \frac{\gamma(k, x/\theta)}{\Gamma(k)} \tag{4}$$

Empirical and theoretical comparison for Weibull and gamma distributions is shown in Figure 2. According to histogram graph in Figure 2, gamma distribution fits data better than Weibull distribution.

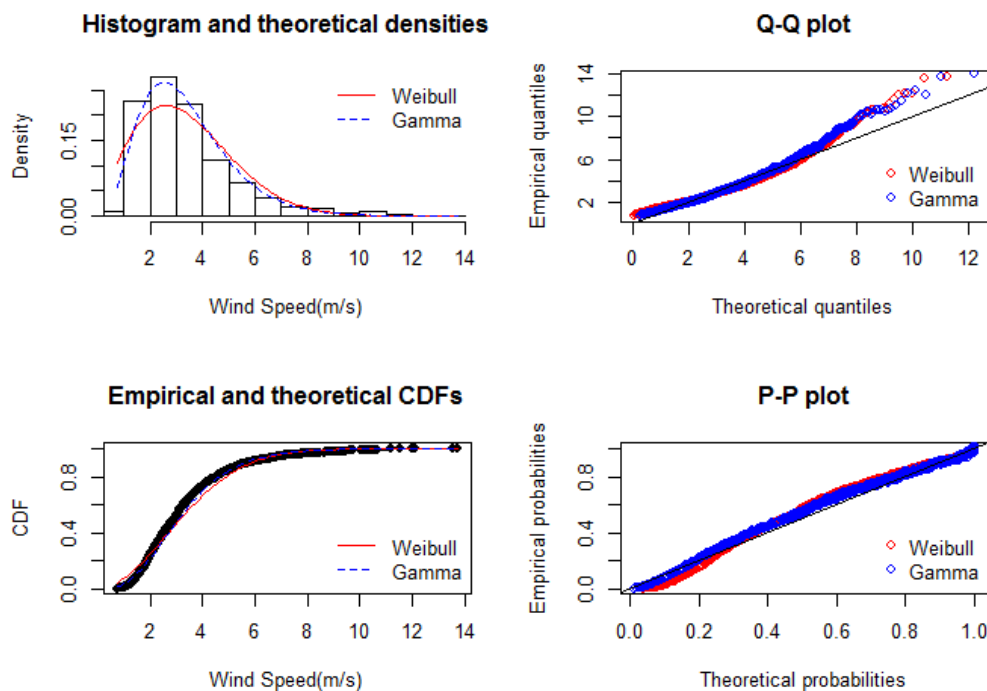


Figure 2. Empirical and theoretical comparison for Weibull and gamma distributions.

2.3. Log-Normal Distribution

Since the log-normal distribution can take many different forms, many data can be modelled by log-normal distribution. It is mainly used for economic production data and reliability analysis [13].

Log-normal probability distribution function is shown in Equation 5 and log-normal cumulative distribution function is located in Equation 6.

$$f(x) = \frac{1}{2\sigma} \cdot \frac{1}{\sqrt{2\pi}} \exp\left[-\frac{(\ln x - \mu)^2}{2\sigma^2}\right], x \geq 0 \tag{5}$$

$$F(x) = P(X \leq x) = P(\ln X \leq \ln x) = \int_{-\infty}^x f(t)dt = \Phi\left(\frac{\ln x}{\sigma\mu}\right) \tag{6}$$

Figure 3 depicts empirical and theoretical comparison for Weibull and lognormal distributions. According to histogram graph in Figure 3, lognormal distribution is more successful than Weibull distribution.

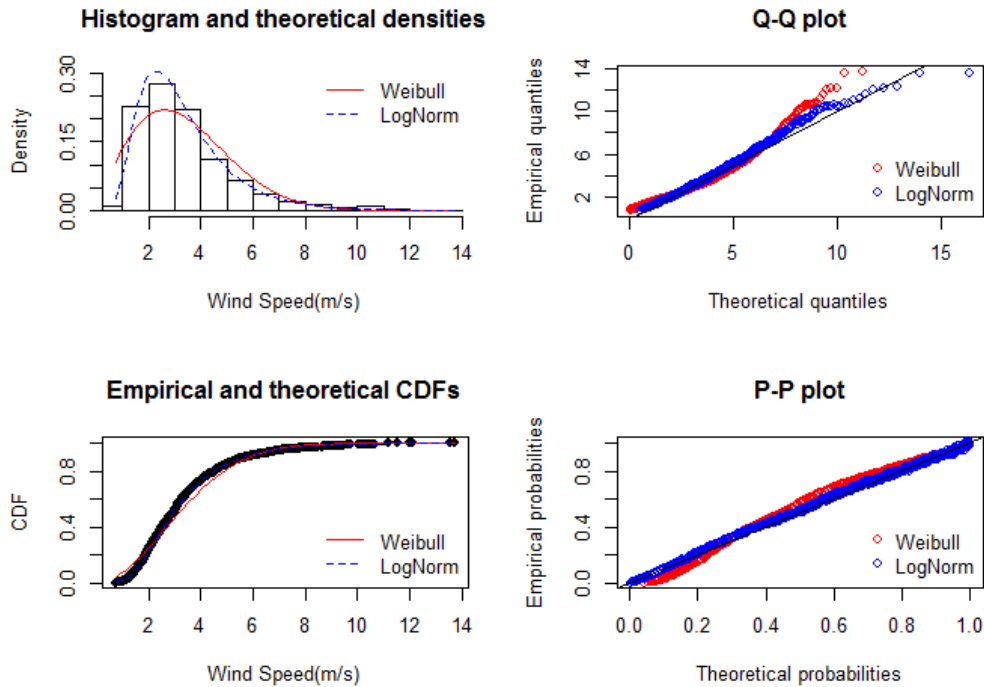


Figure 3. Empirical and theoretical comparison for Weibull and lognormal distributions.

2.4. Logistic Distribution

The logistic distribution function which is given in Equation 7 is a continuous probability distribution and also plays a role in the issues of feed-forward neural networks and logistic regression.

$$f(x; \mu, s) = \frac{e^{-\frac{x-\mu}{s}}}{s\left(1+e^{-\frac{x-\mu}{s}}\right)^2} = \frac{1}{4s} \operatorname{sech}^2\left(\frac{x-\mu}{2s}\right) \tag{7}$$

Cumulative distribution function can be seen in Equation 8 and, x is the random variable, μ is the mean, and s is a scale parameter proportional to the standard deviation.

$$F(x; \mu, s) = \frac{1}{1+e^{-\frac{x-\mu}{s}}} = \frac{1}{2} + \frac{1}{2} \tanh\left(\frac{x-\mu}{2s}\right) \tag{8}$$

Figure 4 shows theoretical and empirical comparison for Weibull and logistic distributions. Graphical results show that the Weibull distribution is more successful than the logistic distribution.

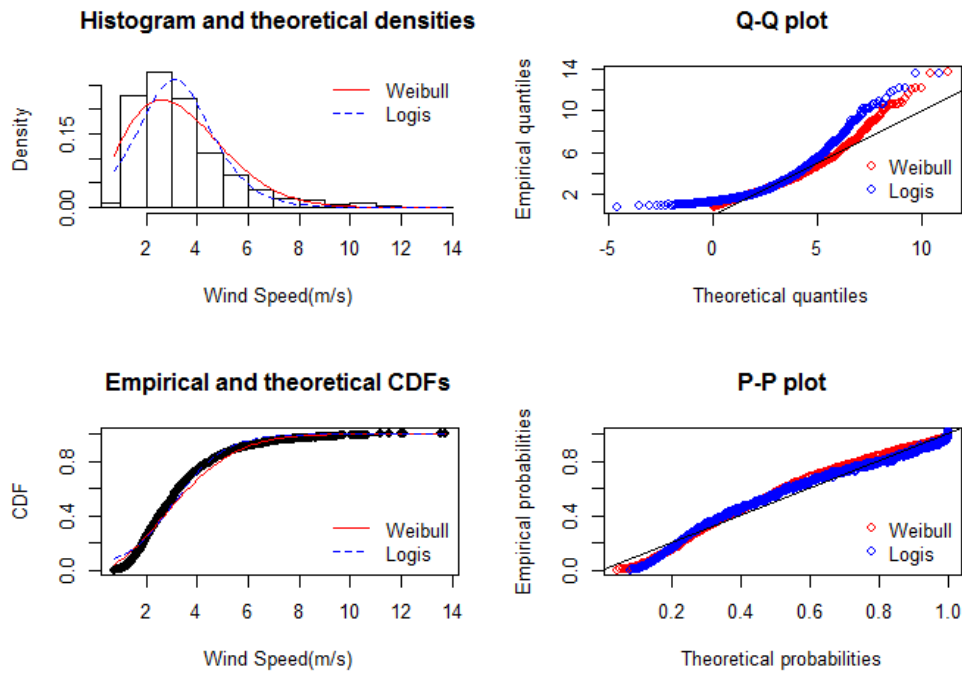


Figure 4. Empirical and theoretical comparison for Weibull and logistic distributions.

3. DISTRIBUTION EVALUATION

In literature, there are many statistical evaluation method to evaluate the developed models. In this study we choose Kolmogorov-Smirnov, Cramer-von Mises, Anderson-Darling, Akaike Information Criterion (AIC) and Schwarz-Bayesian Information Criterion (SBIC). Each model has been evaluated using the model evaluation methods given in Table 2 with the results obtained from the statistical model evaluations.

The Akaike information criterion (AIC) is a quality statistical relative model measure for a given set of data. When a collection of data models is given, the AIC relatively estimates each model quality. Therefore, the AIC provides a way to select the model. The Akaike criterion is based on information theory, the information given is the model data, the process is used to represent, and provides a relative estimation. Thus, the model's goodness of fit and model complexity can be understood. This criterion does not provide a model test for the null hypothesis test; If all candidate models are bad, they will not give any warning. The model with the lowest AIC value has the highest relative performance [2].

AIC value can be calculated using Equation 9 where k represents estimated number of parameters and L symbolize maximum value of the likelihood function for the model.

$$AIC = 2k - 2\ln(L) \quad (9)$$

The Bayesian Information Criterion (BIC) index imposes a penalty for increasing the number of parameters. Thus, it considers both the degree of statistical conformity and the number of parameters to be estimated. The BIC formula is given in Equation 10. Here, k denotes the number of parameters that are modelled, n represents the sample size, and finally L indicates the maximized log likelihood of the model.

$$SBIC = -2 \cdot \ln L + k \cdot \ln(n) \quad (10)$$

In Table 2, 4 different distribution models were compared according to 5 evaluation criteria and the best values were indicated as underlined.

Table 2. Distribution model evaluation results.

Metric	Weibull	Gamma	Logistic	LogNormal
Kolmogorov-Smirnov	0.0838	0.0581	0.0959	<u>0.0292</u>
Cramer-von Mises	3.736	1.581	2.942	<u>0.224</u>
Anderson-Darling	25.377	10.022	28.635	<u>1.546</u>
Akaike's Information Criterion	5661.043	5461.841	5841.270	<u>5350.209</u>
Bayesian Information Criterion	5671.629	5472.427	5851.856	<u>5360.795</u>

A histogram graph of 4 different distribution models is given in figure 5.

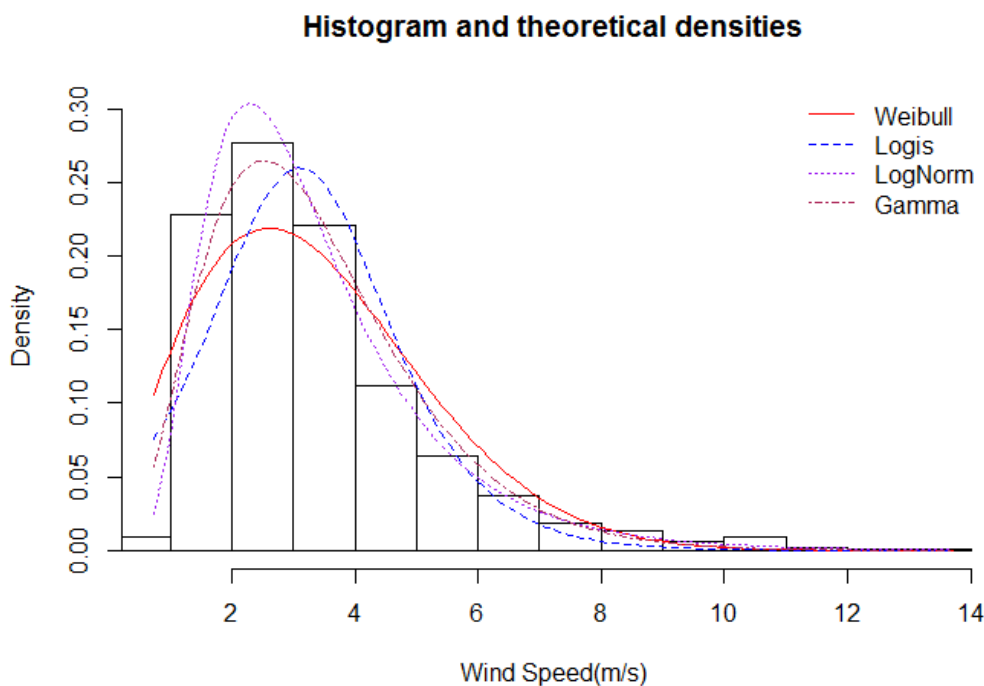


Figure 5. Graphical comparison of 4 different distribution models.

When model evaluation results in Table 2 and graphical representations in Figure 5 are evaluated together, it is seen that the most successful models for data used in the study are lognormal, gamma, Weibull and logistic distribution respectively.

4. CONCLUSION

In this study, four different distribution models were used when performing efficiency analysis before wind energy investment was made. 6-hour average wind speed data of the International Antalya Airport meteorological station was investigated as the case data. An open source software language, R, was used for statistical and graphical analysis.

The distribution models were compared according to 5 different evaluation criteria and their performance was evaluated in Table 2 and Figure 5 respectively. The results show that lognormal and gamma distributions give

better results than the Weibull distribution widely used in the literature for low wind speeds. The logistic distribution has shown the worst performance.

REFERENCES

- [1] I. Kirbas and A. Kerem, "Short-Term Wind Speed Prediction Based on Artificial Neural Network Models," *Meas. Control*, vol. 49, no. 6, pp. 183–190, 2016.
- [2] A. Kerem, I. Kirbas, and A. Saygın, "Performance Analysis of Time Series Forecasting Models for Short Term Wind Speed Prediction," presented at the International Conference on Engineering and Natural Sciences (ICENS), 2016, pp. 2733–2739.
- [3] P. Bhattacharya and R. Bhattacharjee, "A Study On Weibull Distribution For Estimating The Parameters," *J. Appl. Quant. Methods*, vol. 5, no. 2, pp. 234–241, 2010.
- [4] M. Kurban, Y. M. Kantar, and F. O. Hocoğlu, "Weibull Dağılımı Kullanılarak Rüzgar Hız ve Güç Yoğunluklarının İstatistiksel Analizi," *Afyon Kocatepe Univ. J. Sci.*, vol. 7, no. 2, pp. 205–218.
- [5] W.-Y. Chang, "A Literature Review of Wind Forecasting Methods," *J. Power Energy Eng.*, vol. 2, no. 4, pp. 161–168, 2014.
- [6] T. P. Chang, "Estimation of wind energy potential using different probability density functions," *Appl. Energy*, vol. 88, no. 5, pp. 1848–1856, 2011.
- [7] A. F. Özdemir, E. Yıldıztepe, and M. Binar, "İstatistiksel Yazılım Geliştirme Ortamı: R," presented at the XII. Akademik Bilişim Konferansı, Muğla, 2010, vol. 1, pp. 375–379.
- [8] R Core Team, *R: A Language and Environment for Statistical Computing*. Vienna, Austria: R Foundation for Statistical Computing, 2014.
- [9] P. Dalgaard, *Introductory statistics with R*. Springer Science & Business Media, 2008.
- [10] İ. Kirbaş, "Wind Speed Distribution Dataset and R Source Codes," GitHub Page, 23-Apr-2017. [Online]. Available: <https://github.com/ismkir/windSpeedDistribution/>. [Accessed: 24-Apr-2017].
- [11] O. Elitok, "Weibull Distributions and Its Applications," M. Sc. Thesis, Kırıkkale University Institute of Science and Technology, Kırıkkale, 2006.
- [12] D. Indhumathy, C. V. Seshaiyah, and K. Sukkiramathi, "Estimation of Weibull Parameters for Wind speed calculation at Kanyakumari in India," *Int. J. Innov. Res. Sci. Eng. Technol.*, vol. 3, no. 1, pp. 8340–8345, Jan. 2014.
- [13] A.-A. Bromideh, "Discriminating Between Weibull and Log-Normal Distributions Based on Kullback-Leibler Divergence," *Istanb. Üniversitesi İktisat Fakültesi Ekonom. Ve İstat. Derg.*, no. 16, pp. 44–54, 2012.



Investigation of Silica Aerogels Effect on Paint Characteristics

Rana Aksu^{1*}, Berrin Saygi¹

¹*Yildiz Technical University, Department of Chemical and Metallurgical Engineering, 34220, Esenler/Istanbul, Turkey.*

**Corresponding Author email: ranaaksu@yandex.com*

Abstract

New methods of energy saving are being researched by many scientists. An important research area in these studies are insulating paints. Silica aerogels are one of nanostructured insulating materials with low thermal conductivity, high surface area and low density. The main aim of this project is to study on alternative paint insulator by producing silica aerogel. In this research, Na_2SiO_3 and H_2SO_4 solution were used for synthesis of aerogels by using the sol-gel method. Acetonitrile and methanol:hexane solution was used for solvent exchange and surface modification. The effects of the process parameters such as the reaction temperature (35-55°C), the solution amount (150-180ml), the aging temperature (70-90°C) and the drying temperature (50-70°C) were studied. Depends on the reaction parameters, three different kinds of aerogels were synthesized (aerogel1(A1), aerogel2(A2) and aerogel3(A3)). After that production progress, silica aerogels were added to two different kinds of paints (water and solvent-based). Aerogel amounts (%1-%3) and aerogel types were chosen as experiment factors. Properties of these samples, such as viscosity, hydrophobicity and adhesivity were measured. The viscosity measurements showed that the viscosity increase with the increasing amount of aerogel in both types of paint. When compared, the hydrophobic properties, best results were obtained in the using of A2 for water-based paint and using of A1 for the solvent-based paint. For the adhesivity, it can be said that it has an improving effect for all aerogel and paint types. In conclusion, the result of experiments demonstrated that silica aerogels have a positive effect on paint characteristics.

Key words

Aerogel, Insulation materials for paints, Energy saving

1. INTRODUCTION

Aerogels are nanoporous materials usually synthesized from silica, with a high porosity, high specific surface area (500–1200m².g⁻¹), high porosity (80–99.8%), low density (~0.003–0.5g.cm⁻³), low thermal conductivity (0.005–0.1W/mK), low refractive index (~1.05) [1]. First aerogel was produced by S. Kistler in 1930's. He defined the aerogels as a material which is produced by replacing the solvents in the gel by air

without substantially altering the network structure or the volume of the gel body [2]. Aerogels can be synthesized from various raw materials such as Tetramethylorthosilicate (TMOS), Tetraethylortosilicate (TEOS) and sodium silicate. There are lots of production methods to produce aerogels. Co-precursor method, derivatization method and sol-gel can be given as examples. In these several kinds of methods, sol-gel method is the best appropriate method in laboratory conditions. The applications of the method in large scale production increased in recent years [3].

The unique properties of aerogels make them great candidates for many applications. In recent years so much attention has been given to silica aerogels in several technological applications. Chemistry, aerospace, electronics, energy, agriculture and insulation can be given as an examples of the some applications areas [4].

In the present work, the role of different process conditions, such as reaction temperature, the solution amount, the aging temperature and the drying temperature was analyzed. Sol-gel method was chosen for the aerogel production. After the aerogel production has been done, these samples were used as paint additives. In this research, two kinds of paint were chosen; solvent and water based paints. Finally, for the investigation of the aerogels effect on paints, some paint analyses were done.

2. MATERIALS AND METHODS

2.1 Synthesis of aerogels

Sol-gel polymerization is the commonly employed method for the preparation of the aerogels. In this study, Na_2SiO_3 and H_2SO_4 solution were used for synthesis of aerogels by using the sol-gel method. Three different kinds of aerogels were obtained in the end of the polymerization. Sodium silicate solution amounts were determined as 150 ml, 180 ml and 160 ml and also the other reaction parameters such as the drying temperature (70 °C, 70 °C and 50 °C), the aging temperature (70 °C, 90 °C and 90 °C), the reaction temperature (45 °C, 55 °C and 35 °C) were worked on. The mixing rate was 240 rpm for every mixture. Depends on these reaction parameters, three different kinds of aerogels were synthesized (aerogel 1, aerogel 2 and aerogel 3, respectively). In the end of the reaction, the gelation was obtained which is shown in figure 1. After gelation, samples were sent to the oven to aging step at different temperatures for 3 hours. The aging step is shown in figure 2. The aging step to remove the Na^+ ions from the samples, they were washed with distilled water for 24 h. Distilled water was changed at every 6 h of the day. The washing step is shown in figure 3. Acetonitrile was used for solvent exchange and methanol:hexane solution (molar ratio 1:1) was used for surface modification. Finally, the samples were dried at different temperatures for 24 h. The drying step is shown in figure 4.

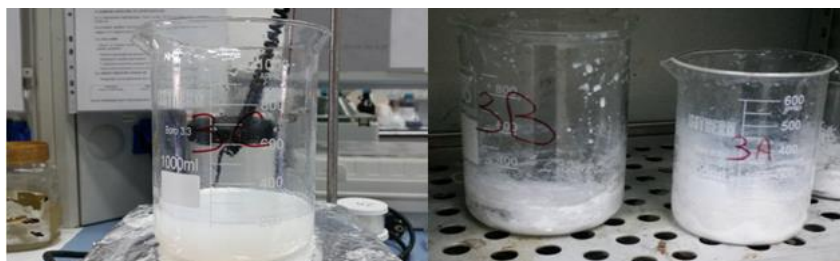


Figure 1. The gelation was occurred after the polymerization step.

Figure 2. The aging step at different temperatures for 3 hours.

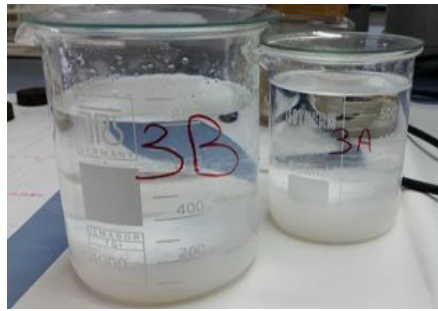


Figure 3. The washing step was done for removing sodium ions.

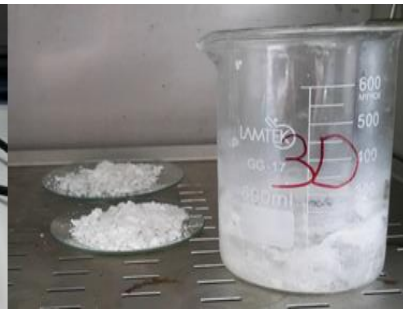


Figure 4. The drying process at different temperatures for 24 h.

2.2 The preparation of the paint samples

After the production progress, silica aerogels were added to two different kinds of paints; water and solvent based. Aerogel amounts (%1, %2 ve %3) and aerogel types were chosen as experiment factors. For these two different kinds of paints, paint amounts were determined as 75 g and due to these ratio 0.75 g, 1.5 g and 2.25 g aerogels were used respectively. As the preparation of the samples Design Expert 7 optimization program was used.

3.RESULTS AND DISCUSSION

After the addition of the aerogels to paints, firstly viscosity measurements were done. Then the hydrophobicity of the samples were investigated and for the each sample, water flowing velocities on the surfaces were measured. For the investigation of the adhesivity, cross-cut tests were applied.

3.1 Viscosity measurements

Viscosity is the resistance of a liquid material with homogeneous structure to flow. Liquids with lower viscosity under the same conditions flow faster than those with higher viscosity.

3.1.1 The analysing of the viscosity graphics for water based paint

The viscosity graphics were created by using Design Expert 7 optimization program. The effect of aerogel types and aerogel amounts on viscosity are shown in Figure 5 and Figure 6.

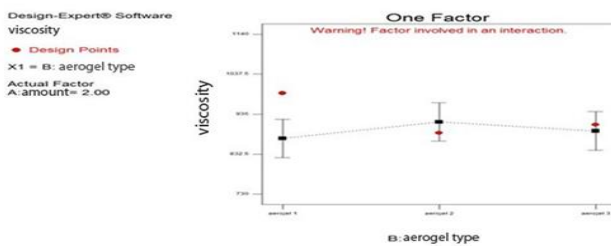


Figure 5. Viscosity vs. aerogel types graphic for the water based paint

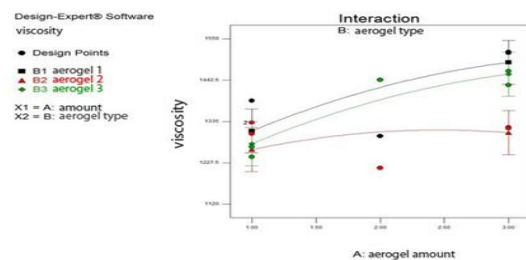


Figure 6. Viscosity vs. aerogel amounts graphic for the water based

These graphics demonstrated that the highest viscosity were reached by using aerogel type 2 and the least viscosity were reached by using aerogel type 1. For all the types, it was observed that the viscosity increases with the increasing amount of the aerogel.

3.1.2 The analysing of the viscosity graphics for solvent-based paint

The effect of aerogel types and aerogel amounts on viscosity for the solvent based paint are shown in Figure 7 and Figure 8.

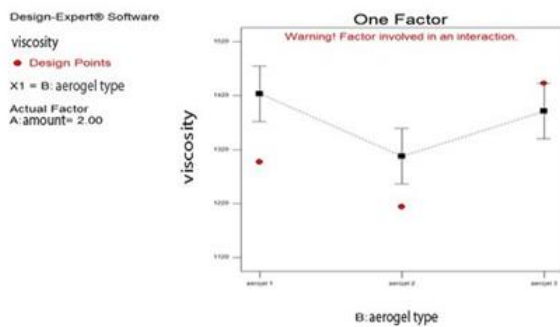


Figure 7. Viscosity vs. aerogel types graphic for the solvent based paint

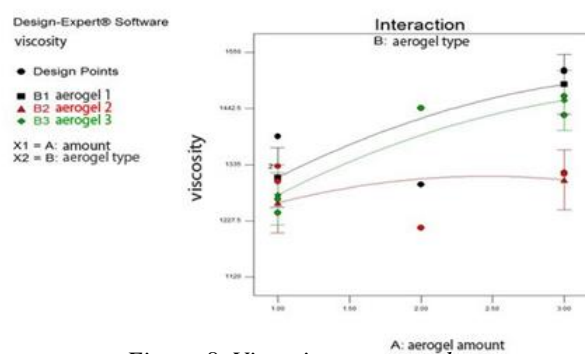


Figure 8. Viscosity vs. aerogel amounts graphic for solvent based paint

The graphics showed that the maximum viscosity were achieved by using aerogel type 1 and the minimum viscosity were achieved by using aerogel type 2. For all the types, it can be said that the viscosity increase with the increasing amount of the aerogel. When compared the behaviour of the solvent and water based paints, it can be seen that there is a similitary in terms of the increasing viscosity with increasing amount of the aerogels.

3.2 Hydrophobicity measurements

Contact angle is a measure of static hydrophobicity. When a pipette injects a liquid into a solid, the liquid will form some contact angle. Contact angle is higher than 90° for hydrophobic surfaces. In this present work, flow appearances and flow velocities of the samples were compared with control samples which includes no aerogels. The results of some samples are given below:



Figure 9. Control sample of water based paint



Figure 10. Flow appearance of control sample for water based paint



Figure 11. Sample with aerogel as a paint additive for water based paint



Figure 12. Flow appearance of sample with aerogel as a paint additive for water based paint



Figure 13. Control sample of solvent based paint

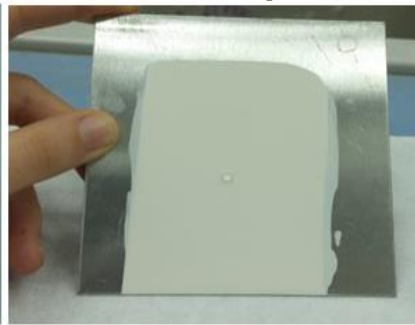


Figure 14. Flow appearance of control sample for solvent based paint

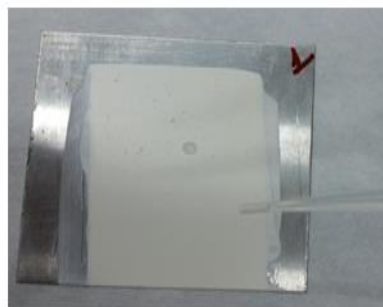


Figure 15. Sample with aerogel as a paint additive for solvent based paint

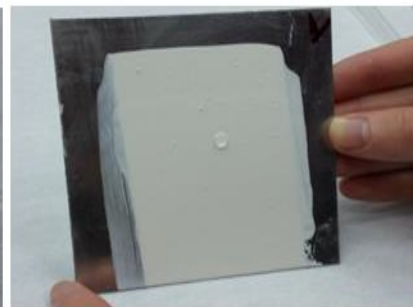


Figure 16. Flow appearance of sample with aerogel as a paint additive for water based paint

3.2.1 The analysing of the hydrophobicity graphics for water based paint

The effect of aerogel types and aerogel amounts on hydrophobicity for the water based paint are shown in Figure 17 and Figure 18.

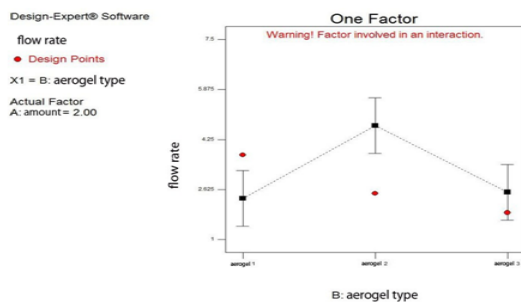


Figure 17. Aerogel type vs flow rate graphic for the water based paint

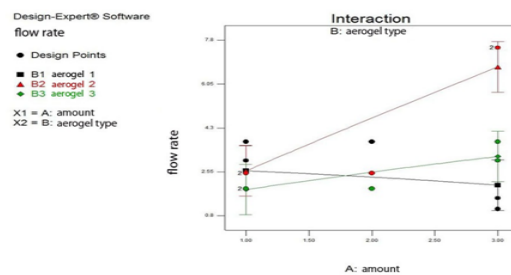


Figure 18. Aerogel amount vs. flow rate graphic for the water based

The graphics demonstrated that the maximum hydrophobicity were achieved by using aerogel type 2 and the minimum hydrophobicity were achieved by using aerogel type 1. For aerogel 2 and aerogel 3, hydrophobicity increased with the increasing amount of aerogel. On the other hand, for the aerogel 1, hydrophobicity decreased with the increasing amount of the aerogel.

3.2.2 The analysing of the hydrophobicity graphics for solvent based paint

The effect of aerogel types and aerogel amounts on hydrophobicity for the solvent based paint are shown in Figure 19 and Figure 20.

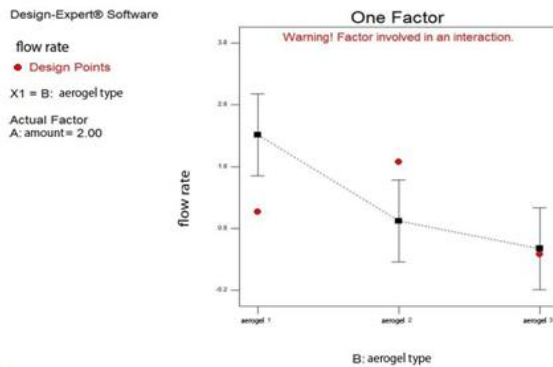


Figure 19. Aerogel type vs. flow rate graphic for the solvent based paint

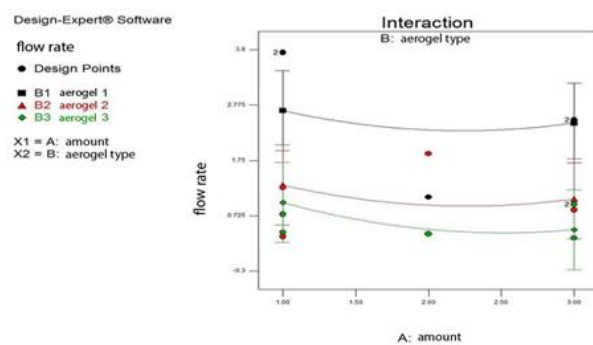


Figure 20. Aerogel amount vs. flow rate graphic for the solvent based paint

The graphics showed that for the solvent based paint, the best results were obtained by using of aerogel type 1. Minimum hydrophobicity was observed in case of using aerogel type 3. For all aerogel types it can be said that hydrophobicity decrease with the increasing amount of aerogels.

3.3 Adhesivity Measurements

For the investigation of the adhesivity, cross-cut tests were applied. This test is a method for measuring the resistance of paints and coatings to separation from surfaces when a right angle cross pattern is cut into the coating, penetrating through to the surface.

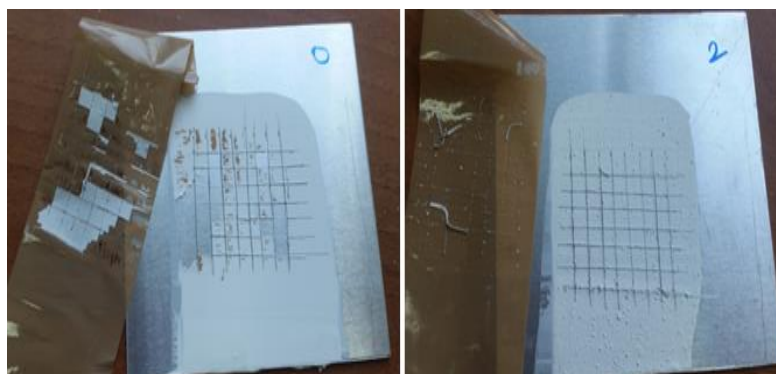


Figure 21. Water based paint without aerogel as a paint additive

Figure 22. Water based paint with aerogel as a paint additive

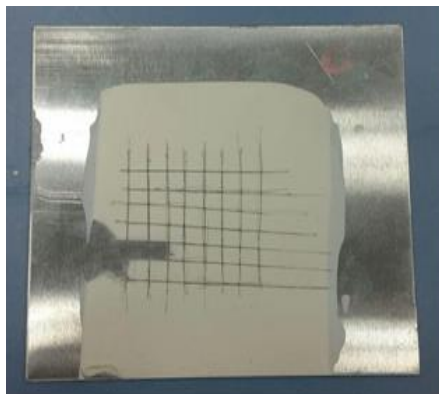


Figure 23. Solvent based paint without aerogel as a paint additive

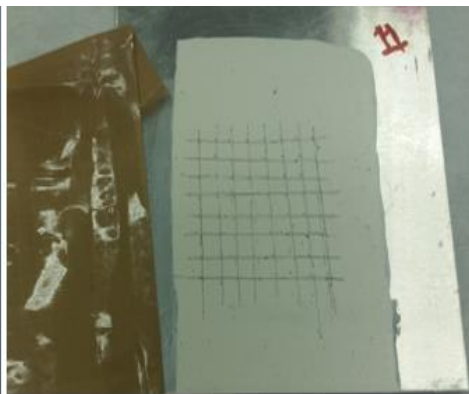


Figure 24. Solvent based paint with aerogel as a paint additive

3.3.1 The analysing of the adhesivity graphics for water based paint

The effect of aerogel types and aerogel amounts on adhesivity for the water based paint are shown in Figure 25 and Figure 26.

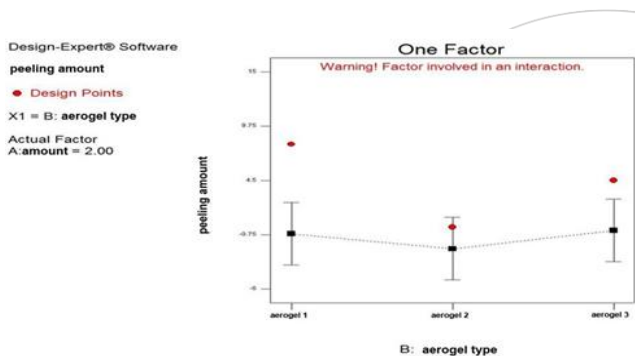


Figure 25. Aerogel type vs. peeling amount graphic for the water based paint

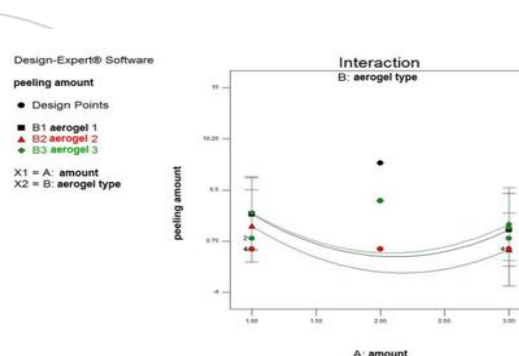


Figure 26. Aerogel amount vs. peeling amount graphic for the water based paint

The graphics showed that the maximum adhesivity was obtained in case of using aerogel type 3 as a paint additive and the minimum adhesivity was obtained with the utilization of aerogel type 2. In addition to this, it has been observed that peeling amount decrease with the increasing amount of aerogel utilization.

3.3.2 The analysing of the adhesivity graphics for solvent based paint

The effect of aerogel types and aerogel amounts on adhesivity for the solvent based paint are shown in Figure 27 and Figure 28.

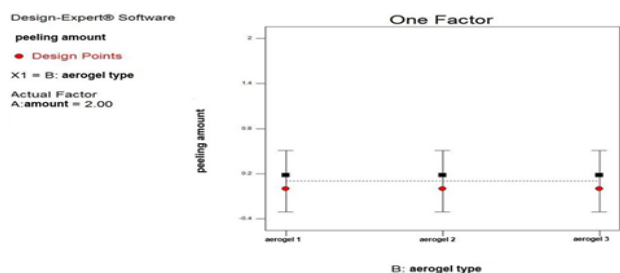


Figure 27. Aerogel type vs. peeling amount graphic for the solvent based paint

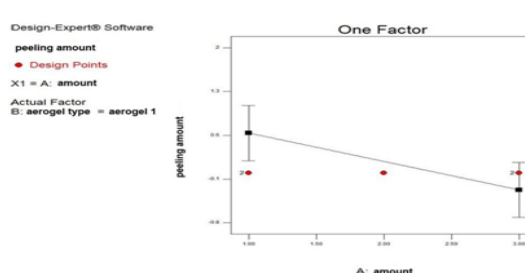


Figure 28. Aerogel amount vs. peeling amount graphic for the solvent based paint

The graphics demonstrated that as a parameter, aerogel type cannot be compared with each other. Because in case of utilization of all types of aerogel as a paint additive, the solvent based paint wasn't peeled. On the other hand, it can be said that aerogel utilization with increasing amount, decrease the peeling amount for the all types of aerogel.

4. CONCLUSION

In this study, experimental and numerical work were performed to investigate the silica aerogels effect on the paints characteristics. Based on the experimental and numerical studies, conclusions can be drawn as follows:

- (1) The viscosity measurements show that the best results were reached in case of using of the aerogel 1 for solvent-based paint and aerogel 2 for water-based paint. It has been observed that the viscosity increase with the increasing amount of aerogel in both types of paint.
- (2) When compared, the hydrophobic properties, the best results were obtained in the using of aerogel 2 for water-based paint and using of aerogel 1 for the solvent-based paint.
- (3) For the adhesivity, it can be said that it has an improving effect of all aerogel types for solvent based paint. For water based paint, the best results are obtained in aerogel 3, and in general, the amount of peeling is reduced as the amount of aerogel increases in all aerogel types.

The result of experiments demonstrated that silica aerogels have a positive effect on paint characteristics. This study is going to continue with the thermal conductivity measurements of the samples.

5. REFERENCES

- [1] Sarawade, P.B., Quang, D.V., Hilonga, A., Jeon, S.J., Kim, H.T., (2012), Synthesis and characterization of micrometer-sized silica aerogel nanoporous beads“, *Materials Letters* 81: 37-40
- [2] S. Kistler, (1931), Coherent expanded aerogels and jellies“, *Nature*, 127: 741-741
- [3] Dorcheh, A., S., Abbasi, M., H. (2008), Silica Aerogel; Synthesis, Properties and Characterization“, *Journal of Materials Processing Technology*, 199: 10-26
- [4] Bi, C., Tang, G. H., Hu, Z. J., (2014), Heat conduction modeling in 3-D ordered structures for prediction of aerogel thermal conductivity“, *International Journal of Heat and Mass Transfer*, 73: 103-109



Numerical Investigation of Hot Ultrasonic Assisted Turning of Titanium Alloy

Fatih Hayati Çakır¹ , Selim Gürgen¹ , M.Alper Sofuoğlu^{2*} , M.Cemal Kuşhan² , Sezan Orak²

¹Vocational School of Transportation, Anadolu University, Eskişehir, 26470, Turkey

²Department of Mechanical Engineering, Eskişehir Osmangazi University, Eskişehir, 26480, Turkey

*Corresponding Author email: asofuoglu@ogu.edu.tr

Abstract

Titanium alloys exhibit superior properties such as high strength-to-weight ratio and corrosion resistance but these alloys possess poor machinability. To overcome this disadvantage, new machining methods (Ultrasonic Assisted Machining, Hot Machining etc.) are developed. Hot Ultrasonic Assisted Turning (HUAT) is a new machining method which changes the cutting system between tool and workpiece therefore reduced cutting forces and better surface finish for workpiece are obtained. In this study, 2D finite element (FE) analysis was carried out to investigate the effects of HUAT for titanium alloys. It was confirmed that HUAT technique reduces cutting forces and effective stress significantly but cutting temperature increases compared to conventional turning.

Key words

Finite element modelling; hot ultrasonic assisted machining; titanium alloys; ultrasonic assisted machining; hot machining

1. INTRODUCTION

In recent years, titanium alloys have wide range of applications in automotive, aerospace and biomedical sectors. The reason is that these alloys are light in weight and they have high strength, fatigue and corrosion resistance. However, machining of these materials is very difficult due to their low thermal conductivity. Therefore, conventional machining methods cause low dimensional accuracy and undesired surface roughness. In addition, these alloys can react with cutting tools [1].

Machining of workpiece with the aid of a heat source is called hot machining. External heat sources such as gas torch, furnace preheating, induction heating, electric current heating, plasma and laser heating are most commonly used methods. In early studies of hot machining, ceramic materials are preheated between room temperature and 1400°C. Also, steel products and titanium alloys are preheated from room temperature to 600°C, and Inconel products are preheated from room temperature to 550°C. The results show that preheating of workpiece has a positive impact on tool life, surface roughness, cutting force and machining cost [2-6].

Ultrasonic assisted turning (UAT) is a non-conventional machining technique by applying vibrations to cutting tool at high frequency (20 kHz) and low amplitude (15-20 microns). Using this machining method, cutting forces and surface roughness are reduced. Also, tool wear is reduced and dimensional accuracy is improved. UAT is effective at low cutting speeds, when cutting speed increases, the process outputs (surface roughness, tool wear, cutting force etc.) approaches the outputs of conventional turning operations [7-9].

Hot ultrasonic assisted turning (HUAT) is a new hybrid machining method which is developed in recent years. The method consists of a combination of hot turning (HT) and UAT. In this method, the disadvantage of UAT at

high cutting speeds can be eliminated. An early study showed that surface roughness and cutting force are decreased by using HUAT [10].

In this study, HUAT and HT methods are investigated for Ti6Al4V. Both methods are compared with conventional turning (CT) and UAT. In the second part of the study, finite element simulation of HT and HUAT is given. The third section shows the results of finite element simulations. In the last section, conclusions and recommendations are given.

2. FE SIMULATION OF HT AND HUAT

Simulations were performed by using DEFORM 2D software. The number of elements used in the simulations was about 3000 for the cutting tool and 5000 for the workpiece. Because of the remeshing, the number of elements was increased to 6000 for workpiece. A previous study was used to compare the results with UAT and CT [11]. Details of the modeling was given in previous study [11]. Ti6Al4V was used as workpiece material. Dimensions of the workpiece were 3 mm in length and 1 mm in width. Plain strain conditions were applied. FE simulations were performed for four different cutting speeds (10, 20, 30 and 40 m/min) and three different cutting temperatures (20°C, 250°C and 500°C). Ultrasonic vibration was also applied with 20 kHz frequency and 20 μ m amplitude. The vibration was applied in the direction of cutting speed. Depth of cut was 0.1 mm and simulations were performed in dry cutting conditions. Table 1 represents the machining conditions of the FE simulations. Fig. 1 shows a screenshot in FE simulation.

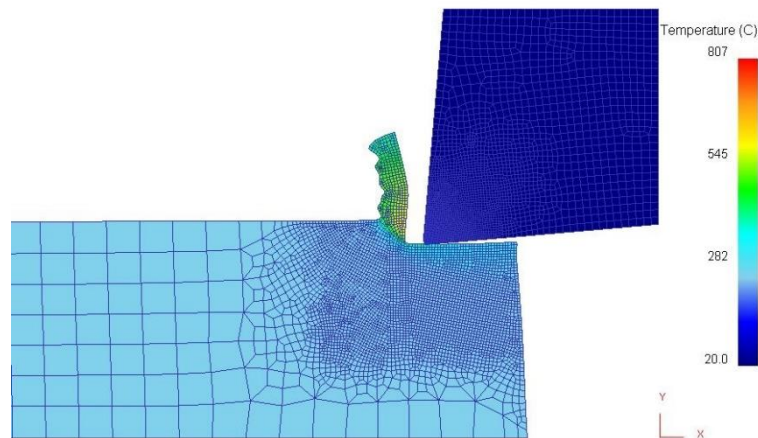


Fig. 1. Screenshot of FE simulation of HUAT

Cutting tool (DNMG 150608 KC 9225) was assumed to be rigid in the simulations. Material of the cutting tool was chosen as non-coated tungsten carbide (WC) and the only thermal calculation for the tool was activated.

Table 1. Machining conditions

Machining Condition	Temperature (°C)	Ultrasonic vibration
CT [11]	20	-
UAT [11]	20	+
HT	250	-
HT	500	-
HUAT	250	+
HUAT	500	+

Johnson-Cook (JC) material model was used in the simulations. The equations of stress and temperature for JC model are given in Eq.1-2. Material parameters used in the simulations for Ti6Al4V alloy are given in Table 2. Values of the parameters were taken from the study performed by Lee [12].

$$\sigma = (A + B\varepsilon^n) \left(1 + C \ln \left(\frac{\dot{\varepsilon}}{\dot{\varepsilon}_0} \right) \right) (1 - T^*)^m \tag{1}$$

$$T^* = \frac{(T - T_{room})}{(T_{melt} - T_{room})} \tag{2}$$

- $\dot{\varepsilon}_0$: reference plastic strain rate
- ε : plastic strain rate
- n : strain rate sensitivity of the material
- T_{room} : room temperature
- T_{melt} : melting temperature of the material
- A, B, C, m : material constants

Table 2. Constants of JC Model suggested for Ti-6Al-4V alloy [12]

A	B	C	n	m	$\dot{\varepsilon}_0$
724.7	683.1	0035	0.47	1	2000 s ⁻¹

Fracture criterion has considerable effect on the chip separation therefore Cockcroft & Latham fracture criterion was chosen for the simulations. Similar to materials toughness, fracture limit changes with the temperature. At higher temperatures, continuous chip formation is observed.

3. RESULTS AND DISCUSSION

3.1. Cutting Force Prediction

Improving cutting performance has many aspects. One of the most common approaches is to observe cutting forces. Cutting force results for different machining conditions are presented in Fig.2. The results of the numerical simulation indicate that heating workpiece and applying ultrasonic vibration decrease average cutting force. Simulation results of 30 m/min cutting speed show that at 250°C, cutting force reduction is about 10% and at 500°C, it is nearly 15% compared to CT. One of the most significant advantages of UAT method is the effect of the average cutting forces. At the same conditions, effect of UAT at room temperatures reduces average cutting forces about 35% compared to CT. HUAT at 250°C and 500°C lowers cutting forces about 42% and 57%, respectively compared to CT. HUAT decreases average cutting forces and this hybrid approach is much more efficient compared to the other techniques. According to the numerical results, the lowest cutting force is obtained in HUAT at 500°C. HUAT at 250°C produces promising results therefore heating of workpiece may not be necessary and probably not cost effective at higher temperatures (500°C).

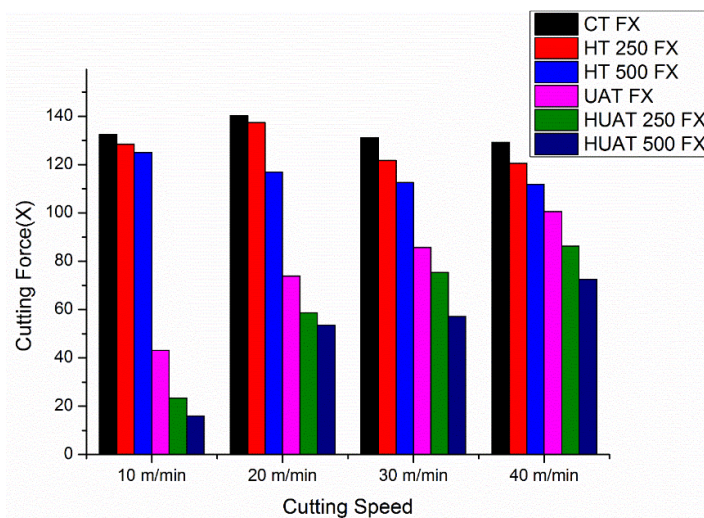


Fig. 2. Average load data for various cutting speeds

3.2. Cutting Temperature

Numerical results show that maximum cutting temperature in HUAT process is slightly higher compared to HT. Fig.3 shows the results of thermal analyses for different cutting conditions.

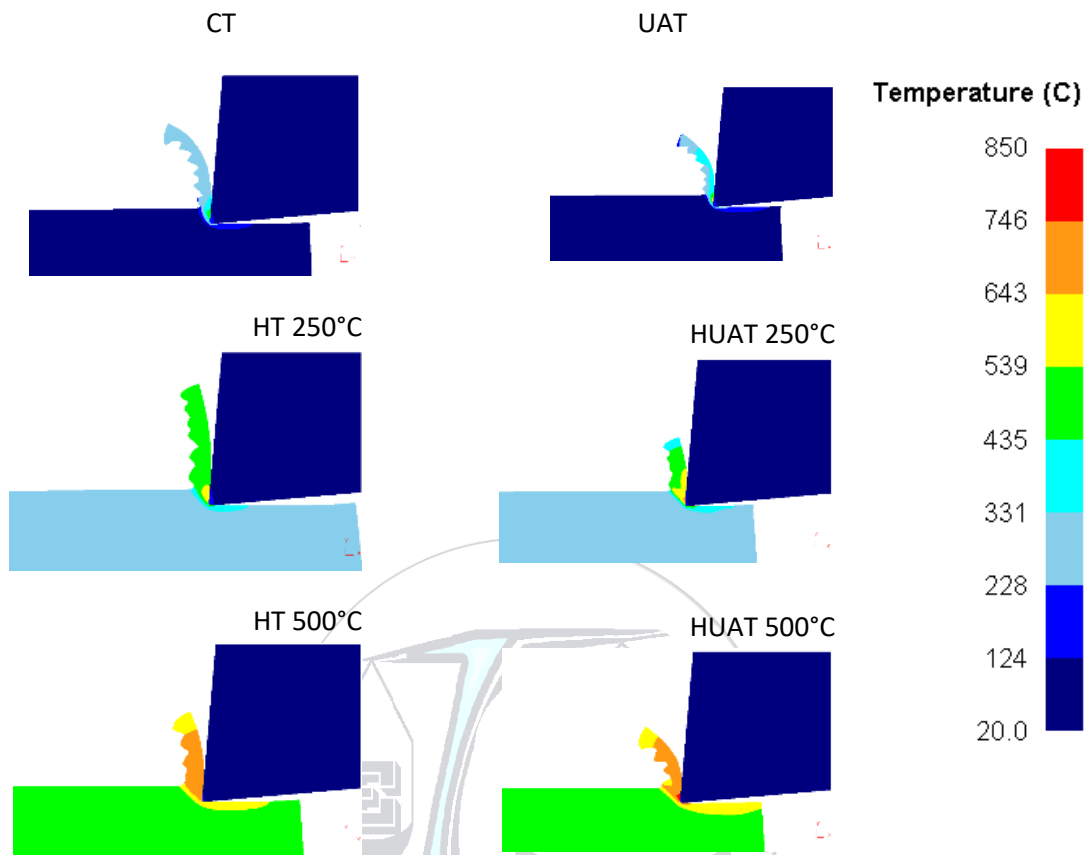


Fig. 3. Temperature distributions in the cutting zone (Cutting speed: 30 m/min)

In HT at 500°C, maximum cutting temperature is nearly 700°C, whereas it is about 800°C in HUAT at 500°C. Applying additional heat increases cutting zone temperature. In HT at 250°C, maximum cutting temperature is nearly 600°C, whereas in HUAT at 500°C, it is about 700°C. Maximum temperatures in the simulations of CT and UAT are about 513°C and 670°C, respectively. In UAT, the maximum cutting temperature increases compared to CT.

3.3. Effective Stresses in the Process Zone

The calculated distributions of effective stresses in the cutting regions of the Ti6Al4V are shown in Fig.4. These stresses are taken at UAT penetration stage because in UAT, stress distribution is changed during each vibration cycle. Maximum effective stress decreases by the increase in temperature as expected. The average levels of the effective stress in the cutting region in HUAT and HT are lower than UAT and CT. Maximum effective stresses in the simulations of CT, HT at 250°C, HT at 500°C are 1300 MPa, 985 MPa, 800 MPa, respectively, whereas in UAT, UAT at 250°C, HUAT at 500°C are 1260 MPa, 995 MPa, 795 MPa, respectively. There are similar findings from previous studies [10].

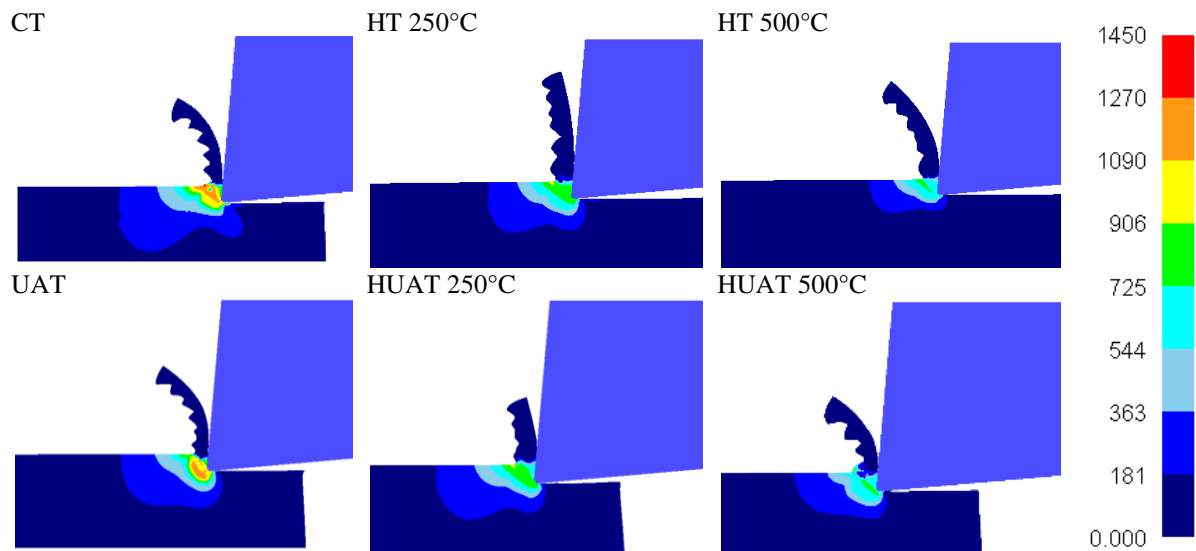


Fig. 4. Effective stresses (MPa) (Cutting speed: 30 m/min)

4. CONCLUSION

In this study, HT and HUAT processes were modeled by FE. The results of simulations demonstrate that HUAT technique reduces average cutting forces significantly but maximum cutting temperature increases compared to the other techniques. Increasing workpiece temperature lowers its yield strength and decreases cutting forces. Reduced cutting forces have many advantages on machining operations. However, lower tool life is obtained because of high cutting temperature. Heat treatments might be applied for cutting tools to avoid increased tool wear. In UAT, reduction of cutting forces is obtained by reducing the tool-workpiece contact area. Furthermore, in HT, thermal softening of workpiece results in reduction in the cutting forces. The average levels of the effective stress in the cutting region in HUAT were lower than UAT and CT. HUAT is much more effective than CT, UAT and HT. Integrating ultrasonic vibrations and heat supply improves machinability of Ti6Al4V. Developed numerical model is useful to understand the effects of process parameters.

ACKNOWLEDGMENT

The authors M.A.Sofuoğlu and S.Gürgen acknowledge the support by TUBITAK under programs 2228 and 2211.

REFERENCES

- [1]. C. R. Dandekar, Y. C. Shin, J. Barnes, "Machinability improvement of titanium alloy (Ti-6Al-4V) via LAM and hybrid machining", *International Journal of Machine Tools and Manufacture* 50/2,174-182, 2010
- [2]. L.Özler, A. İnan, C. Özel, "Theoretical And Experimental Determination Of Tool Life In Hot Machining Of Austenitic Manganese Steel", *International Journal Of Machine Tools And Manufacture* 41/2,163-172, 2001
- [3]. P.A Rebroy, Y.C. Shin, F.P. Incropera, "Desing Of Operating Conditions For Crackfree Laser- Assisted Machinig Of Mullite", *International Journal Of Machine Tools And Manufacture* 44/7-8, 677-694, 2004
- [4]. M.C. Anderson, Y. C. Shin, "Laser-Assisted Machining Of An Austenitic Stainless Steel: P550", *J. Engineering Manufacture* 220/12, 2055-2067, 2006
- [5]. T. Özel, F. Pfefferkorn, "Pulsed Laser Assisted Micromilling For Die/Mold Manufacturing", *ASME 2007 International Manufacturing Science and Engineering Conference*, 337-342, 2007
- [6]. F.E. Pfefferkorn, S. Lei, Y. Jeon, G. Haddad, "A Metric For Defining The Energy Efficiency Of Thermally Assisted Machining ", *International Journal Of Machine Tools & Manufacture* 49/5, 357-365, 2009
- [7]. V.I Babitsky, A.V Mitrofanov, V.V Silberschmidt, "Ultrasonically assisted turning of aviation materials: simulations and experimental study", *Ultrasonics* 42/1-9, 81-86, 2004
- [8]. A. Maurotto, R. Muhammad, A. Roy, V. V. Silberschmidt, "Enhanced ultrasonically assisted turning of a β -titanium alloy", *Ultrasonics* 53/7, 1242-1250, 2013
- [9]. M.J. Nategh, H. Razavi, A. Abdullah, "Analytical modeling and experimental investigation of ultrasonic-vibration assisted oblique turning, part I: Kinematics analysis", *International Journal of Mechanical Sciences*, 63/1, 1-11, 2012
- [10]. R. Muhammad, A.Maurotto, M.Demiral, A.Roy, V. V. Silberschmidt, "Thermally enhanced ultrasonically assisted machining of Ti alloy", *CIRP Journal of Manufacturing Science and Technology* 7/2, 159-167, 2014
- [11]. F. H. Cakir, S. Gurgen, M. A. Sofuoglu, O. N. Celik, and M. C. Kushan, "Finite Element Modeling of Ultrasonic Assisted Turning of Ti6Al4V Alloy", *Procedia - Soc. Behav. Sci.*195, 2839-2848, 2015
- [12]. W.S. Lee and C.F. Lin, "High-temperature deformation behaviour of Ti6Al4V alloy evaluated by high strain-rate compression tests," *J. Mater. Process. Technol.* 75/1-3, 127-136, 1998



Shape Features Based Conic Arcs for Unclassified Wheat Identification

Ahmet Okan Onarcan¹, Kemal Özkan^{2*}

¹ Anadolu University, School of Foreign Languages , 26555, Eskişehir, Turkey. aoonarcan@anadolu.edu.tr.

² Eskişehir Osmangazi University, Faculty of Engineering and Architecture, Computer Engineering Department, 26480, Eskişehir, Turkey. kozkan@ogu.edu.tr.

*Corresponding Author email: kozkan@ogu.edu.tr

Abstract

Wheat is one of the main nutrients used in the world. Consumption of foodstuff produced from quality wheat is of great importance for healthy generations. It is necessary to separate the high and low quality wheat. In this paper, a new recognition method for quality wheat and unclassified wheat is presented. The most distinctive feature for determination of wheat quality is its shape. In this study, objects are first represented by a few descriptive points on their contours obtained from their images. Neighboring points are connected by linear or conical curve fitting. The objects are then represented by an attribute vector constructed from parameters of the curves. Finally, these vectors are used to classify objects (wheat) using support vector machines (svm). Performance is improved with cross validation for each class.

Key words

feature extraction; wheat; unclassified wheat; shape descriptor

1. INTRODUCTION

Here we are recognizing quality wheat and unclassified wheat. In computer vision shape is a distinctive feature for object recognition. The presence of curvature and straight lines and soft and sharp transitions, helps us visually identify and analyze the object more easily. Therefore, there are many studies in literature related to shape-based descriptors. A good descriptor should be robust, fast running, distinctive against noise and geometric transformations with few attributes. Shape-based descriptors are generally divided into regional and contour based representatives. Contour based descriptors first extract the outer line of the object in binary format and try to identify the object through this line. Sometimes it is too complicated to describe large images. Especially on large shapes when there is occlusion, and overlapping with each other is one of the problems encountered in recognition performance. In order to get rid of them we can make meaningful interpretations of the whole shape by separating small parts. On the contrary, we can construct a whole shape by adding the vertices and curves from specific dominant points. These dominant points are mostly the corner points on the boundary (Figure 1). The points where the curvature is broken by other expressions are referred to by such terms as dominant point, interesting point, corner point. The dominant point extraction is usually achieved by two basic methods; polygonal approach methods and direct methods (corner detection algorithms). The main idea in the polygonal approach is to determine meaningful points on the contour of the shape. The polygonal approach is applied in two different ways by joining or separating the parts of the shape. During joining process; small changes are eliminated by trying to express the shape by curves and straight lines. In separating process, is made by fitting the curves and lines between points.

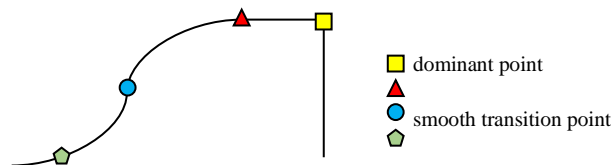


Figure 1. Dominant, smooth transition, inflection and candidate points

In direct methods, the points which have the highest values are generally determined as the dominant point. At later stages, curvature correction can be achieved in a variety of ways [1,2,3]. To find the dominant points, Wu proposed the adaptive inflection value for each point on the boundaries of the shape, and determined the dominant points depending on this measure [4]. In another study, an algorithm is developed to eliminate contiguous points on the same line on the contour [5]. The area to the right and left of the dominant points is called the support region [1]. At that study, to find the support region, a ratio was developed to find the distance between each point to its beam [1]. In another method, the k-cosine [3] measurement was used to calculate the support region [6]. In [7], Z. Kurt and et al proposed a method based on the difference of the absolute angle between the support points on the right and left side of the candidate point on the contour. They used Principle Component Analysis (PCA) to calculate the support regions.

This work has been done with an object-based identifier and object parsing [7,8]. In the second section, the method used is mentioned, in the third section the experiences are explained and in the fourth section the result is explained.

2. METHOD

Here we use the progressively developed method [8]. In the method, as expressed in Figure 2, the contour of the shape is extracted by an edge detection algorithm. Each point on the contour is determined as a candidate point and tried to find which one is more important (Figure 1). The meaningful points are fitted by line and curve. In this way, the contour have been tried to be described in the most obvious way. First Canny edge detector is used to find the contour of the shape (Figure 4.a.). Each of the points p_i , on the contour is treated as the candidate point. Then on the candidate meaningful points, the right and left support regions are calculated by Principal Component Analysis (PCA) method [7]. Here, the neighboring pixels in the vicinity of the candidate point are searched for the presence of the support region (Figure 3). The direction of the eigenvector gives us the support region which is the largest eigenvalue of the covariance matrix of the data. At the beginning, PCA is applied by taking three points and the angle that the largest eigenvalue is made with the coordinate axis is calculated. The operation is performed by increasing the number of the points. The obtained angle is compared with the previous ones. This process continues until the angle reaches a significant threshold value. This process is applied to both the right and left sides of the candidate point. In this way, the right S_r and left S_l support regions are calculated (Figure 3). Meaningful points are found by the means of right and left support regions of the candidate point. The angle θ between the distribution directions of the support regions is calculated (Figure 3).

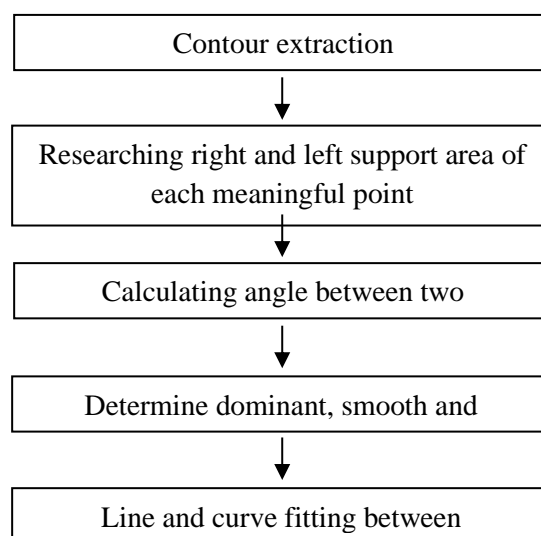


Figure 2. Block diagram of shape description

Table 1. Feature representation of a shape

type	s-ll	s-lp	s-le	s-lh	s-pp	s-pe	s-ph	s-ee	s-eh	s-hh	c-ll	c-lp	c-le
count	0	1	0	0	0	0	2	0	2	0	0	2	1
type	c-lh	c-pp	c-pe	c-ph	c-ee	c-eh	c-hh	c-ie	c-ip	c-ih	s-ie	s-ip	s-ih
count	0	1	4	0	0	3	2	0	0	1	0	2	0

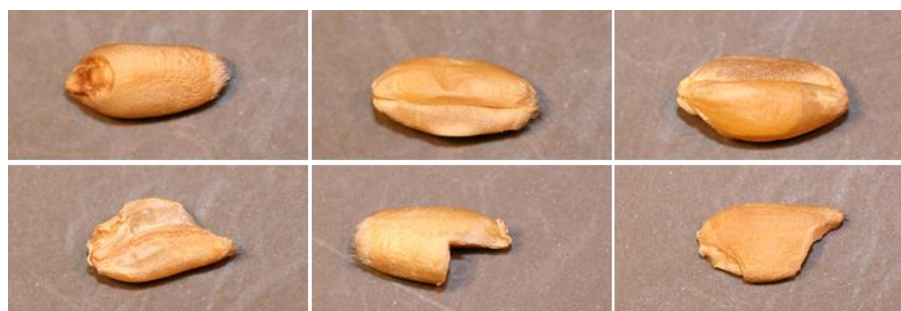


Figure 5. Top side: quality wheat, bottom side: unclassified wheat images.

was selected 1.0 and the kernel 2.0 for high performance. Images are divided as training and test clusters. As a result of the randomly chosen pictures, the classes were separated by a performance ratio of 70.83%.

4. CONCLUSION

The method used is a recent shape-based descriptor. Instead of a whole shape, it represents shapes, by dividing them into lines and arcs is an advantage, especially in case of occlusion. With this way, the synchronization speed is also increasing. It is obvious to improve meaningful points and calculating support regions which are referenced in the creation of the feature vector. Different variations can have better results depending on the type of data set. In the next phase of the study, different classifiers are planned in order to increase the recognition performance and the result will be examined.

ACKNOWLEDGMENT

This paper was granted by the Turkey Scientific and Technological Research Projects Support Program of as project number 1160576. This work was also supported by the Eskisehir Osmangazi University Scientific Research Project Commissions (grant no.: 2016-1120).

REFERENCES

- [1]. C.H. Teh, R.T. Chin, "On the detection of dominant points on digital curves", IEEE Transactions Pattern Analysis and Machine intelligence 11 (1989) 859-872.
- [2]. B. Kerautret, J.-O. Lachaud, B. Naegel, Comparison of discrete curvature estimators and application to corner detection, in:ISVC (1), Vol. 5358 of LNCS, 2008, pp. 710-719.
- [3]. A. Rosenfeld, E. Johnston, Angle detection on digital curves, IEEE Trans. Comput. 22 (1973) 940-941.
- [4]. Wen-Yen Wu, "Dominant point detection using adaptive bending value", Image and Vision Computing 21 (2003) 517-525
- [5]. M. Marji, P. Siy, "Polygonal representation of digital planar curves through dominant point detection - a nonparametric algorithm", Pattern Recognition 37 (2004) 2113-2130.
- [6]. B.K. Ray, K.S. Ray, "Detection of significant points and polygonal approximation of digitized curves", Pattern Recognition Letters 22 (1992) 443-452.
- [7]. Z. Kurt, K. Özkan, "Description of Contour with Meaningful Points", SIU 2013 Sempodium, Cyprus – Girne (2013).
- [8]. T. Avcı, G. Kökdemir, Z. Kurt, K. Özkan, "Shape Features Based Conic Arcs for Leaf Recognition", IEEE 22nd Signal Processing and Communications Applications Conference (SIU 2014), Trabzon, Turkey. 2014 22nd Signal Processing and Communications Applications Conference (SIU).

- [9]. D. Cremers, M. Rousson and R. Deriche, "A Review of Statistical Approaches to Level Set Segmentation: Integrating Color, Texture, Motion and Shape", *International Journal of Computer Vision* Vol. 72, no. 2, (2007) 195-215.
- [10]. H.T. Sheu, W.c. Hu, "Multiprimitive segmentation of planar curves- A two-level breakpoint classification and tuning approach", *IEEE Transactions on Pattern Analysis and Machine Intelligence* 21 (1999) 791-797.
- [11]. Wu-Chih Hu, "Multiprimitive segmentation based on meaningful breakpoints for fitting digital planar curves with line segments and conic arcs", *Image and Vision Computing* 23 (2005) 783-789.
- [12]. Hsu, Chih-Wei; Chang, Chih-Chung & Lin, Chih-Jen, "A Practical Guide to Support Vector Classification", Department of Computer Science and Information Engineering, National Taiwan University (2003).





Optimization of Cutting Parameters in Hard Turning of AISI H10A Steel under Minimum Quantity Lubrication

Halil DEMİR¹, Mehmet Erdi KORKMAZ², Ramazan ÇAKIROĞLU³, Mustafa GÜNAY^{2,*}

¹Karabük University, Department of Manufacturing Engineering, 78050, Karabük, Turkey

²Karabük University, Department of Mechanical Engineering, 78050, Karabük, Turkey

³Gazi University, Ostim Vocational High School, 34300, Ankara, Turkey

*Corresponding Author email: mgunay@karabuk.edu.tr

Abstract

In this study, influences of cutting parameters in hard turning of hot work tool steel by applying minimum quantity lubrication (MQL) were investigated and optimized by using Taguchi methodology. Firstly, the machinability experiments on hardened AISI H10A hot work tool steel with CBN inserts were performed under the MQL condition. The experiments were carried out by Taguchi's L9 orthogonal array. The machinability of AISI H10A steel were evaluated in terms of average surface roughness (Ra) and main cutting force (Fc). The analysis of variance (ANOVA) was applied to determine the effects of cutting parameters (cutting speed, feed rate and depth of cut) on surface roughness and cutting force. It was observed that surface roughness and cutting force increased with increasing feed rate and depth of cut in machining by applying MQL with uncoated CBN inserts. Depth of cut was determined as the most important parameter on surface roughness with 66.57% PCR while feed rate was determined on cutting force with 50.68% PCR. On the other hand, optimum cutting parameters for surface roughness and cutting force were found at different levels as a result of Taguchi optimization.

Key words

AISI H10A, MQL, optimization, cutting force, surface roughness

1. INTRODUCTION

Hot work tool steels having high temperature strength, high toughness and resistance to thermal fatigue and shock are preferred frequently in many industrial applications. The chromium hot work steels are widely used for extrusion of aluminum, die casting of light metals and steel forging applications [1]. On the other hand, these steels due to chemical composition, microstructure, inclusions and thermo-mechanical properties are difficult to machine. When the die is subjected to heat treatment, some distortion usually occurs. Thus, machining allowance is left on the die prior to hardening in order to overcome these negativities as well as to ensure measurement and surface integrity. It is possible to adjust the die after the hardening and tempering by finish machining processes such as grinding, hard machining, etc.

Hard turning are mainly concentrated on the tool materials cost and the effect of the cutting conditions on machinability criteria. The machining of hardened steels using cubic boron nitride and ceramic tool are commonly known as a best replacement instead of grinding in order to reduce the tooling time and machining cost, keep off

the lubrication [2]. Also, it is very difficult to develop a comprehensive model with related to any machinability criteria involving all machining conditions due to contain many factors. The machinability criteria such as cutting forces, surface roughness, tool life, dimensional accuracy can be significantly affected by machining parameters, mechanical properties of workpiece material, rigidity of machine tools, tool material and coolant technique [3,4].

The control of the machinability criteria can be primarily provided by choosing appropriate values of cutting speed, feed rate and depth of cut in hard turning [5]. However, unsuitable cutting parameters have negative effects on the machining outputs such as machining time, cost. In this context, design of experiment and analysis for machining process, then optimization of machining output is great importance with regards to decrease machining cost [6]. Also, some scientists observed that there is a disagreement between the researchers in terms of the use of coolants or lubricants in hard turning. Thus, it is required to identify eco-friendly alternatives to conventional cutting fluids during hard turning as can be specified in many investigations [7]. Recently, scientists used nanoparticles in conventional lubricants owing to its remarkable improvement in thermo-mechanical, and heat transfer capabilities, decrease the friction coefficient and wear effect to enhance the efficiency and reliability of machine tools [8].

Newly, there are performed numerous experimental and statistical studies which are based on design and analysis of experiment methods to determine the effects of cutting conditions on machinability criteria. Aouici et al. conducted response surface methodology (RSM) in hard turning of DIN 1.2343 steel with CBN tool in order to obtain mathematical models for the cutting forces and surface roughness. They specified that the depth of cut and workpiece hardness are the most important factor on cutting forces while the feed rate and workpiece hardness have the most significant for surface roughness [9]. Boy et al. addressed on optimizing the cutting conditions to minimize the surface roughness, inner-diameter error and roundness in bearing rings produced by hard turning of AISI 52100 steel with coated CBN insert. The analysis of variance results indicated that the feed rate is the main factor for the surface roughness while the cutting speed is the major factor for the roundness and inner-diameter error [10]. Kaçal investigated the cutting performance of ceramic insert in terms of surface roughness and tool wear in turning of hardened PMD 23 steel with three different cutting speeds, feed rates and depth of cuts. The experimental results indicated that feed rate is the most significant factor affecting Ra followed by depth of cut [11]. Islam investigated the surface roughness and dimensional accuracy properties (diameter error and circularity) via dry, wet and minimum quantity lubrication turning processes applied to different materials. The author indicated that surface roughness and dimensional values are affected by different cooling methods and the best result is obtained with MQL application [12]. Sarıkaya and Güllü focused on the use of the Taguchi based grey relation analysis to optimize the MQL process parameters such as cutting fluid, flow rate and cutting speed in terms of tool wear forms and surface roughness during the turning of Haynes 25 super alloy. According to the ANOVA results, the contribution percentage of process parameters were found as the cutting fluid, fluid flow rate and cutting speed, respectively [13]. Paul et al. examined parameters of minimum fluid application for minimizing surface roughness, flank wear, cutting force, tool vibration and cutting temperature in machining of AISI 4340 steel. The authors emphasized that tool vibration reduced in hard turning with minimal fluid application and the better cutting performance was provided as compared with dry turning and wet turning where a commercial cutting fluid was applied at a rate of 5 l/min [14]. Mia et al. investigated surface roughness during turning of hardened steel of 600 BHN with uncoated carbide tool under MQL application. The researchers stated that the cutting speed is insignificant factor surface roughness while feed rate is important factor for roughness [15].

2. MATERIAL AND METHOD

2.1. Material and Equipment

The workpiece material was used AISI H10A tool steel with the following chemical composition: 0.32% C; 0.40% Mn; 2.75% Co; 2.95% Cr; 2.8% Mo; 0.55% V and balance Fe. The material is a hot work tool steel having high toughness, high thermal shock resistant and high wear resistance in high temperatures. The hardness of AISI H10A workpiece was increased to 54-55 HRC with vacuumed hardening method. CNGA120404 coded uncoated CBN (KB1610) inserts and PCLNR 2525M12 coded tool holder produced by Kenna Metal Company were used in hard turning experiments. Hard turning experiments were carried out on Johnford TC 35 CNC having 20 HP motor under minimum quantity lubricant (MQL) cutting condition. UFB20-Basic cooling system branded SKF was preferred as MQL applicator. The Lubri-Oil was used as lubricant type because of AISI H10A steel. It was decided after preliminary experiments used MQL that the flow rate should be 16.25 ml/min.

The main cutting force (F_c) and average surface roughness (R_a) were considered on as the machinability criteria of AISI H10A steel. The cutting forces were measured by using Kistler 9257B type piezoelectric dynamometer during turning of workpiece material. Mahr Perthometer M1 type roughness device was used to measure surface roughness in hard turning experiments. The surface roughness values were taken into account in evaluating the roughness of machined surface. The experiments were repeated two times and evaluations were done by taking arithmetic mean of surface roughness.

2.2. Experimental Design and Optimization

The cutting parameters directly effecting machinability criteria were determined in experimental design according to Taguchi method. For this purpose, three factors were chosen as depth of cut (a), feed rate (f) and cutting speed (V) (seen Table 1). The levels of these parameters were preferred by reference to the recommendation of cutting tool firm and researches on hard turning. Taguchi L_9 orthogonal array was used for experimental design in terms of the factor and levels. Moreover, the experiments conducted with uncoated CBN tools were performed in MQL cutting condition.

Table 1. Factors and their levels

Factors	Unit	Level 1	Level 2	Level 3
Depth of cut (a)	mm	0.1	0.2	0.3
Feed rate (f)	mm/rev	0.05	0.1	0.15
Cutting speed (V)	m/min	100	150	200

In the light of experimental results, the effects of factors on the main cutting force (F_c) and average surface roughness (R_a) were determined by analysis of variance (ANOVA) with 95% confidence level. Finally, cutting parameters for F_c and R_a were optimized based on Taguchi method. Therefore, the-smaller-the-better approach were applied due to desire of minimum F_c and R_a which is selected as performance characteristic in hard turning experiments. The cutting parameters giving optimum cutting force and surface roughness were determined in optimization study according to S/N ratio. The S/N ratios for the-smaller-the-better approach is calculated as follows [16].

$$S/N = -10 \cdot \log \left(\frac{1}{n} \cdot \sum_{i=1}^n y_i^2 \right) \quad (1)$$

Here, y_i is the i th measure of the experimental results in a run and n gives the number of measurements in each experiment. The function '-log' is a monotonically decreasing one, it means that we should maximize the S/N ratio. Statistical analyses and optimization studies were performed by Minitab software.

3. RESULTS AND DISCUSSION

3.1. Evaluation of Experimental Results

The variations of main cutting force and surface roughness values obtained with uncoated CBN tools in MQL cutting condition are given in separate graphs. Variations of F_c and R_a depending on feed rate (f), cutting speed (V) and depth of cut (a) are shown in Figure 1 and 2, respectively.

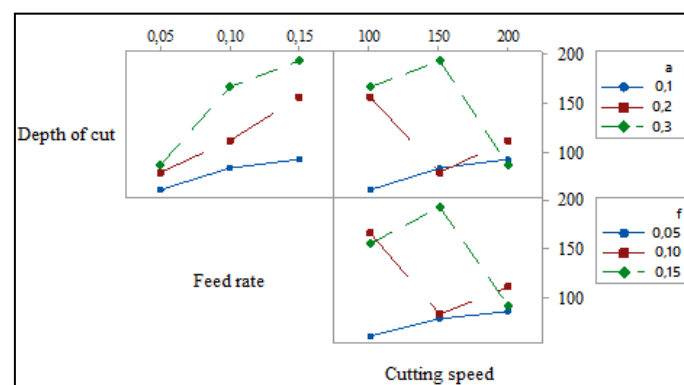


Figure 1. Variations of F_c in MQL cutting condition.

As can be seen from Figure 1, it was observed that main cutting force (F_c) generally increase with increasing feed rate and depth of cut. It was attracted from Figure 1 that the force values have irregularities in terms of cutting speed-depth of cut and cutting speed-feed rate interactions. This can be attributed with design of experiment that distribution of cutting speed is complicated in L_9 orthogonal array. The lowest surface roughness value was

obtained as 62.73 N with feed rate of 0.05 mm/rev, cutting depth of 0.1 mm and cutting speed of 100 m/min in MQL cutting condition with uncoated CBN inserts.

Average surface roughness (Ra) values increase with increasing feed rate and depth of cut (seen Fig.2). In a similar way, it was determined that Ra values does not decrease with increasing cutting speed because of hybrid experimental design. The lowest surface roughness value was obtained as 0.139 μm with the lowest feed rate, depth of cut and cutting speed in MQL cutting conditions with uncoated CBN inserts. The highest surface roughness was obtained as 0.36 μm with feed rate of 0.15 mm/rev, depth of cut of 0.3 mm and cutting speed of 150 m/min.

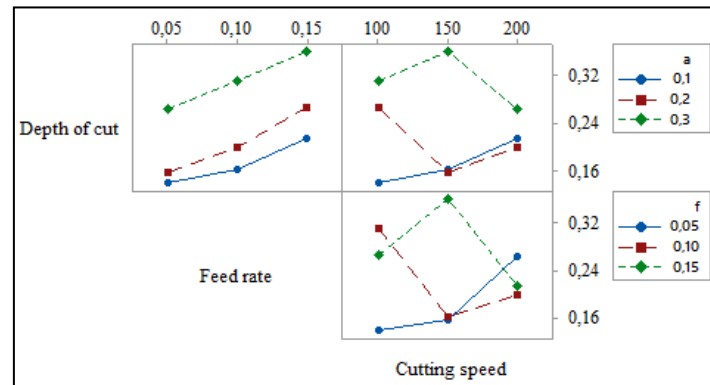


Figure 2. Variations of Ra in MQL cutting condition.

ANOVA was performed to determine the effectiveness of cutting parameters on main cutting force and average surface roughness during machining with uncoated CBN insert of AISI H10A hot work tool steel under minimum quantity lubrication (MQL) cutting environment. The results of ANOVA analysis of the cutting force and the surface roughness are presented in Tables 2 and 3, respectively.

Table 2. ANOVA results for cutting force

Factor	DF	SS	MS	F-ratio	P-value	PCR (%)
Depth of cut	2	39.1134	19.5567	114.24	0.009	43.27
Feed rate	2	45.7484	22.8742	133.62	0.007	50.68
Cutting speed	2	4.3925	2.1962	12.83	0.072	4.52
Residual error	2	0.3424	0.1712			1.53
Total	8	89.5966				100

DF: Degrees of freedom; SS: Sequential sum of squares; MS: Mean sum of squares

Table 3. ANOVA results for surface roughness

Factor	DF	SS	MS	F-ratio	P-value	PCR (%)
Depth of cut	2	44.2369	22.1185	201.57	0.005	66.57
Feed rate	2	20.7335	10.3668	94.47	0.000	31.03
Cutting speed	2	0.9312	0.4656	4.24	0.191	1.08
Residual error	2	0.2195	0.1097			1.32
Total	8	66.1211				100

DF: Degrees of freedom; SS: Sequential sum of squares; MS: Mean sum of squares

P value should be lower than 0.05 in 95% confidence level in order to determine that any parameter acting on the cutting force or surface roughness is effective on them. The feed rate (f) was the most important parameter affecting the cutting force with a PCR of 50.68% while the most significant parameter for surface roughness was obtained

as depth of cut (a) with a PCR of 66.57%, as can be seen from Table 2 and 3. The other statistically significant parameters on F_c and R_a are depth of cut and feed rate with PCR of 43.27% and 31.03%, respectively.

3.2. Optimization with Taguchi Method

The main cutting force and surface roughness values were obtained as a result of hard turning experiments performed based on the Taguchi L_9 orthogonal array. According to Taguchi method, the experimental results have been transformed into S/N ratios to measure the quality characteristics diverging from the desired value. The S/N ratio is the ratio of the mean (signal) to the standard deviation (noise). In the present study, S/N ratio is calculated as the logarithmic transformation of the loss function by using the-smaller-the-better approach as minimum values of F_c and R_a is required. The experimental results and S/N ratios is calculated by using Eq. (1) for F_c and R_a are shown in Table 4.

The mean values of S/N ratios (η) of the factors for each of the levels were determined by Equation (1). Figure 3 and Figure 4 shows the graphic of the η values for main cutting force and surface roughness, respectively. Regardless of category of the performance characteristics, a maximum η value corresponds to a better performance according to Taguchi method. Therefore, the optimal level of the cutting parameters is the level with the maximum η value. As can be observed from Figure 3 that the optimum cutting parameters for main cutting force were: a1 (0.1 mm), f1 (0.05 mm/rev) and V3 (200 m/min). Figure 4 also displayed that, the optimum cutting parameters for surface roughness were obtained as a1 (0.1 mm), f1 (0.05 mm/rev) and V2 (150 m/min).

Table 4. Experimental results based on L_9 orthogonal array and their S/N ratios

Exp. no	Depth of cut (a)	Feed rate (f)	Cutting speed (V)	R_a (μ)	S/N (dB)	F_c (N)	S/N (dB)
1	0.1	0.05	100	0.139	17.1397	62.73	-35.9495
2	0.1	0.1	150	0.16	15.9176	84.01	-38.4866
3	0.1	0.15	200	0.212	13.4732	93.08	-39.3771
4	0.2	0.05	150	0.155	16.1933	79.88	-38.0488
5	0.2	0.1	200	0.198	14.0667	112.22	-41.0014
6	0.2	0.15	100	0.267	11.4697	157.24	-43.9313
7	0.3	0.05	200	0.263	11.6008	87.54	-38.8441
8	0.3	0.1	100	0.31	10.1727	166.78	-44.4429
9	0.3	0.15	150	0.36	8.8739	193.62	-45.7390

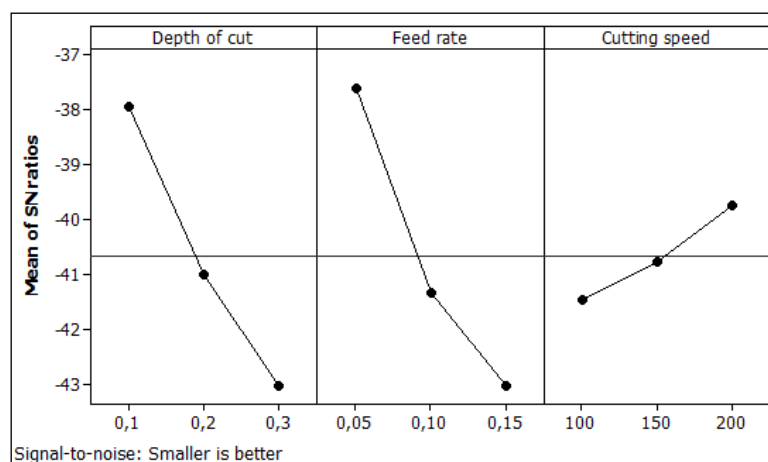


Figure 3. Main effect plot for S/N ratios of F_c

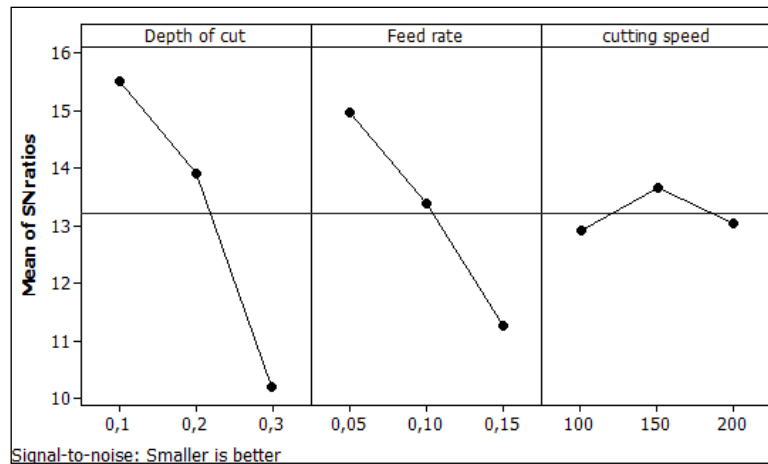


Figure 4. Main effect plot for S/N ratios of Ra

In the last stage of Taguchi method after the estimation of the optimum parameters, confirmation experiments are performed to display the accuracy of the optimization and to determine the improvement grade. Hence, the S/N ratio of performance characteristic for the experiments conducted at optimum parameters are calculated by using equation (2). Equation (1), which is the expression for performance characteristic, can be derived from by equation (3).

$$\eta_G = \bar{\eta}_G + (\bar{T}_o - \bar{\eta}_G) + (V_o - \bar{\eta}_G) + (f_o - \bar{\eta}_G) \quad (2)$$

$$F_c, Ra = 10^{-\eta_G/20} \quad (3)$$

Here, η_G is the S/N ratio calculated at optimal level of factors (dB), $\bar{\eta}_G$ is the mean S/N ratio of all parameters (dB), \bar{T}_o , \bar{V}_o and \bar{f}_o are the mean S/N ratio once depth of cut, feed rate and cutting speed are at optimum levels, F_c and Ra are the calculated cutting force and surface roughness value, respectively. Consequently, comparison of predicted and experimental results for main cutting force and average surface roughness are given in Table 5 and Table 6, respectively.

Table 5. Results of confirmation experiments for main cutting force

	Initial cutting parameters	Optimal cutting parameters	
		Prediction	Experimental
Level	a2f1V2	a1f1V3	a1f1V3
Main cutting force, (N)	79.88	50.09	53.81
S/N ratio (dB)	-38.0488	-33.9965	-34.6172
Improvement of S/N ratio	3.4316 dB		
Prediction error (dB)	0.6207		

Table 6. Results of confirmation experiments for surface roughness

	Initial cutting	Optimal cutting parameters	
		Prediction	Experimental
Level	a2f1V2	a1f1V2	a1f1V2
Surface roughness, (μm)	0.155	0.122	0.132
S/N ratio (dB)	16.1933	17.7259	17.5885
Improvement of S/N ratio	1.3952 dB		
Prediction error (dB)	0.1374		

The confirmation experiments results showed that prediction error became 0.6207 dB for the main cutting force and 0.1374 dB for the average surface roughness. It has been confirmed that the cutting force and surface roughness can be reduced significantly with Taguchi optimization, as a result of the machinability research on hardened AISI H10A hot work tool steel with uncoated CBN cutting tools and minimum quantity lubrication (MQL) cutting environment. Considering the differences between the predicted results for the cutting force and the surface roughness with the results of confirmation experiments, it was concluded that a remarkable success has been achieved by Taguchi method.

4. CONCLUSIONS

In this study, machinability experiments on hardened AISI H10A hot work tool steel with uncoated CBN inserts were performed under minimum quantity lubrication (MQL) condition. The effects of cutting parameters (feed rate, depth of cut and cutting speed) on the F_c and R_a were analyzed according to Taguchi experimental design. Obtained results were summarized below

- It was determined that F_c and R_a increased with increasing depth of cut and feed rate in MQL cutting conditions and this situation was referred to increasing chip cross-section with increasing feed rate and depth of cut.
- In the optimization of the cutting parameters for the cutting force by the Taguchi method, cutting depth of 0.1 mm, feed rate of 0.05 mm/rev and cutting speed of 200 m/min were found to be optimum conditions.
- In the optimization performed for the surface roughness, cutting depth of 0.1 mm, feed rate of 0.05 mm/rev and cutting speed of 150 m/min were found to be optimum conditions.
- MQL application is strongly recommended in order to increase efficiency in hard turning processes on account of the above-mentioned evaluations.

ACKNOWLEDGMENT

This study is supported by Scientific Research Project Unit of Karabük University (KBÜ-BAP-14/1-YL-019) and the authors express their appreciation for this support.

REFERENCES

- [1]. R. Shivpuri, *Dies and die materials for hot forging*. ASM Handbook, Metalworking: Bulk Forming, USA, 2005.
- [2]. I. Meddour, M.A. Yallese, R. Khattabi, M. Elbah, L. Boulanouar, Investigation and modeling of cutting forces and surface roughness when hard turning of AISI 52100 steel with mixed ceramic tool: cutting conditions optimization. *Int J Adv Manuf Technol.* 77, 1387–1399, 2015.
- [3]. T. Özel, T.K. Hsu, E. Zeren, Effects of cutting edge geometry, workpiece hardness, feed rate and cutting speed on surface roughness and forces in finish turning of hardened AISI H13 steel. *Int J Adv Manuf Technol.* 25, 262–269, 2005.
- [4]. J.E. Stahl, *Metal Cutting-Theories and models*, Lund University in cooperation with Seco Tools AB, Lund/Fagersta, Sweden, 2012.
- [5]. E. Yücel, M. Günay, Modelling and optimization of the cutting conditions in hard turning of high-alloy white cast iron (Ni-Hard). *Proc IMechE Part C: J Mech Eng Sci.* 227(10), 2280-2290, 2013.
- [6]. H. Yurtkuran, M.E. Korkmaz, M. Günay, Modelling and Optimization of the Surface Roughness in High Speed Hard Turning with Coated and Uncoated CBN Insert. *Gazi Uni J Sci.* 29(4), 987-995, 2016.
- [7]. S. Chinchankar, S.K. Choudhury, Machining of hardened steel-Experimental investigations, performance modeling and cooling techniques: A review. *Int J Mach Tools Manuf.* 89, 95–109, 2015.
- [8]. N.A.C. Sidik, S. Samion, J. Ghaderian, M.N.A.W.M. Yazid, Recent progress on the application of nanofluids in minimum quantity lubrication machining: A review. *Int J Heat Mass Transf.* 108, 79–89, 2017.
- [9]. H. Aouici, M.A. Yallese, K. Chaoui, T. Mabrouki, J.F. Rigal, Analysis of surface roughness and cutting force components in hard turning with CBN tool: prediction model and cutting conditions optimization. *Measurement* 45, 344–353, 2012.
- [10]. M. Boy, I. Ciftci, M. Gunay, F. Ozhan, Application of the taguchi method to optimize the cutting conditions in hard turning of a ring bore. *Materials and Technology* 49 (5), 765–772, 2015.

- [11]. A. Kaçal, Investigation of Cutting Performance of the Ceramic Inserts in Terms of the Surface Roughness and Tool Wear at Turning of PMD 23 Steel. *Applied Mechanics and Materials*, 686, 10-16, 2014.
- [12]. M.N. Islam, Effect of additional factors on dimensional accuracy and surface finish of turned parts. *Machining Science and Technology* 17, 145–162, 2013.
- [13]. M. Sarıkaya, A. Güllü, Multi-response optimization of minimum quantity lubrication parameters using Taguchi-based grey relational analysis in turning of difficult-to-cut alloy Haynes 25. *Journal of Cleaner Production* 91, 347-357, 2015.
- [14]. P.S. Paul, A.S. Varadarajan, R.R. Gnanadurai, Study on the influence of fluid application parameters on tool vibration and cutting performance during turning of hardened steel. *Engineering Science and Technology, an International Journal*, 19, 241-253, 2016.
- [15]. M. Mia, M.H. Razi, I. Ahmad, R. Mostafa, S.M.S. Rahman, D.H. Ahmed, P.R. Dey, N.R. Dhar, Effect of time-controlled MQL pulsing on surface roughness in hard turning by statistical analysis and artificial neural network. *Int J Adv Manuf Technol.* 1-13, 2017.
- [16]. M. Günay, Optimization with Taguchi method of cutting parameters and tool nose radius in machining of AISI 316L steel. *Journal of Faculty Engineering Architecture of Gazi University*, 28(3), 437-444, 2013.





Influence of Different Si Levels on Mechanical Properties of Aluminium Casting Alloys

Onur Ozaydin^{1}, Alper Kaya¹*

¹*Cevher Wheels, R&D Department, 35411, Gazimir/Izmir, Turkey.*

**Corresponding Author email: oozaydin@cevherwheels.com*

Abstract

AlSi7 and AlSi11 are the most commonly used materials in aluminum alloy wheel production. The main difference is the heat treatment application; for wheel production AlSi7 is usually used in heat treated form while AlSi11 is not. Heat treatment processes play a vital role on production costs. More than fifty percent of aluminum wheels are heat treated however the exact value varies between different manufacturers. Additional heat treatment costs directly affect the competitiveness of the manufacturer. In this study the material properties of an alternative Si level between AlSi7 and AlSi11 are examined and the effects of these intermediate Si levels on mechanical properties are compared with that of AlSi7 and AlSi11. The aim of this study to examine the possibility of obtaining mechanical properties of heat treated AlSi7 with a non-heat-treated material differing only in Si content. In this experiment all processes and casting parameters for different material types are the same except for the Si content. In addition to an experimental study, the mechanical properties of the alternative material are simulated by utilizing a material analysis software and these properties are compared with experimental results. Thus, correlation between simulation and experimental study results can also be examined. As a conclusion, the alternative non-heat-treated material is presented to manufacturers. These results may be used to bypass the heat treatment process and to decrease the cost of final product.

Key words

Aluminum, Heat Treatment, Mechanical Properties,
Simulation of Material Properties

1. INTRODUCTION

In the last decades, the importance of weight reduction is growing dramatically in the automotive industry. Not only fuel efficiency, but also emission values which is regulated by rule-maker lead the automotive manufacturer to use lightweight materials. Considering the low density, better mechanical properties, easier machinability, corrosion resistance and recyclability, Al-Si based alloys are widely used in automotive components. Especially, AlSi7 and AlSi11 dominate the Al-Si based alloys as a main material in wheel production. The main difference is the heat treatment application; for wheel production AlSi7 is usually used in heat treated form while AlSi11 is not. The primary reason of heat treatment is improving the mechanical properties. Many authors investigate the optimization of heat treatment to get better mechanical properties [1],[2],[3]. Main purpose of these optimization studies is cost reduction because the heat treatment processes play a vital role on production costs. The exact value varies between different wheel manufacturers, but more than fifty percent of products are heat treated and

heat treatment costs directly affect the competitiveness of the wheel manufacturer. In this study the properties of an alternative Si level between AlSi7 and AlSi11 is examined and the effects of these intermediate Si levels on mechanical properties are compared with that of AlSi7 and AlSi11. The aim of this study to examine the possibility of obtaining mechanical properties of heat treated AlSi7 with a non-heat-treated material differing only in Si content.

2. MATERIALS AND METHODS

In addition to two main materials, the alternative Si level material was produced by mixing 50% percentage of each two main material ingots. Thus, AlSi9Mg which is known as hypoeutectic silumin is obtained as an alternative alloy. The alternative alloy was melted in a SiC crucible furnace and all serial production procedures such as grain refinement, modification and degassing were applied in accordance with related regulations. Grain refinement was provided by Al-5Ti-1B rods, alloys were modified by Strontium (AlSr15) and degassed by nitrogen. Quantity of Al-5Ti-1B rods and Strontium (AlSr15) were calculated and added according to chemical content which was measured by OES (Optical Emission Spectrometry) (As shown in Table 1.). [5],[6],[7]

Table 1. Chemical composition [7]

	Si	Fe	Cu	Mn	Mg	Zn	Ti
AlSi7	6,5-7,5	0,15	0,02	0,10	0,30-0,45	0,07	0,10-0,18
AlSi9	9,0-10,0	0,15	0,02	0,05	0,30-0,45	0,07	0,15
AlSi11	10,0-11,8	0,15	0,02	0,05	0,1-0,45	0,07	0,15

The first step of casting process is mold preparation. In mold preparation step, wheel mold was coated and preheated to minimize the casting defects such as shrinkage, cracks and metal flow problems. Directional solidification leads to an increase in mechanical properties and a decrease of casting defects. The directional solidification can be controlled by utilizing the cooling channels in the mold. All casting process parameters such as pouring temperature, mold coating type, preheating mold temperature and cooling channels properties were the same as in serial production.

The second step of casting process is the die casting. 36 Wheel specimens were casted by LPDC (Low Pressure Die Casting) method at 720 ± 20 °C for each 3 samples sets (AlSi7 – AlSi9 – AlSi11) to investigate differences in metallurgical and mechanical tests.

Table 2. Specimen configuration

	Metallurgical Tests				Mechanical Tests	
	As Cast	With HT* Without Wheel Base Coating	Without HT* With Wheel Base Coating	With HT* With Wheel Base Coating	Without HT* With Wheel Base Coating	With HT* With Wheel Base Coating
AlSi7	1	1	1	1	16	16
AlSi9	1	1	1	1	16	16
AlSi11	1	1	1	1	16	16

*HT: Heat Treatment

Production process was finished with heat treatment application. Heat treatment starts with solution treatment and continues with water quenching and is finalized with artificial aging. The next step of production process is machining. Machining parameters depend on the technical drawing, tolerances, wheel types and milling tools.

To minimize these complexity, all wheel specimens were casted into same mold and machined with same machining program and parameters. Machined wheels were deburred and inspected, all specimens were also controlled by a helium-based leakage detector to detect cracks in rim section.

The final step of wheel production process is painting. This process contains three phases; first phase is primary coating; second phase is the color coating and third phase is clear coating. All coatings are applied in an oven since a certain curing temperature is required. Curing temperature is between 100 °C - 210 °C. In a sense, the wheel base coating can be called as secondary artificial ageing. In this study, two different sets, one with wheel base coating and one without wheel base coating were investigated with regarding to metallurgical properties to understand the effect base coating.

In addition to tensile test specimens obtained by machining of wheels, some tensile test specimens were produced by gravity casting method. Figure (1.a) shows LPDC (Low Pressure Die Casting) method and Figure (1.b) shows permanent mold for gravity casting tensile test specimens.

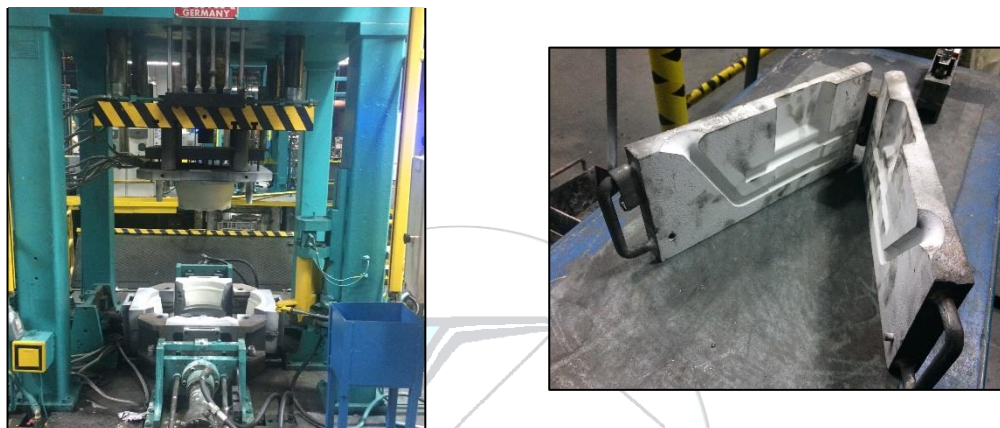


Figure 1. (a) LPDC (Low Pressure Die Casting) method (b) Permanent mold for tensile specimen

All microstructure samples were prepared in accordance with standard metallographic techniques. First, samples were grinded with SiC paper and polished. Second, samples were etched with 0.5% HF solution and examined with an optical microscope. Thermal analysis was conducted by an IDECO thermal analyser that can measure with $\pm 0,1$ °C accuracy and can report the grain size. Both types of tensile test specimens were machined and finalized according to DIN 50125 [9] and tested according to EN ISO 6892-1:2016 [10] with a Zwick Z100 model test machine.

Impact tests are applied to verify the wheel shock loading resistance. The impact test can simulate a curb stone or pothole hit and the impact load is dependent on axle load of the car.

Damage on wheels is evaluated in accordance with related specifications and standards. [11],[12]The wheel is considered to fail when the following are observed: visible fractures / cracks, separation of the centre from the rim and air pressure loss in 1 min. [12]

Finally, all metallurgical and mechanical tests are completed in laboratory environment at room temperature.

3. RESULTS AND DISCUSSION

Specimens were investigated with regards to metallurgical and mechanical properties. First, microstructure and macrostructure were obtained. Differences between the samples were examined. Second, UTS (Ultimate Tensile Strength), YS (Yield Strength) and Elongation ($\epsilon\%$) and hardness values were measured. Finally, impact tests were applied to final product. All these steps play a vital role in validation of a wheel.

Chemical contents of the samples are shown in Table 3.

Table 3. Chemical composition of samples

	Si	Fe	Cu	Mn	Mg	Zn	Ti
Sample Group #1	10,765	0,1113	0,0013	0,0029	0,173	0,0031	0,1206
Sample Group #2	9,000	0,1076	0,0012	0,0027	0,304	0,0039	0,1166
Sample Group #3	7,151	0,1070	0,0011	0,0025	0,302	0,0033	0,1203

3.1. Microstructure Analysis

The microstructures of the alloys with different Si level are shown below. All microstructures in Figure 2 are as cast and before heat treatment. Figure 2 (a) shows the sample with highest Si level and higher amount of Al-Si eutectic structures may be observed. Figure 2 (b) shows intermetallic phases and structure. Figure 2 (c) shows lowest Si level and a higher amount of α -Al dendrite may be remarked.

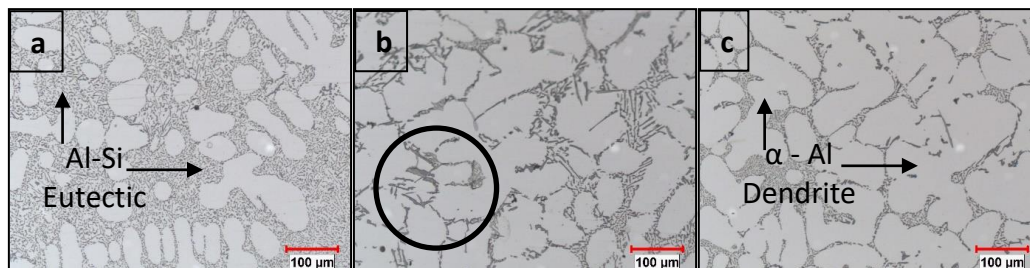


Figure 2. Microstructure of (a) Sample Group #1 as cast (b) Sample Group #2 as cast (c) Sample Group #3 as cast

All microstructures in Figure 3 are obtained from the final product, i.e. after heat treatment and base coating. Figure 3 (a) shows globular structures which are more invisible after heat treatment. Figure 3 (b) shows a decrease in intermetallic phases. Figure 3 (c) shows that Si particles are distributed in the Al matrix uniformly.

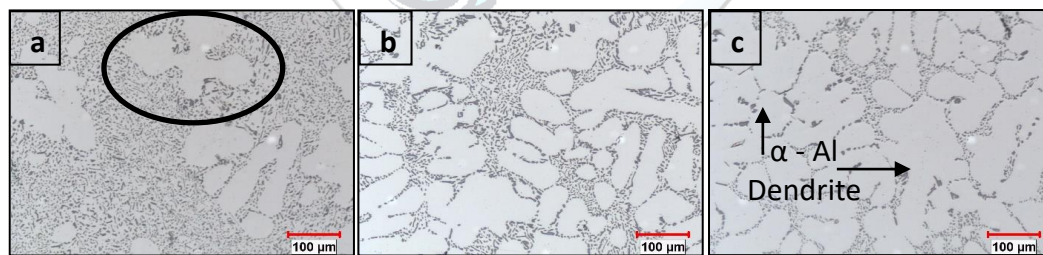


Figure 3. Microstructure of (a) Sample Group #1 as final product (b) Sample Group #2 as final product (c) Sample Group #3 as final product

3.2. Tensile Test Results

Tensile specimens are obtained by two different approaches. Firstly, by gravity casting into a permanent mold and secondly by obtaining from wheel spoke directly with machining. Elongation values of sample group #2 are at the lowest level. On the other hand, UTS and YS are better as sample group #3. As expected, heat treatment plays an important role.

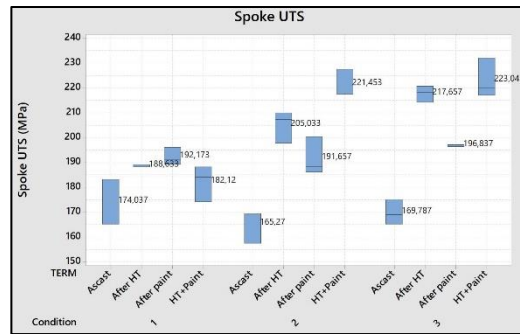
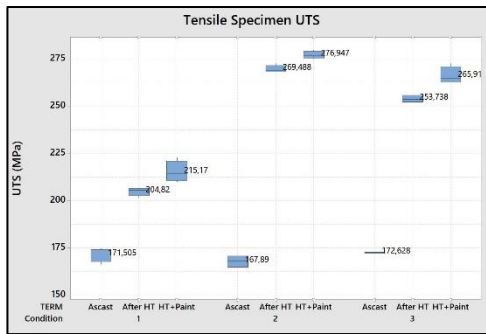


Figure 4. (a) UTS of Tensile Test Specimen (Permanent Mold)

(b) UTS of Wheel Spoke

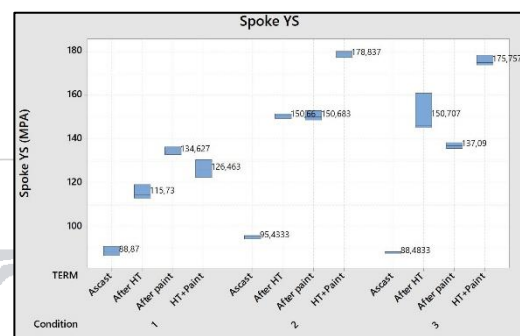
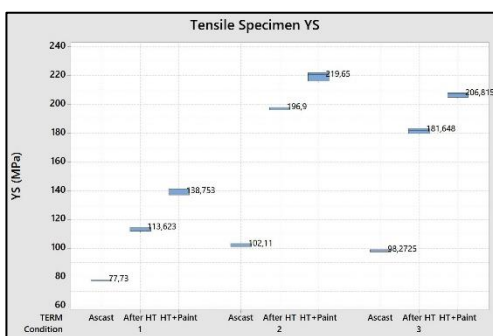


Figure 5. (a) YS of Tensile Test Specimen (Permanent Mold)

(b) YS of Wheel Spoke

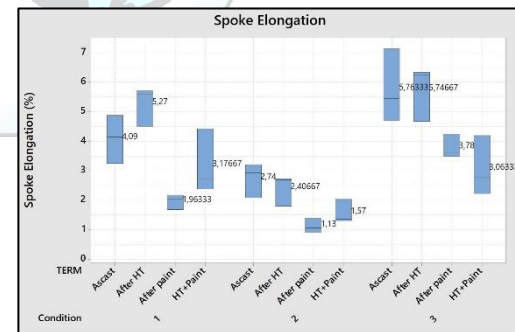
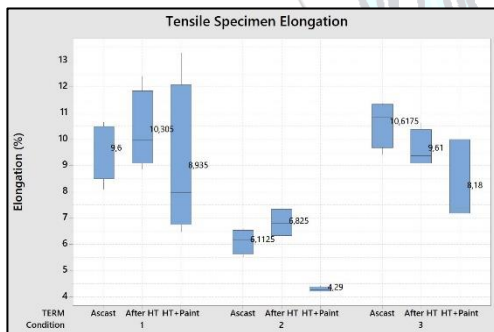


Figure 6. (a) Elongation of Tensile Test Specimen (Permanent Mold)

(b) Elongation of Wheel Spoke

3.3. Hardness Results

Hardness Brinell values were measured for (Sample group #1, Sample group #2, Sample group #3) at 3 stages: After heat treatment, after base coating and after heat treatment + base coating.

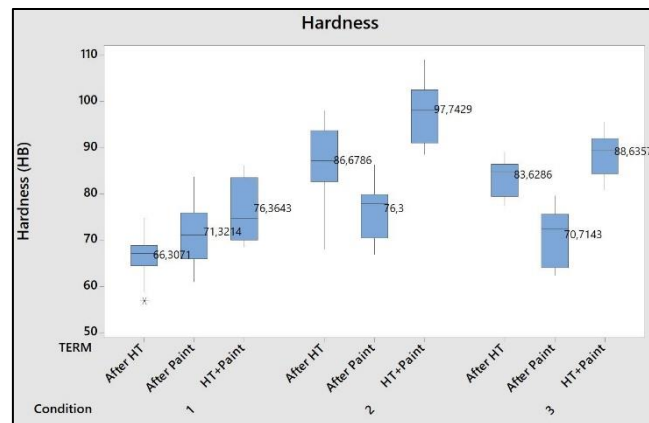


Figure 7. Hardness values

As seen figure above, sample group #2 (AlSi9 set) shows a higher average hardness at all 3 stages. The hardness may affect the impact values negatively.

3.4. Charpy Impact Test Results

Six test specimens which are prepared according to 'ISO 148-1: Metallic materials – Charpy pendulum – Impact Test' have been used to evaluate the toughness. [14] The results for all specimens are tabled below:

Table 4. Charpy Impact Test Results

	Sample Group #1		Sample Group #2		Sample Group #3	
	Heat Treated	Non – Heat Treated	Heat Treated	Non – Heat Treated	Heat Treated	Non – Heat Treated
	J (Joule)					
Specimen #1	4	4	2	2	3	3
Specimen #2	4	4	2	2	3	2,5
Specimen #3	4,5	3	3	2	4	3
Specimen #4	4	3	2	2	3	2
Specimen #5	4	3	2,5	2	3	3
Specimen #6	4	3	2	2	4	3
Average	4,08	3,33	2,25	2,00	3,33	2,75

According to results, the worst Charpy impact values are obtained from sample group #2. In addition to this, heat treatment helps to improve the impact values. Standard deviation is max. 0,5 for all measurements.

3.5. 13° Impact Test Results

Conducted according to 'Light alloy wheels – Impact test / ISO – 7141' Standard.

Table 5. 13° Impact Test Results

		OK	NOK
Sample Group #1	Heat Treated	650 Kg.	675 Kg.
	Non – Heat Treated	600 Kg.	625 Kg.
Sample Group #2	Heat Treated	-	450 Kg.
	Non – Heat Treated	-	450 Kg.
Sample Group #3	Heat Treated	575 Kg.	600 Kg.
	Non – Heat Treated	500 Kg.	525 Kg.

The weight is calculated according to wheel model. In this study, the weight is 450 Kg. and stopped with failure. The load is increased with extra 25 kg and the load reach final value which cause failure. As a result, sample group #2 failed with 13° impact tests, on the other hand, sample group #1 and #3 show better result from %11 to %44 according to calculated wheel load. Clearly, heat treated samples give better impact values, these results are actually in agreement with Charpy impact tests.

4. CONCLUSION

The chemical contents of all samples are in good agreement with literature. Microstructures and macrostructures were evaluated according to related specifications and results are approved. Al-Si eutectic, α -Al dendrite, modified Si structures may be observed.

'Permanent Tensile Specimen Mold' specimens of sample group #2 display almost same UTS and YS values with sample group #3 and better values than sample group #1. But, elongation (% ϵ) is lower than others. Chemical content differences –especially higher Mg- may lead these low elongation values.

Similarly, sample group #2 obtained by machining of 'wheel spoke' have similar UTS and YS values to sample group #3 and are better than sample group #1. Elongation (% ϵ) is lower than sample group #1 and #3.

The results of specimen obtained by machining 'wheel outer flange' displays the same trend with previous specimens; better UTS and YS, lower elongation (% ϵ).

The highest hardness (Brinell) results are obtained from sample group #2.

ACKNOWLEDGMENT

The authors would thank to all colleagues, especially A. Oktem, Z. Gokcen, E. Armakan, O. Beyter and Y. Sagnak from Cevher Alloy Wheels for their collaboration and Assoc. Dr. O. Culha for academic support.

REFERENCES

- [1]. J. Pezda and A. Jarco, *Effect of T6 Heat Treatment Parameters on Technological Quality of the AlSi7Mg Alloy*, Archives of Foundry Engineering Volume 16, Issue 4 / 95 – 100, 2016
- [2]. L.Y. Pio, *Effect of T6 Heat Treatment on the Mechanical Properties of Gravity Die Cast A356 Aluminium Alloy*, Journal of Applied Sciences 11 (11): 2048-2052, 2011
- [3]. V. Grubisic, *Air Tightness Control of Passenger Car Wheels*, Scientific Research Publishing, 171-180, 2017
- [4]. T. LIPIŃSKI, *Double Modification of AlSi₉Mg Alloy with Boron, Titanium and Strontium*, Archives of Metallurgy and Materials, Volume 60 Issue 3: 2415-2419, 2015
- [5]. *AlSiMg Alloy, Sr-Refined, Artificially Aged*, Cevher Inner Standard – Specification, 2014
- [6]. *Sr-Refined Eutectic AlSi Alloy*, Cevher Inner Standard – Specification, 2004
- [7]. *Rheinfelden, Primary Aluminium Casting Alloys*, Datasheet L 2.06/3-KH
- [8]. Y. Birol, *Effect of solution heat treatment on the age hardening capacity of dendritic and globular AlSi7Mg0.6 Alloys*, International Journal of Materials Research (formerly Zeitschrift fuer Metallkunde): 439-444, March 2010
- [9]. *Testing of metallic materials – Tensile test pieces, Prüfung metallischer Werkstoffe – Zugproben Deutsche Norm DIN 50125*, 2016
- [10]. *Metallic materials - Tensile testing - Part 1: Method of test at room temperature, Metalik malzemeler - Çekme deneyi - Bölüm 1: Ortam sıcaklığında deney metodu*, TS EN ISO 6892-1:2016, 2016

- [11]. *Road vehicles — Wheels/rims for commercial vehicles — Test methods, Karayolu taşıtları - Ticari taşıtlar için tekerlekler/jantlar - Deney yöntemleri*, TS ISO 3894, 2015
- [12]. *Road vehicles — Light alloy wheels – Impact test*, ISO 7141, 2005
- [13]. R.B. Thakare, *Stress Analysis in Wheel Rim by using Dynamic Cornering Fatigue Test Under Different Conditions*, IJARIE: International Journal of Advance Research and Innovative Ideas Vol-3 Issue-2, 2017
- [14]. *Metallic materials — Charpy pendulum impact test — Part 1: Test method*, ISO 148-1 2009





Recent advances in membrane fouling control in wastewater treatment processes

Amar Cemanovic¹, Neslihan Manav², Abdullah Kizilet³, Ozer Cinar^{2*}

¹Istanbul Technical University, Department of Environmental Engineering, 34300, Maslak/Istanbul, Turkey.

²Yildiz Technical University, Department of Environmental Engineering, 34220, Esenler/Istanbul, Turkey.

³Kahramanmaraş Sutcu Imam University, Department of Bioengineering and Sciences, 46100, Kahramanmaraş, Turkey.

*Corresponding Author email: ocinar@yildiz.edu.tr

Abstract

Membrane bioreactors (MBRs) are systems performing biological wastewater treatment with membranes utilized for solids separation. These systems have a wide range of applications since they offer some important advantages over conventional processes (e.g. high solids removal, low sludge production etc.). One of their main drawbacks, however, is the occurrence of membrane fouling – the occlusion of membrane pores by the various components found in the mixed liquor. Factors contributing to this phenomenon are various and stem from all the aspects of the treatment process, including membrane-, biomass- and wastewater characteristics as well as operating conditions. Efficient fouling control requires a thorough insight into reactor operation and the mechanisms leading to membrane fouling in the first place. While there are some universal remedies, proper tackling of this problem requires an individual approach tailored to the system of concern, since best results originate from the utilization of several methods together. This review outlines novel and emerging methods having a potential to contribute to sustainable and economical membrane fouling mitigation in the future.

Key words

Biological processes, wastewater treatment, membrane bioreactors, membrane fouling

1. INTRODUCTION

The first use of membrane bioreactor technology has been reported in 1969 by Smith et al. [1]. It was utilized with ultrafiltration membranes in a pilot-scale plant treating industrial wastewater. Even though the initial systems had many disadvantages, such as high capital costs and challenges in operation (mainly due to excessive membrane fouling), MBR slowly started to gain recognition and popularity. The advantages that allowed the MBR to start replacing many of the conventional systems widely in use are its low footprint (since no settling tank is necessary), high treatment efficiency, low sludge production, ease of retrofitting to existing systems etc.

Membranes utilized in MBR systems have a pore size range of 103 - 10⁴ µm. Based on it, the process is called microfiltration (MF), ultrafiltration (UF), nanofiltration (NF) or reverse osmosis (RO). Another division among MBR systems takes into account the system setup. Namely, the membrane modules may be located in the treatment tank itself (submerged system) or in a separate tank (side-stream system). For either of the mentioned configurations, the membrane itself can be in the form of a flat sheet or hollow fibers. All of these options are an important aspect of reactor design and operation and need to be carefully chosen based on the specific needs of the system in question.

2. FACTORS AFFECTING MEMBRANE FOULING

Due to the vast number of factors involved in wastewater treatment, there is no single system which suits all applications. Each system comes with its inherent advantages and disadvantages, and the membrane bioreactor systems are no exception. Apart from the aforementioned advantages, there are certain drawbacks as well when compared to conventional systems (CAS). Those include process complexity, relatively high capital and operating costs, increased foaming propensity and, most prominently, membrane fouling.

Membrane fouling can best be described as occlusion of membrane pores leading to decrease in filtration flux (in case of constant pressure operation mode) or increase in transmembrane pressure (TMP; in case of constant flux operation mode). It is not to be confused with clogging which occurs between membrane sheets or fibers inside modules/cassettes. There are many factors that affect the fouling propensity of a given system, and they can be broadly grouped into: membrane-, wastewater-, and biomass characteristics, as well as operating conditions (Figure 1).

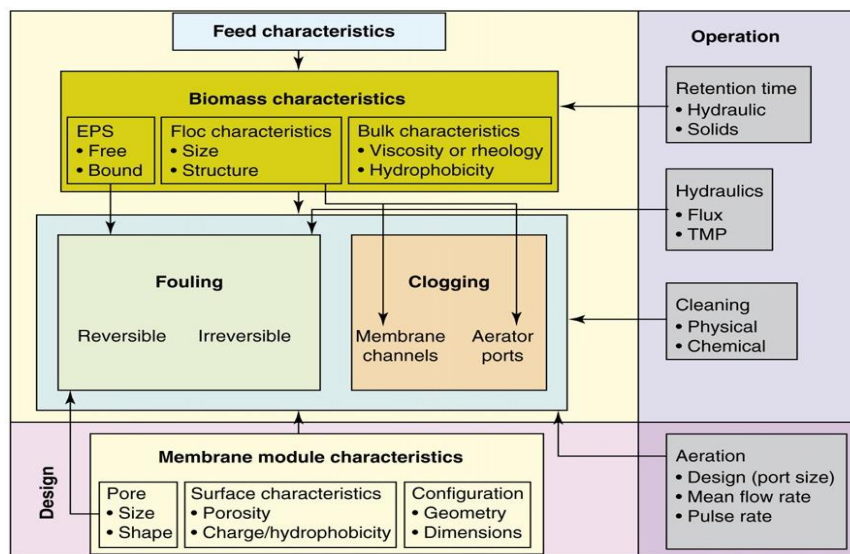


Figure 1. Interrelationship between MBR parameters and fouling [2]

2.1. Membrane characteristics

The proper choice of membranes for MBR systems is of crucial importance for the proper functioning and maintaining of the system. Membranes differ in the following aspects: material, pore size, porosity, hydrophobicity, charge, module etc. [3].

Membranes utilized in MBR systems are generally of polymeric nature, although inorganic membranes are also being used, as well as support materials (mostly textile) which are utilized for dynamic MBR (DMBR) systems. The main property they have to display is durability when exposed to various chemicals, varying pH levels, oxidants, varying temperatures as well as mechanical wear. While inorganic membranes are quite robust, their high price and limitations in their manipulation render them a relatively unpopular choice for MBRs. The most commonly used polymeric membrane material is PVDF (Polyvinylidene Difluoride), but others are also popular and include PTFE (polytetrafluoroethylene), polyolefins, PSF (polysulfonate), CA (cellulose acetate) etc. The support materials used for DMBR systems are generally of a larger pore size than commercial membranes and can be obtained at a much lower cost. They include different textile materials, woven and non-woven meshes etc.

Pore size has to be determined by considering the size of particles from the feed solution, since in the event that the two are similar, an increase in fouling probability occurs. Hereby, pore size distribution and the average pore size are the parameters considered. Porosity refers to the fraction of pores/voids in a material. Hydrophobicity is important since hydrophobic membranes are more prone to fouling, as they interact more closely with hydrophobic components of the feed solution. In order to alleviate this drawback, such membranes may be surface-modified. Charge is similarly important due to interactions on the membrane surface. Finally, module design and placement directly correlate with feed flow and particle occlusion, and have to be optimized in order to preclude fouling or clogging.

2.2. Wastewater characteristics

While domestic wastewater is mostly of similar composition everywhere, industrial wastewater is much more specific and differs largely based on the type of industry and the processes being applied. The influent wastewater affects both the biomass in the reactor as well as the membrane directly. Parameters such as turbidity and suspended solids concentration may represent the effect on the membrane, while COD, nutrient content, and potential toxicity exert their effect largely on the biomass. Other important parameters include temperature, pH, alkalinity etc.

2.3. Biomass characteristics

Biomass characteristics depend on its composition, the type of wastewater as well as the operating conditions. The main characteristics considered in MBR fouling studies include floc structure and floc size distribution, MLSS concentration, dissolved matter and EPS concentration etc. [3].

2.4. Operating conditions

The specific parameters that govern reactor operation and have a direct or indirect effect on membrane fouling are: aeration, HRT, SRT, F/M ratio, TMP/critical flux, hydrodynamics configuration, crossflow velocity etc. [3]. The reactor concentration of oxygen affects microbial growth and metabolism directly, but aeration in MBR systems also has an additional role. Namely, coarse air bubbles applied on the membrane surface in submerged systems cause shear stress which can maintain the thickness of the cake layer at a tolerable level [4]. When it comes to HRT, SRT and the F/M ratio, these parameters mostly affect the microbial biomass, i.e. its growth, flocking, EPS concentration etc. TMP and critical flux, on the other hand, are directly related to the fouling process and thus have to be closely controlled. Operating the reactor at a flux higher than the critical flux value leads to excessive fouling.

3. CLASSIFICATION OF MEMBRANE FOULING

There are various classifications of membrane fouling found in the literature. One of them is based on the possibility to remove fouling using specific cleaning processes. Namely, Park et al. [3] divide it into reversible and irreversible fouling, meaning that the former can be removed by physical or chemical cleaning (or a combination thereof), whereas the latter cannot be removed whatsoever. After irreversible fouling accumulates to a certain extent, the only way to recover initial flux/TMP values is to replace the membrane. Additionally, reversible fouling is further divided into recoverable and irrecoverable. Recoverable fouling can be removed by simple means, i.e. physical cleaning, backwashing etc., whereas irrecoverable requires the use of chemicals.

Another way fouling is classified is based on the place of its occurrence. Accordingly, it can be cake layer deposition or internal pore fouling. The former refers to the accumulation of solids on the surface of the membrane, whereby they form a so-called cake layer. That layer acts as a secondary membrane, with its own pores and permeability. This property is being exploited in DMBR systems, since the original membrane, called support material, has a relatively large pore size. On the other hand, internal pore fouling occurs when particles smaller than the pore diameter get stuck inside, thereby decreasing the amount of permeate that can pass through.

A further way of classification is according to the solids deposition pattern. Hereby, the solids that enter the pores of the membrane may either cause its narrowing or block it completely. Those that accumulate on the surface, however, form a cake layer, as previously mentioned (Figure 2).

4. ESTABLISHED MEMBRANE FOULING CONTROL METHODS

When it comes to membrane fouling control, there are two principle ways to approach the issue: membrane cleaning and fouling prevention.

Membrane cleaning can be physical in nature, including processes such as air sparging, intermittent aeration, backwashing (with air or permeate) as well as sponge scouring. It can also be chemical, which is usually the submersion of the membrane in an acid and/or basic solution. Physicochemical methods such as chemically enhanced backwashing are also in use.

Prevention of membrane fouling is performed in different ways, the most common of which is pretreatment of the influent wastewater. This involves methods such as coarse and fine screening, grit removal, primary sedimentation etc. Pretreatment is performed in conventional systems as well, but has a special importance in MBR systems due to their propensity for fouling. Another way of fouling prevention is operation of the reactor at subcritical flux level, as well as close control of sludge parameters, including MLSS, HRT, SRT, DO, F/M ratio.

One of the more advanced approaches to the problem of membrane fouling is biological control. There are several established methods, such as quorum quenching, enzymatic digestion, as well as utilization of nitric oxide (NO) and bacteriophages.

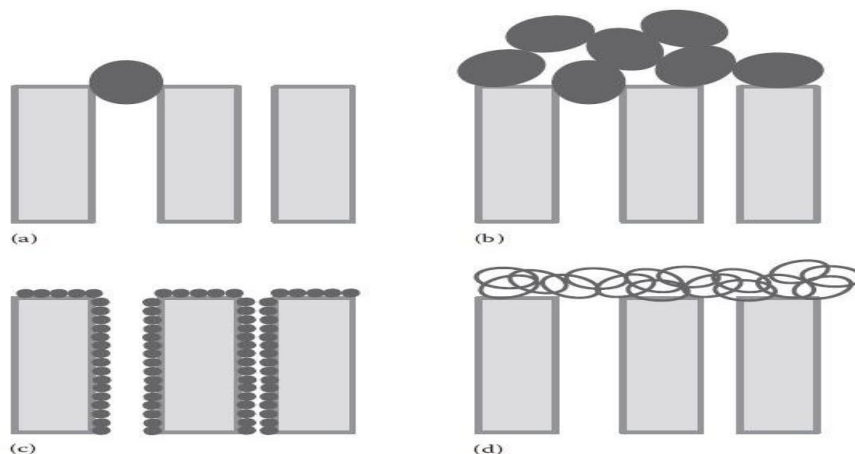


Figure 2. Mechanisms of membrane fouling according to solids deposition pattern: a) complete blocking, b) internal pore blocking, c) intermediate blocking, and d) cake formation [3].

Quorum quenching is basically the inhibition of quorum sensing (QS), a means of bacterial communication through signal molecules which enables them to produce biofilms [5]. The main approaches hereby are prevention of the production of these signal molecules, interference with the receptor of the signal or inactivation of the signals [6]. An example of the latter can be found in studies [7] and [8].

When it comes to enzymatic digestion, it can be applied on different levels, be it to biodegrade the aforementioned signal molecules or the biofilm directly. The latter works by targeting EPS, the main building material that connects bacteria into a biofilm. Several groups reported success applying this approach ([9], [10], [11]), but some concerns remain due to the short catalytic lifetime and loss of free enzymes.

Nitric oxide is a biological messenger molecule which signals bacteria to disperse their biofilm [5]. It has been shown to work for a wide range of bacterial species. The downside to this approach is the low solubility of NO in water.

Bacteriophages are a type of virus which specifically attacks bacteria, wherein it propagates eventually killing its host. In wastewater treatment applications, they have been shown to inhibit or disrupt biofilm formation on membrane surfaces ([12], [13], [14]). One of the major disadvantages of this method is the high specificity of bacteriophages against the target bacteria.

Another important approach to fouling control is through the use of electricity-based methods, the most prominent being electrocoagulation and electrophoresis.

Electrocoagulation works in-situ by creating metal cations at the anode (e.g. Fe^{3+} , Al^{3+} etc.) which then act as coagulating agents, reducing the charge difference between particles in the solution and thereby enabling them to coagulate into larger flocs. The method has been proven efficient ([15], [16]) and has a major advantage over chemical coagulation – no chemical sludge is produced. However, with this approach, care has to be taken to provide optimized conditions so as not to cause bacterial inactivation.

Electrophoresis applications, on the other hand, exploit the negative charge found on particles in the aqueous solution of the reactor. Namely, a direct current (DC) electric field applied close to the membrane drives off the particles from the membrane and towards the anode ([17], [18]). The main limiting factors in the utilization of this method are electrode corrosion and high energy consumption.

There is a variety of methods dealing with modifications of the properties of both membranes and modules. Membrane modification is most often performed by surface modification to decrease the hydrophobicity, which is performed either by coating or grafting a functional group. Another prominent method involves modification of the surface morphology to reduce microbial deposition. When it comes to module modification, it most often comes down to alterations of shape in order to create more favorable hydrodynamic conditions.

Finally, dynamic MBR systems are viewed as an improvement over conventional MBRs when it comes to cost and membrane fouling. These systems rely on support materials with a larger pore size, on top of which a secondary (cake) layer forms (dynamic membrane). This layer is composed of solids from the solution, and has a

pore size comparable to that of microfiltration membranes. Due to the fact that mostly inexpensive textile materials and meshes are used as support material, these systems have a lower capital cost than conventional MBRs. Furthermore, since biomass retention is performed by the secondary layer, the support material is much less prone to fouling. Flux/TMP recovery is mostly as easy as removing the cake layer. However, the drawback of DMBRs is that initial effluent quality is low, until the secondary membrane is fully formed (unless pre-formed dynamic membrane is used).

5. ESTABLISHED MEMBRANE FOULING CONTROL METHODS

Being a major drawback of MBR systems, membrane fouling is being addressed by a considerable number of studies. New fouling control methods are being devised regularly, and the following sections describe some of the most promising among them.

5.1. Addition of adsorbents

Adsorbents are porous compounds having the ability to bind different molecules from the surrounding medium to their surface. When it comes to MBR systems, these compounds can help control membrane fouling by removing organics and other pollutants from solution, or providing a surface for attached growth of biomass. The most commonly applied adsorbents are powdered and granular activated carbon (PAC and GAC, respectively) [19]. PAC concentration has to be determined carefully, since the small size of the particles coupled with a high dosage can worsen the fouling of membranes. GAC, on the other hand, has a larger particle size and is therefore suitable as biologically activated carbon, which is covered in the next section.

5.2. Mechanically assisted membrane aeration scouring

This method encompasses the addition of abrasive particles to the reactor solution so as to enhance the membrane surface scouring. Most often used are GAC, plastic beads or other biofilm carriers. With the exception of GAC, they all perform a dual role, acting both as abrasive for the membrane and as a surface for attached growth of the biomass. GAC has the added property of being a potent adsorbent (in this context termed biologically activated carbon), and as such has been shown to be able to provide a 20-60% enhancement of flux ([20] and [21]). Additionally, the property of having both suspended and attached growth in the same reactor contributes significantly to the wastewater treatment efficiency of the system. Not all types of biofilm carrier work for all systems, though, so more research is needed in this field.

5.3. Novel membrane developments

Increase in turbulence near the membrane surface has been shown to be an efficient tool against membrane fouling. This is generally accomplished with rotating and vibrating membranes. The idea behind this is to provide a force that would be able to scour or shake off loosely bound particles on the surface of the membrane, before they achieve a stable integration into the existing cake layer/biofilm. Different studies showed the benefits of this approach, whereby a higher rotation speed has been associated with higher fouling mitigation, but only up to a certain threshold ([22], [23], and [24]).

5.4. Ultrasonic cleaning of membranes

An advanced method of physical cleaning of membranes is with the use of ultrasonic sound waves. These waves are in the frequency range of $>20\text{kHz}$ and act by agitating the particles in the membrane, thereby loosening them and causing them to become detached. The main advantage of this method is high flux recovery and the possibility to apply it in-situ [25].

5.5. Cell immobilization

This method limits the free movement of bacterial cells by one of two ways: attachment to a support (mostly biofilm carriers) or cell entrapment (CE) with the use of porous polymer matrices [26]. The former mainly refers to operating an attached growth system, whereas the latter can also offer some level of protection of the biomass from toxic compounds. Materials applied for the matrices range from natural materials such as alginate, agar, and carrageenan, to synthetic polymers including polyacrylamide, polyvinyl alcohol, xanthan gum etc. [5]. An important advantage of CE is that in addition to preventing the biomass from reaching the membrane, it also lowers the levels of bound SMP and EPS, which are known to contribute to fouling.

5.6. Improvements in chemical cleaning

The main innovation when it comes to chemical cleaning of MBR membranes comes in the form a novel biosurfactant – rhamnolipids. These compounds offer advantages in the form of lower cost, higher solubility and less toxicity than conventional methods [5]. Their mode of action is based on biofilm reduction and detachment [27]. It was also reported that, when added during reactor operation, they increased contact between bacteria and lipid molecules, thereby enhancing their removal [28].

5.7. Novel biological control methods

D-amino acids are compounds shown to be able to trigger biofilm disassembly even in trace amounts [29]. Since they can be produced and secreted by a number of bacterial species, they offer a low-cost strategy in fouling control. However, D-amino acids have been shown to be species-specific, which significantly limits their application.

In addition, some naturally derived compounds have also shown promise in biofilm inhibition. Those include extracts from ginger [30], garlic [31], ginseng [32] and brominated alkylidene lactams [33]. Their advantage is that they have low- to no toxicity to the biomass, and may offer a cheap solution depending on their accessibility.

5.8. Addition of engineered nanomaterials (ENMs)

Various engineered nanomaterials (ENMs) can be utilized in MBR systems for efficient fouling control. These materials have specific properties which make them particularly suitable for this purpose, such as antimicrobial ability, photocatalytic activity, and hydrophilicity. Among these ENMs are silver nanoparticles (NPs), graphene, graphene oxide, fullerenes, carbon nanotubes, titanium dioxide NPs etc. [34]. They can be used as membrane surface additions or supplied to the reactor directly. Some of the disadvantages of these systems include the potentially high cost and limited accessibility, as well as limited photocatalytic activity in systems with a high turbidity.

6. CONCLUSION

Membrane fouling is the major disadvantage of MBR systems and has, accordingly, received much attention in the literature. A large number of factors contributes to this phenomenon, which makes its mitigation much harder a task. Apart from established methods, researchers all over the world are constantly devising new ways to enrich the toolbox of reactor operators in their struggle to get fouling under control. Often several methods have to be used in conjunction in order to achieve the best results, and there is no single approach which suits all systems. Therefore, a delicate balance has to be found between gains (lower fouling propensity, improved flux etc.) and losses (cost, higher sludge production etc.) in the application of fouling control methods.

ACKNOWLEDGMENT

Author Amar Ćemanović is supported by the Scientific and Technological Research Council of Turkey (Tübitak) through the 2215 Graduate Scholarship Programme.

REFERENCES

- [1]. C.V. Smith, D.D. Gregorio and R.M. Talcott, "The use of ultrafiltration membranes for activated sludge separation", 24th Annual Purdue Industrial Waste Conference, Lafayette, IN pp. 130-1310, 1969.
- [2]. S. Judd, "The status of membrane bioreactor technology", Trends in Biotechnology, 26, 2, 109 – 116., 2008.
- [3]. H.-D. Park, I.-S. Chang and K.-J. Lee, Principles of Membrane Bioreactors for Wastewater Treatment, Boca Raton, FL, USA: CRC Press, Taylor and Francis Group, 2015.
- [4]. P. Le-Clech, V. Chen, T.A. Fane, "Fouling in membrane bioreactors used in wastewater treatment." J. Membr. Sci. 284 (1), 17–53, 2006.
- [5]. M. Bagheri, S.A. Mirbagheri, "Critical review of fouling mitigation strategies in membrane bioreactors treating water and wastewater." Bioresource Technology 258, 318–334, 2018.
- [6]. T.B. Rasmussen, M. Givskov, "Quorum sensing inhibitors: a bargain of effects." Microbiology 152 (4), 895–904, 2006.
- [7]. D.M Roche, J.T. Byers, D.S. Smith, et al., "Communications blackout? Do N-acylhomoserine-lactone-degrading enzymes have any role in quorum sensing?" Microbiology 150 (7), 2023–2028, 2004.
- [8]. K.-M. Yeon, W.-S. Cheong, H.-S. Oh, et al., "Quorum sensing: a new biofouling control paradigm in a membrane bioreactor for advanced wastewater treatment." Environ. Sci. Technol. 43 (2), 380–385, 2008.
- [9]. I.P. Molobela, "Protease and amylase enzymes for biofilm removal and degradation of extracellular polymeric substances (EPS) produced by Pseudomonas fluorescens bacteria." Afr. J. Microbiol. Res. 4 (14), 1515–1524, 2010.

- [10]. M. Loisel, K.W. Anderson, "The use of cellulase in inhibiting biofilm formation from organisms commonly found on medical implants." *Biofouling* 19 (2), 77–85, 2003.
- [11]. S. Te Poele, J. Van der Graaf, "Enzymatic cleaning in ultrafiltration of wastewater treatment plant effluent." *Desalination* 179 (1–3), 73–81, 2005.
- [12]. A. Branch, T. Trinh, G. Carvajal, et al., "Hazardous events in membrane bioreactors–Part 3: impacts on microorganism log removal efficiencies." *J. Membr. Sci.* 497, 514–523, 2016.
- [13]. R.M. Chaudhry, K.L. Nelson, J.r.E. Drewes, "Mechanisms of pathogenic virus removal in a full-scale membrane bioreactor." *Environ. Sci. Technol.* 49 (5), 2815–2822, 2015.
- [14]. S. Purnell, J. Ebdon, A. Buck, et al., "Bacteriophage removal in a full-scale membrane bioreactor (MBR)–implications for wastewater reuse." *Water Res.* 73, 109–117, 2015.
- [15]. W. Den, C.-J. Wang, "Removal of silica from brackish water by electrocoagulation pretreatment to prevent fouling of reverse osmosis membranes." *Sep. Purif. Technol.* 59 (3), 318–325, 2008.
- [16]. K. Bani-Melhem, M. Elektorowicz, "Development of a novel submerged membrane electro-bioreactor (SMEBR): performance for fouling reduction." *Environ. Sci. Technol.* 44 (9), 3298–3304, 2010.
- [17]. L. Liu, J. Liu, B. Gao, B., et al., "Fouling reductions in a membrane bioreactor using an intermittent electric field and cathodic membrane modified by vapor phase polymerized pyrrole." *J. Membr. Sci.* 394, 202–208, 2012.
- [18]. J.-P. Chen, C.-Z. Yang, J.-H. Zhou, et al., "Study of the influence of the electric field on membrane flux of a new type of membrane bioreactor." *Chem. Eng. J.* 128 (2), 177–180, 2007.
- [19]. O. Kulesha, Z. Maletskyi, H. Ratnaweera, "State-of-the-art of membrane flux enhancement in membrane bioreactor". *Cogent Engineering*, 5: 1489700, 2018.
- [20]. M.A.H. Johir, R. Aryal, S. Vigneswaran, et al., "Influence of supporting media in suspension on membrane fouling reduction in submerged membrane bioreactor (SMBR)." *Journal of Membrane Science*, 374(1–2), 121–128, 2011.
- [21]. M.A. Johir, S. Shanmuganathan, S. Vigneswaran, et al., (2013), "Performance of submerged membrane bioreactor (SMBR) with and without the addition of the different particle sizes of GAC as suspended medium." *Bioresource Technology*, 141, 13–18, 2013.
- [22]. D.-Y. Zuo, H.-J. Li, H.-T. Liu, et al., "A study on submerged rotating MBR for wastewater treatment and membrane cleaning." *Korean J. Chem. Eng.* 27 (3), 881–885, 2010.
- [23]. T. Jiang, H. Zhang, D. Gao, et al., "Fouling characteristics of a novel rotating tubular membrane bioreactor." *Chem. Eng. Process.: Process Intensif.* 62, 39–46, 2012.
- [24]. T. Jiang, H. Zhang, H. Qiang, et al., "Start-up of the anammox process and membrane fouling analysis in a novel rotating membrane bioreactor." *Desalination* 311, 46–53, 2013.
- [25]. L. M. Ruiz, J. I. Perez, A. Gómez et al., "Ultrasonic irradiation for ultrafiltration membrane cleaning in MBR systems: operational conditions and consequences." *Water Sci Technol*, 75 (4): 802-812., 2016.
- [26]. C. Juntawang, C. Rongsayamanont, E. Khan, "Entrapped cells-based-anaerobic membrane bioreactor treating domestic wastewater: performances, fouling, and bacterial community structure." *Chemosphere* 187, 147–155, 2017.
- [27]. L.H. Kim, Y. Jung, S.-J. Kim, et al., "Use of rhamnolipid biosurfactant for membrane biofouling prevention and cleaning." *Biofouling* 31 (2), 211–220, 2015.
- [28]. L. Qin, G. Zhang, Q. Meng, et al., "Enhanced submerged membrane bioreactor combined with biosurfactant rhamnolipids: performance for frying oil degradation and membrane fouling reduction." *Bioresour. Technol.* 126, 314–320, 2012.
- [29]. I. Kolodkin-Gal, D. Romero, S.G. Cao, et al., "D-Amino Acids Trigger Biofilm Disassembly." *Science* 328 (5978), 2010.
- [30]. H.S. Kim, H.D. Park, "Ginger Extract Inhibits Biofilm Formation by *Pseudomonas aeruginosa* PA14." *PLoS One* 8 (9), 2013.
- [31]. T. Bjarnsholt, P.O. Jensen, T.B. Rasmussen, et al. "Garlic blocks quorum sensing and promotes rapid clearing of pulmonary *Pseudomonas aeruginosa* infections." *Microbiol. Sgm* 151, 2005.
- [32]. H. Wu, B. Lee, L. Yang, et al., "Effects of ginseng on *Pseudomonas aeruginosa* motility and biofilm formation. *Fems Immunol.*" *Med. Microbiol.* 62 (1), 2011.
- [33]. U.A. Pereira, L.C.A. Barbosa, C.R.A. Maltha, et al., "Gamma-Alkylidene-gamma-lactones and isobutylpyrrol- 2(5H)-ones analogues to rubrolides as inhibitors of biofilm formation by Gram-positive and Gram-negative bacteria." *Bioorg. Med. Chem. Lett.* 24 (8), 1052, 2008-2008, 2014.
- [34]. F. Meng, S. Zhang, Y. Oh, et al., "Fouling in membrane bioreactors: An updated review." *Water Research* 114: 151-180, 2017.